

ΠΟΛΥΤΕΧΝΕΙΟ ΚΡΗΤΗΣ

ΓΕΝΙΚΟ ΤΜΗΜΑ



ΠΡΟΓΡΑΜΜΑ ΜΕΤΑΠΤΥΧΙΑΚΩΝ ΣΠΟΥΔΩΝ

ΕΦΑΡΜΟΣΜΕΝΕΣ ΕΠΙΣΤΗΜΕΣ ΚΑΙ ΤΕΧΝΟΛΟΓΙΑ

ΔΙΠΛΩΜΑΤΙΚΗ ΔΙΑΤΡΙΒΗ ΜΕΤΑΠΤΥΧΙΑΚΟΥ ΔΙΠΛΩΜΑΤΟΣ ΕΙΔΙΚΕΥΣΗΣ

ΚΑΤΕΥΘΥΝΣΗ : «ΜΗΧΑΝΙΚΗ ΚΑΙ ΤΕΧΝΟΛΟΓΙΑ ΥΛΙΚΩΝ ΚΑΙ ΚΑΤΑΣΚΕΥΩΝ»

**Development of an innovative damage detection monitoring system
for concrete structures using smart piezoelectric materials**

*Ανάπτυξη ενός καινοτόμου συστήματος παρακολούθησης βλάβης σε κατασκευές από
σκυρόδεμα με χρήση έξυπνων πιεζοηλεκτρικών υλικών*

ΤΣΙΣΤΡΑΚΗΣ Ε. ΣΤΑΥΡΟΣ

Επιβλέπων : Καθηγητής **Προβιδάκης Π. Κωνσταντίνος**

ΧΑΝΙΑ , 2013

ΔΙΠΛΩΜΑΤΙΚΗ ΔΙΑΤΡΙΒΗ ΜΕΤΑΠΤΥΧΙΑΚΟΥ ΔΙΠΛΩΜΑΤΟΣ ΕΙΔΙΚΕΥΣΗΣ

Τσιστράκης Ε. Σταύρος

αρ. μητρώου: 2010040267

e-mail: stsistrakis@isc.tuc.gr , stavros1510@hotmail.com

Η εργασία εγκρίθηκε από την ακόλουθη τριμελή συμβουλευτική επιτροπή:

1. Προβιδάκης Π. Κωνσταντίνος , Καθηγητής Πολυτεχνείου Κρήτης, Επιβλέπων
2. Σταυρουλάκη Μαρία, Λέκτωρ Πολυτεχνείου Κρήτης
3. Τσομπανάκης Ιωάννης, Αναπ. καθηγητής Πολυτεχνείου Κρήτης

Πέμπτη, 25 Ιουλίου 2013

ΔΙΕΥΘΥΝΣΗ ΕΡΓΑΣΤΗΡΙΟΥ:

ΠΟΛΥΤΕΧΝΕΙΟ ΚΡΗΤΗΣ, ΓΕΝΙΚΟ ΤΜΗΜΑ

ΕΡΓΑΣΤΗΡΙΟ ΕΦΑΡΜΟΣΜΕΝΗΣ ΜΗΧΑΝΙΚΗΣ

Κτήριο Επιστημών, Πανεπιστημιούπολη, Κουνουπιδιανά, 73100 Χανιά

τηλ. 2821037637

e-mail: cpprov@science.tuc.gr

DECLARATION

I hereby declare that the work presented here has been my independent work and has been performed during the course of my M.Sc. studies at the Department of Applied Sciences, Technical University of Crete, Chania.

All contributions drawn from external sources have been acknowledged with due reference to the literature.

ΔΗΛΩΣΗ

Δηλώνω υπεύθυνα ότι η παρούσα διατριβή είναι προϊόν ανεξάρτητης εργασίας μου που διεξήχθη κατά τις μεταπτυχιακές μου σπουδές στο Γενικό τμήμα του Πολυτεχνείου Κρήτης, στα Χανιά.

Για ότι δεδομένα ή πληροφορίες χρησιμοποίησα που προέρχονται από εξωτερικές πηγές έχουν δοθεί οι αρμόζουσες αναγνωρίσεις και αναφορές.

Contents

Acknowledgements	7
Abstract	8
Σύνοψη (Στα ελληνικά).....	10
Part I Basic Theory	33
1 Introduction.....	34
2 Wave propagation in solids	36
2.1 Stress-Strain relationships and equations governing elastic solids.....	36
2.2 Wave propagation in extended (isotropic and anisotropic) media	40
2.3 Wave propagation in reflection and refraction semi-extended media.....	42
2.4 Wave propagation in concrete	45
3 History and applications of piezoelectric materials	47
3.1 History of piezoelectricity and piezoelectric materials	47
3.2 Applications of piezoelectric materials	49
4 Electro-mechanical impedance (EMI) technique	53
4.1 Impedance	53
4.2 Structural Health Monitoring (SHM) systems and the Electro-Mechanical Impedance (EMI) technique	55
4.3 The Electro-mechanical principle	56
4.4 Existing PZT-Structure interaction models	58
4.5 Comparison with other NDE methods for concrete.....	64
Part II Experimental Procedure	67
5 Organization	68
6 Materials and methods	69
6.1 Concrete	69
6.2 PZT PIC 151	69
6.3 Epoxy adhesive	73
6.4 Silicon Rubber.....	73
6.5 Measurement System	75
6.6 Experimental data analysis.....	76
7 “Smart” aggregates	78
7.1 Aggregate No 4.....	81

7.2	Aggregate No 5	84
7.3	Aggregates No 6 and 7	85
7.4	Aggregate No 9	86
7.5	Aggregate No 10	89
7.6	Aggregate No 11	91
8	Monitoring of the curing process	93
8.1	Monitoring of the curing process of Cube 1 (14/12/2012)	99
8.2	Monitoring of the curing process of Beam 1 (4/2/2013)	103
8.2.1	Aggregate 4	103
8.2.2	Aggregate 7	107
8.3	Monitoring of the curing process of Cube 2 (24/4/2013)	111
8.4	Monitoring of the curing process of Beam 2 (24/4/2013)	115
8.4.1	Aggregate 11	115
8.4.2	Aggregate 10	118
8.5	Conclusions for monitoring of curing process	120
9	Damage Induction	121
9.1	Damage holes	121
9.2	Compression	128
9.3	Bending	134
9.3.1	Aggregate 10	136
9.3.2	Aggregate 11	139
9.3.3	Custom-made admittance measuring system to increase sensing area	141
9.4	Conclusions for damage detection	146
10	Conclusions and topics for further discussion	147
	Appendix A – Ferroelectricity and Piezoelectricity	149
	Appendix B – Perovskite structure	153
	References	156

Acknowledgements

First and foremost, I would like to thank my supervising professor Prof. K. P. Provdakis for the opportunity to carry out this master thesis and his overall guidance throughout the duration of my studies.

I would also like to thank all the staff of the Applied Mechanics Lab of the Science Department of the Technical University of Crete for their guidance, cooperation and patience and for welcoming me and making me feel a part of the lab.

Special thanks to PhD candidate Evangelos Liarakos without whose assistance this master thesis would never have been completed. From the hours spent during the creation and casting of concrete to his constant availability to help with any question that would arise from the experimental procedure.

Finally, I would also wish to thank my friends and family for their patience and support throughout my studies, especially M.Ch. for her help and support during the measurements for early age strength monitoring.

Abstract

In spite of substantial improvements in material strength and increased accuracy in analysis and design with the aid of digital computers, gradual deterioration of structures during prolonged usage cannot be completely ruled out. In 1987 a research made by National Materials Advisory Board in the U.S.A. showed that 253,000 bridges made of concrete demonstrated problems because of non durability of the concrete in less than 20 years of use [4]. Similar conclusions came up in similar researches in Canada concerning parking lot floors. Research showed that even in bridges made of high strength concrete (50-80 MPa), cracks with length of 1-3 m appeared on the deck in less than a month. Gardner and Scanlon demonstrated that high construction loads applied to immature concrete slabs lead to large non-recoverable creep deflections that have a significant impact on the long term deflections of the structure. The collapse of the Willow Island (West Virginia) cooling tower during its construction is another example that highlights the importance of early concrete strength monitoring, as the primary cause of the collapse, which killed 51 workers, was insufficient strength development of the concrete due to low temperature (midthirties Fahrenheit, 1-5 °C), a temperature at which a much longer time is required for the concrete to gain sufficient strength [23].

All the above evidence indicates that life expectancy of a concrete structure depends not only from concrete strength, but also from the efficiency of the curing process and the durability of the concrete which is linked with its permeability and the presence of cracks. It is estimated that about the one third of the annual construction budget is spent on repairs. In addition to the financial aspect, sudden collapse of a structure causes immense loss to lives especially in large scale constructions. Hence, the idea of equipping structures with sensors and actuators in an attempt to impart 'smartness' has great potential in cost-effective predictive maintenance of structures, particularly for high performance components not easily accessible for manual inspections.

The scientific community across the globe is thrusting significant efforts toward the development of new techniques for structural health monitoring (SHM) and non-destructive evaluation (NDE), which could be equally suitable for civil-structures, heavy machinery, aircraft and spaceships. In this endeavor, the advent of the smart materials and structures and the related technologies have triggered a new revolution. Smart piezoelectric-ceramic lead zirconate titanate (PZT) materials, for example, have recently emerged as high frequency impedance transducers for SHM and NDE. In this role, the PZT patches act as collocated actuators and sensors and employ ultrasonic vibrations (typically in 10-500 kHz range) to glean out a characteristic admittance or resistance 'signature' of the structure. The signature encompasses vital information governing the phenomenological nature of the structure, and can be analyzed to predict the onset of structural damages. As impedance transducers, the PZT patches exhibit excellent performance as far as damage sensitivity and cost-effectiveness are concerned. Typically, their sensitivity is high enough to capture any structural damage at the incipient stage,

well before it acquires detectable macroscopic dimensions. This new SHM/ NDE technique is popularly called the electro-mechanical impedance (EMI) technique in the literature.

Purpose of this master thesis is to extend the method using a smart aggregate, which is embedded into freshly poured concrete to monitor initial curing and subsequent structural health. The results show that the hydrating concrete has an effect on the sensing system and that it is sensitive enough to monitor the strength development of concrete. The response of the system to compressive testing is also investigated, and the initial results show a good correlation with previously published reports on compressive testing of concrete.

In the first part of this master thesis, a brief introduction in subjects important in understanding the EMI technique is attempted, such as wave propagation in solids, as well as a description of the recent theoretical and technological developments in the field of EMI technique.

Specifically, the first chapter of the first part of this master thesis is an introduction to the recently emerged EMI technique (was introduced the last 15 years), general scope of this method, comparison with other preexisting NDE and SHE techniques and finally drawbacks and areas of further research until commercialization is achieved.

The second chapter is a brief introduction in wave propagation in solids. It contains the stress-strain relationships and equations governing elastic solids (as the waves produced by PZTs are low in amplitude, we are only concerned about the elastic region), wave propagation in extended media and finally wave propagation in reflection and refraction in semi extended media. This theory covers the basics in our area of interest which is body waves (P and S) as well as surface waves (Rayleigh waves) and laws of reflection and refraction.

The third chapter attempts a brief presentation of the history of piezoelectricity and piezoelectric materials as well as their applications throughout the history. The fourth, and final chapter of the first part, is an introduction in fundamental meanings essential to understand the EMI technique, such as electrical and mechanical impedance, resistance, reactance, conductance, etc. It also presents the piezoelectric constitutive relations and describes the existing PZT-Structure interaction models.

The second part of this master thesis is the description of the experimental procedure. Specifically in the first chapter is an introduction to the experimental procedure that will later be described in detail. The second chapter is an analytical description of all the materials and instruments that were used to take the measurements.

The third chapter is a description of the “smart” aggregates that were later embedded in larger structures. It includes specimen preparation as well as data measurements that were made before they were embedded in cube and beam specimens.

The fourth chapter is the monitoring of the curing process of two cubic 150x150x150 mm and two beam 150x150x750 mm concrete specimens, respectively, using the embedded “smart” aggregates. Measurements are presented as well as conclusions and description of protecting the smart aggregate from the extremely aggressive conditions within the concrete.

The fifth chapter is a presentation of the results after inducing damage and compressing the cubic specimens and after bending the beam specimen.

Σύνοψη

Σκοπός της παρούσας διπλωματικής διατριβής, είναι η δημιουργία ενός καινοτόμου συστήματος μη-καταστρεπτικής αξιολόγησης κατασκευών σκυροδέματος, με χρήση εμβαπτισμένων πιεζοηλεκτρικών κεραμικών υλικών. Αυτό επιτυγχάνεται με τη χρήση έξυπνων αδρανών (τα οποία θα περιγραφούν αναλυτικά στη συνέχεια) τα οποία εμβαπτίζονται στη μάζα της κατασκευής κατά τη διαδικασία της σκυροδέτησης.

Η έρευνα στον τομέα της ανάπτυξης συστημάτων παρακολούθησης της υγείας των κατασκευών (SHM-Structural Health Monitoring) καθώς και συστημάτων εντοπισμού βλάβης και μη-καταστρεπτικής αξιολόγησης κατασκευών (NDE-Non Destructive Evaluation) έχει γνωρίσει ιδιαίτερη ανάπτυξη τα τελευταία χρόνια. Πολλά εργαστήρια τόσο εμπορικά όσο και ακαδημαϊκά έχουν διατυπώσει διάφορες μεθοδολογίες στον τομέα αυτό. Οι δυναμικές μέθοδοι, για παράδειγμα, διεγείρουν την κατασκευή σε χαμηλές συχνότητες ώστε να ληφθούν οι πρώτες ιδιοσυχνότητες και ιδιομορφές της κατασκευής. Οποιαδήποτε αλλαγή στα δυναμικά χαρακτηριστικά της κατασκευής θα οφείλεται στην ύπαρξη βλάβης σε αυτή. Βασικό μειονέκτημα της μεθόδου είναι ότι ασχολείται με τις πρώτες ιδιομορφές της κατασκευής και σε επίπεδο κατασκευής και όχι σε τοπικό με αποτέλεσμα να μην είναι αποτελεσματική στον εντοπισμό τοπικής βλάβης. Μια ζημιά ανιχνεύσιμη με την μέθοδο αυτή, ενδεχομένως να είναι ήδη μοιραία για την κατασκευή.

Μια άλλη κατηγορία συστημάτων SHM/NDE είναι τα τοπικής παρακολούθησης συστήματα όπως η χρήση υπερήχων (ultrasonic technique), ακουστικές μέθοδοι (impact echo technique), χρήση ακτίνων x (X-ray radiography) κ.α.. Οι τεχνικές αυτές δίνουν καλά αποτελέσματα στον εντοπισμό τοπικών βλαβών, αλλά παρουσιάζουν διάφορα μειονεκτήματα, όπως ογκώδης και ακριβός εξοπλισμός, ανάγκη διακοπής λειτουργίας της κατασκευής κάνοντάς τις ακατάλληλες για ένα συνεχές σύστημα SHM. Ειδικότερα η χρήση υπερήχων, που βασίζεται στην διάδοση ελαστικών κυμάτων και την ανάκλαση μέσα στο υλικό για την αναγνώριση ανομοιογενειών ή βλάβης, έχει αποδειχθεί ιδιαίτερα αποτελεσματική στον εντοπισμό βλάβης. Παρόλα αυτά, η περιπλοκότητα των αποτελεσμάτων τα οποία λαμβάνονται στο πεδίο του χρόνου και χρειάζονται επεξεργασία, τα ακριβά μηχανήματα και προγράμματα επεξεργασίας καθώς και η αδυναμία ελέγχου του συνόλου της κατασκευής, ειδικά σε μεγάλο μεγέθους κατασκευές, παρά μόνο τοπικά σε επιλεγμένα και προσβάσιμα σημεία της, καθιστούν την μέθοδο αυτή ακατάλληλη για ένα διαδραστικό σύστημα ελέγχου.

Η μέθοδος της ηλεκτρομηχανικής εμπέδησης (Electro-Mechanical Impedance – EMI) έχει κάνει σημαντικά βήματα προόδου τα τελευταία 15 χρόνια. Οι εφαρμογές της μεθοδολογίας αυτής περιορίζονταν μέχρι το πρόσφατο παρελθόν στον τομέα της αεροναυπηγικής, όμως πολλοί ερευνητές προσπαθούν να επεκτείνουν τη χρήση της και σε κατασκευές πολιτικού μηχανικού. Η τεχνική αυτή βασίζεται στην παρακολούθηση της μηχανικής εμπέδησης μέσω της ηλεκτρομηχανικής «υπογραφής» της διαπερατότητας (admittance) ή εμπέδησης (impedance) ενός πιεζοηλεκτρικού κεραμικού πλακιδίου (PZT), χρησιμοποιώντας το ευθύ και αντίστροφο πιεζοηλεκτρικό φαινόμενο. Το πλακίδιο διεγείρεται μέσω ενός Impedance Analyzer με εναλλασσόμενο ρεύμα (διαφοράς δυναμικού 1-2 Volt για τους τωρινούς διαθέσιμους

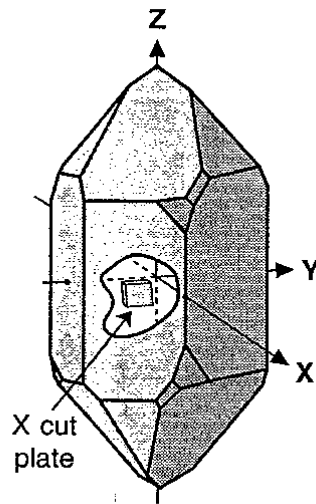
Analyzers), σαρώνοντας μια μπάντα συχνοτήτων, συνήθως 10-500 kHz. Το παλλόμενο πλακίδιο διεγείρει την κατασκευή και η απόκριση της κατασκευής μετريέται μέσω της μετρούμενης ηλεκτρομηχανικής διαπερατότητας ή εμπέδησης του πλακιδίου, δρώντας ταυτόχρονα το ίδιο πλακίδιο τόσο σαν διεγέρτης όσο και σαν αισθητήρας. Έτσι, λαμβάνουμε διαγράμματα αγωγιμότητας ή εμπέδησης ως προς την συχνότητα τα οποία είναι χαρακτηριστικά της κατασκευής και αποτελούν την «υπογραφή» της. Οποιαδήποτε αλλαγή στην κατάσταση της κατασκευής εκδηλώνεται σαν αλλαγή στο αντίστοιχο διάγραμμα, θεωρώντας την αρχική κατάσταση σαν κατάσταση αναφοράς.

Η βασικές αρχές της μεθοδολογίας αυτής είναι ίδιες με αυτές των δυναμικών μεθόδων με την διαφορά της μεγάλης ευαισθησίας σε τοπικές βλάβες. Τα κεραμικά πλακίδια μένουν μόνιμα στην κατασκευή χωρίς να επηρεάζουν λόγω του πολύ μικρού μεγέθους τους τα δυναμικά χαρακτηριστικά της κατασκευής. Επίσης δεν χρειάζεται σύνθετη επεξεργασία των αποτελεσμάτων, καθώς αυτά λαμβάνονται κατευθείαν στο πεδίο των συχνοτήτων.

Η προτεινόμενη στην παρούσα εργασία μεθοδολογία με την εμβάπτιση των πλακιδίων μέσω στη μάζα της κατασκευής μέσω ενός έξυπνου αδρανούς έχει το πλεονέκτημα έναντι της συμβατικής EMI της δυνατότητας παρακολούθησης της πορείας ενυδάτωσης του σκυροδέματος από την πρώτη ώρα μετά την σκυροδέτηση. Η συμβατική EMI απαιτεί σκληρυμένη επιφάνεια για την κόλληση του PZT καθώς και τουλάχιστον 24 ώρες για την σκλήρυνση της εποξικής κόλλας. Έτσι η συμβατική EMI αγνοεί το πολύ σημαντικό διάστημα των πρώτων 36 ωρών το οποίο είναι πολύ σημαντικό στην ανάπτυξη της αντοχής του σκυροδέματος, καθώς σε αυτό το διάστημα σχηματίζεται η μικροδομή του. Με αυτόν τον τρόπο μπορεί να επιταχυνθεί η πορεία της κατασκευής καθώς σε περίπτωση ανάπτυξης της απαιτούμενης αντοχής μπορεί να επιταχυνθεί η διαδικασία του ξεκαλουπώματος με σημαντικό αντίκτυπο στον χρόνο καθώς και στο κόστος κατασκευής. Παρόλα αυτά πρέπει να τονιστεί ότι αυξάνεται η περιπλοκότητα της καθώς ο αισθητήρας πρέπει να είναι προστατευμένος από τις εχθρικές συνθήκες μέσα στο σκυρόδεμα.

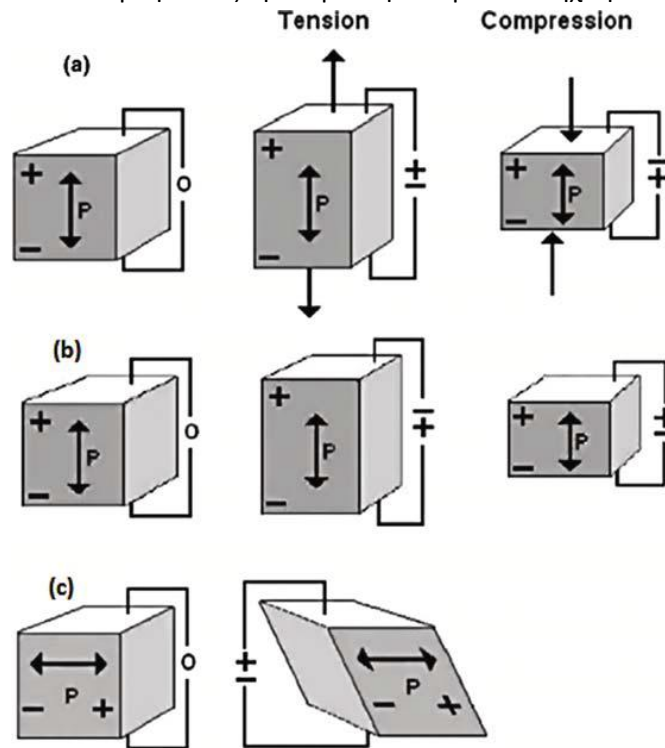
Ιστορική αναδρομή και εφαρμογές πιεζοηλεκτρικών υλικών

Η υποψία ότι σε μερικούς κρυστάλλους υπήρχε δυνατότητα παραγωγής ηλεκτρικού ρεύματος με την εφαρμογή μηχανικής τάσης είχε προταθεί από τον Charles Coulomb [36]. Μελλοντικές μελέτες από τους Hauy [37] και Becquerel [38] από το 1825 συνηγορούσαν σε αυτή την κατεύθυνση, όμως αδιαμφισβήτητη απόδειξη δεν υπήρξε παρά μόνο μετά από έξι δεκαετίες. Η απόδειξη δόθηκε από τους αδελφούς Curie [39] το 1880 στο πανεπιστήμιο του Παρισιού μελετώντας κρυστάλλους quartz. Παρατηρήθηκε ότι για ορισμένες τομές του κρύσταλλου (X cut quartz) με την εφαρμογή βάρους πάνω του εμφανιζόταν διαφορά δυναμικού, η ένταση του οποίου ήταν ανάλογη του εφαρμοζόμενου βάρους (ευθύ πιεζοηλεκτρικό φαινόμενο).



Εικόνα 1 Right-handed quartz crystal and an X cut plate [32] (D. F. Jones, S. E. Prasad, J. B. Wallace, *Piezoelectric Materials and Their Applications*)

Το αντίστροφο πιεζοηλεκτρικό φαινόμενο είχε προβλεφθεί από τον Lippmann [40] το 1881 μέσω των αρχών της θερμοδυναμικής, πριν επιβεβαιωθεί πειραματικά πάλι από τους αδελφούς Curie. Μετά από τις δημοσιεύσεις αυτές, προτάθηκε από τον Hankel ο όρος πιεζοηλεκτρισμός που προκύπτει από το ελληνικό ρήμα πιέζω. Έτσι οι όροι πιεζοηλεκτρισμός καθώς και το ευθύ και αντίστροφο πιεζοηλεκτρικό φαινόμενο εισήχθησαν στην βιβλιογραφία.



Εικόνα 2 Schematic representations of the longitudinal direct (a), converse (b), and shear (c) piezoelectric effects [34] (A.L. Kholkin, N. A. Pertsev, A. V. Goltsev, *Piezoelectric and Acoustic Materials for Transducer Application*)

Οι πρώτη εφαρμογή του πιεζοηλεκτρισμού ήταν μια συσκευή μέτρησης δύναμης και ηλεκτρικού φορτίου πατενταρισμένη από τους αδελφούς Curie το 1887 [46]. Στις αρχές του 1917 οι πρώτοι υποθαλάσσιοι αισθητήρες για μέτρηση βάθους δημιουργήθηκαν από τον Paul Langevin στο School of Industrial Physics and Chemistry του Παρισιού [47]. Επίσης το 1919, ο Nicolson [48] απέδειξε την χρήση κρυστάλλων άλατος Rochelle σε ηχεία, μικρόφωνα, ακουστικά τηλεφώνου και πικ απ. Μετά από προσπάθειες των Cady [44] και Pierce [49] στις αρχές της δεκαετίας του 1920 φτιάχτηκαν οι πρώτοι παλμογράφοι με χρήση κρυστάλλων. Επίσης οι κρύσταλλοι χρησιμοποιήθηκαν στην δεκαετία του 1940 για συστήματα ραντάρ.

Οι Jaffe, Cook και Jaffe [54] ανέπτυξαν και δημιούργησαν τα πρώτα πολυκρυσταλλικά πιεζοηλεκτρικά κεραμικά (barium titanate $BaTiO_3$) στα 1940. Με την διαδικασία της πόλωσης και την δημιουργία των κεραμικών, η χρήση των κρυστάλλων περιορίστηκε και τελικά αντικαταστάθηκαν πλήρως. Ένα από τα σημαντικότερα πλεονεκτήματα έναντι των κρυστάλλων είναι η μεγάλη ποικιλία σε σχήματα και μεγέθη καθώς και η δυνατότητα καθορισμού της διεύθυνσης πόλωσης. Τα κεραμικά $BaTiO_3$ χρησιμοποιήθηκαν από το 1947 σε φωνόγραφους, ενώ στη δεκαετία του '50 σε επιταχυνσιογράφους και σε συστήματα κατεύθυνσης πυραύλων.

Διάφορα άλλα κεραμικά προτάθηκαν στην δεκαετία του 1950 όπως τα lead titanate ($PbTiO_3$) [66, 67], lead zirconate ($PbZrO_3$) [68, 69], lead metaniobate ($PbNb_2O_6$) [70], και lead zirconate titanate [$Pb(Zr,Ti)O_3$] [71, 72, 73]. Οι εφαρμογές των κεραμικών αυτών περιλαμβάνουν αναφλεκτήρες, παραγωγή και εγγραφή ήχου, μικρόφωνα, ακουστικά, ηχεία, ρολόγια κ.α..

Μέθοδος της ηλεκτρομηχανικής εμπέδησης (EMI technique)

Με τον όρο εμπέδηση ή σύνθετη αντίσταση εννοούμε την βασική ηλεκτρική παράμετρο που χαρακτηρίζει όλα τα ηλεκτρονικά κυκλώματα. Ορίζεται ως ο λόγος της διαφοράς δυναμικού προς την ένταση του ρεύματος και είναι μέτρο της αντίστασης που παρουσιάζει ένα υλικό όταν διαπερνάται από ηλεκτρικό ρεύμα. Στην περίπτωση συνεχούς ρεύματος ταυτίζεται με την ωμική αντίσταση. Στην περίπτωση εναλλασσόμενου ρεύματος, πρόκειται για έναν μιγαδικό αριθμό με πραγματικό μέρος (R_s - resistance – ωμική αντίσταση) και φανταστικό μέρος (X_s - reactance – ανάδραση). Το αντίστροφο μέγεθος ορίζεται σαν αγωγιμότητα το οποίο είναι επίσης μιγαδικό μέγεθος με πραγματικό μέρος (G_p - Conductance – αγωγιμότητα) και φανταστικό μέρος (B_p - Susceptance – επιδεκτικότητα).

Ο όρος μηχανική εμπέδηση, ορίζεται σαν ο λόγος της δύναμης που ασκείται σε ένα σημείο της κατασκευής προς την ταχύτητα απόκρισης στο σημείο αυτό και είναι μέτρο της αντίστασης της κατασκευής στην κίνηση. Δηλαδή:

$$Z = \frac{F}{\dot{u}} = \frac{F_0 \cdot e^{j\omega t}}{\dot{u}_0 \cdot e^{j(\omega t - \varphi)}} = \frac{F_0}{\dot{u}_0} \cdot e^{j\varphi} \quad (1)$$

Στις συχνότητες συντονισμού η μηχανική εμπέδηση έχει μικρότερο μέγεθος. Αντίστροφο μέγεθος είναι η κινητικότητα της κατασκευής.

Πίνακας 1 Impedance terms and equations

Parameter	Quantity	Symbol	Formula
Z	Εμπέδηση (Σύνθετη αντίσταση)	Ohm, Ω	$Z = R_s + j \cdot X_s = \frac{1}{Y} = Z \cdot e^{j\theta}$
Z	Μέτρο της εμπέδησης	Ohm, Ω	$ Z = \sqrt{R_s^2 + X_s^2} = \frac{1}{ Y }$
R _s	Αντίσταση, πραγματικό μέρος Z	Ohm, Ω	$R_s = \frac{G_p}{G_p^2 + B_p^2}$
X _s	Ανάδραση, φανταστικό μέρος Z	Ohm, Ω	$X_s = -\frac{B_p}{G_p^2 + B_p^2}$
Y	Αγωγιμότητα	Siemens, S	$Y = G_p + j \cdot B_p = \frac{1}{Z} = Y \cdot e^{j\varphi}$
Y	Μέτρο της αγωγιμότητας	Siemens, S	$ Y = \sqrt{G_p^2 + B_p^2} = \frac{1}{ Z }$
G _p	Αγωγιμότητα,πραγματικό μέρος Y	Siemens, S	$G_p = \frac{R_s}{R_s^2 + X_s^2}$
B _p	Επιδεκτικότητα,φανταστικό μέρος Y	Siemens, S	$B_p = -\frac{X_s}{R_s^2 + X_s^2}$

Η ηλεκτρομηχανική αρχή στα πιεζοηλεκτρικά υλικά

Το φαινόμενο του πιεζοηλεκτρισμού εμφανίζεται σε ορισμένες κλάσεις μη κεντροσυμμετρικών κρυστάλλων, στους οποίους τα δίπολα υπόκεινται σε μηχανική παραμόρφωση. Οι ίδιοι κρύσταλλοι εμφανίζουν και το αντίστροφο φαινόμενο, δηλαδή εμφανίζουν μηχανική παραμόρφωση όταν βρίσκονται σε ηλεκτρικό πεδίο. Τα πιεζοηλεκτρικά κεραμικά πλακίδια (PZT) παίζουν σημαντικό ρόλο στην μέθοδο αυτή. Η ηλεκτρική φόρτιση και η παραμόρφωσή τους εκφράζεται μαθηματικά με τις ακόλουθες σχέσεις [30]:

$$D_i = \overline{\varepsilon_{ij}^T} \cdot E_j + d_{im} \cdot T_m \quad (2)$$

$$S_k = d_{jk} \cdot E_j + \overline{s_{km}^E} \cdot T_m \quad (3)$$

όπου:

D → ηλεκτρική μετατόπιση

S_k → μηχανική παραμόρφωση

E_j → ένταση ηλεκτρικού πεδίου

T_m → μηχανική τάση

$\overline{\varepsilon_{ij}^T}$ → σύνθετη ηλεκτρική διαπερατότητα του PZT για σταθερή τάση

d_{im} και d_{jk} → πιεζοηλεκτρικές σταθερές παραμόρφωσης

$\overline{s_{km}^E}$ → σταθερές ελαστικής συμβατότητας για σταθερή ένταση ηλεκτρικού πεδίου.

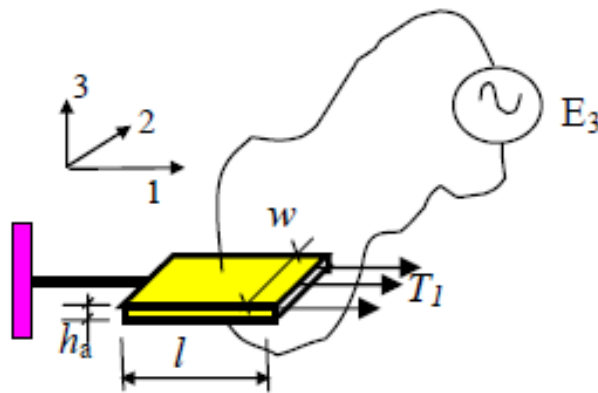
Οι δείκτες 'T' και 'E' εκφράζουν ότι η ποσότητα μετρήθηκε για σταθερές συνθήκες τάσης και έντασης ηλεκτρικού πεδίου.

Έστω ένα PZT όπως φαίνεται στην εικόνα 3, κάτω από σταθερό ηλεκτρικό πεδίο E_3 στη διεύθυνση 3 και τάση T_1 στη διεύθυνση 1, όπως στην περίπτωση των πειραμάτων της εργασίας. Το πλακίδιο συστέλλεται και διαστέλλεται στη διεύθυνση 1 όταν το ηλεκτρικό πεδίο εφαρμόζεται στη διεύθυνση 3. Οι εξισώσεις (2) και (3) γίνονται [30]:

$$D_3 = \overline{\varepsilon_{33}^T} \cdot E_3 + d_{31} \cdot T_1 \quad (4)$$

$$S_1 = d_{31} \cdot E_3 + \frac{T_1}{Y_{11}^E} \quad (5)$$

όπου $\overline{Y_{11}^E} = Y_{11}^E(1 + \eta_j)$ το σύνθετο μέτρο ελαστικότητας του PZT

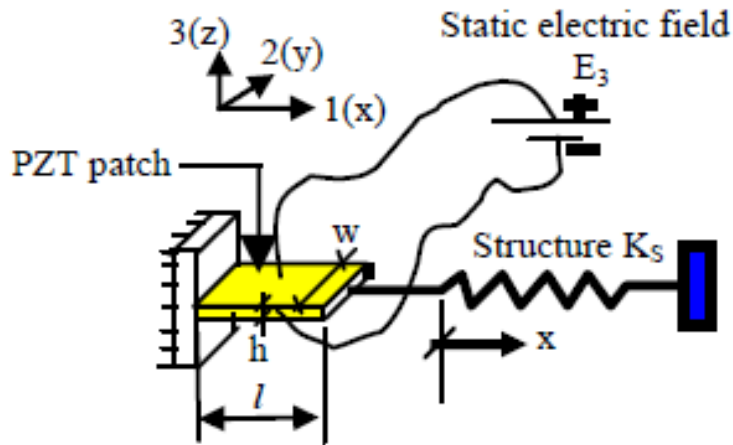


Εικόνα 3 A PZT patch under electric field and mechanical stress [18] (S. Bhalla, A. Gupta, *Modelling Shear Lag Phenomenon for Adhesively Bonded Piezo-Transducers*)

Η εξίσωση (4) είναι η έκφραση για το ευθύ πιεζοηλεκτρικό φαινόμενο, δηλαδή δημιουργία διαφοράς δυναμικού στους πόλους του για εφαρμογή μηχανικής τάσης. Με την ιδιότητα του αυτή, το PZT λειτουργεί σαν αισθητήρας. Η εξίσωση (5) είναι η έκφραση για το αντίστροφο πιεζοηλεκτρικό φαινόμενο, δηλαδή μηχανική παραμόρφωση για εφαρμογή διαφοράς δυναμικού στους πόλους του PZT.

Μοντέλο αλληλεπίδρασης PZT - κατασκευής

Τα τελευταία 15 χρόνια έγιναν διάφορες προτάσεις για την μοντελοποίηση του συστήματος PZT – κατασκευής. Η αρχή έγινε με το «στατικό» μοντέλο των Crawley και De Luis (1987) [9] το οποίο αντικαταστάθηκε αργότερα από το μοντέλο της εμπέδησης (impedance approach) του Liang, et al. (1994) [30]. Το στατικό μοντέλο θεωρούσε την δύναμη του διεγέρτη ανεξάρτητη της συχνότητας βασιζόμενο σε αρχές στατικής. Όμως η παραδοχή αυτή οδηγούσε σε σημαντικά σφάλματα, ιδιαίτερα στις συχνότητες συντονισμού.



Εικόνα 4 Static approach modeling of PZT-Structure interaction stress [18] (S. Bhalla, A. Gupta, *Modelling Shear Lag Phenomenon for Adhesively Bonded Piezo-Transducers*)

Για να εξαλείφει η συγκεκριμένη αδυναμία του εν λόγω μοντέλου, προτάθηκε το μοντέλο της εμπέδησης, όπου σε αντίθεση με το στατικό μοντέλο που η κατασκευή προσομοιάζονταν σαν ένα ελατήριο δυσκαμψίας K , ο Liang και οι συνεργάτες του προσομοίωσαν την κατασκευή σαν μηχανική εμπέδηση Z_s , βασισμένη στις εξισώσεις δυναμικής ισορροπίας και όχι της στατικής. Στην εικόνα 5 φαίνεται το μοντέλο των Liang, et al. Η εξίσωση της κίνησης στην περίπτωση αυτή δίνεται από τον [30]:

$$\overline{Y^E} \frac{\partial^2 u}{\partial x^2} = \rho \frac{\partial^2 u}{\partial t^2} \quad (6)$$

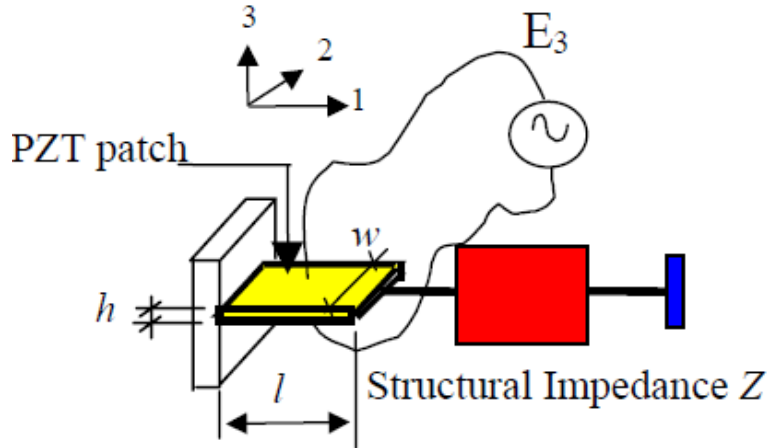
όπου u η μετατόπιση σε οποιοδήποτε σημείο του PZT στην διεύθυνση 1 για οποιαδήποτε χρονική στιγμή t . Η μηχανική εμπέδηση Z_s συνδέεται μαθηματικά με την F και την ταχύτητα \dot{u} , με τον τύπο :

$$F = -Z_s \cdot \dot{u} \quad (7)$$

όπου το αρνητικό πρόσημο δείχνει ότι μια θετική μετατόπιση (ή ταχύτητα) προκαλεί μια θλιπτική δύναμη στο PZT. Επίσης αντί για την στατική δυσκαμψία του διεγέρτη, δηλ του PZT, έχουμε την μηχανική του εμπέδηση η οποία ορίζεται από τον τύπο:

$$Z_a = \frac{k \cdot w \cdot h \cdot \overline{Y^E}}{j \cdot \omega \cdot \tan(kl)} \quad (8)$$

λαμβάνοντας υπ όψιν την δυναμική δυσκαμψία και απόσβεση του διεγέρτη.



Εικόνα 5 Liang's impedance approach modeling of PZT-Structure interaction [18] (S. Bhalla, A. Gupta, *Modelling Shear Lag Phenomenon for Adhesively Bonded Piezo-Transducers*)

Χρησιμοποιώντας την καταστατική εξίσωση PZT και ολοκληρώνοντας την πυκνότητα φόρτισης ως προς την επιφάνεια του μισού PZT ($x = 0$ to l), ο Liang και οι συνεργάτες του κατέληξαν στην ακόλουθη έκφραση για την σύνθετη ηλεκτρομηχανική αγωγιμότητα (αντίστροφο της εμπέδησης) για μισό μήκος του:

$$\bar{Y} = G + B \cdot j = \omega \cdot j \cdot \frac{w \cdot l}{h} \cdot \left[(\bar{\epsilon}_{33}^T - d_{31}^2 \cdot \bar{Y}^E) + \left(\frac{Z_a}{Z_s + Z_a} \right) \cdot d_{31}^2 \cdot \bar{Y}^E \cdot \left(\frac{\tan \kappa \cdot l}{\kappa \cdot l} \right) \right] \quad (9)$$

όπου w , l και h οι διαστάσεις του PZT, d_{31} η πιεζοηλεκτρική σταθερά παραμόρφωσης για τους άξονες 1-3 axes και ω η κυκλική συχνότητα. $\bar{Y}^E = Y^E \cdot (1 + n \cdot j)$ είναι το σύνθετο μέτρο ελαστικότητας PZT (για σταθερό ηλεκτρικό πεδίο) και $\bar{\epsilon}_{33}^E = \epsilon_{33}^E \cdot (1 - \delta \cdot j)$ η σύνθετη ηλεκτρική διαπερατότητα (για σταθερή τάση), με τα σύμβολα n και δ να αναπαριστούν τους συντελεστές μηχανικής και ηλεκτρικής απώλειας αντίστοιχα. Το Z_a παριστάνει την μηχανική εμπέδηση του PZT όπως ορίζεται από την εξίσωση (8) με το k , ο κυματάριθμος, να σχετίζεται με την πυκνότητα ρ και το μέτρο ελαστικότητας \bar{Y}^E του PZT με την εξίσωση:

$$k = \omega \cdot \sqrt{\frac{\rho}{Y^E}} \quad (10)$$

Στις πραγματικές εφαρμογές όπου το PZT κολλάται στην επιφάνεια της κατασκευής, εικόνα 6, το σύστημα μπορεί να περιγραφεί σαν μηχανική εμπέδηση σε κάθε πλευρά PZT. Στην περίπτωση αυτή, το l συμβολίζει το μισό μήκος του PZT και η εξίσωση (9) πρέπει να πολλαπλασιαστεί επί 2.

$$\bar{Y} = G + B \cdot j = 2 \cdot \omega \cdot j \cdot \frac{w \cdot l}{h} \cdot \left[(\bar{\epsilon}_{33}^T - d_{31}^2 \cdot \bar{Y}^E) + \left(\frac{Z_a}{Z_s + Z_a} \right) \cdot d_{31}^2 \cdot \bar{Y}^E \cdot \left(\frac{\tan \kappa \cdot l}{\kappa \cdot l} \right) \right] \quad (11)$$

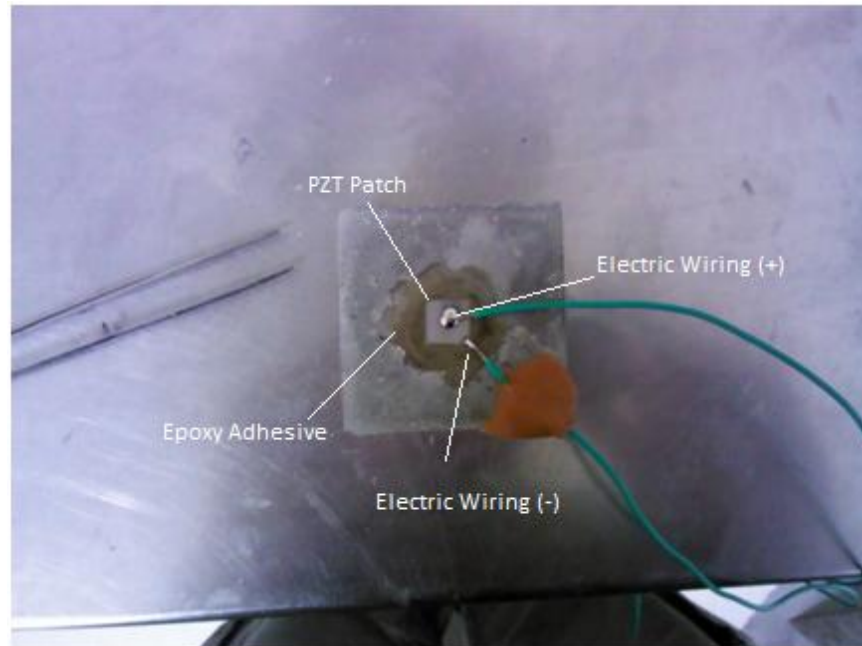
Είναι εμφανές από την εξίσωση (11) ότι οποιαδήποτε αλλαγή στην μηχανική εμπέδηση της κατασκευής θα αλλάξει την υπογραφή της ηλεκτρικής αγωγιμότητας του PZT (admittance signature). Με άλλα λόγια, η δομική ακεραιότητα της κατασκευής (καθώς μεγέθη όπως αντοχή και μέτρο ελαστικότητας συνδέονται με την μηχανική εμπέδηση) μπορεί να αξιολογηθεί μετρώντας την σύνθετη ηλεκτρική αγωγιμότητα του PZT. Η σύνθετη ηλεκτρική αγωγιμότητα όπως φαίνεται και από την εξίσωση είναι μιγαδικός αριθμός. Το G , το πραγματικό μέρος, ονομάζεται αγωγιμότητα ενώ το B , το φανταστικό μέρος, ονομάζεται επιδεκτικότητα. Στις τεχνικές SHM χρησιμοποιούνται συνήθως το πραγματικό μέρος της αγωγιμότητας και της εμπέδησης καθώς οι αλλαγές στην υπογραφή είναι εμφανής από τις απλές μετρήσεις που λαμβάνουμε από τον Analyzer. Τα φανταστικά μέρη επίσης αλλάζουν, όμως οι αλλαγές είναι ανεπαίσθητες και για να γίνει αξιολόγηση της δομικής κατάστασης της κατασκευής από αυτές χρειάζεται περεταίρω επεξεργασία. Οι αλλαγές είναι ανεπαίσθητες λόγω της έντονης λειτουργίας του PZT σαν πυκνωτή στις συχνότητες που εξετάζουμε.

«Έξυπνα» αδρανή

Η εμφάνιση των πιεζοηλεκτρικών μέσα στη μάζα των κατασκευών σκυροδέματος έγινε μέσω των «έξυπνων» αδρανών. Πρόκειται για κυβικά δοκίμια ακμής 50 mm σκληρυμένης τσιμεντόπαστας στα οποία στο κέντρο τους είναι κολλημένο ένα πιεζοηλεκτρικό κεραμικό πλακίδιο PZT διαστάσεων 10x10x0.2 mm. Αποτελούνται από δύο κομμάτια μεγέθους 50x50x25 mm όπου στο ένα κολλητείται το PZT. Έπειτα τοποθετείται μια λεπτή στρώση σιλικόνης πάχους περίπου 2 χιλιοστών (τόσο ώστε να καλυφθούν τα καλώδια) και από πάνω τοποθετείται το δεύτερο κομμάτι 50x50x25 mm (εικόνες 6, 7). Η αναλογία νερού/τσιμέντου είναι 0.4.

Η κατασκευή αυτή ουσιαστικά προσομοιάζει ένα κυβικό δοκίμιο με μια ρωγμή στην μέση. Η τοποθέτηση της στρώσης σιλικόνης γίνεται για να προστατευτεί το PZT από τις περιβαλλοντικές συνθήκες, την υγρασία και τις έντονες θερμοκρασιακές διαφορές όπου επηρεάζουν τις μετρήσεις. Επίσης το δεύτερο κομμάτι σκληρυμένης τσιμεντόπαστας τοποθετείται για να προστατεύσει το PZT από κρούσεις καθώς και για να προστατέψει την στρώση σιλικόνης από σκίσιμο από τις τάσεις που αναπτύσσονται στο εσωτερικό του φρέσκου σκυροδέματος.

Τα αδρανή αυτά τοποθετούνται σε δοκίμια σκυροδέματος, συγκεκριμένα σε δύο κυβικά δοκίμια διαστάσεων 15x15x15 mm και δύο δοκούς διαστάσεων 15x15x75 mm. Η αναλογία σκυροδέτησης είναι 1:0.62:1.36:1.35:2.75 αντίστοιχα για τσιμέντο, νερό, άμμο, γαρμπίλι, και χαλίκι (αναλογία μάζα προς μάζα τσιμέντου).



Εικόνα 6 PZT patch agglutinated on cement paste specimen ("Smart" aggregate)



Εικόνα 7 Final form of "smart" aggregates

Στις επόμενες σελίδες ακολουθούν εικόνες από την διαδικασία της σκυροδέτησης (εικόνες 8, 9). Τα έξυπνα αδρανή τοποθετήθηκαν στο κέντρο των κυβικών δοκιμίων, ενώ σε κάθε δοκό τοποθετήθηκαν δύο, σε απόσταση 110 mm εκατέρωθεν του μέσου της δοκού και σε απόσταση 220 mm μεταξύ τους.



Εικόνα 8 Smart aggregate inside the cubic specimen



Εικόνα 9 Creation of the beam specimen

Χρησιμοποιούμενα υλικά και επεξεργασία αποτελεσμάτων

Για την δημιουργία των δοκιμών καθώς και των έξυπνων αδρανών χρησιμοποιήθηκε τσιμέντο TITAN CEM IV/B 32.5 N. Για την κόλληση του PZT στην επιφάνεια της σκληρυμένης τσιμεντόπαστας χρησιμοποιήθηκε εποξική κόλλα δύο συστατικών Bison Epoxy Universal, με αναλογία ανάμιξης 1:1. Η κόλλα σε συνθήκες δωματίου παραμένει εργάσιμη για 1.5 ώρες ενώ ο απαιτούμενος χρόνος σκλήρυνσης είναι 24 ώρες. Η σιλικόνη που επιλέχτηκε για την προστασία του PZT ήταν η Dow Corning 3140 RTV Coating.

Για την λήψη των μετρήσεων χρησιμοποιήθηκε ο Quadtech 7600 Precision LCR meter. Το μηχάνημα έχει δυνατότητα καταγραφής 200 τιμών σε κάθε σάρωση. Για μεγαλύτερη ακρίβεια στις μετρήσεις το διάστημα σάρωσης 10-500 kHz χωρίστηκε σε τρία μέρη, 10-100, 100-300 και 300-500 kHz για μεγαλύτερη ακρίβεια, λαμβάνοντας τελικά 600 τιμές ανά σάρωση.

Επειδή τα διαγράμματα που λαμβάνονται από τις μετρήσεις με τον analyzer δίνουν μόνο μια ποιοτική προσέγγιση για την κατάσταση της κατασκευής μέσω της οπτικής σύγκρισης τους με την κατάσταση αναφοράς, ακατάλληλη για ένα on line σύστημα παρακολούθησης της δομικής κατάστασης, πρέπει τα αποτελέσματα των μετρήσεων να ποσοτικοποιηθούν. Για το σκοπό αυτό πρέπει να οριστεί ένας δείκτης βλάβης. Με αυτό τον τρόπο μειώνεται σημαντικά και το μεγάλο μέγεθος δεδομένων που κρατάμε μετά από κάθε μέτρηση.

Διάφοροι στατιστικοί συντελεστές έχουν κατά καιρούς προταθεί σαν δείκτες βλάβης όπως η διαφορά τετραγώνων (root means square deviation (RMSD)), η μέση απόκλιση (mean absolute percentage deviation (MAPD)) και η τυπική απόκλιση (correlation coefficient deviation (CCD)). Ο πιο συχνά χρησιμοποιούμενος δείκτης, και αυτός που χρησιμοποιείται στην παρούσα εργασία, είναι ο δείκτης των ελαχίστων τετραγώνων (RMSD), που βασίζεται στην σύγκριση ανά συχνότητα των μετρήσεων.

$$RMSD = \sqrt{\frac{\sum_{j=1}^N (G_j^1 - G_j^0)^2}{\sum_{j=1}^N (G_j^0)^2}}, \text{ όπου}$$

$G_j^1 \rightarrow$ διαπερατότητα/αντίσταση μετά την ζημιά για την f^1 συχνότητα

$G_j^0 \rightarrow$ διαπερατότητα/αντίσταση πριν την ζημιά (κατάσταση αναφοράς) για την f^1 συχνότητα

Όσο μεγαλύτερη είναι η απόκλιση μεταξύ της υγιούς και της κατάστασης στην οποία λήφθηκε η μέτρηση, τόσο μεγαλύτερη είναι η τιμή του δείκτη. Η χρήση του δείκτη έχει περιορισμούς, καθώς πρέπει να οριστεί ένα όριο τιμής το οποίο να ξεχωρίζει και να αποτελεί ένα όριο ανάμεσα στην κατάσταση όπου η κατασκευή είναι ακόμα λειτουργική και την κατάσταση όπου έχει υποστεί βλάβη.

Μετρήσεις και Αποτελέσματα

Οι μετρήσεις που έγιναν στα πλαίσια της παρούσας εργασίας ήταν οι εξής:

- (i) Σε επίπεδο αδρανούς πριν την εμφάνισή τους στα δοκίμια σκυροδέματος για διάφορα θλιπτικά φορτία. Η θλίψη των δοκιμών έγινε χρησιμοποιώντας μια μέγγενη (εικόνα 10) χωρίς ποσοτικοποίηση του φορτίου. Το φορτίο ήταν αυξανόμενο ($load\ 1 < load\ 2 < load\ 3$ κλπ) φροντίζοντας να παραμένει στην ελαστική περιοχή.



Εικόνα 10 Manual compression of “smart” aggregates

- (ii) Παρακολούθηση της διαδικασίας σκλήρυνσης του σκυροδέματος για τα τέσσερα προαναφερθέντα δοκίμια (Κύβος 1 & 2 και Δοκός 1 & 2). Οι μετρήσεις λαμβάνονταν κάθε 2 ώρες για τις πρώτες 12 ώρες μετά την σκυροδέτηση. Στη συνέχεια και μέχρι 48 ώρες μετά τη σκυροδέτηση οι μετρήσεις λαμβάνονταν κάθε 6 ώρες. Στη συνέχεια από την 2^η μέχρι και την 7^η ημέρα λαμβάνονταν μετρήσεις κάθε 24 ώρες και τέλος από την 7^η μέχρι και την 28^η μέρα κάθε 3 ημέρες. Ουσιαστικά η πυκνότητα των μετρήσεων ακολουθούσε την σπουδαιότητα της κάθε περιόδου στην μελλοντική αντοχή του σκυροδέματος. Έτσι το διάστημα των πρώτων 7 ημερών κατά το οποίο το σκυρόδεμα αποκτά το 75% της συνολικής του αντοχής οι λήψεις των μετρήσεων ήταν αρκετά συχνή, και ιδιαίτερα τις πρώτες ώρες μετά τη σκυροδέτηση όπου σχηματίζεται η μικροδομή του.
- (iii) Πρόκληση ζημιάς στον Κύβο 1 χρησιμοποιώντας κρουστικό τρυπάνι. Οι μετρήσεις λαμβάνονταν 24 ώρες μετά την πρόκληση βλάβης καθώς λόγω των ισχυρών δονήσεων και της αύξησης της θερμοκρασίας του σκυροδέματος οι άμεσες μετρήσεις ήταν αναξιόπιστες.
- (iv) Κυκλική θλιπτική φόρτιση του κύβου 2 στην μηχανή θλίψης. Οι μετρήσεις λαμβάνονταν μετά την αποφόρτιση του δοκιμίου. Ο ρυθμός φόρτισης ήταν 0.5 kN/sec και η πρώτη φόρτιση ήταν στο 1/3 του εκτιμώμενου φορτίου κατάρρευσης. Έπειτα το δοκίμιο

αποφορτίστηκε και έγινε λήψη της πρώτης μέτρησης. Έπειτα το δοκίμιο φορτίστηκε μέχρι το επόμενο επιθυμητό επίπεδο, αποφορτίστηκε και έπειτα έγινε η επόμενη μέτρηση. Η διαδικασία αυτή επαναλήφθηκε μέχρι το σπάσιμο του δοκιμίου. Στον πίνακα που ακολουθεί παρατίθενται όλες οι φορτίσεις.

Cycle No	Load (kN)	Stress (MPa)
Cycle 1	161.9	7.2
Cycle 2	181.4	8.1
Cycle 3	190.4	8.5
Cycle 4	202.1	9.0
Cycle 5	208.8	9.3
Cycle 6	220.0	9.8
Cycle 7	233.1	10.4
Cycle 8	256.4	11.4
Cycle 9	281.0	12.5
Cycle 10	301.9	13.4
Cycle 11	319.9	14.2
Cycle 12	337.7	15.0
Cycle 13	366.4	16.3
Cycle 14	406.3	18.1
Cycle 15	451.0	20.1
Cycle 16 (Failure)	430.4	19.1

Πίνακας 2 – Load cycles (Compression)

- (v) Κυκλική κάμψη 3 σημείων της δοκού 2. Η λογική είναι πανομοιότυπη με αυτή της κυκλικής θλίψης του κύβου που περιγράφηκε στο (iii). Ακολουθεί ο πίνακας φορτίσεων καθώς και εικόνες (εικόνες 10, 11) από την διάταξη τόσο της δοκιμής θλίψης όσο και της κάμψης.

Cycle No	Load (kN)
Cycle 1	6.49
Cycle 2	10.07
Cycle 3	12.57
Cycle 4	14.87
Cycle 5	18.47

Πίνακας 3 – Load cycles (Bending)

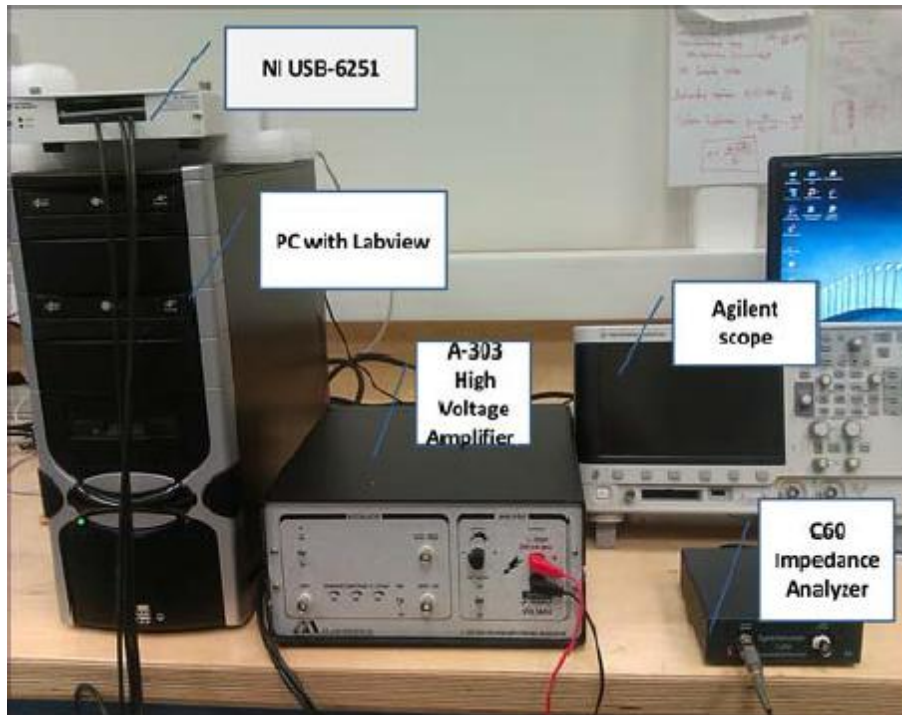


Εικόνες 10, 11 Experimental setup

(vi) Σε μια προσπάθεια να μεγαλώσει η εμβέλεια των αισθητήρων, η δοκός 2 επισκευάστηκε χρησιμοποιώντας ισχυρή τσιμεντοκονία αναλογίας νερού προς τσιμέντο (w/c) 0.4 και έγιναν μετρήσεις χρησιμοποιώντας μια χαμηλού κόστους διάταξη που αποτελείται από μια γεννήτρια συχνοτήτων, ένα ψηφιακό παλμογράφο και μια ωμική αντίσταση. Η διάταξη αυτή χρησιμοποιήθηκε καθώς οι διαθέσιμοι Impedance Analyzers μπορούν να διεγείρουν το PZT με εναλλασσόμενο ρεύμα έως 2 Volt. Με αυτόν τον τρόπο η κατασκευή διεγείρεται με κύματα χαμηλού πλάτους τα οποία αποσβήνονται πολύ γρήγορα σε ένα έντονα ετερογενές υλικό με πολύ υψηλή απόσβεση όπως το σκυρόδεμα. Με την διάταξη αυτή δεν έχουμε περιορισμό στα Volt και μπορούμε να διεγείρουμε το PZT με εναλλασσόμενο ρεύμα ως και 10 Volt χωρίς την χρήση ενισχυτή. Οι μετρήσεις έγιναν για διαφορετικές επιφάνειες επαφής ανάμεσα στα δυο τμήματα της δοκού 2, καθώς φθείραμε σταδιακά την αποκατάσταση που είχε γίνει προηγουμένως με καλέμι και σφυρί. Η επιλογή της επισκευασμένης δοκού έγινε λόγω έλλειψης χρόνου για την δημιουργία καινούριου υγιούς δοκιμίου. Οι μετρήσεις αυτές ξεφεύγουν κάπως από το αντικείμενο της παρούσας εργασίας, παρόλα αυτά αποτελούν μια πρώτη προσέγγιση της συγκεκριμένης διάταξης και μεθοδολογίας και είναι ενδεικτικές της ευαισθησίας του ισοδύναμου κυκλώματος στην ανίχνευση βλάβης.

Για την διέγερση του PZT, χρησιμοποιήθηκε μια κάρτα National Instruments USB-6251 high-speed M series multifunction data acquisition (DAQ) σαν γεννήτρια συχνοτήτων. Το σήμα διέγερσης ήταν ημιτονοειδές με $V_{in}=7$ Volt και η σάρωση έγινε σε συχνότητες 10-100 kHz. Επίσης χρησιμοποιήθηκε ένας ψηφιακός παλμογράφος δύο Agilent 2000X για την καταγραφή της διαφοράς δυναμικού $V_{in}(t)$ και της πτώσης τάσης $V_{out}(t)$ μετά από μια γνωστή ωμική αντίσταση αναφοράς Ref. Το ρεύμα $I(t)$ συναρτήσει του χρόνου που περνάει από το PZT θα περνάει και από την αντίσταση αναφοράς. Έτσι η ένταση του ρεύματος που ρέει στο κύκλωμα μπορεί να υπολογιστεί ως: $I(t)=V_{out}(t)/Ref$. Επομένως η ηλεκτρική διαπερατότητα του PZT μπορεί να υπολογιστεί με χρήση του τύπου [5]:

$$Y(t) = \frac{I(t)}{V(t)} = \frac{V_{out}(t) \cdot (1/Ref)}{V_{in}(t) - V_{out}(t)}$$



Εικόνα 12 Experimental arrangement [5] (C. Providakis, K. Stefanaki, M. Voutetaki, J. Tsompanakis, M. Stavroulaki and J. Agadakos, *An Integrated Approach for Structural Health Monitoring of Concrete Structures Based on Electromechanical Admittance and Guided Waves*)

Με μετασχηματισμό Fourier μετατρέπουμε την παραπάνω εξίσωση από το πεδίο του χρόνου στο πεδίο των [5]:

$$Y(i\omega) = \frac{I(i\omega)}{V(i\omega)}$$

Άρα η σύνθετη ηλεκτρική διαπερατότητα του PZT θα είναι:

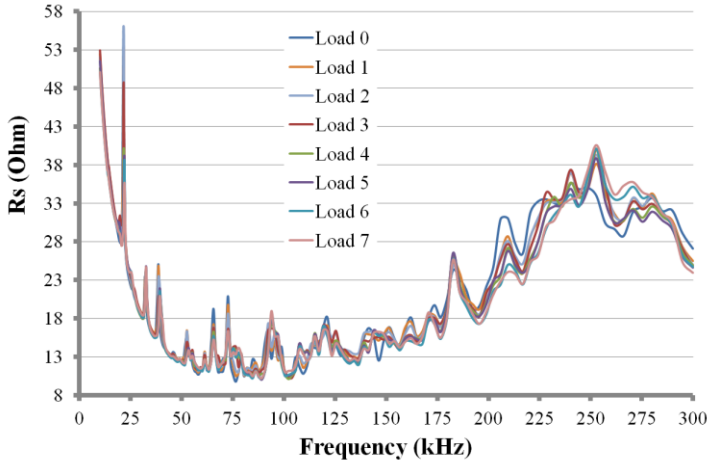
$$Y = \frac{FFT(V_{out}(t) \cdot (1/Ref))}{FFT(V_{in}(t) - V_{out}(t))} = G + j \cdot B$$

όπου, FFT{} συμβολίζει τον μετασχηματισμό Fourier. Με αυτή την προσέγγιση μπορούμε να σαρώσουμε και ολόκληρες περιοχές συχνοτήτων. Για την επίτευξη της σάρωσης στέλνεται ένα ημιτονοειδές σήμα διάφορων συχνοτήτων (digitally synthesized linear chirp signal) χρησιμοποιώντας το πρόγραμμα Labview Signal Express. Η πραγματική διέγερση του PZT, V_{in} καθώς και η απόκρισή του, V_{out} , καταγράφονται συγχρόνως στα δύο κανάλια του παλμογράφου.

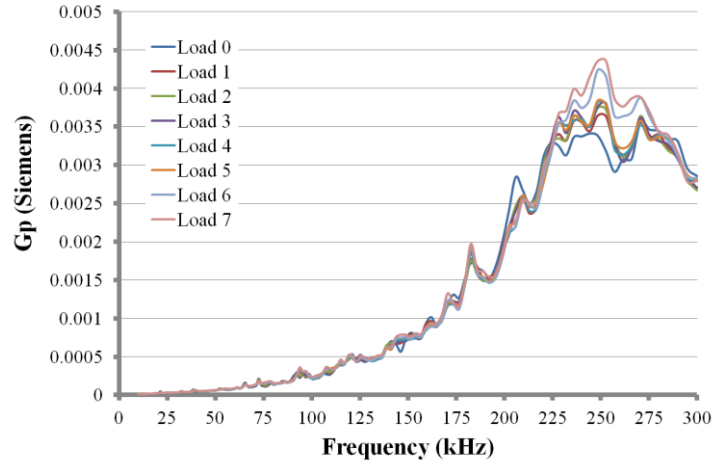
Τα αποτελέσματα που προέκυψαν από τις μετρήσεις ήταν τα εξής (ενδεικτικά παρατίθενται κάποια αντιπροσωπευτικά, αναλυτική παρουσίαση στα επόμενα κεφάλαια):

- Όσον αφορά την συμπίεση των αδρανών πριν την τοποθέτησή τους σε κατασκευές σκυροδέματος, παρατηρήθηκε με την αύξηση του φορτίου μια μείωση της έντασης των peak και μια ελαφριά μετατόπισή τους προς τα δεξιά. Το γεγονός αυτό οφείλεται στην

συμπύση της εύκαμπτης στρώσης σιλικόνης που έχει σαν αποτέλεσμα να έρχονται τα δυο κομμάτια του αδρανούς πιο κοντά, επιτρέποντας κύματα μικρότερου μήκους κύματος να περάσουν στο δεύτερο κομμάτι του αδρανούς. Όσο το φορτίο λοιπόν αυξάνεται η κατασκευή τείνει να συμπεριφερθεί σαν ενιαίος κύβος 50x50x50 mm, ενώ παρατηρείται και μια σταθερή άνοδος της τιμής του RMSD. Ενδεικτικά παρατίθενται τα αποτελέσματα για το αδρανές No 4:



(a)

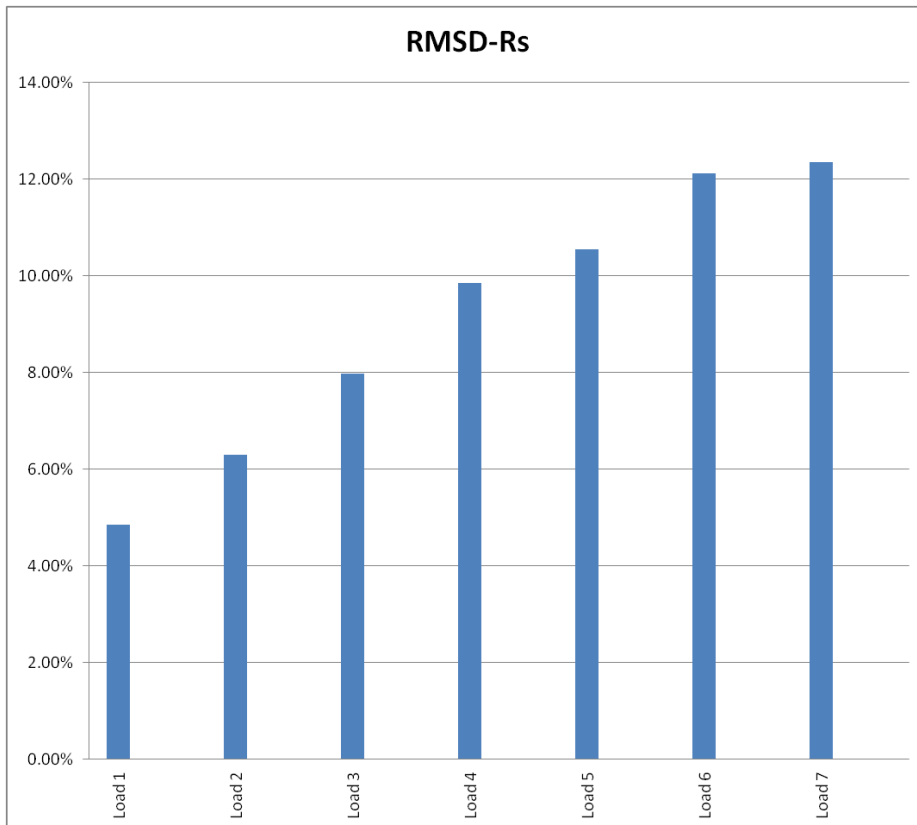


(b)

Διάγραμμα 1: Aggregate 4 signature plots

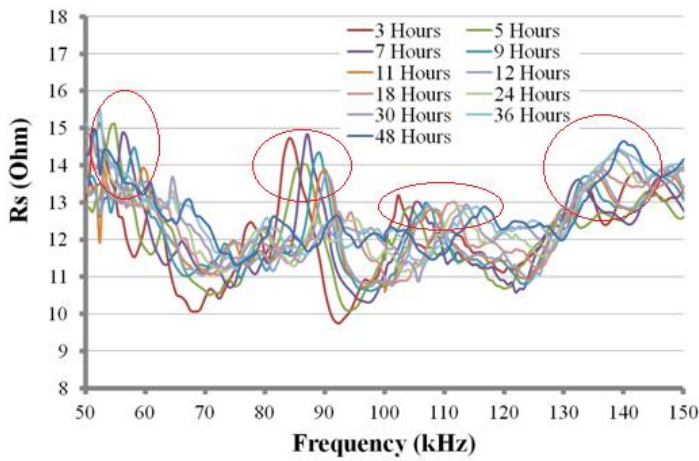
a) Resistance

b) Conductance

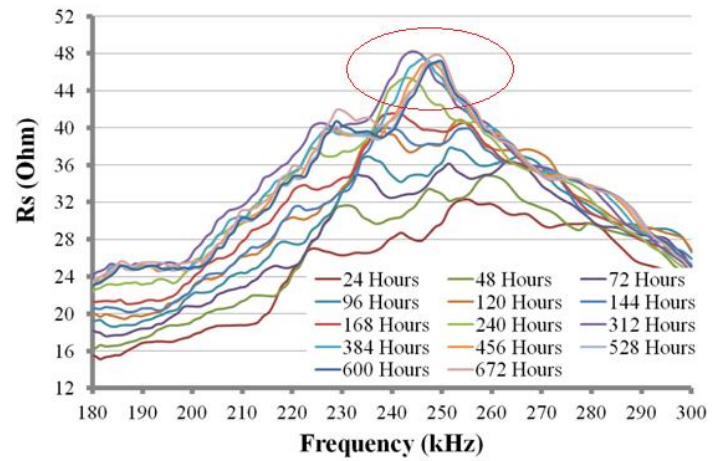


Διάγραμμα 2 - RMSD chart for various compressive loads of S.A. 4

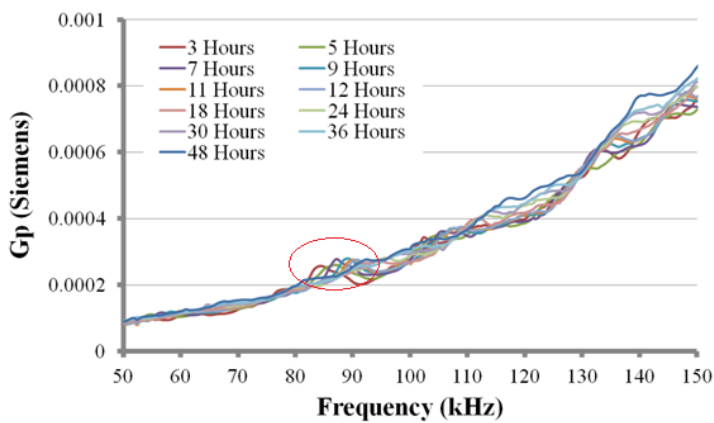
- Όσον αφορά τα αποτελέσματα της παρακολούθησης της διαδικασίας σκλήρυνσης των δοκιμίων, παρατηρήθηκε ότι με την πάροδο του χρόνου τα peaks, και ιδιαίτερα στην συχνότητα συντονισμού του PZT, παρουσίασαν μετατόπιση προς τα δεξιά ενώ ταυτόχρονα παρατηρήθηκε αύξηση της τιμής τους. Η δεξιά μετατόπιση στον άξονα των συχνοτήτων οφείλεται στην απόκτηση δυσκαμψίας του σκυροδέματος, ενώ η αύξηση της τιμής των μετρήσεων οφείλεται στην μείωση της απόσβεσης και την καλύτερη διάδοση των κυμάτων μέσα στη μάζα του σκληρυμένου σκυροδέματος. Όσον αφορά την τιμή του RMSD παρατηρήθηκε συνεχής άνοδος μέχρι και την 7^η μέρα μετά τη σκυροδέτηση και μετά σταθεροποίηση της τιμής του. Ενδεικτικά παρατίθενται τα αποτελέσματα του κύβου 2:



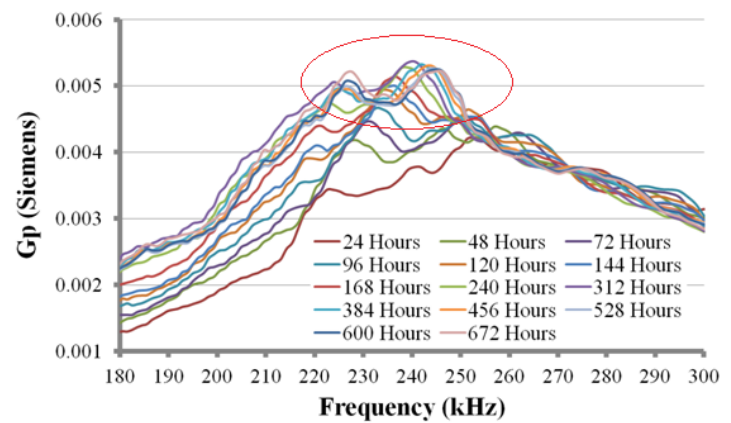
(c)



(d)

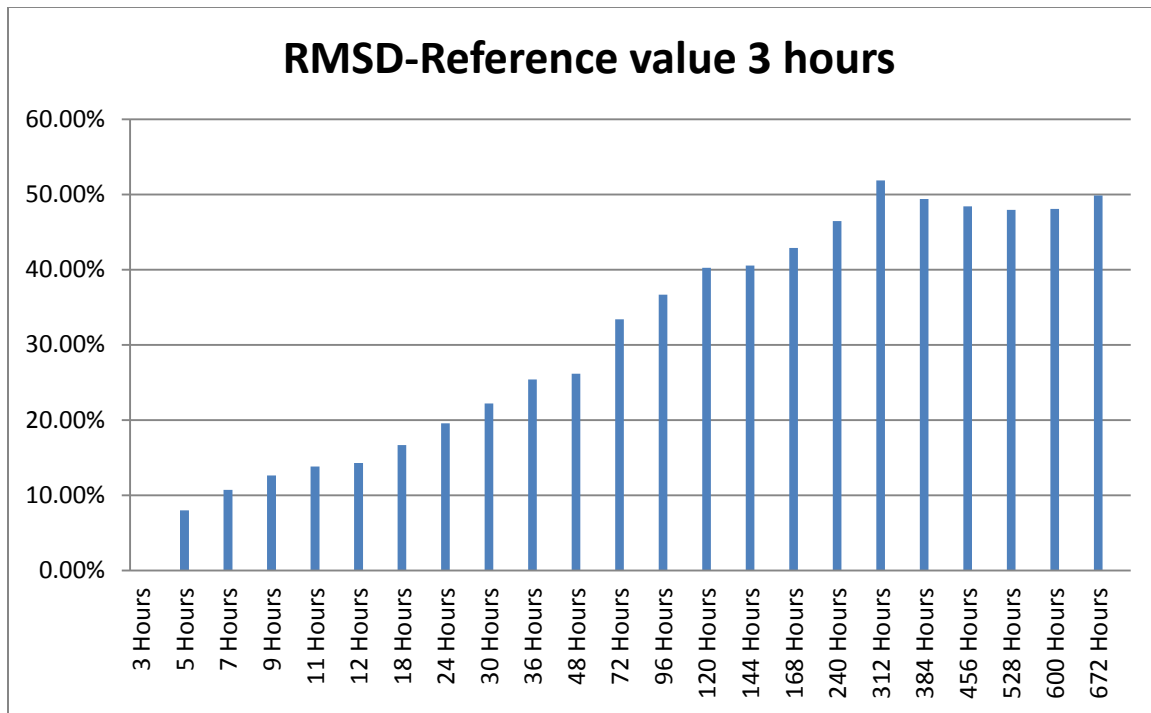


(c)



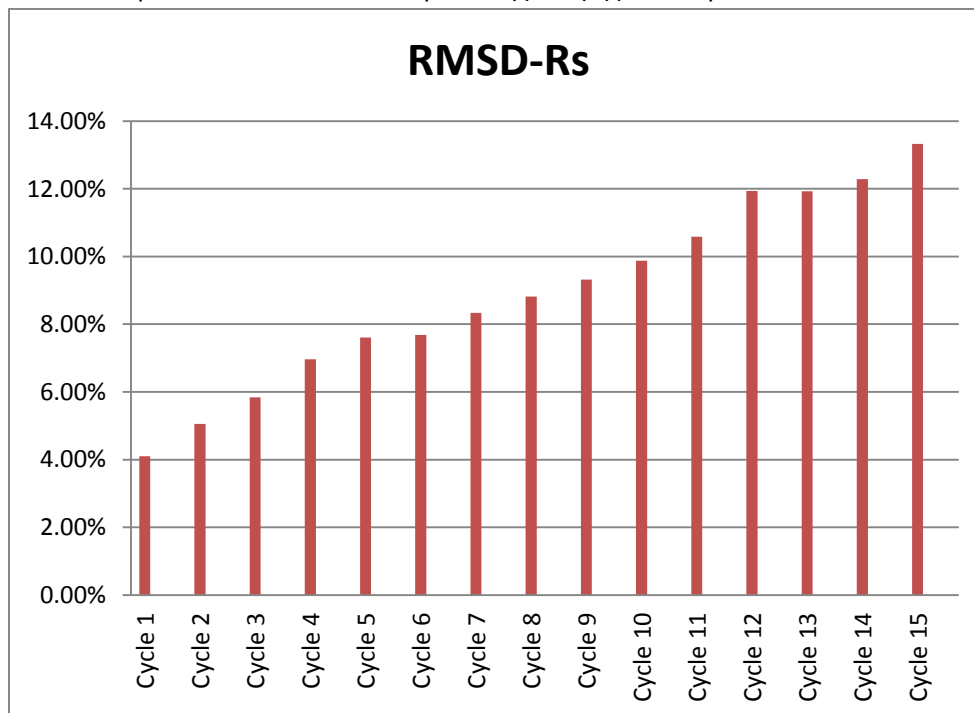
(d)

Διάγραμμα 3 – (a) Resistance plot 50-150 kHz for the first 48 Hours (b) Resistance plot 180-300 kHz for the first 28 Days (c) Conductance plot 50-150 kHz for the first 48 Hours (d) Conductance plot 180-300 kHz for the first 28 Days

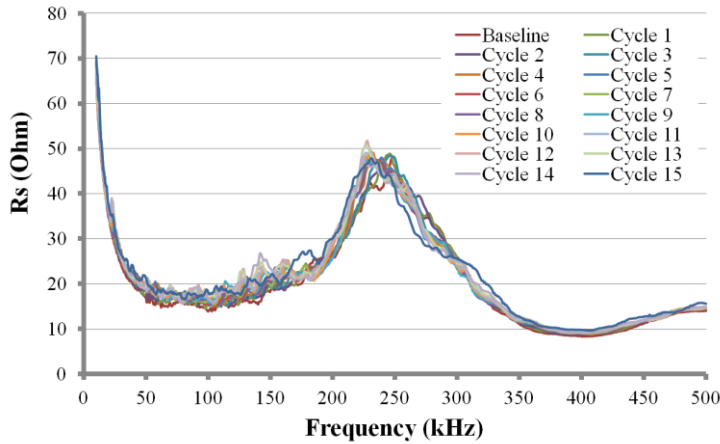


Διάγραμμα 4 - RMSD chart for curing process of Cube 2 (Reference value-3 hours)

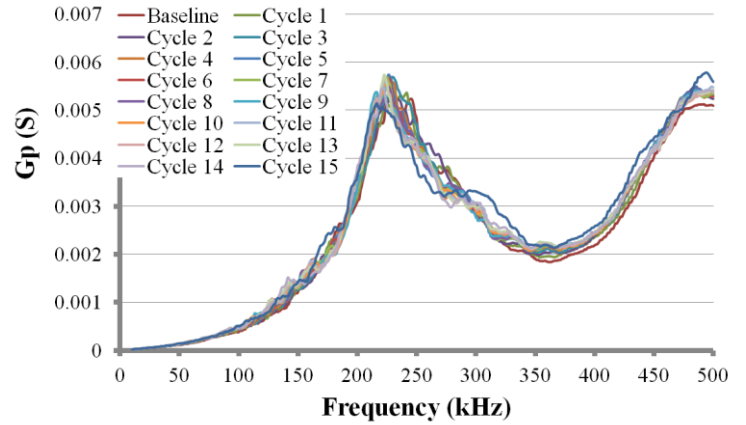
- Ακριβώς αντίστροφη ήταν η τάση κατά την επιβολή ζημιάς. Παρατηρήθηκε δηλαδή μετατόπιση των peaks προς τα αριστερά, δείχνοντας απώλεια δυσκαμψίας της κατασκευής. Οι τιμές του RMSD αυξάνονταν σταθερά όσο υπήρχε αύξηση του μεγέθους της ζημιάς. Ενδεικτικά παρατίθενται τα αποτελέσματα της θλίψης του κύβου 2:



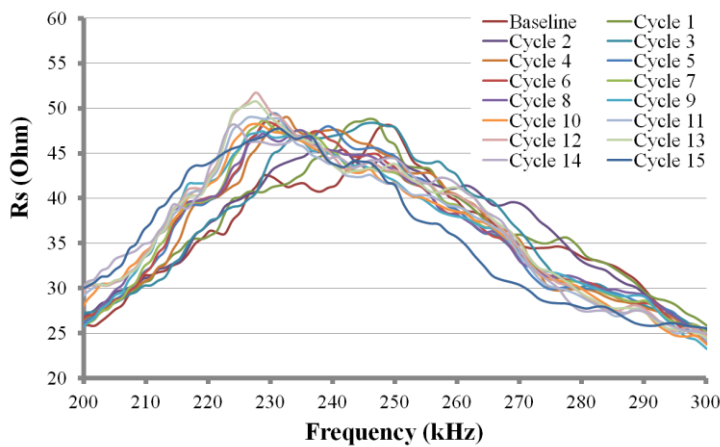
Διάγραμμα 5 - RMSD chart – Compression of Cube 2



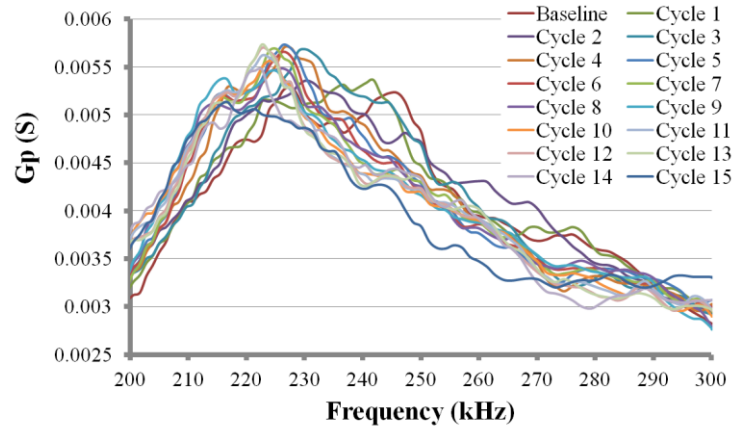
(e)



(f)



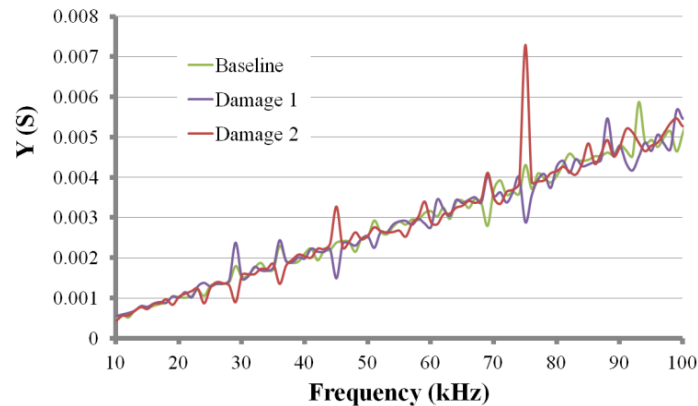
(c)



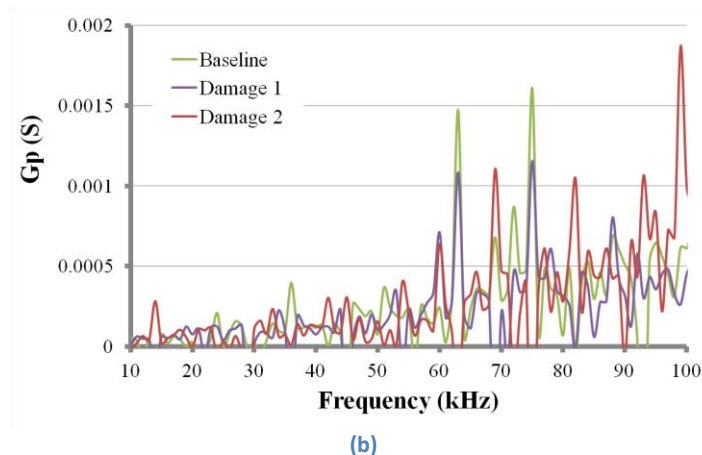
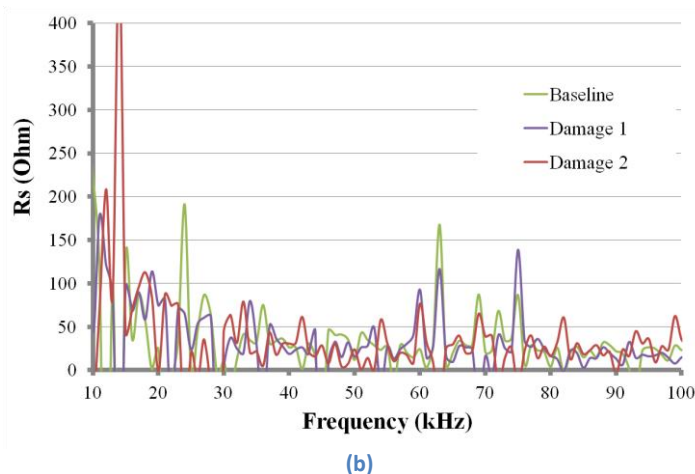
(d)

Διάγραμμα 6 – (a) Resistance plot 0-500 kHz (b) Resistance plot 50-150 kHz
(c) Resistance plot 200-300 kHz (d) Conductance plot 200-300 kHz

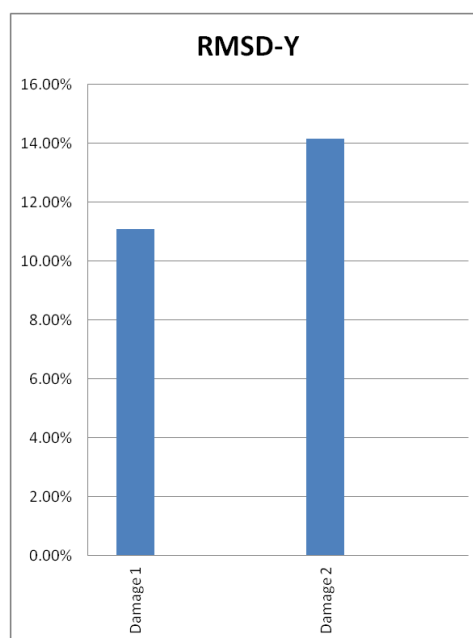
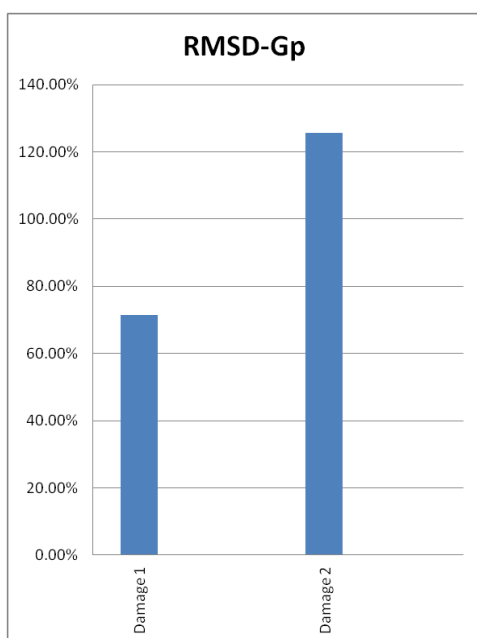
- Η ζημιά από την κάμψη της δοκού έγινε σε απόσταση 110 mm από τους αισθητήρες, στο μέσο δηλαδή της δοκού, και δεν ήταν ανιχνεύσιμη από τα PZT κατά τις μετρήσεις με τον Analyzer. Για τον λόγο αυτό έγιναν οι μετρήσεις με το ισοδύναμο κύκλωμα, για να αυξηθεί η εμβέλεια του PZT. Παρατίθενται τα ακόλουθα αποτελέσματα:



(a)



Διάγραμμα 7 – (a) Admittance magnitude plot 0-100 kHz
(b) Resistance plot 0-100 kHz (c) Conductance plot 0-100 kHz



Διάγραμμα 8– RMSD plots

Συμπεράσματα-Προτάσεις για βελτιώσεις

Τα πλεονεκτήματα και τα μειονεκτήματα της τεχνικής EMI έναντι των συμβατικών μεθόδων NDE έχουν ήδη συζητηθεί στα προηγούμενα κεφάλαια, καθώς και σε άλλες ερευνητικές εργασίες. Συνοψίζοντας, τα βασικά πλεονεκτήματα είναι τα εξής: i) δεν απαιτείται ογκώδης εξοπλισμός, ενώ τα PZT μπορούν να παραμείνουν μόνιμα πάνω στην κατασκευή καθώς είναι πολύ μικρά (10x10x0.2 mm) και δεν επηρεάζουν τα δυναμικά χαρακτηριστικά της κατασκευής, ii) έχει μεγάλη ευαισθησία στην ανίχνευση τοπικής βλάβης σε σύγκριση με τις τεχνικές που χρησιμοποιούν τις ιδιομορφές της κατασκευής, iii) των αποτελεσμάτων που

λαμβάνονται στο πεδίο συχνοτήτων χωρίς να χρειάζονται περαιτέρω επεξεργασία, iv) παρέχει τη δυνατότητα ενός on line SHM συστήματος.

Τα βασικά μειονεκτήματα της μεθόδου είναι i) η μεγάλη ευαισθησία των PZT στις περιβαλλοντικές συνθήκες (υγρασία και θερμοκρασία), ii) η ευαισθησία των PZT σε κρούσεις και φορτίσεις, και iii) η μικρή εμβέλεια των PZT (παρόλο που βοηθάει στον προσδιορισμό της θέσης της ζημίας) που καθιστά αναγκαία τη χρήση του μεγάλου αριθμού PZTs, αυξάνοντας το κόστος της κατασκευής.

Όσον αφορά την τεχνική με τα PZT εμβαπτισμένα μέσα στη μάζα της κατασκευής μέσω των έξυπνων αδρανών, που προτείνεται στην παρούσα εργασία, σε σύγκριση με τη συμβατική τεχνική EMI, υπάρχουν ορισμένα πλεονεκτήματα και μειονεκτήματα, καθώς τα σημεία που χρειάζονται περαιτέρω εξέταση. Τα βασικά πλεονεκτήματα είναι: i) η δυνατότητα παρακολούθησης της ενυδάτωσης του σκυροδέματος από την πρώτη ώρα μετά τη σκυροδέτηση, ii) προστασία του PZT από τις περιβαλλοντικές συνθήκες και από συγκρούσεις και iii) καλύτερη εισαγωγή των κυμάτων στην κατασκευή, καθώς έχουμε κύματα χώρου που διαδίδονται σε όλη τη μάζα της κατασκευής και όχι μόνο επιφανειακά.

Τα βασικά μειονεκτήματα της τεχνικής αυτής είναι: i) η αδυναμία επιδιόρθωσης σε περίπτωση βλάβης στο PZT (κακή καλωδίωση, κλπ.), ii) η υψηλή πιθανότητα σχισίματος της καλωδίωσης στο σκυρόδεμα με αποτέλεσμα κακής ποιότητας μετρήσεων και iii) η εμπλοκή περισσότερων υλικών κάνει την κατασκευή πιο περίπλοκη, με αποτέλεσμα μεγαλύτερη δυσκολία δημιουργίας ενός ικανοποιητικού μοντέλου προσομοίωσης.

Υπάρχει ακόμα πολύς δρόμος που πρέπει να διανυθεί πριν από την εμπορευματοποίηση αυτής της πολλά υποσχόμενης τεχνικής. Μεγάλος αριθμός ερευνητικών εργασιών μπορεί να βρεθεί στην βιβλιογραφία με σκοπό να αμβλυνθούν οι αδυναμίες της τεχνικής EMI. Διαφορές εργασίες έχουν δημοσιευθεί με προτάσεις για επαναχρησιμοποιούμενους αισθητήρες, ή για την εφαρμογή ενός on-line συστήματος SHM χρησιμοποιώντας κάρτες AD5933, για να αναφέρουμε μερικές. Συγκεκριμένα, όσον αφορά την τεχνική EMI χρησιμοποιώντας εμβαπτισμένα PZTs, τα θέματα συζήτησης που προκύπτουν από τα πειραματικά αποτελέσματα που πραγματοποιήθηκαν για την παρούσα εργασία είναι τα εξής: i) η επέκταση της περιοχής εμβέλειας του PZT. Καταβάλλονται προσπάθειες σε αυτή την κατεύθυνση με την εφαρμογή του κυκλώματος που περιγράφεται στο κεφάλαιο 9.3.3. Η δυνατότητα διέγερσης με υψηλότερη τάση, και ως εκ τούτου μεγαλύτερη ενέργεια στην κατασκευή, ακόμη και χωρίς ενισχυτή μας επιτρέπει να διευρυνθεί η αισθητήρια περιοχή. ii) Το μέγεθος του έξυπνου αδρανούς. Το μέγεθος του έξυπνου αδρανούς πρέπει να μειωθεί στο μέγεθος ενός χοντρόκοκκου αδρανούς. Η τοποθέτηση ενός κύβου 50x50x50 mm, για παράδειγμα, σε κόμβο ενός πλαισίου από οπλισμένο σκυρόδεμα, θα δημιουργούσε τεράστια προβλήματα (αν όχι καθιστώντας αδύνατη) την διαδικασία της σκυροδέτησης λόγω της έλλειψης χώρου. iii) Η ανάγκη να αντικατασταθεί η στρώση σιλικόνης, που χρησιμεύει ως αδιαβροχοποίηση του PZT, με ένα πιο δύσκαμπτο υλικό, καθώς λόγω της μεγάλης παραμορφωσιμότητάς της απορροφά μέρος της ενέργειας του PZT λειτουργώντας σαν αποσβεστήρας

Part I Basic Theory

1 Introduction

The research of structural health monitoring and damage detection has recently become an area of interest for a large number of academic and commercial laboratories and over the past two decades, several SHM and NDE techniques have been reported in the literature, based on either the global or the local interrogation of structures. The global dynamic techniques involve subjecting the structure under consideration to low frequency excitations so as to obtain the first few natural frequencies and extract the corresponding mode shapes. These are then processed to obtain information pertaining to the location and severity of the damages. However, the main drawback of the global dynamic techniques is that they rely on relatively small number of first few structural modes, which, being global in character, are not sensitive enough to be affected by localized damages. The global parameters (on which these techniques heavily rely) are not appreciably affected by the localized damages. It could be possible that a damage large enough to be detected might already be detrimental to the health of the structure. Another limitation of these techniques is that owing to low frequency, typically less than 100Hz, the measurement data is prone to contamination by ambient noise, which too happens to be in the low frequency range. Another category of the SHM/ NDE techniques are the local techniques, which, as opposed to the global techniques, rely on the localized interrogation of the structures. Some techniques in this category are the ultrasonic wave propagation technique, acoustic emission, magnetic field analysis, electrical methods, penetrant dye testing, impact echo testing and X-ray radiography, to name a few. However, they share several drawbacks, which hinder their autonomous application for SHM, especially on large civil-structures. The ultrasonic techniques, for example, are based on elastic wave propagation and reflection within the host structure's material to identify field inhomogeneities due to local damages and flaws. Their potential in identifying damage as well as for non-destructive strength characterization of concrete has been well demonstrated. However, they need large transducers for excitation and generation of measurement data, in time domain, that requires complex processing. In addition, they involve expensive operational hardware and render the structure unavailable throughout the length of the test.

The electro-mechanical impedance (EMI) technique has made significant forays in the domains Structural Health Monitoring (SHM) and Non-destructive Evaluation (NDE) during the last 15 years. The applications of this technology were mostly for aerospace use until several years ago. However, many researchers have been trying to apply this technology to civil engineering structures. The technique is essentially based on monitoring the structural mechanical impedance via the electromechanical admittance or impedance signature of a lead zirconate titanate piezoelectric-ceramic (PZT) patch, by utilizing its direct and converse piezoelectric properties. The patch is subjected to an alternating voltage excitation from an impedance analyzer/LCR meter, sweeping through a particular frequency range, typically 10–500 kHz. At a given frequency, the patch actuates the structure and the structural response is in turn sensed and measured in terms of the electromechanical admittance or resistance of the patch. In this manner, frequency plots, termed conductance and susceptance (or resistance and

reactance) signatures, are generated across the specified frequency range. Any change in the condition of the structure manifests itself as an alteration in these signatures, which is utilized for SHM and NDE, considering the signatures of the healthy state structure as the baseline.

This new emerging technique is in principle similar to the global dynamic techniques but its sensitivity is of the order of the local ultrasonic techniques. By employing low-cost transducers, which can be permanently bonded to the structure and can be interrogated without removal of any finishes or rendering the structure unusable. No complex data processing or any expensive hardware is warranted. The data is directly generated in the frequency domain as opposed to time domain in the ultrasonic techniques.

The use of an embedded “smart” aggregate is very important as it allows us to monitor the hydration process of concrete. A sensor that monitors the hydration process would provide information on instantaneous condition of the concrete and when critical actions can be taken, for example, framework removal, which has the possibility of reducing construction times and reducing the overall costs of a project. The main disadvantage of conventional EMI method is that the patches must be attached after the concrete has hardened and moulds removed. This neglects an extremely important time in the strength development of the concrete – the first 36 hours. It is in this time that the microstructure of the concrete is formed. This has obvious benefits as the effects of the bonding issues are reduced, although it does increase the complexity of the sensor as increased packaging is required.

2 Wave propagation in solids

Physical manifestations of waves are numerous. The transmission of the transverse shape of a wire, the distribution of density in a fluid, a perturbation of air in a pipe, a high-intensity shock in a solid and current in a conductor are only some examples of disturbance propagation. The most easily visualized illustration of wave motion, and probably the oldest observed, is provided by the propagation of disturbances on the surface of water. Through such observations, evidence had existed for many years that force could be communicated from one body to another without the transport of matter.

The phrase “propagating disturbance” is interpreted to mean a process or an influence (as some form of energy) which moves through a medium with a finite velocity, but without causing bulk transfer of the medium as a whole. The motion can be linear or nonlinear, steady or unsteady. The last condition for example occurs in the case of transient disturbances or when boundaries of a region move and interact with the wave.

In this chapter we concern ourselves with the wave propagation phenomena in deformable elastic solids which obey Hooke’s law so that the response is linear and internal friction negligible. The scope of this chapter is merely an introduction to a field that has been studied extensively in specific fields of physics and engineering. In this brief introduction, only certain kinds of waves are selected to be investigated, the ones that serve the purposes of this master thesis.

2.1 Stress-Strain relationships and equations governing elastic solids

The notion of stress can be introduced by considering the distribution of surface forces over a tetrahedron of infinitesimal volume imbedded in equilibrium in the interior of a continuous solid body. The specifications of nine stress components S_{ij} are sufficient to characterize completely the state of stress at any point in the medium. The components S_{ii} (i not summed) are the normal stress components; the others are the shearing components. In general, these numbers are different at different points and constitute a stress field. The stress can be proved to be a second rank tensor. Moreover, it is symmetric so that among its components the relation $S_{ij}=S_{ji}$ holds, providing there exists no distribution of body torques within the body. This property of symmetry allows complete specification of stress at a point in a body with at most six independent numbers.

The notion of strain can be introduced by considering the relative displacement of two points in a deformable body. If δu_i is the relative displacement between any two points δx_j apart in a deformed body, and assuming the small strain approximation holds, we can write this relative displacement in rectilinear Cartesian coordinates from Taylor's series as [1]:

$$\delta u_i = \frac{\partial u_i}{\partial x_j} \cdot \delta x_j = \varepsilon_{ij} \cdot \delta x_j + \omega_{ij} \cdot \delta x_j \quad (2.1)$$

Where

$$\varepsilon_{ij} = \frac{1}{2} \left(\frac{\partial u_i}{\partial x_j} + \frac{\partial u_j}{\partial x_i} \right) \quad (2.2)$$

and are defined as components of strain, and

$$\omega_{ij} = \frac{1}{2} \left(\frac{\partial u_i}{\partial x_j} - \frac{\partial u_j}{\partial x_i} \right) \quad (2.3)$$

and are defined as the components of body rotation. The strain components ε_{ij} ($i=j$, I not summed) are tensions and/or compressions; the components ε_{ij} ($i \neq j$) are shearing strains. Strain has an arbitrary definition, but displacement is a consequence of the nature of the body and the boundary conditions imposed upon it and cannot be arbitrarily specified. Strain can be shown to be a symmetrical second rank tensor. The rotation tensor can also be shown to be of second rank, but it is found to be antisymmetrical, i.e. , $\omega_{ij} = -\omega_{ji}$.

The stress and strain fields are interrelated by means of some mathematical model. For small deformations, application of a generalization of Hooke's law of elasticity allows a connection between stress and strain that is satisfactory for the description of both the quasistatic and dynamic mechanical behavior of a great number of materials of physical interest, and yet is generally amenable to mathematical analysis. In three dimensions, this law can be written as

$$S_{ij} = C_{ijkl} \cdot \varepsilon_{kl} , \quad (2.4)$$

where the numbers C_{ijkl} form a fourth rank tensor and are called the elastic stiffness constants of the material. From symmetry and thermodynamical considerations, the number of stiffness constants is reduced to 21 in the most general anisotropic situation.

For the most part, we consider bodies as isotropic (with properties identical in all directions) and homogeneous (with properties identical at all points). The condition of isotropy reduces the number of independent elastic constants to two, λ and μ , called Lamé's constants. The quantity μ is also called the shear modulus or modulus of rigidity and in engineering literature is usually designated by the symbol G. Hooke's law then becomes

$$S_{ij} = \lambda \cdot \Delta \cdot \delta_{ij} + 2 \cdot \mu \cdot \varepsilon_{ij} , \quad (2.5)$$

where δ_{ij} is the Kronecker delta, defined as

$$\delta_{ij} = \begin{cases} 0 & \text{if } i \neq j \\ 1 & \text{if } i = j \end{cases} ,$$

and where Δ is the dilatation defined, $\Delta = \varepsilon_{ii}$.

Engineering texts often treat the subject of Hooke's law from a less sophisticated approach (e.g. text by Timoshenko and Goodier). It is helpful to consider briefly this approach so as to examine the simplified physical aspects of Hooke's law and to gain some understanding of the significance and interrelation of the various elastic constants for isotropic media. Written in its simplest one-dimensional form, applicable for example to a thin rod, Hooke's law is $F=g(\delta x)$, where F is the applied uniaxial force, x is the resulting displacement, and g is the proportionality constant. By dividing F by the original area A to obtain the nominal engineering stress, and by writing the displacement as the relative displacement $\delta x/x_0$, we can express Hooke's law in the form

$$F/A = E \cdot (\delta x/x_0)$$

Or

$$S_{11} = E \cdot \varepsilon_{11}, \quad (2.6)$$

where E is the modulus of elasticity (Young's modulus). The modulus equals the slope of the line in a plot of uniaxial stress versus strain in the elastic regime.

Accompanying this elongation in the 11-direction, there will be contractions in the 22- and 33- directions, given by

$$\varepsilon_{22} = \varepsilon_{33} = -\nu \cdot \varepsilon_{11} = -\nu \cdot (S_{11}/E), \quad (2.7)$$

where ν is Poisson's ratio, constant within the elastic range. Thus, if a volume element is subjected to a triaxial state of normal stress, the total strain in the 11-direction becomes to first order

$$\varepsilon_{11} = \frac{1}{E} \cdot [S_{11} - \nu \cdot (S_{22} + S_{33})],$$

with two other similar equations for ε_{22} and ε_{33} . The elastic stress-strain relation under a two dimensional pure shear condition takes the form

$$\varepsilon_{12} = \frac{1}{\mu} \cdot S_{12},$$

with two other similar equations for ε_{13} and ε_{23} . Inverting the last two equations we have

$$S_{11} = \frac{\nu \cdot E}{(1+\nu) \cdot (1-2\nu)} \cdot \Delta + \frac{E}{1+\nu} \cdot \varepsilon_{11}, \quad (2.8)$$

with two other similar equations for S_{22} and S_{33} , and

$$S_{12} = \mu \cdot \varepsilon_{12}, \quad (2.9)$$

with two other similar equations for S_{13} and S_{23} . By defining

$$\lambda = \frac{\nu \cdot E}{(1+\nu) \cdot (1-2\nu)} \text{ and } \mu = \frac{1}{2} \cdot \left(\frac{E}{1+\nu} \right)$$

and inverting them, we obtain

$$E = \frac{3\lambda+2\mu}{\lambda+\mu} \text{ and } \nu = \frac{\lambda}{2(\lambda+\mu)}.$$

The equations of motion appropriate to continuous media in which all strains can be considered small are

$$\rho \cdot \frac{\partial^2 u_i}{\partial t^2} = \frac{\partial S_{ij}}{\partial x_j} \quad (2.10)$$

where ρ is the mass density, u_i are the displacements and S_{ij} are the stress components. These relations hold irrespective of the stress-strain behavior of the medium, although the behavior must be consistent with certain physical and mathematical idealizations, mostly associated with the condition of small strain.

The field equations of motion in terms of the three displacement quantities u_i for an isotropic, homogeneous, perfectly elastic solid under conditions of small displacements and negligible body forces are

$$\rho \cdot \frac{\partial^2 u_i}{\partial t^2} = (\lambda + \mu) \cdot \frac{\partial \Delta}{\partial x_i} + \mu \cdot \frac{\partial^2 u_i}{\partial x_i \partial x_j} \quad (2.11)$$

Although the above relations are couched in terms of a rectilinear Cartesian coordinate system, other systems can be used. The system selected depends primarily upon the governing physical geometry of a given problem.

In solutions of elastic stress wave problems, using the above equation, we are led in the process to an expression in the form of the wave equation, a linear, homogeneous, second-order, partial differential relation with constant coefficients. The wave equation can be written

$$\frac{\partial^2 \psi}{\partial t^2} = c^2 \cdot \frac{\partial^2 \psi}{\partial x_i \partial x_j}$$

where $\psi = \psi(x_i, t)$ is the dependent variable and is a measure of some property of the disturbance such as displacement or velocity, and c is a physical constant which can be

interpreted as the propagation velocity of the wave. Boundary conditions must be applied in addition to the differential equation in order to define properly and sufficiently a given problem.

There are two general alternate methods of solution to the wave equation boundary value problem: (1) the method of separation of variables in which the equation is separated into a set of ordinary differential equations, and (2) the method of transformation in which the equation is transformed to a new set of independent variables (natural coordinates) so as to simplify analysis. The method of separation lends itself to a standing wave or normal mode solution of the wave equation that is appropriate to problems in elastic vibration in systems of finite physical dimensions; the method of transformation (or method of characteristics) lends itself to a traveling wave or progressive wave solution of that equation which is appropriate to problems in elastic wave propagation. Both solutions are interrelated, although we are more concerned with the latter.

The general traveling wave solution of the wave equation in one space dimension is [1]:

$$\psi = f(x_1 - ct) + g(x_1 + ct) \quad (2.12)$$

where f and g are arbitrary functions of the arguments and are obtained from the boundary conditions of the problem. The solution represents two waves, one moving in the direction of the positive x_1 axis with a constant velocity c , and one traveling in the direction of the negative x_1 axis with the same velocity c .

The use of a single simple harmonic progressive wave train of infinite duration is of considerable mathematical utility. This periodic motion can be expressed as [1]:

$$\psi = U \exp[i(kx_1 - pt)] \quad (2.13)$$

where U is a real coefficient related to the amplitude of the wave, i is the imaginary unit, k is the wave number (defined as $2\pi/\lambda$, in which λ is the wavelength), and p is the circular frequency (defined as $2\pi f$, in which f is the frequency).

2.2 Wave propagation in extended (isotropic and anisotropic) media

The propagation of small disturbances in anisotropic media can be examined by direct substitution of an expression representing a simple harmonic wave into the field equations of motion. Although this is essentially the technique employed in treating wave propagation in isotropic media, two simplifications are introduced in order to emphasize the mechanics involved: A specialized representation of a plane wave front is used in conjunction with a step by step development of the governing equations. This method provides the equations of small motion

$$\lambda_{ik} \frac{\partial^2 u_k}{\partial \psi'^2} = \rho \cdot c^2 \cdot \frac{\partial^2 u_i}{\partial \psi'^2} \quad (2.14)$$

where the independent variable ψ' is defined as $(l_i x_i - ct)$ (l_i being the direction cosines of the wave front normal), and the coefficients are given by

$$\lambda_{ik} = \frac{1}{2} \cdot (C_{ijmk} l_j l_m + C_{ijkn} l_j l_n) \quad (2.15)$$

By rewriting the above expressions, a system of linear homogeneous simultaneous equations can be formed. Such a system can be solved nontrivially only if the determinant of the coefficients vanishes. Hence, the condition is

$$|\lambda_{ik} - \delta_{ik}(\rho c^2)| = 0 \quad (2.16)$$

This condition is called the secular determinant. The three roots of it are positive and real and represent the three wave velocities that can be possibly transmitted in a completely anisotropic medium under the restriction of infinitesimal strains.

When treating isotropic elastic materials, two methods are appropriate to the investigation of the propagation of plane waves. First, the determinantal equation directly reduces to

$$|l_i l_k (\lambda + \mu) - \delta_{ik} (\mu - \rho c^2)| = 0 \quad (2.17)$$

Evaluation of the determinant leads to the solutions

$$c_l = \sqrt{\frac{\lambda + 2\mu}{\rho}} \quad (2.18)$$

$$c_s = \sqrt{\frac{\mu}{\rho}} \quad (2.19)$$

showing that, in the interior of an elastic isotropic solid, a planar wave (or nonplanar wave for that matter) may be transmitted with only two velocities (assuming that the limitation of infinitesimal strains is imposed).

The second method essentially performs various manipulations with the equations of motion and examines the consequences of allowing first the dilatation and then the rotation to become zero. This latter approach enables conclusions to be obtained concerning the physical nature of (2.18) and (2.19). Thus, solution (2.18) represents a disturbance traveling with no rotation. It is known as a longitudinal wave (hence the subscript l); other names are irrotational, dilatational, and P waves. Equation (2.19) represents a wave propagating with no dilatation. It is known as a shear wave (hence the subscript s); other names are equivoluminal, transverse, distortional, and SV or SH waves (the latter depending upon whether the displacements are in a vertical or horizontal plane, respectively). An important feature of these disturbances is that plane shear waves involve distortion without dilatation, but that plane longitudinal waves involve both phenomena.

It is proved that the direction cosines m_k for the particle motions are related to the λ_{ik} constants in expressions (2.14) by

$$\lambda_{ik}m_k = m_i\rho c^2 \quad (2.20)$$

By applying Eqs. (2.20) to isotropic bodies, we find that c_l corresponds to a wave in which the particle motion is in the direction of propagation (hence the term “longitudinal wave”), and c_s corresponds to a wave for which the direction of particle motion is perpendicular to the direction of propagation (hence the term “shear wave”). Moreover, these conditions are the only ones possible in the plane wave situation.

Under some conditions of elastic wave propagation in solids, e.g. pulse transmission, adequate analysis is not possible using the concept of a simple harmonic progressive wave of infinite extent. Then a standard method of solution applies the principles of Fourier series analysis over a limited range of some space or time variable that is representative of the wave. Although this approach is only approximate, often in many practical situations one can adequately reproduce isolated pulses using a series analysis by taking longer and longer ranges of representation. Exact mathematical description of a completely aperiodic pulse can be developed by extending the principles of Fourier series analysis and using Fourier transform theory and integral theorem solutions.

2.3 Wave propagation in reflection and refraction semi-extended media

To examine the propagation of elastic disturbances in a semi-infinite homogeneous isotropic solid with a plane boundary (a semi-extended medium), it is necessary to stipulate the direction of propagation of the disturbances. Waves can either propagate parallel and near to the boundary or at some arbitrary angle to it. Under the first condition, the disturbances are called surface waves. Under the second, the phenomenon of wave reflection occurs.

There are several kinds of elastic surface waves that can be transmitted in semi-extended solids. One of the most important types is plane Rayleigh waves.

The general mathematical procedure for studying Rayleigh waves is to determine the solution of the equations of small motion using the expression for a progressive continuous simple harmonic plane wave and the boundary condition of a stress-free interface. A two-dimensional coordinate system is used in formulating the problem. The technique allows us to obtain the propagation condition, which, in turn, enables us to find the velocity of the Rayleigh surface waves by the relationship

$$\frac{v^2}{c_s^2 \cdot k^2} = \frac{c_r^2}{c_s^2}$$

providing the shear wave velocity c_s and Poisson's ratio ν are known. The displacements, u_1 and u_3 , follow from the above and are written

$$u_1 = -ak \left[\exp(-\xi_l x_3) - 2\xi_l \xi_s \left(2k^2 - \frac{v^2}{c_s^2} \right)^{-1} \exp(-\xi_s x_3) \right] \sin(kx_1 - vt) \quad (2.21)$$

$$u_3 = -a\xi_l \left[\exp(-\xi_l x_3) - 2k^2 \left(2k^2 - \frac{v^2}{c_s^2} \right)^{-1} \exp(-\xi_s x_3) \right] \cos(kx_1 - vt) \quad (2.22)$$

where $\xi_l = (k^2 - v^2/c_l^2)^{1/2}$ and $\xi_s = (k^2 - v^2/c_s^2)^{1/2}$. Equations (2.21) and (2.22) define completely the solution because of the two dimensional formulation, i.e., $u_2 = 0$ everywhere.

When a plane wave propagates at some arbitrary angle to the bounding surface, wave reflection occurs. The simplest reflection occurs when the wave strikes the free surface normally. If the incident wave is longitudinal with a given sense, then the reflected wave is normal and must also be longitudinal but with its sense and direction opposite to the incident wave. A transverse disturbance that impinges normally upon a free surface is found to produce a reflection that is also a transverse wave normal to the surface.

When an elastic wave strikes a plane free surface obliquely reflection is more complicated because, in general, the energy of the incident wave is partitioned into two reflected waves instead of only one. A longitudinal plane wave that is obliquely incident upon a plane free surface results in a reflected longitudinal and a reflected shear wave. The conditions of reflection direction are

$$a_{LI} = a_{LR} \quad (2.23)$$

$$\frac{\sin a_{LI}}{\sin a_{SR}} = \frac{c_l}{c_s} = \sqrt{\frac{\lambda+2\mu}{\mu}} \quad (2.24)$$

where a is the propagation direction angle of the particular wave in question, and the subscripts LI, LR and SR refer to the incident longitudinal, reflected longitudinal and reflected shear waves, respectively. The relations among the amplitudes of the waves are

$$\frac{A_{LR}}{A_{LI}} = \frac{2 \cos(a_{LI}) \sin^2(a_{SR}) \sin(2a_{SR}) - \cos^2(2a_{SR}) \sin(a_{LI})}{2 \cos(a_{LI}) \sin^2(a_{SR}) \sin(2a_{SR}) + \cos^2(2a_{SR}) \sin(a_{LI})} \quad (2.25)$$

and

$$\frac{A_{SR}}{A_{LI}} = \frac{2 \sin(2a_{LI}) \cos(2a_{SR}) \sin(a_{SR})}{2 \cos(a_{LI}) \sin^2(a_{SR}) \sin(2a_{SR}) + \cos^2(2a_{SR}) \sin(a_{LI})} \quad (2.26)$$

With regard to the planes of vibration of the various waves, the following theorem can be proved: If a longitudinal wave that is incident on a free surface produces no displacement parallel to the coordinate axis x_2 (see Fig. 1), then the reflected waves, one longitudinal and one transverse, also do not produce displacement parallel to x_2 and the problem is two-dimensional. The direction of displacement of the free surface is found to be in a very simple relation with the

propagation direction of the reflected shear wave, namely

$$a_e = -2a_{SR}$$

when a_e is the angle of emergence and is taken with respect to the normal as before.

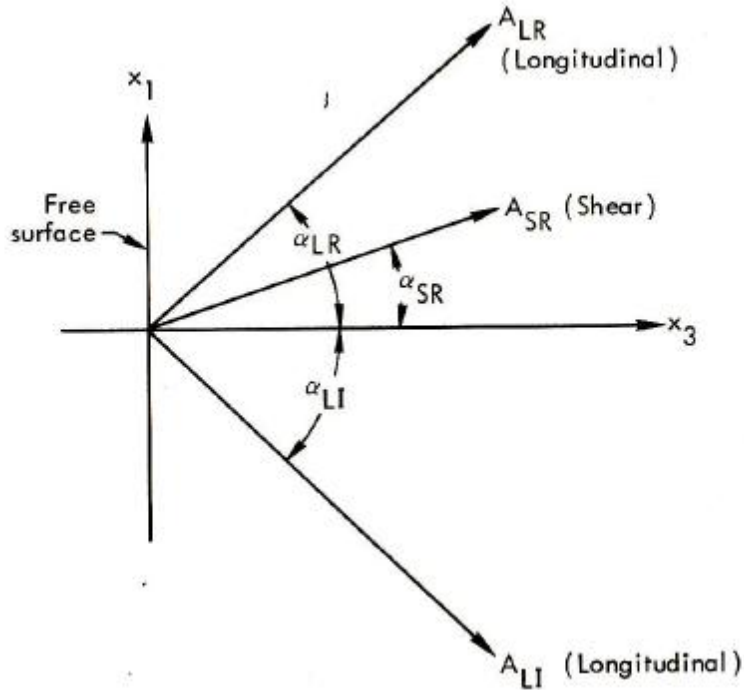


Figure 2.1 Reflection of a longitudinal wave obliquely incident upon a plane free surface [1] (R.J. Wasley, *Stress Wave Propagation in Solids, An Introduction*)

A shear wave that is obliquely incident upon a plane free surface can be described mathematically in a similar fashion. For the more important situation in which the vibration direction of the incident shear wave is in the x_1x_3 plane, it is found that

$$\beta_{LI} = \beta_{LR} \quad (2.27)$$

$$\frac{\sin \beta_{LI}}{\sin \beta_{SR}} = \frac{c_l}{c_s} \quad (2.28)$$

and

$$\frac{B_{SR}}{B_{SI}} = -\frac{\cos^2(2\beta_{SI}) \sin(\beta_{LR}) - 2 \sin^2(\beta_{SI}) \sin(2\beta_{SI}) \cos(\beta_{LR})}{\cos^2(2\beta_{SI}) \sin(\beta_{LR}) + 2 \sin^2(\beta_{SI}) \sin(2\beta_{SI}) \cos(\beta_{LR})} \quad (2.29)$$

and

$$\frac{B_{LR}}{B_{SI}} = -\frac{2 \sin(\beta_{SI}) \sin(\beta_{SI}) \cos(\beta_{SI})}{\cos^2(2\beta_{SI}) \sin(\beta_{LR}) + 2 \sin^2(\beta_{SI}) \sin(2\beta_{SI}) \cos(\beta_{LR})} \quad (2.30)$$

The notation is comparable to that given earlier.

Using similar techniques, extension can be made of the above concepts and results to reflection and refraction at a plane slip-free interface between two different elastic isotropic media. Under these conditions, a disturbance incident obliquely upon this interface will generate, in general, four waves; two of these waves (one longitudinal and one shear) are refracted into the second medium, and two (again one longitudinal and one shear) are reflected from the boundary.

A special case of significant practical interest is the situation in which an initial longitudinal wave is incident normally upon the boundary. We find for this condition that only normal longitudinal waves result and that

$$\frac{A_{LR}}{A_{LI}} = \frac{\rho_2 c_{l2} - \rho_1 c_{l1}}{\rho_2 c_{l2} + \rho_1 c_{l1}} \quad (2.31)$$

And

$$\frac{A_{LRf}}{A_{LI}} = \frac{2\rho_2 c_{l2}}{\rho_2 c_{l2} + \rho_1 c_{l1}} \quad (2.32)$$

where A_{LRf} refers to the amplitude of the refracted wave, subscript 1 refers to the medium in which the incident disturbance propagates, and subscript 2 refers to the other medium; ρc is known as the acoustic impedance. When treating interfaces that are not plane, the phenomenon of scattering results and rather involved mathematical techniques are required for analysis.

2.4 Wave propagation in concrete

As mentioned in the introduction, the EMI technique utilizes the direct and converse piezoelectric effect of a PZT patch bonded to a host structure to introduce stress waves in the structure and sense the response of the structure. Concrete is a heterogenous material consisting of cement, water, air and various sized aggregates. The stress waves excited by the actuator are very complex due to reflection, attenuation and transmitting when they propagated inside concrete structures. The mix of concrete, profile and size of concrete structures, micro-cracks in concrete, wave form, amplitude and frequencies of excitation signal will all affect the velocity and attenuation of output signal which will be received by the sensors.

The stress waves generated by PZT actuators carry the information of the host structure, and thus can be used to identify the existence and nature of the damage. The wave propagation of stress waves in concrete structures can be viewed as one dimensional longitudinal wave propagation. The wave equation can be written as [24]:

$$\frac{d^2 u}{dx^2} = \frac{1}{c_b^2} \cdot \frac{d^2 u}{dt^2} \quad (2.33)$$

where c_b^2 equals E/ρ , u is the displacement of an element, E is the Young's modulus and ρ is the density of the material. The average power p of the harmonic response over a period can be expressed as

$$p = E \cdot A^2 \cdot \omega^2 / 2 \cdot c_b = \sqrt{E \cdot \rho} \cdot A^2 \cdot \omega^2 / 2 \quad (2.34)$$

where A is the harmonic amplitude and ω is the circular, or angular, frequency. Equation (2.34) can be rewritten as

$$A = \left(\frac{1}{\omega}\right) \cdot \left(\frac{4 \cdot \rho^2}{E \cdot \rho}\right)^{1/4} \quad (2.35)$$

As shown in equation (2.35), the harmonic amplitude is affected by the Young's modulus, E , of the medium. During the early-age development of concrete material, the Young's modulus, E , increases as the concrete gains strength during the hydration process. Consequently, the harmonic amplitude will decrease with the increase of the Young's modulus, E . Moreover, the Young's modulus, E , is the major affecting factor in determining concrete strength. Therefore, the harmonic amplitude is correlated with the concrete strength through the Young's modulus. By observing the amplitude change of harmonic stress wave, the strength development of concrete specimens can be monitored and evaluated. In addition, according to the study conducted by Hu and Yang, the material damping reduces (concrete was initially 'soft') during the curing age. As moisture content drops, concrete damping tends to fall down. To take the damping coefficient into account, Song et al. proposed replacing E by $E(1+n)$ in Equation (2.35), where n is the damping coefficient. Due to the material and structural damping, waves generated by the PZT actuator attenuate while propagating through the concrete specimens.

The above are valid for both EMI technique (with changes in the wave travelling through the structure manifesting with changes in the impedance signatures) as well as in SHM techniques using wavelet packet analysis (with changes manifesting with time delay and energy dissipation).

3 History and applications of piezoelectric materials

3.1 History of piezoelectricity and piezoelectric materials

The notion that electricity could be produced in some crystals by subjecting them to mechanical pressure is believed to have been suggested by Charles Coulomb [36]. Subsequent investigations by Hauy [37] and Becquerel [38] prior to 1825 hinted that this pressure-electric effect was a possibility, however, irrefutable evidence of the effect did not emerge for about six decades. This evidence was provided by the research efforts of Jacques and Pierre Curie [39] in 1880 at the University of Paris, while studying crystals such as quartz, sodium potassium tartrate (Rochelle salt), and tourmaline. By placing weights on the faces of particular crystal cuts, like the X cut quartz plate shown in Fig. 3.1.1, they succeeded in detecting charges on the crystal surfaces and demonstrated that the magnitude of charge was proportional to the applied weight, thus verifying the direct pressure-electric effect. This discovery was not by chance; rather such an effect was anticipated by the Curie brothers from consideration of crystal structure and the pyroelectric phenomena (thermo-electric coupling effect) (Cady, 1964).

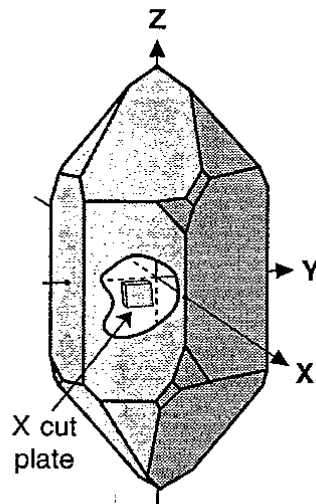


Figure 3.1 Right-handed quartz crystal and an X cut plate [32] (D. F. Jones, S. E. Prasad, J. B. Wallace, *Piezoelectric Materials and Their Applications*)

However, it was through thermodynamic reasoning which led Lippmann to predict the converse piezoelectric effect that prompted the Curie brothers to discover it shortly after. The converse pressure-electric effect, that is the development of a mechanical strain when an electric field is applied to a crystal such as quartz, was predicted in 1881 by Lippmann [40] who based his theory on fundamental thermodynamic principles. In the same year, this theoretical converse effect was supported experimentally by the Curies [41]. Shortly after these works on the converse effect were published, Hankel suggested the name “piezoelectricity” to describe

the effect, with “piezo” being a Greek derivative meaning “to press” [36]. Thus the terms direct and converse piezoelectric effects were introduced into the literature and have been entrenched therein for more than a century.

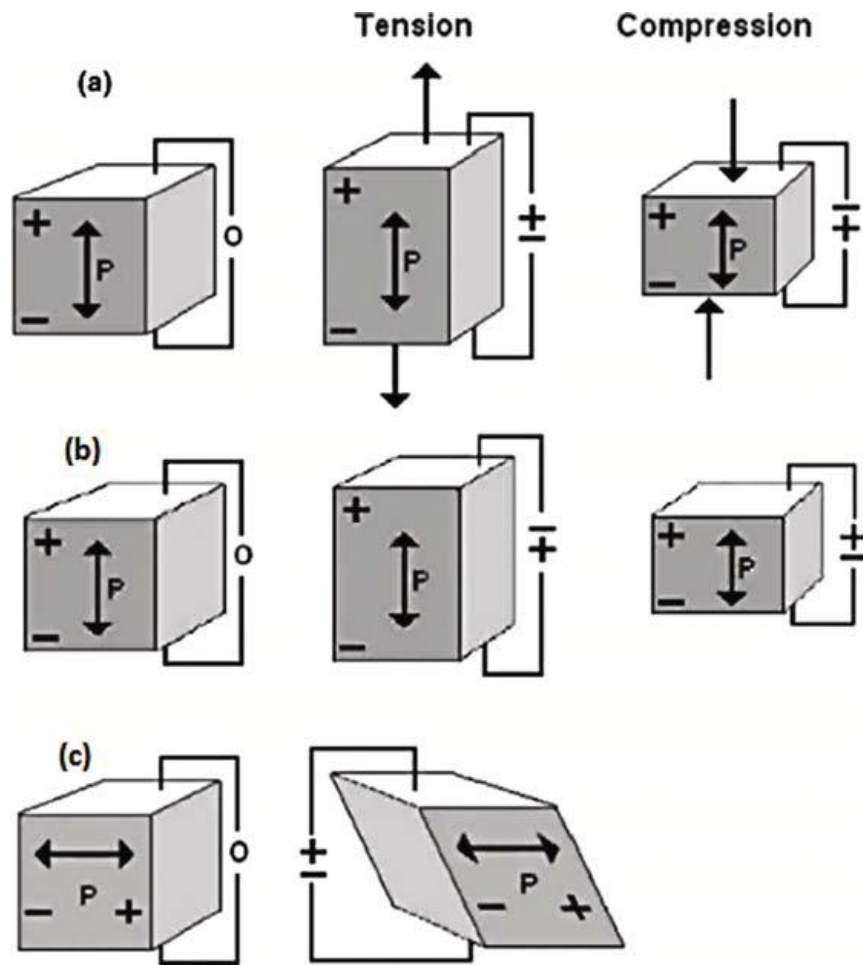


Figure 3.2 Schematic representations of the longitudinal direct (a), converse (b), and shear (c) piezoelectric effects [34] (A.L. Kholkin, N. A. Pertsev, A. V. Goltsev, *Piezoelectric and Acoustic Materials for Transducer Application*)

Significant experimental contributions to the evolution and exploitation of the piezoelectric effect came from the field of crystallography, which received an enormous boost in 1912 with the discovery that crystals could act as three-dimensional X-ray diffraction gratings. This led to a number of studies that linked observed piezoelectric properties to internal crystalline structures [42].

Another concept that would play a useful role in the development of piezoelectric devices was that of the equivalent circuit. Butterworth [43] first realized that vibrating mechanical systems sustained by electrical currents or voltages could be represented by lumped-parameter electrical circuits consisting of inductors, capacitors, and resistors. It was Cady [44] and Van Dyke [45], colleagues at Wesleyan University in Middletown, Connecticut, who first derived the equivalent circuit shown in Fig. 3.1.3 for the piezoelectric resonator at an isolated resonance

frequency. In this circuit, a clamped capacitance C_0 representing the dielectric property of the resonator is placed in parallel with a motional arm consisting of L_1 , C_1 , and R_1 , representing the inertial, elastic, and frictional properties of the resonator, respectively. Hence, the direct correspondences between mechanical and electrical quantities, such as mass and inductance or compliance and capacitance, allow the designer of electromechanical devices and systems to formulate appropriate equivalent circuits that can be analyzed using the well-known laws, theorems, and procedures established in electrical circuit theory.

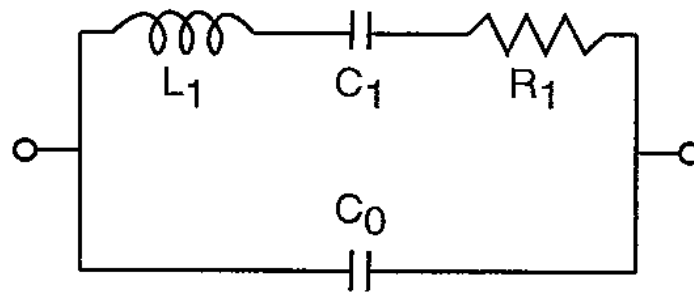


Figure 3.3 Equivalent circuit of a piezoelectric resonator [32] (D. F. Jones, S. E. Prasad, J. B. Wallace, *Piezoelectric Materials and Their Applications*)

3.2 Applications of piezoelectric materials

The first application of the piezoelectric effect was a force and charge measuring apparatus patented by the Curies in 1887 [46]. They used the piezoelectric effect to measure voltages and forces by constructing bimorphs from two X cut quartz plates of opposite polarity. The bimorphs consisted of two plates bonded together and electrically excited in such a way that each plate deformed in the opposite direction, resulting in a net bimorph bending motion. The deflections of the bimorph were much greater than the displacements of single quartz plates. Observations of these bimorph deflections using a microscope, and measurements of the charge on the bimorph when it was mechanically deformed, permitted the measurements of voltages and forces, respectively. Other applications for the piezoelectric effect in crystals would have to wait for about thirty years.

In early 1917 the first piezoelectric quartz transducers for underwater echo ranging and depth sounding were built by Paul Langevin at the School of Industrial Physics and Chemistry in Paris [47]. Using high-frequency vacuum tube amplifiers and quartz-steel sandwich transducers, Langevin was able to detect echoes from submarines at ranges exceeding one kilometer in 1918. Depth sounding equipment based on Langevin's ultrasonic quartz-steel transducers became commercially available in Great Britain and the United States by 1925.

In 1919, Nicolson [48] demonstrated the use of Rochelle salt crystals in loudspeakers, microphones, telephone receivers, and phonograph pick-ups. A stereo phonograph pick-up head

utilizing Rochelle salt bender elements (i.e. bimorphs) is illustrated in Fig. 3.2.1. In this figure, the pick-up is drawn vertically and the view is looking up at the stylus from the surface of the record disc. The stylus vibrations, generated from signals recorded on the walls of the record grooves plus the rotation of the record itself, are coupled into the crystal benders and converted into electrical signals.

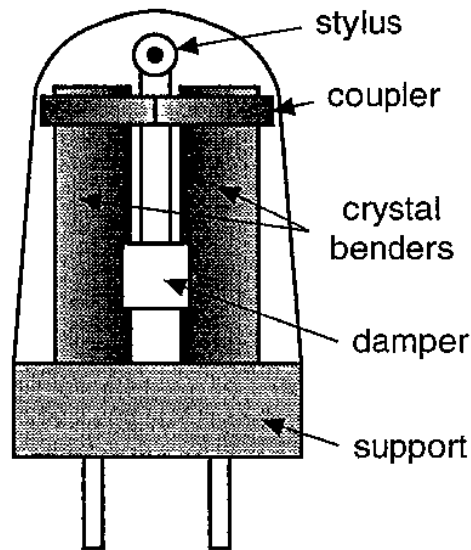


Figure 3.4 Rochelle salt crystal phonograph pick-up (bottom view) [32] (D. F. Jones, S. E. Prasad, J. B. Wallace, *Piezoelectric Materials and Their Applications*)

The field of crystal controlled oscillators began in the early 1920s with the pioneering efforts of Cady [44] and Pierce [49] using high Q piezoelectric quartz resonators. Quality factors exceeding a million can be achieved in these oscillators. The importance of these devices to radio transmitters and receivers led to a number of important patents and associated patent interferences, with legal battles that lasted for more than three decades [50]. The need for large quantities of pure quartz crystals was so great for communications applications that natural sources became strained with the demand. This sparked many researchers to investigate growing techniques for quartz [51]. Today, cultured quartz oscillators are used primarily by the electronics industry in applications ranging from computer clocks and wrist-watches to radio and television broadcasting, which is testimony to the stability and reliability of the quartz resonator.

Piezoelectric quartz crystal transducers were used extensively in delay lines for moving-target indicator radar systems in the 1940s [52]. In these systems, moving and stationary targets were distinguished by storing a radar pulse in a delay line and comparing it to subsequent pulses. Using this methodology, moving targets were prominently displayed on a plan-position

indicator display while stationary targets were suppressed. Delay lines were also used in digital computers and color televisions.

The piezoelectric quartz transducer was also employed as an ultrasonic wave transmitter in an acoustic interferometer described by Pierce in 1925 [53]. By generating standing waves between the crystal transducer and a movable reflector, this instrument was capable of measuring velocity and attenuation as a function of composition and temperature in a variety of gases and liquids.

Jaffe, Cook, and Jaffe [54] have reviewed the discovery and development of the first polycrystalline piezoelectric ceramic, barium titanate (BaTiO_3), which took place in the 1940s. They pointed out that three key areas of investigation were responsible for our understanding of the piezoelectric effect in this ceramic. First of all, although barium titanate perovskites had been known since the 1920s [55], the discovery of high dielectric constants in various barium and titanium oxide compositions in 1941 [56] became the catalyst for further research on these materials. Secondly, by the mid 1940s it was realized that the high dielectric constant observed in barium titanate ceramic was a consequence of ferroelectricity [57, 58]. Finally, it was demonstrated that isotropic samples of ferroelectric barium titanate ceramic could be made piezoelectric, and necessarily anisotropic, by applying a large electric field at an elevated temperature, thereby creating an internal remnant polarization that persists long after the removal of the electric and thermal fields [59, 60]. This process, known as poling in the ceramics industry, was the revolutionary finding that signaled the decline of piezoelectric crystal use in many applications.

One of the significant advantages of piezoelectric ceramics over piezoelectric crystals is the ability to form ceramics into a variety of shapes and sizes. Discs, rings, washers, cylinders, tubes, bars, plates, and hemispheres are some of the possibilities. When combined with the freedom to determine the poling direction and electrode configuration, ceramics manufacturers possess great versatility to tailor ceramic components for specific device requirements.

Barium titanate was first used for phonograph pick-ups in 1947, replacing Rochelle salt crystal pick-ups used since about 1935 [54]. In the field of instrumentation standards, barium titanate accelerometers and accelerometer calibration shakers were developed in the early 1950s to support improvements to missile guidance systems [61, 62]. Barium titanate was also used in the medical field in the late 1950s for intracardiac phonocatheters [63, 64]. Non-piezoelectric applications for barium titanate included monolithic multilayer ceramic capacitors, and positive temperature coefficient resistors for overload protection devices and heating elements [65].

Several other perovskite and oxide ceramic compositions investigated during the early 1950s form the basic constituents of modern piezoelectric ceramics. These compositions included lead titanate (PbTiO_3) in 1950 [66, 67], lead zirconate (PbZrO_3) in 1950 [68, 69], lead metaniobate (PbNb_2O_6) in 1952 [70], and in lead zirconate titanate [$\text{Pb}(\text{Zr,Ti})\text{O}_3$] in 1952 [71, 72, 73]. Lead zirconate titanate became the dominant piezoelectric ceramic material for transducers primarily due to its high coupling coefficient.

Transducers made from lead zirconate titanate ceramic elements can be used to generate sparks in a high-voltage spark gap. This effect has led to a number of applications that require the ignition of combustible gases. When subjected to static or dynamic loads via the end plate, the ceramic cylinders can generate voltages as high as 20,000 volts in the high tension lead; sufficient to produce a spark in a spark gap. Piezoelectric igniters have been used in gas run domestic appliances, lawn mowers, welding equipment, and pocket lighters.

Lead zirconate titanate flexural transducers have a broad range of applications involving the generation and reception of sound. Examples include microphones, headphones, loudspeakers, and buzzers. The latter device, the piezoelectric buzzer, has been used as a compact alarm in wrist-watches, clocks, and calculators.

Piezoelectric lead zirconate titanate ceramics are also used as the active elements in hydrophones and projectors that receive and generate underwater sound, respectively. In this design there are two piezoelectric ceramic cylinders that generate electrical signals in response to incident sound waves.

The vinylidene fluoride monomer $\text{CH}_2 - \text{CF}_2$ has been known for over ninety years and forms the basic building block of the semicrystalline polymer polyvinylidene fluoride (PVDF) [74]. This long chain polymer was discovered to be highly piezoelectric in 1969 by Kawai [79] and rapid development and commercialization followed shortly afterward. PVDF is manufactured in sheet form starting with nonpolar α -phase film extruded from the melt. The extruded film material is stretched uniaxially, a process that rotates the long chain molecules and produces the polar β -phase needed for high piezoelectric activity. Finally, the randomly directed dipoles associated with the stretched β -phase film are reoriented by applying a poling field in a direction normal to the plane of the film. Further details on the structure and production of PVDF are given by Sessler [75], Lovinger [76], Bloomfield and Marcus [77], and Davis [78].

Polyvinylidene fluoride has also been combined with other polymers in an attempt to synthesize copolymer materials with strong piezoelectric activities [76]. One such material is the piezoelectric copolymer polyvinylidene fluoride-trifluoroethylene, abbreviated here as $\text{VF}_2 - \text{VF}_3$. This copolymer can be used in underwater hydrophone applications, as discussed below in connection with PVDF.

For some applications, PVDF has attractive advantages over piezoelectric ceramics. For example, since PVDF film is flexible and lightweight, it has been used for audio transducers such as microphones, tone generators, headphones, and high-frequency loudspeakers [79]. One application of note for PVDF film transducers is the musical instrument pick-up. Small polymer strips can be attached to a variety of instruments from guitars and pianos to woodwinds and drums with good sound reproduction characteristics [80]. Other application areas for PVDF devices include medical transducers, electromechanical transducers, and pyroelectric and optical devices.

4 Electro-mechanical impedance (EMI) technique

4.1 Impedance

Electrical Impedance: (or impedance) is the basic electrical parameter used to characterize electronic circuits, components and materials. It is defined as the ratio of the voltage applied to the device and the resulting current running through it. It is the measure of the opposition that an electric circuit presents to the passage of a current when a voltage is applied. In other words impedance is the total opposition a circuit offers to the flow of an alternate current (AC circuit) at a given frequency. It is generally represented as a complex quantity which can be shown graphically. The basic elements that make up electrical impedances are inductance, capacitance and resistance (L, C and R respectively). In the real world, electronic components are not purely resistors, inductors or capacitors, but a combination of the three.

The definition of resistance for direct current circuits is given by Ohm's law, i.e. the ratio of applied voltage to the resulting current. In alternate current circuits (AC) the voltage reverses its direction or polarity. For AC circuits Ohm's law must be modified to $Z=V/I$, where Z is a complex number with a real component R_s (resistance) and an imaginary component X_s (reactance) ($Z = R_s + j \cdot X_s$ in Cartesian form, or $Z = |Z| \cdot e^{j\theta}$ in polar form).

The phase shift can be drawn in a vector diagram showing its real part R_s , its imaginary part X_s and the phase angle θ . The reciprocal of Z is admittance Y. Admittance is also a complex number having a real part conductance (G_p) and susceptance (B_p) with a phase angle ϕ . The connection of phase of impedance and admittance is $\theta=-\phi$. The following table shows all the impedance terms and equations.

Mechanical impedance: A harmonic force applied on a structure can be represented as a rotating phasor on a complex plane. The mathematical expression of this force is [30]:

$$F(t) = F_0 \cdot (\cos\omega t + j \cdot \sin\omega t) = F_0 \cdot e^{j\omega t}, \quad (4.1)$$

where:

$F_0 \rightarrow$ the magnitude of the phasor

$\omega \rightarrow$ the angular frequency of the phasor (anti-clockwise)

The resulting velocity response of the structure \dot{u} , at the point of application of the force, is also harmonic in nature. It lags behind the force by a phase angle ϕ due to the mechanical impedance of the structure. Mathematically, velocity can be expressed as [30]:

$$\dot{u} = \dot{u}_0 \cdot \cos(\omega t - \phi) + \dot{u}_0 \cdot j \cdot \sin(\omega t - \phi) = \dot{u}_0 \cdot e^{j(\omega t - \phi)}. \quad (4.2)$$

The mechanical impedance of a structure, at the point of application of the force, is defined as the ratio of the driving harmonic force to the resulting velocity at that point, mathematically expressed as [30]:

$$Z = \frac{F}{\dot{u}} = \frac{F_0 \cdot e^{j\omega t}}{\dot{u}_0 \cdot e^{j(\omega t - \varphi)}} = \frac{F_0}{\dot{u}_0} \cdot e^{j\varphi} \quad (4.3)$$

and basically is a measure of how much a structure resists motion when subjected to a given force. It relates forces with velocities acting on a mechanical system. Mechanical impedance is the inverse of mechanical admittance or mobility. The mechanical impedance is a function of the frequency ω of the applied force and can vary greatly over frequency. At resonance frequencies, the mechanical impedance will be lower, meaning less force is needed to cause a structure to move at a given velocity. The simplest example of this is when a child pushes another on a swing. For the greatest swing amplitude, the frequency of the pushes must be near the resonant frequency of the system.

Table 4.1 Impedance terms and equations

Parameter	Quantity	Unit Symbol	Formula
Z	Impedance	Ohm, Ω	$Z = R_s + j \cdot X_s = \frac{1}{Y}$ $= Z \cdot e^{j\theta}$
Z	Magnitude of Z	Ohm, Ω	$ Z = \sqrt{R_s^2 + X_s^2} = \frac{1}{ Y }$
R _s	Resistance, real part of Z	Ohm, Ω	$R_s = \frac{G_p}{G_p^2 + B_p^2}$
X _s	Reactance, imaginary part of Z	Ohm, Ω	$X_s = -\frac{B_p}{G_p^2 + B_p^2}$
Y	Admittance	Siemens, S	$Y = G_p + j \cdot B_p = \frac{1}{Z}$ $= Y \cdot e^{j\varphi}$
Y	Magnitude of Y	Siemens, S	$ Y = \sqrt{G_p^2 + B_p^2} = \frac{1}{ Z }$
G _p	Conductance, real part of Y	Siemens, S	$G_p = \frac{R_s}{R_s^2 + X_s^2}$
B _p	Susceptance, imaginary part of Y	Siemens, S	$B_p = -\frac{X_s}{R_s^2 + X_s^2}$
Q	Quality factor	None	$Q = -\frac{1}{D} = \frac{R_s}{X_s} = \frac{G_p}{B_p} = \tan\theta$
D, Df or tan δ	Dissipation factor	None	
θ	Phase angle of Z	Degree or rad	$\theta = -\phi$
ϕ	Phase angle of Y	Degree or rad	$\phi = -\theta$

4.2 Structural Health Monitoring (SHM) systems and the Electro-Mechanical Impedance (EMI) technique

An on-line structural health monitoring system should meet the following three requirements: i) it must be small, non-intrusive, and must offer the possibility of being located in inaccessible remote areas of the structure, ii) it must be as sensitive as conventional non-destructive evaluation (NDE) techniques, *i.e.* it must be able to detect minor damages such as small cracks, delaminations or loose connections and iii) it must be able to monitor a certain minimum area of the structure as opposed to the point measurements offered by presently available NDE equipment.

Conventionally, automated structural health monitoring (SHM) has been attempted by measuring static displacements or static strains or low frequency vibration data. These techniques typically rely upon conventional sensors such as strain gauges or accelerometers, which can only extract load or strain histories. Conventional NDE techniques such as ultrasonic testing and X-radiography can provide significant details about the nature of damage. However, these techniques usually require direct access to the structure being investigated and involve bulky equipment. Moreover, these techniques usually require the structure be out of service during the inspection and this may cause major disruptions. For these reasons, these techniques are inadequate for on-line structural health monitoring.

However, during the last few years, the advent of smart materials, such as piezoelectric materials, optical fibers, shape memory alloys and magnetostrictive materials, has added a new dimension to SHM by enabling the development of system with higher resolution, faster response and greater reliability. The term “Smart Structures” or “Intelligent Material Systems” is fast becoming a common phrase among the engineering community. Although there is no agreed definition for intelligent material systems, Rogers proposed two definitions. The first one is based upon a technology paradigm: “the integration of actuators, sensors, and controls with a material or structural component.” The second one is based upon a science paradigm and addresses the goal of intelligent material systems: “material systems with intelligence and life features integrated in the microstructure of the material system to reduce mass and energy and produce adaptive functionality.”

The piezoelectric impedance-based structural health monitoring technique may meet these requirements for on-line structural health monitoring. This technique utilizes the direct and the converse electromechanical properties of piezoelectric materials, allowing simultaneous actuation and sensing of the structure. In this technique, a piezoelectric-ceramic (PZT) patch is bonded to the monitored structure and excited by an alternating voltage sweep signal, typically in kHz range, by an impedance analyzer. The vibrating patch transfers its vibrations to the host structure and simultaneously, the structure influences the electrical circuit comprising the bonded patch and the AC source. A plot of conductance (real part of admittance) or resistance (real part of impedance) as a function of frequency constitutes a unique vibrational signature of the structure, reflecting structural characteristics such as inherent stiffness, damping and mass distribution. In this manner, the same patch acts as an actuator as well as a sensor. The

technique is characterized by a high order of sensitivity to damage. Typically, in concrete, the piezo-impedance transducers can detect cracks before they actually become visible to the naked eyes.

Nevertheless, there are still some problems to be solved before full scale development and commercialization can take place. These problems basically include the sensitivity of piezoelectric materials in temperature and humidity changes and the small sensing area of each PZT patch resulting in a large number of piezoelectric sensors and actuators to be required in practical use, especially in large structures.

In general, structural health monitoring or damage detection techniques using the vibration response of the structure can be classified into two categories: model-based and non model-based. Furthermore, model-based techniques can be classified into modal-dependent and modal-independent. The impedance-based technique belongs to the non-model-based. Each technique has both advantages and disadvantages as shown in Table 4.2.

Table 4.1 Comparison of structural health monitoring techniques using vibration response

	Model-Based		Non-Model-Based	
	Modal	Non-Modal	Impedance	Others
Quantitative Evaluation	Fair	Fair	Poor	Poor
Small Damage Detection	Poor	Good	Good	Unknown
Complex Structures	Fair	Poor	Good	Unknown

A model-based technique may assess damage quantitatively if the model is appropriate. However, it is difficult to apply this technique to complex structures for which we can hardly make satisfactory models. In addition, a modal-dependent model-based technique cannot detect very small damage. The reason is that this technique basically deals with low-frequency global modes that are relatively unaffected by small damage. On the contrary, the impedance-based method cannot quantify damage precisely because this method evaluates damage merely by comparing each impedance measurement with a baseline measurement. Nevertheless, it is sensitive enough to detect very small damage as well as incipient damage and can be applied to complex structures.

4.3 The Electro-mechanical principle

The phenomenon of piezoelectricity occurs in certain classes of non-centrosymmetric crystals, such as quartz, in which electric dipoles are generated due to mechanical deformations. The same crystal will also exhibit the converse effect, that is, they undergo mechanical deformations when subjected to electric fields. In EMI the lead zirconate titanate piezoelectric-ceramic (PZT) patches play key role to the technique. The charges and the deformations they

manifest in the direct and converse effect respectively, is expressed mathematically by the formulas [30]:

$$D_i = \overline{\varepsilon_{ij}^T} \cdot E_j + d_{im} \cdot T_m \quad (4.4)$$

$$S_k = d_{jk} \cdot E_j + \overline{s_{km}^E} \cdot T_m \quad (4.5)$$

Where:

D	→	the electric displacement
S_k	→	the mechanical strain
E_j	→	the electric field
T_m	→	the mechanical stress
$\overline{\varepsilon_{ij}^T}$	→	the complex electric permittivity of the PZT material at constant stress
d_{im} and d_{jk}	→	the piezoelectric strain coefficients
$\overline{s_{km}^E}$	→	the complex elastic compliance at constant electric field.

The superscripts 'T' and 'E' indicate that the quantity has been measured at constant stress and constant electric field respectively.

Now consider a PZT patch, shown schematically in Fig.4.1, under an electric field E_3 along direction 3 and a stress T_1 along direction 1, which is the actual case in our measurements. It is assumed that the patch expands and contracts in direction 1 when the electric field is applied in direction 3. The fundamental constitutive relationships described by equations (4.4) and (4.5) of the PZT patch can now be expressed as [30]:

$$D_3 = \overline{\varepsilon_{33}^T} \cdot E_3 + d_{31} \cdot T_1 \quad (4.6)$$

$$S_1 = d_{31} \cdot E_3 + \frac{T_1}{\overline{Y_{11}^E}} \quad (4.7)$$

where $\overline{Y_{11}^E} = Y_{11}^E (1 + nj)$ is the complex Young's modulus of the PZT.

Equation (4.6) represents the so-called 'direct effect', that is, application of a mechanical stress produces charge on the surfaces of the PZT patch. This effect is taken advantage of in using PZT material as a sensor. Equation (4.7) represents the 'converse effect', that is, application of an electric field induces elastic strain in the material. Same coupling constant d_{31} appears in both the equations.

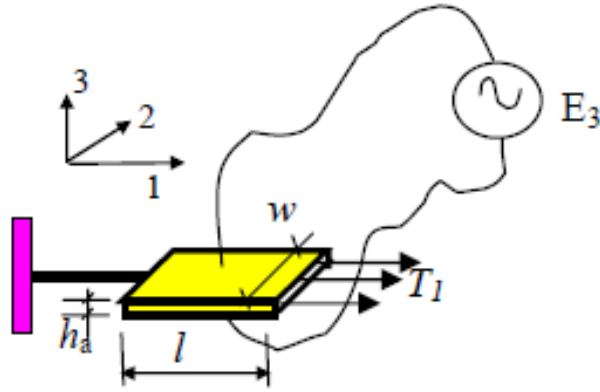


Figure 4.1 A PZT patch under electric field and mechanical stress [18] (S. Bhalla, A. Gupta, *Modelling Shear Lag Phenomenon for Adhesively Bonded Piezo-Transducers*)

4.4 Existing PZT-Structure interaction models

During the last one and half decades, several attempts have been made to model the PZT-structure electromechanical interaction. The beginning was made by Crawley and De Luis (1987) [9] in the form of ‘static approach’, later substituted by the ‘impedance approach’ of Liang, et al. (1994) [30]. The *static approach* assumes frequency independent actuator force, determined from the static equilibrium and the strain compatibility between the PZT patch and the host structure.

The PZT patch is assumed to be a thin bar with length l , width w and thickness h , under static equilibrium with the structure, which is represented by its static stiffness K_s , as shown in figure 4.2. As mentioned earlier applying voltage in this direction reduces the equations (4.4) and (4.5) to [30]:

$$D_3 = \overline{\varepsilon_{33}^T} \cdot E_3 + d_{31} \cdot T_1 \quad (4.6)$$

$$S_1 = d_{31} \cdot E_3 + \frac{T_1}{\overline{Y^E}} \quad (4.7)$$

Where $\overline{Y^E}$ is the complex Young’s modulus under constant electric field. Owing to static conditions, the imaginary component of the complex terms in the PZT constitutive relations can be dropped. Therefore for the PZT patch, the expression of the axial force using eq. (4.7) is:

$$F_p = w \cdot h \cdot T_1 = w \cdot h \cdot (S_1 - d_{31} \cdot E_3) \cdot \overline{Y^E} \quad (4.8)$$

where w denotes the width and h the thickness of the PZT patch. Similarly the axial force of the structure can be determined as

$$F_s = -K_s \cdot x = -K_s \cdot l \cdot S_1 \quad (4.9)$$

where x is the displacement at the end of the PZT patch and l denotes the length of the patch. The negative sign signifies that a positive displacement x causes compressive force in the spring. Force equilibrium in the system implies that $F_p = F_s$. Substituting equations (4.8), (4.9) in the force equilibrium equation, we can derive an equilibrium strain S_{eq} , as

$$S_{eq} = \frac{d_{31} \cdot E_3}{(1 + K_s \cdot l / Y^E \cdot w \cdot h)} \quad (4.10)$$

$$F_s = F_p = K_s \cdot l \cdot S_{eq} \quad (4.11)$$

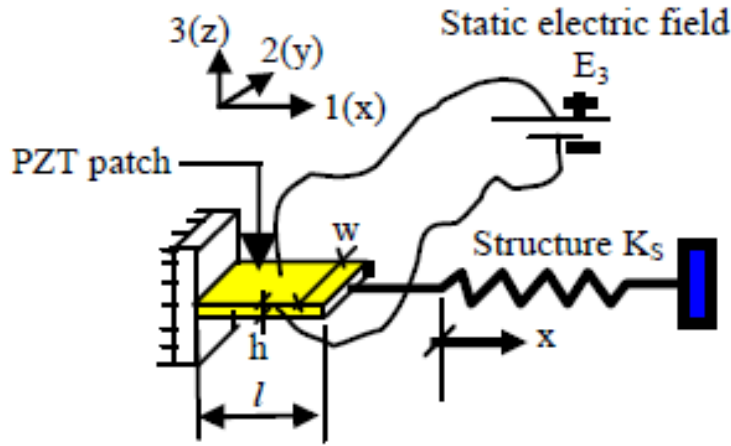


Figure 4.2 Static approach modeling of PZT-Structure interaction stress [18] (S. Bhalla, A. Gupta, *Modelling Shear Lag Phenomenon for Adhesively Bonded Piezo-Transducers*)

Now, for determining the system response under an alternating electric field, Crawley and de Luis (1987) simply recommended that a dynamic force $F_{eq}=F_s=F_p$ will be considered acting upon the host structure, irrespective of the frequency of actuation. However, assumption of frequency independent actuator force, determined purely from static equilibrium and strain compatibility between the PZT patch and the host structure, is only an approximation valid under frequencies sufficiently low to give rise to quasi-static conditions. In addition, since only static PZT properties are considered, the effects of damping and inertia are not considered. Because of these reasons, the static approach often leads to significant errors, especially near the resonant frequency of the structure or the patch.

In order to eliminate this inaccuracy, Liang and coworkers modeled the host structure as mechanical impedance Z_s , based on dynamic equilibrium rather than static, connected to the

PZT patch at the end, as shown in Fig. 4.3, with the patch undergoing axial vibrations under an alternating electric field E_3 . Considering the dynamic equilibrium of an infinitesimal element of the patch, they derived the governing differential equation as [30]:

$$\overline{Y^E} \frac{\partial^2 u}{\partial x^2} = \rho \frac{\partial^2 u}{\partial t^2} \quad (4.12)$$

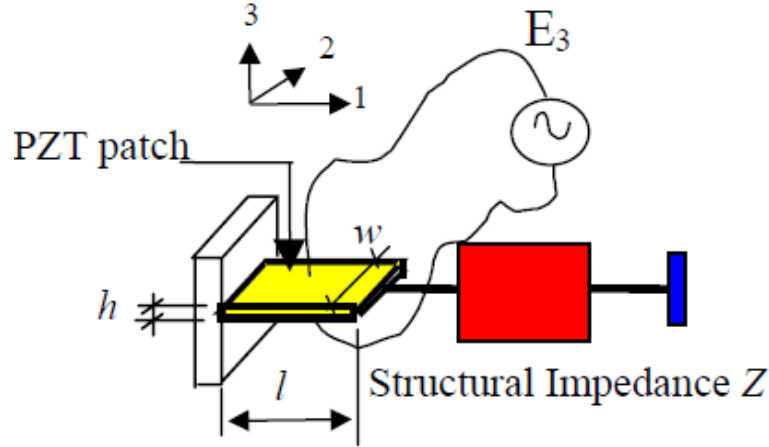


Figure 4.3 Liang's impedance approach modeling of PZT-Structure interaction [18] (S. Bhalla, A. Gupta, *Modelling Shear Lag Phenomenon for Adhesively Bonded Piezo-Transducers*)

where u is the displacement at any point of the patch in direction 1 at any instant time t . Furthermore the mechanical impedance Z_s is mathematically related to the force F and the velocity \dot{u} , by :

$$F = -Z_s \cdot \dot{u} \quad (4.13)$$

where the negative sign, as in the case of static approach, signifies the fact that a positive displacement (or velocity) causes a compressive force in the PZT patch. Further, instead of actuator's static stiffness, actuator's mechanical impedance, Z , was derived as

$$Z_a = \frac{k \cdot w \cdot h \cdot \overline{Y^E}}{j \cdot \omega \cdot \tan(kl)} \quad (4.14)$$

so as to rigorously include the actuator's dynamic stiffness and damping. Making use of the PZT constitutive relation, and integrating the charge density over the surface of the right half of the PZT patch ($x = 0$ to l), Liang and coworkers obtained the following expression for the electromechanical admittance (the inverse of electro-mechanical impedance) for the right half of the PZT patch:

$$\bar{Y} = G + B \cdot j = \omega \cdot j \cdot \frac{w \cdot l}{h} \cdot \left[\left(\overline{\varepsilon_{33}^T} - d_{31}^2 \cdot \overline{Y^E} \right) + \left(\frac{Z_a}{Z_s + Z_a} \right) \cdot d_{31}^2 \cdot \overline{Y^E} \cdot \left(\frac{\tan \kappa \cdot l}{\kappa \cdot l} \right) \right] \quad (4.15)$$

Where w, l and h represent the PZT patch's dimensions, d_{31} the piezoelectric strain coefficient for the 1-3 axes and ω the angular frequency. $\overline{Y^E} = Y^E \cdot (1 + n \cdot j)$ is the complex Young's modulus of the PZT patch (at constant electric field) and $\overline{\varepsilon_{33}^E} = \varepsilon_{33}^E \cdot (1 - \delta \cdot j)$ the complex electric permittivity (at constant stress), with the symbols n and δ denoting the mechanical loss factor and the dielectric loss factor respectively. Z_a represents the mechanical impedance of the PZT patch (in short circuited condition), given by equation (4.14) where k , the wave number, is related to the density ρ and the Young's modulus $\overline{Y^E}$ of the patch by

$$k = \omega \cdot \sqrt{\frac{\rho}{\overline{Y^E}}} \quad (4.16)$$

In real-life applications, where the PZT patch is surface-bonded on a structure, as shown in Fig. 4.4, the nodal plane passes through the centre line of the patch. The structure can be represented as a set of two impedances Z_s connected on the either side of the patch, as illustrated in Fig. 4.5. For this scenario, l would be the half-length of the patch and Eq. (4.15) needs to be modified as (simply by multiplying eq. 4.4.12 by a factor 2)

$$\bar{Y} = G + B \cdot j = 2 \cdot \omega \cdot j \cdot \frac{w \cdot l}{h} \cdot \left[\left(\overline{\varepsilon_{33}^T} - d_{31}^2 \cdot \overline{Y^E} \right) + \left(\frac{Z_a}{Z_s + Z_a} \right) \cdot d_{31}^2 \cdot \overline{Y^E} \cdot \left(\frac{\tan \kappa \cdot l}{\kappa \cdot l} \right) \right] \quad (4.17)$$

It is clear from the above equation that any change in the mechanical impedance of the structure will alter the resulting admittance signature. In other words, structural integrity can be evaluated by measuring the electrical impedance of the PZT. As observed, the electro-mechanical admittance across the terminals of the PZT patch is mathematically a complex number. G , the real part, is called the conductance whereas B , the imaginary part, is called the susceptance. A plot of G as a function of frequency is called the conductance signature, and that of B as susceptance signature. In SHM techniques the conductance or resistance plot is usually monitored as the difference is obvious from the raw measurements of an impedance analyzer. Susceptance and reactance also undergo changes due to damage but the difference is feebly apparent from raw measurements. The imaginary components are generally drowned by the capacitive contribution of the PZT patch and cannot be used for SHM without further processing.

derivations of Liang and co-workers to model the interactions of a generic PZT element coupled to a 2D host structure. Their analytical model is schematically illustrated in Figure 4.6.

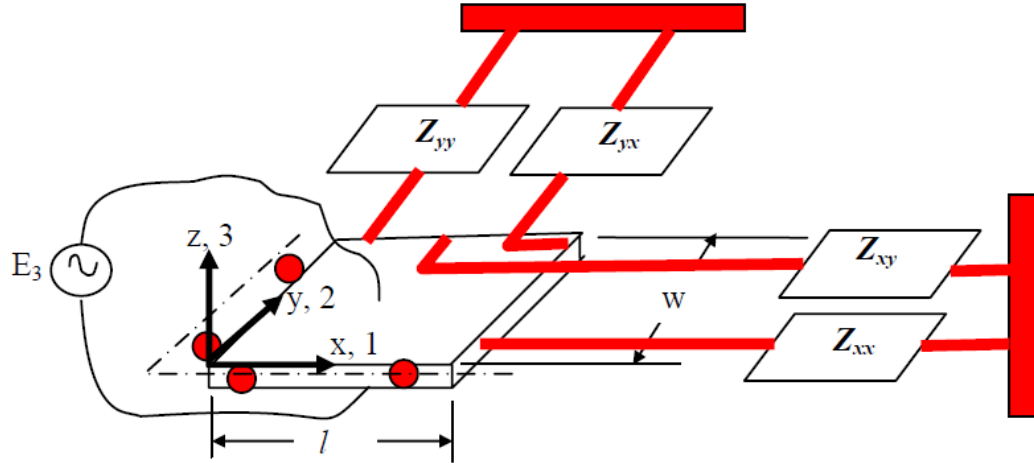


Figure 4.6 Modeling PZT-structure 2D physical coupling by impedance [30] (S. Bhalla, C. G. Soh, *Structural Health Monitoring by Piezo-Impedance Transducer, I: Modelling*)

They represented the structural mechanical impedance by direct impedances Z_{xx} and Z_{yy} and the cross impedances Z_{xy} and Z_{yx} , related to the planar forces F_1 and F_2 (in directions 1 and 2 respectively) and the corresponding planar velocities \dot{u}_1 and \dot{u}_2 by

$$\begin{bmatrix} F_1 \\ F_2 \end{bmatrix} = - \begin{bmatrix} Z_{xx} & Z_{xy} \\ Z_{yx} & Z_{yy} \end{bmatrix} \begin{bmatrix} \dot{u}_1 \\ \dot{u}_2 \end{bmatrix} \quad (4.18)$$

Applying governing differential equation along the two principal axes and imposing boundary conditions, Zhou et al. (1995) derived the following expression.

$$\bar{Y} = G + B \cdot j = \omega \cdot j \cdot \frac{w \cdot l}{h} \cdot \left[\bar{\epsilon}_{33}^T - \frac{2d_{31}^d \bar{Y}^E}{(1+\nu)} + \frac{d_{31}^d \bar{Y}^E}{(1+\nu)} \left\{ \frac{\sin kl}{l} \frac{\sin kw}{w} \right\} N^{-1} \begin{Bmatrix} 1 \\ 1 \end{Bmatrix} \right] \quad (4.19)$$

where k is the 2D wave number given by

$$k = \omega \cdot \sqrt{\frac{\rho(1-\nu^2)}{\gamma^E}}$$

and N is a 2x2 matrix given by

$$N = \begin{bmatrix} k \cos(kl) \left\{ 1 - \nu \frac{w}{l} \frac{Z_{xy}}{Z_{axx}} + \frac{Z_{xx}}{Z_{axx}} \right\} & k \cos(kw) \left\{ \frac{l}{w} \frac{Z_{yx}}{Z_{ayy}} + \nu \frac{Z_{yy}}{Z_{ayy}} \right\} \\ k \cos(kl) \left\{ \frac{w}{l} \frac{Z_{xy}}{Z_{axx}} + \nu \frac{Z_{xx}}{Z_{axx}} \right\} & k \cos(kw) \left\{ 1 - \nu \frac{l}{w} \frac{Z_{yx}}{Z_{ayy}} + \frac{Z_{yy}}{Z_{ayy}} \right\} \end{bmatrix} \quad (4.20)$$

As pointed out before, at a given frequency, G and B can be measured experimentally via an impedance analyzer. To obtain complete information about the host structure, four complex unknowns- Z_{xx} , Z_{yy} , Z_{xy} , Z_{yx} (or 8 real unknowns) are needed. This is not possible using Eq. (4.20).

Thus, the system of equations is highly indeterminate (8 unknowns with 2 equations only). As such, Zhou et al.'s model cannot be employed for experimental determination of the drive point mechanical impedance. To alleviate the shortcomings inherent in the existing models, a new PZT-structure interaction model, based on the concept of 'effective impedance' was proposed by Bhalla and Soh (2004b). The description of this model is not in the area of interest of this master thesis, however a simple reference is made because using this model we are able to extract structural information from raw experimental measurements of electrical impedance or admittance.

4.5 Comparison with other NDE methods for concrete

From the point of view of NDE, concrete technologists are interested in concrete strength determination and concrete damage detection. Special interest is shown in strength determination because its elastic behavior and service behavior can be predicted from its strength characteristics. The most commonly used non destructive strength estimation methods are surface hardness method, penetration technique, the pull-out test, the rebound hammer method, the resonant frequency method and the ultrasonic pulse velocity test. These tests measure certain properties of concrete from which an estimate of strength and elastic parameters can be derived.

The surface hardness method is based on the principle that the strength of concrete is proportional to its surface hardness. However, these strength prediction methods share many limitations. For example, the calibration charts of the surface hardness method, the rebound method and the penetration technique are valid for the particular type of the cement and aggregates used and the age and moisture content of the specimen. In addition, the results are not very reproducible. The penetration and the pullout techniques cause a small amount of damage to the concrete surface, which must be repaired. The resonant frequency method and the ultrasonic pulse velocity technique demand that the transducers must be placed on the opposite faces of the component for accurate results. Very often, this is not possible and thus limits the application of the two techniques.

The other aspect of NDE, namely damage detection, is conventionally carried out, as mentioned earlier, by *global* and *local* techniques. The global techniques rely on global structural response for damage identification. For example, in global dynamic techniques the structure is subjected to low-frequency excitations, and from the resulting structural response,

the first few mode shapes and their corresponding natural frequencies are extracted to deduce the location and the severity of structural damage. The main drawback of these techniques is that they rely on a relatively small number of the first few modes, which, being global in nature, are not very sensitive to localized incipient damage. It could be possible that a damage large enough to be detected by these techniques may already exist critically in many parts of the structure.

The *local* damage detection techniques, such as ultrasonic wave propagation, impact echo and acoustic emission techniques, on the other hand, employ localized structural interrogation for damage detection. In *ultrasonic* techniques, typically, high-frequency elastic waves are propagated into the monitored structural component. The waves reflect back when encountering any crack. The crack location is estimated from the time difference between the applied and the reflected waves. The ultrasonic techniques exhibit much higher damage sensitivity than the global techniques. However, they typically employ large and expensive transducers and render the structure unavailable for service throughout the duration of the test. The measurement data are collected in the time domain and require complex processing. Since ultrasonic waves cannot be induced at right angles to the surface, they cannot detect transverse surface cracks (Giurgiutiu and Rogers 1997) [10]. In addition, they do not lend themselves to automated use since experienced technicians are required to interpret the data.

In the *acoustic emission* technique, elastic waves generated by plastic deformations (such as at the tip of a newly developed crack), moving dislocations and disbonds are utilized for the analysis and detection of structural defects. This technique requires stress or chemical activity to generate elastic waves. However, the main problem for damage identification is the existence of multiple travel paths from the source to the sensors. Also, contamination by electrical interference and ambient mechanical noise degrades the quality of the emission signals.

In *impact echo* testing, a stress pulse is introduced into the interrogated structural component using an impact source. As the pulse propagates through the component, it is reflected by cracks and disbonds. The reflected waves are measured and analyzed to deduce the location of the cracks or disbonds. Though the technique is very good for detecting large-size voids and delaminations, it is insensitive to small-sized cracks (Park *et al* 2000) [10].

A common drawback of the *local* techniques is that probes, fixtures and other accessories are required to be physically carried around the test-structure for recording the data. Often, this not only prevents autonomous application of the techniques, but may also demand the removal of existing finishes or covers such as false ceilings. As it is impractical to freely move the probe everywhere, these techniques are often applied at few selected probable damage locations (often based on preliminary visual inspection or past experience), which is almost tantamount to knowing the damage location *a priori*.

The electro-mechanical impedance (EMI) technique, on the other hand, offers an interface between the *global* and the *local* techniques, thereby enabling a more cost-effective and hassle free alternative for both strength estimation and damage detection of concrete structures.

Part II Experimental Procedure

5 Organization

A number of experiments were conducted as proof of concept. This second part of this master thesis is a description of all the experiments that were conducted, the results that came up, as well as a description of all the materials and instruments used in this process.

In the second chapter of this part, an analytical presentation of all the materials is done as well as of all the instruments used to take the experimental measurements. A description of the experimental data analysis is done, introducing the meaning of damage indices as well as an analytical description of the RMSD damage metric which is used in this thesis.

The third chapter is a description of the creation of the 50x50x50 mm cubic sandwiched smart aggregates. Before embedding the S.A. in larger concrete structures, a series of measurements were conducted to ensure their functionality. The results of these measurements are also presented.

In the fourth chapter, the results of early age monitoring of two cubic 150x150x150 mm and two beam 150x150x750 mm specimens is presented, along with conclusions concerning the efficiency of the EMI technique in strength gain monitoring of concrete structures.

The fifth chapter is a presentation of the results after inducing damage to the concrete specimens described above. Damage induction was achieved using two ways: a) the drilling of holes in the concrete mass using a rotary drill and b) cyclic loading (compression and bending test for cubic and beam specimens respectively). This way different degree of damage was achieved, observing the relation of the damage metric with the actual damage.

Finally the sixth and last chapter of this master thesis presents the conclusions that derived from the conducted experiments as well as points of discussion and further research.

6 Materials and methods

6.1 Concrete

For the creation of the cement paste “smart” aggregates as well as the concrete cubes and beams, cement TITAN CEM IV/B 32.5 N was used.



Picture 6.1 TITAN CEM IV/B 32.5 N

The water cement ratio for the cement paste aggregates was 0,4. The analogy of aggregates for the creation of concrete specimens was:

Concrete → 20.05 kg

Water → 12.52 kg

Sand → 27.34 kg (24.9 % of aggregates)

Gravel → 27.04 kg (24.7 % of aggregates)

Coarse → 55.28 kg (50.4 % of aggregates)

6.2 PZT PIC 151

As mentioned earlier, electromechanical impedance (EMI) based SHM technique, utilizes small lead zirconate titanate piezo-electric ceramic patches (PZT) attached to a host structure employing sonic and ultrasonic vibrations to the host structure by applying alternate current. The AC current excitation is introduced using an impedance analyzer/LCR meter, sweeping through a particular frequency range (in this master thesis 10-500 kHz).

PZT materials are available in a wide variety of compositions that are optimized for different applications. PZT is a mixture of lead zirconate (PbZrO_3) and lead titanate (PbTiO_3) and

has the perovskite structure. Various additives and Ti/Zr ratios may be used to yield material that has one or more desired properties such as high piezoelectric activity, low loss or temperature and time stability. Trade-offs are generally required to obtain the best values of the most important properties at the expense of some degradation of others. PZT ceramics are often classified as “hard” or “soft”, according to the characteristics shown in Table 6.1.

Harder	⇔ PZT ⇔	Softer
↓	piezoelectric d constants	↑
↓	dielectric constant	↑
↓	dielectric loss	↑
↓	hysteresis	↑
↑	mechanical Q	↓
↓	coupling factor	↑
↓	resistivity	↑
↑	coercive field	↓
↓	elastic compliance	↑
↑	aging effects	↓

Table 6.1 Comparison of hard and soft PZT ceramic properties

Generally the antonyms “soft” and “hard” PZT ceramics refer to the ferroelectric properties of the patch, i.e. the mobility of the dipoles or domains and the polarization/depolarization behavior. “Soft” piezoceramics are characterized by comparatively high domain mobility and a resulting ferroelectrically soft behavior, which means easy polarization. On the contrary, ferroelectrically “hard” PZT materials can be subjected to high electrical and mechanical stresses. This stability of their properties destines them for high-power applications.

In the present master thesis, the PZT patches used were PIC 151. These patches are characterized as “soft” PZTs. Generally PIC 151 is a modified lead zirconate titanate material with high permittivity, high coupling factor and high piezoelectric charge constant. This material is the standard material for actuators and suitable for low-power ultrasonic transducers and low-frequency sound transducers. The physical and dielectric properties are shown in the table below:

		Unit	PIC151
Physical and dielectric properties			
Density	ρ	g/cm ³	7.80
Curie temperature	T_c	°C	250
Relative permittivity	in the polarization	$\epsilon_{33}^T / \epsilon_0$	2400
	direction \perp to polarity	$\epsilon_{11}^T / \epsilon_0$	1980
Dielectric loss factor	$\tan \delta$	10 ⁻³	20
Electro-mechanical properties			
Coupling factor	k_p		0.62
	k_t		0.53
	k_{31}		0.38
	k_{33}		0.69
	k_{15}		
Piezoelectric voltage coefficient	d_{31}		-210
	d_{33}	10 ⁻¹² C/N	500
	d_{15}		
Piezoelectric voltage coefficient	g_{31}	10 ⁻³ Vm/N	-11.5
	g_{33}		22
Acousto-mechanical properties			
Frequency coefficients of the series resonance frequency	N_p		1950
	N_1	Hz · m	1500
	N_3		1750
	N_t		1950
Elastic compliance coefficient	S_{11}^F		10 ⁻¹² m ² /N
	S_{33}^F		19.0
Elastic stiffness coefficient	C_{33}^P	10 ¹⁰ N/m ²	10.0
Mechanical quality factor	Q_m		100
Temperature stability			
Temperature coefficient of ϵ_{33}^T (in the range -20 °C to +125 °C)	$TK \epsilon_{33}$	10 ⁻³ /K	6
Time stability (relative change of the parameter per decade of time in %)			
Relative permittivity	C_ϵ	%	
Coupling factor	C_K		

Table 6.2 Material data

The patches are of size 10 mm by 10 mm and 0.2 mm thickness, manufactured by PI-Ceramic. A unique feature of these patches is that both the electrodes are available on one side of the patch itself, when the other side is bonded to the structure. This detail is shown in figure 6.1 and picture 6.2.

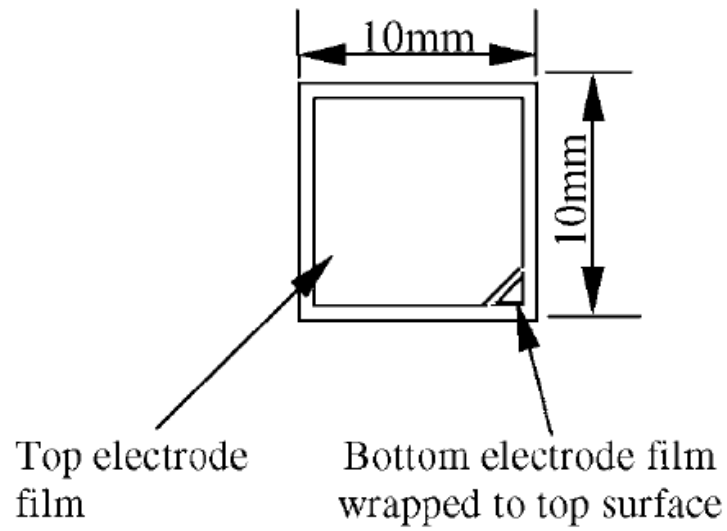
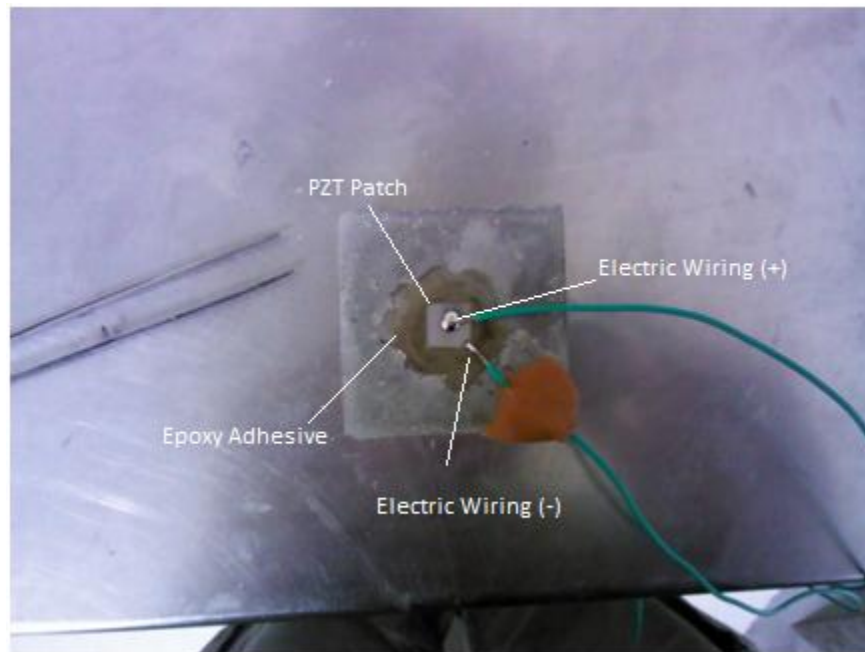


Figure 6.1 Details of the PIC 151 PZT patch



Picture 6.2 PZT patch agglutinated on cement paste specimen ("Smart" aggregate)

6.3 Epoxy adhesive

For the agglutination of the PZT patch on the cement paste, Bison Epoxy Universal was used. It is a two component epoxy adhesive, used with mixing ratio 1:1. The mixture must be stirred until having a uniform color. At room temperature the mixture remains workable for approximately 1.5 hours. The curing time is approximately 24 hours, depending on the temperature conditions of the room (less for higher temperatures). It has good moisture resistance and a temperature resistance of -20°C to $+60^{\circ}\text{C}$. It also has good chemical resistance and filling capacity.



Picture 6.3 Two component epoxy adhesive

6.4 Silicon Rubber

PZT patches are quite sensitive in environmental conditions. It has been demonstrated in previous studies that humidity and temperature changes affect the conductance or resistance signatures. It has been observed (Bhalla & Soh et al. 2008) that humidity causes a vertical shift in the conductance signature. Probably the presence of humidity increases the electrical permittivity of the patch. Therefore it is obvious that a protection layer is necessary to protect the patch from humidity, as well as impact or surface damage.

Silicon rubber was chosen as a candidate protective material since it is known to be a good water proofing material, chemically inert, and at the same time a very good electric insulator. It is commercially available as paste which can be solidified by curing at room temperature. The silicone rubber chosen for coating was Dow Corning 3140 RTV Coating. It has also been found that the presence of the silicon layer has only a negligible effect on the sensitivity of the PZT patch, as it absorbs a small amount of energy, adding damping to the structure as it is “softer” (the effect is shown clearly in the R_s -frequency plots in the next chapter). The proposed

protection, using silicon rubber, offers a simple and economical solution to the problem of humidity. The properties of the silicon rubber used are shown in the following table:



Picture 6.4 Dow Corning 3140 RTV Coating

TYPICAL PROPERTIES

Specifications writers: These values are not intended for use in preparing specifications. Please contact your local Dow Corning sales representative prior to writing specifications on this product.

CTM*	ASTM*	Property	Unit	Value
		As supplied		
		Consistency		Flowable
0176		Color		Clear
0050	D1084	Viscosity at 23°C ¹	mPa.s	28,000
		Coating thickness per dip	mm	0.4
0098		Skin-over time	minutes	25
0095		Tack-free time	hours	1.5
		Cure time - 0.5mm thickness	hours	24
		Cure time - 3.2mm thickness	hours	72
		Full cure - 3.2mm thickness	days	7
0010		Non-volatile content	%	98
		Physical properties, after curing 7 days at 23°C and 50% relative humidity		
		Colour		Clear
0022	D792	Specific gravity		1.05
0099	D2240	Durometer hardness	Shore A	32
0137A	D412	Tensile strength	MPa	3.1
0137A	D412	Elongation at break	%	420
0159A	D624	Tear strength - die B	kN/m	3.6
0293	D403	Peel strength, primed aluminium panel	kN/m	4.2
		Volume coefficient of thermal expansion	1/K	8.8x10 ⁻⁴
		Coefficient of thermal conductivity	W/(m.K)	0.14

TYPICAL PROPERTIES (continued)

CTM*	ASTM*	Property	Unit	Value
Electrical properties, cured 7 days at 23°C and 50% relative humidity				
0114	D149	Dielectric strength	kV/mm	18
0112	D150	Permittivity at 100Hz		2.52
0112	D150	Dissipation factor at 100Hz		0.000098
0249	D257	Volume resistivity	Ohm.cm	2.1x10 ¹⁵
		Comparative tracking index (IEC112)		600

1. Brookfield HAF, spindle #5 at 10rpm.

* CTM: Corporate Test Method, copies of CTMs are available on request.

ASTM: American Society for Testing and Materials.

Table 6.3 Typical properties of Dow Corning 3140 RTV Coating

6.5 Measurement System

For the measurements, a Quadtech 7600 Precision LCR meter was used with the following characteristics (as mentioned in the device's manual):

- Wide frequency range
- Programmable test voltage and current
- Graphical and tabular display
- Automatic test sequencing
- Swept frequency and signal level measurements
- Internal, external or manual trigger
- Built-in calibration routine
- Internal storage of test setups and floppy drive
- 14 measurement parameters
- Basic accuracy: 0.05% LCR, 0.0005 DQ
- Programmable test frequency: 10 Hz to 2 MHz
- Programmable test voltage: 20 mV to 1 V
- Programmable test current: 20 uA to 100 mA
- Up to 25 measurements/second
- Internal storage /recall of 25 setups
- 15 Pass/Fail bins
- Measurement averaging (1-1000)
- Measurement delay (0-1000 ms)
- Charged capacitor protection
- Displays usage and calibration data

The frequency sweeps were made in a range of 10-500 kHz. The sweeps were divided in three parts as the analyzer has a maximum of 200 steps per sweep. So the range was subdivided in

three ranges: 10-100 kHz, 100-300 kHz and 300-500 kHz making a total of 600 measurements per plot.



Picture 6.5 Quadtech 7600 Precision LCR meter

6.6 Experimental data analysis

The response plots provide a qualitative approach for damage detection. However, the visual analysis of the impedance measurement graph is not suitable for on-line implementation of the impedance-based health monitoring technique. To quantify the interpretation of the impedance variations, a scalar damage metric, referred to as correlation coefficients between two impedance measurements, is used to analyze the information from each PZT. The damage metric chart is constructed after each measurement has been taken in order to give some indication of the conditions of a structure through comparison with the reference measurement.

In structural health monitoring, the process of feature extraction is required for the selection of the key information from the measured data that distinguishes between a damaged and an undamaged structure. The extractions also accomplish the condensation of large amount of available data into a much smaller dataset that provides concise damage indication. In

impedance methods, the damage sensitive features traditionally employed are based on a scalar damage metric.

Many statistics metrics have been used as damage indices in structural health monitoring to account for the overall change in the EMI spectra such as root means square deviation (RMSD), mean absolute percentage deviation (MAPD) and correlation coefficient deviation (CCD). The most common damage metric used based on frequency-by-frequency comparisons, and the one used in our experiments, is the root mean square deviation (RMSD).

$$RMSD = \sqrt{\frac{\sum_{j=1}^N (G_j^1 - G_j^0)^2}{\sum_{j=1}^N (G_j^0)^2}}, \text{ where}$$

G_j^1 → post-damage conductance/resistance at the j^{th} frequency

G_j^0 → pre-damage conductance/resistance at the j^{th} frequency

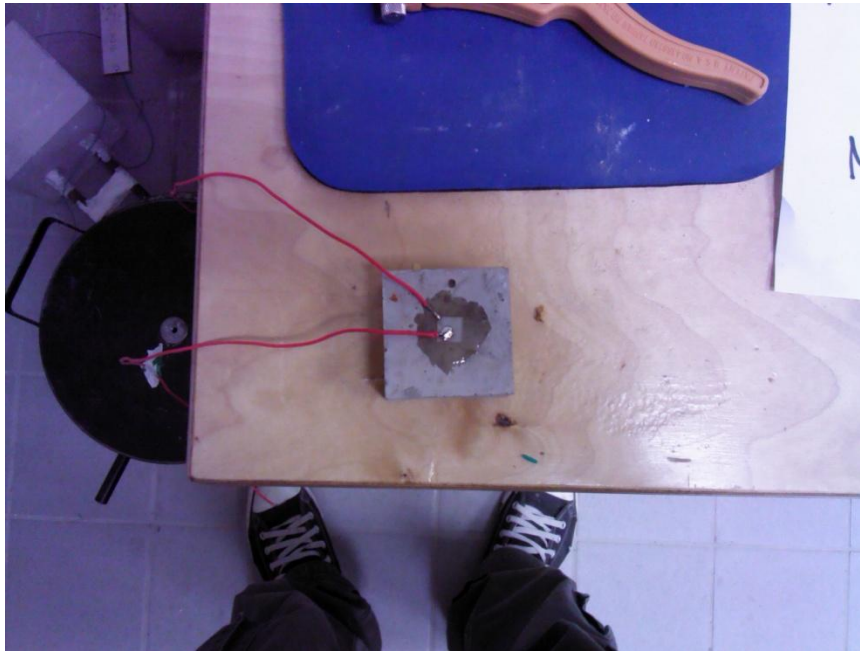
In the RMSD damage index chart, the larger the difference between the baseline reading and the subsequent reading, the greater the numerical RMSD value is. The RMSD damage index values denote the changes of structural dynamic properties. These changes may be caused by the variations in the geometrical conditions, the environmental temperature and the presence of structural damage. For a damage detection technique, larger RMSD values detected by a PZT sensor indicate the higher sensitivity to structural damage of this PZT sensor.

Using RMSD or any other damage indicator has a number of limitations. One of the main limitations of using a traditional damage index is how to establish appropriate decision limits or thresholds values to indicate the presence of structural damage. Damage metric charts are useful only when a qualitative comparison between datasets needs to be made. Since the impedance-based method relies on experimental data with inherent uncertainties, statistical analysis procedures are inevitable if one is to state in a quantifiable manner that changes in the impedance of a structural system are indicative of damage as opposed to operational and environmental variability.

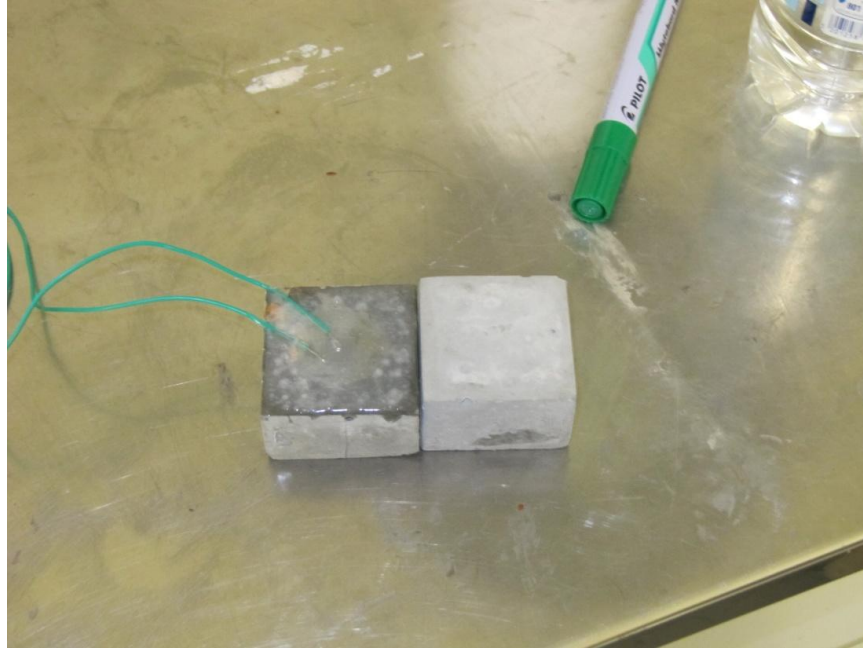
7 “Smart” aggregates

As mentioned earlier, purpose of the present master thesis is the development of an innovative damage detection monitoring system using piezoelectric ceramic plates (PZT PIC151). This is achieved with the creation of a smart aggregate, which is a cubic hardened cement paste specimen 50x50x50 mm with a PZT patch “sandwiched” in its center, which is later embedded in a concrete structure. The smart aggregate consists of a 50x50x25 mm concrete member on which a PZT patch is agglutinated on it using an epoxy. A thin layer of silicone rubber is used to protect the patch from humidity and temperature changes and the second concrete member is placed on top of the silicon layer to protect the film of silicon from tearing from the stresses of concrete during the curing process. This way the patch is completely protected from the aggressive conditions within the concrete.

Basically, this structure resembles a 50x50x50 mm cement cubic specimen with a crack in the middle. During the compression of the specimen, the two members of concrete come closer, due to the flexibility of the silicon, approaching the behavior of an intact 50x50x50 mm specimen.



Picture 7.1 PZT patch agglutinated on the 50x50x25 mm cement specimen before silicone coating



Picture 7.2 After silicone coating



Picture 7.3 Final form of "smart" aggregates

A total of 11 smart aggregates were created with only six of them later being embedded in a concrete structure. Some of the specimens could not be used as they manifested problems with the most common being the detachment of electrode cables.

Before embedding the smart aggregates in the concrete structures, cube and beam, a number of measurements were made to ensure their efficiency. The specimens were manually compressed trying to keep their structural integrity intact. The application of load was not

quantified, but it was ascending (load 1<load 2<load 3 etc). The results are shown in the following chapters.



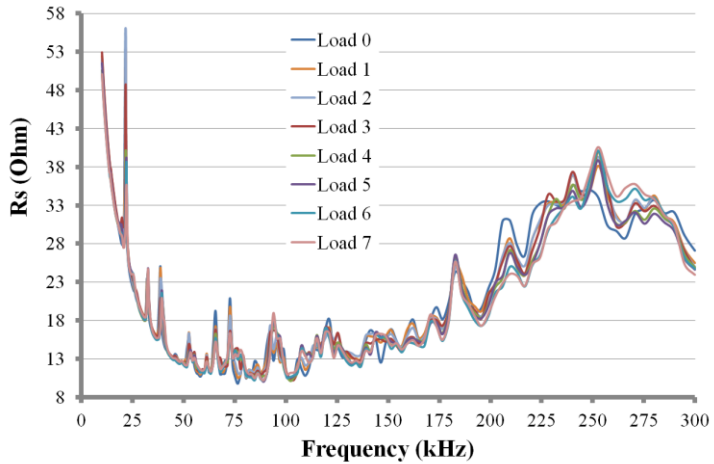
Picture 7.4 Manual compression of “smart” aggregates



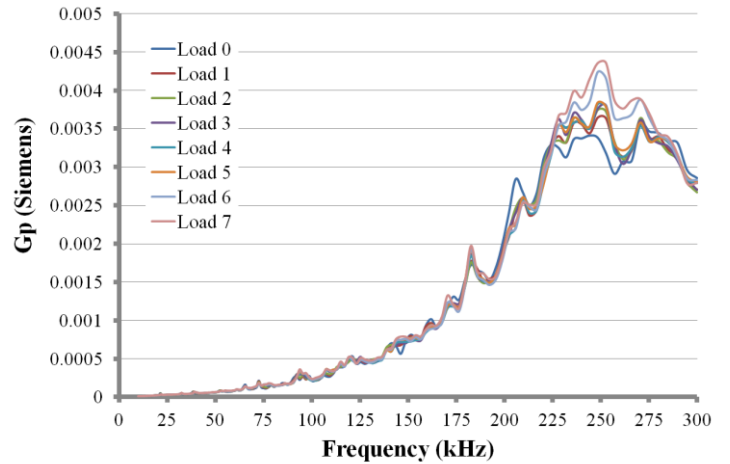
Picture 7.5 Manual compression of “smart” aggregates

7.1 Aggregate No 4

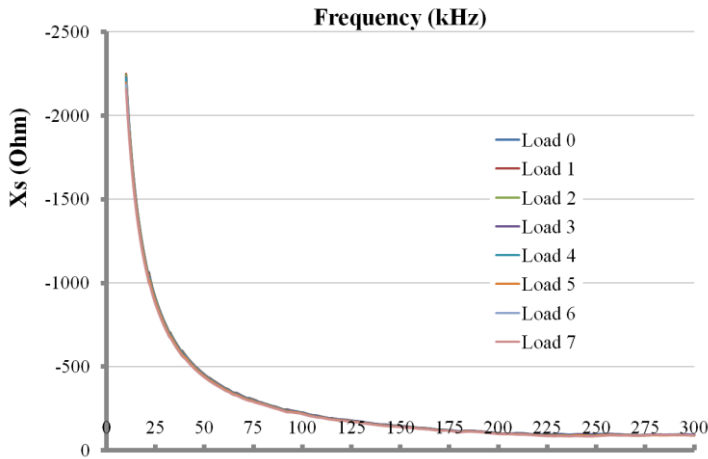
Aggregate No 4 was later embedded in the first beam specimen. The following charts are R_s (Resistance, real part of Z), X_s (Reactance, imaginary part of Z), $|Z|$ (Magnitude of Z) and G_p (Conductance, real part of Y) vs Frequency. The RMSD values later calculated are for baseline measurement of the unloaded state.



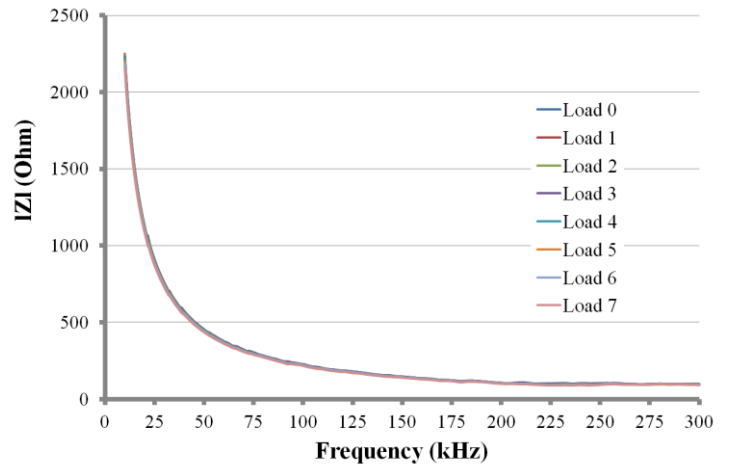
(g)



(h)



(i)



(j)

Plots 7.1: Aggregate 4 signature plots a) Resistance b) Conductance c) Reactance d) Magnitude IZI

Observing the resistance plot, we can see that due to the flexibility of the silicon rubber layer, when compressing the aggregate, we basically make it stiffer and as the compression rises the specimen tends to act like a whole 50x50x50 mm structure, rather than two combined. We can see the difference by observing the peaks, in particular the ones of the structure. There is a slight right hand vertical shift of the peaks, which means the structure is getting stiffer and a reduction in the peak value, which means the damping is smaller. The same thing is observed in the conductance plot but not as easily due to greater value fluctuation we must concentrate on

a smaller bandwidth. The difference in the conductance plot is that the value of the peak rises due to reduction of damping.

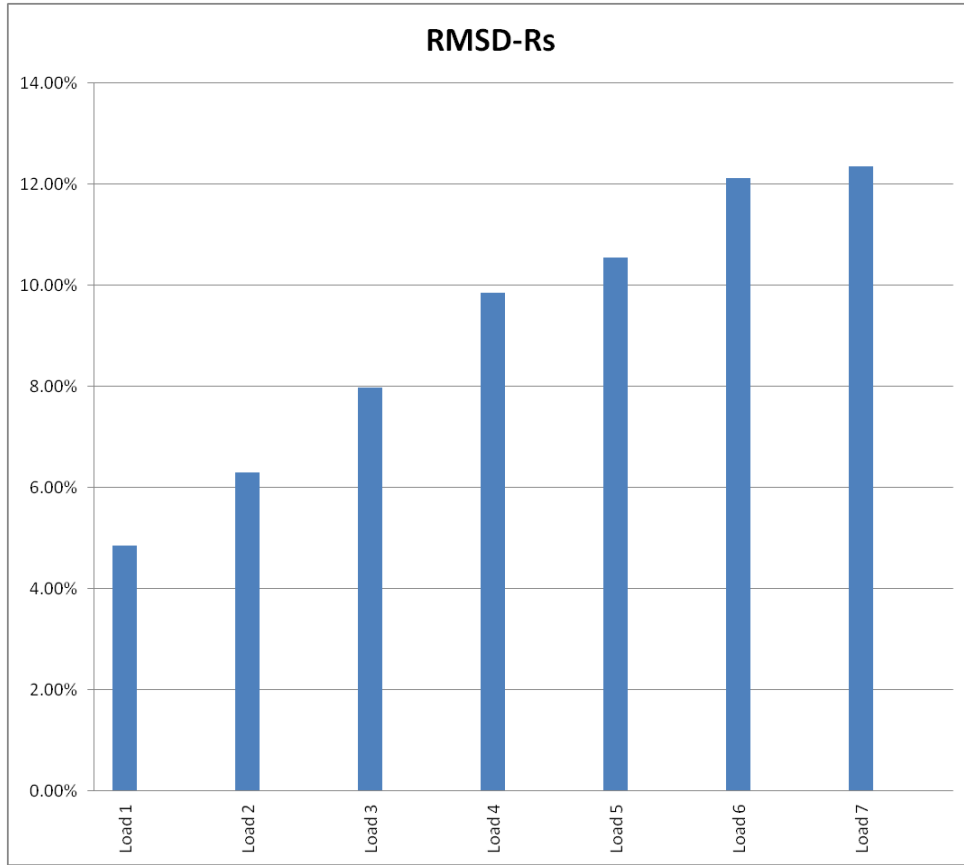
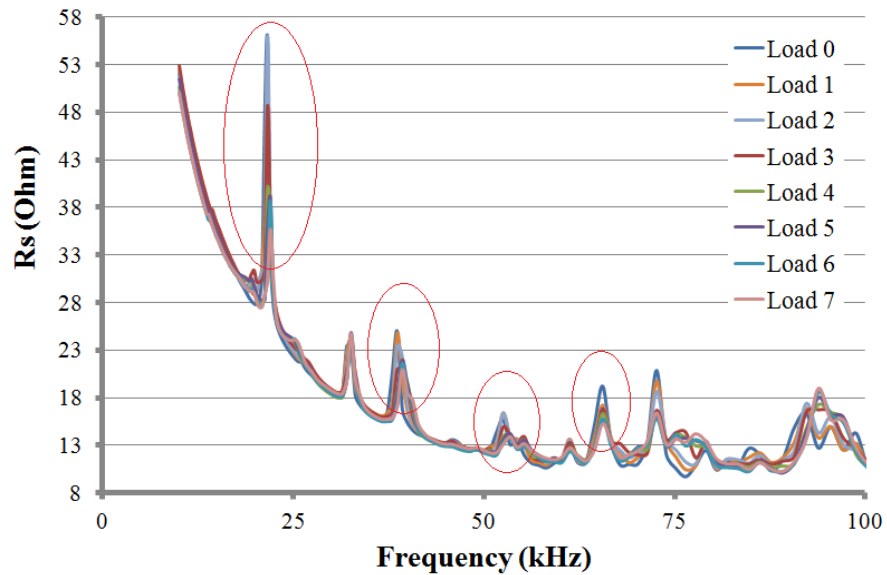


Chart 7.1 - RMSD chart for various compressive loads of S.A. 4



Resistance plot of aggregate 4 – Zoomed at bandwidth 0-100 kHz

We can also see what was earlier mentioned about the unsuitability of the raw measurements of imaginary part of impedance in SHM techniques. There is no visual difference between the plots which is a result of the capacitive behavior of the patch in this bandwidth.

As frequency increases in value, the wavelength of the induced stress wave is getting smaller, therefore making it more sensitive to the occurrence of damage. So for every bandwidth we observe different size of damage. Generally, changes in the plot are more easily observed near the resonance frequencies of either the PZT patch or the structure. However differences are observed even in the non-resonant frequencies.

As shown in the spectrum of the real component of impedance and admittance of the free PZT below (plot 7.2), the resonant frequencies of the free PZT are located at about 170, 240 and 450 kHz (specifically 178.5, 241.8 and 445.4 kHz). The selected frequency range of 10-500 kHz is selected because beyond 500 kHz the change in the spectrum is influenced by the conditions of the PZT rather than the host structure.

The initial EMI spectra of bonded PZT patches may differ depending on the surface condition and characteristics of the structure. An unbonded PZT is free to vibrate when excited by an alternating voltage source. Thus bonding the PZT to a host structure restricts the vibration, changing the resonant frequency and reducing its amplitude as the coupled PZT-structure is stiffer and part of the energy is absorbed due to the damping of the host structure. Since there is no change in the bonding condition, changes in the EMI spectra implies change in the characteristics of the structure. Therefore shifting of the resonance peak with time is on account of hardening of concrete during the curing process or loss of stiffness during compression. So monitoring of the resonance peak is the basis for monitoring strength gain or loss of concrete. In all the specimens monitored, irrespective of the size of the structure (given that the size of it is larger than the sensing range of the PZT, i.e. approximately a radius of 5 cm for concrete) the resonance peak was shifted in the area of 230-250 kHz.

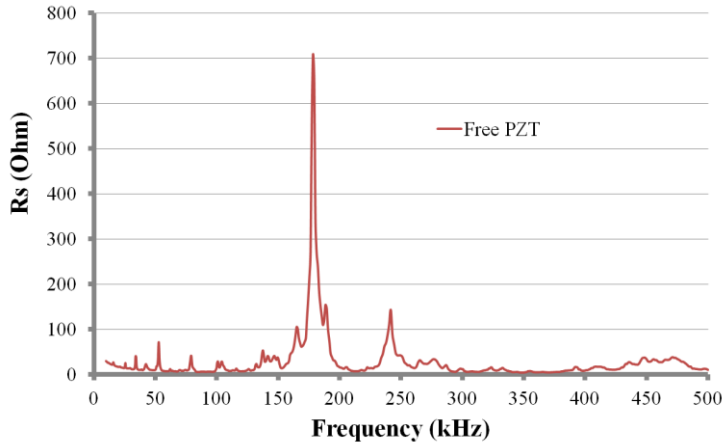
Another area of interest is of 50-150 kHz, as changes are also obvious in the minor peaks that occur in this area but not all of them exhibit the same behavior mentioned above. Changes in this area are also due to the host structure. For frequencies larger than 350-500 kHz the patch becomes more sensitive to its own conditions rather than the ones of the host structure and thus making these bandwidths inappropriate for SHM.

The initial EMI signature varies from patch to patch, because of the stiffness of the bonding layer. By using the equation (14) of Bhalla and Soh described in §4.4 derived the theoretical response spectra for both free and perfectly fixed conditions substituting Z_s equal to 0 and ∞ respectively. The equations become

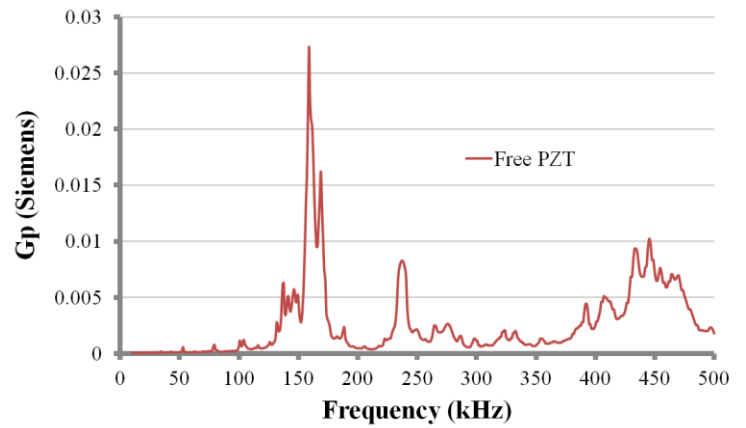
$$\bar{Y}_{free} = 2 \cdot \omega \cdot j \cdot \frac{w \cdot l}{h} \cdot \left[\frac{\bar{\epsilon}_{33}^T}{\epsilon_{33}^T} + \frac{2 \cdot d_{31}^2 \cdot \bar{Y}^E}{(1-\nu)} \cdot \left(\frac{\tan \kappa \cdot l}{\kappa \cdot l} - 1 \right) \right] \text{ and}$$

$$\bar{Y}_{fixed} = 2 \cdot \omega \cdot j \cdot \frac{w \cdot l}{h} \cdot \left[\frac{\bar{\epsilon}_{33}^T}{\epsilon_{33}^T} + \frac{2 \cdot d_{31}^2 \cdot \bar{Y}^E}{(1-\nu)} \right]$$

The actual conditions of the bonded PZT will be somewhere between the two extreme theoretical conditions.



(a)

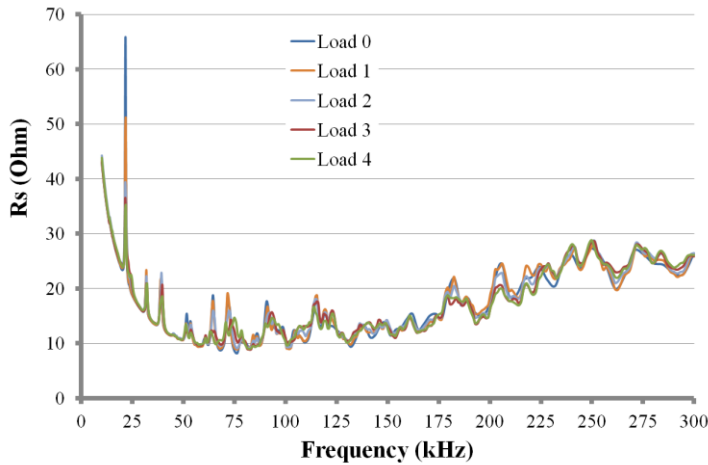


(b)

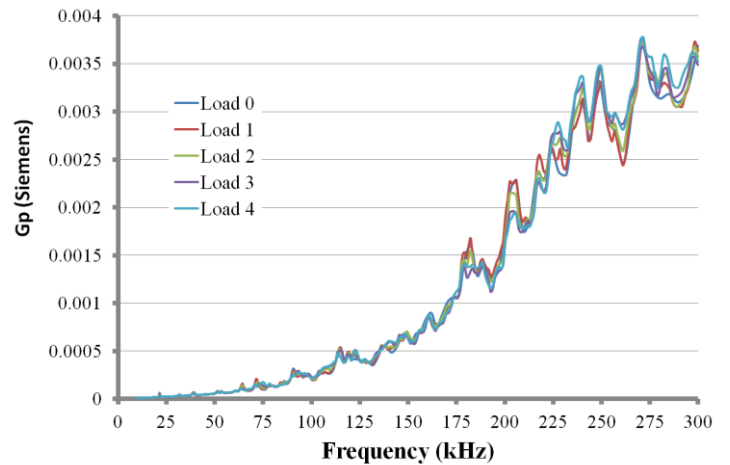
Plots 7.2 – Free PZT signature plots (a) Resistance (b) Conductance

7.2 Aggregate No 5

Aggregate No 5 was not later embedded in any structure. The results are similar to the previous specimen (No 4). RMSD was calculated taking Load 1 condition as baseline, as the unloaded state was measured with different number of sweep steps.



(a)



(b)

Plots 7.3 – Aggregate 5 signature plots (a) Resistance (b) Conductance

The Bp, Xs and IZI signature plots will not be displayed, as no conclusion can be made about the state of the structure from the raw measurements, without further processing.

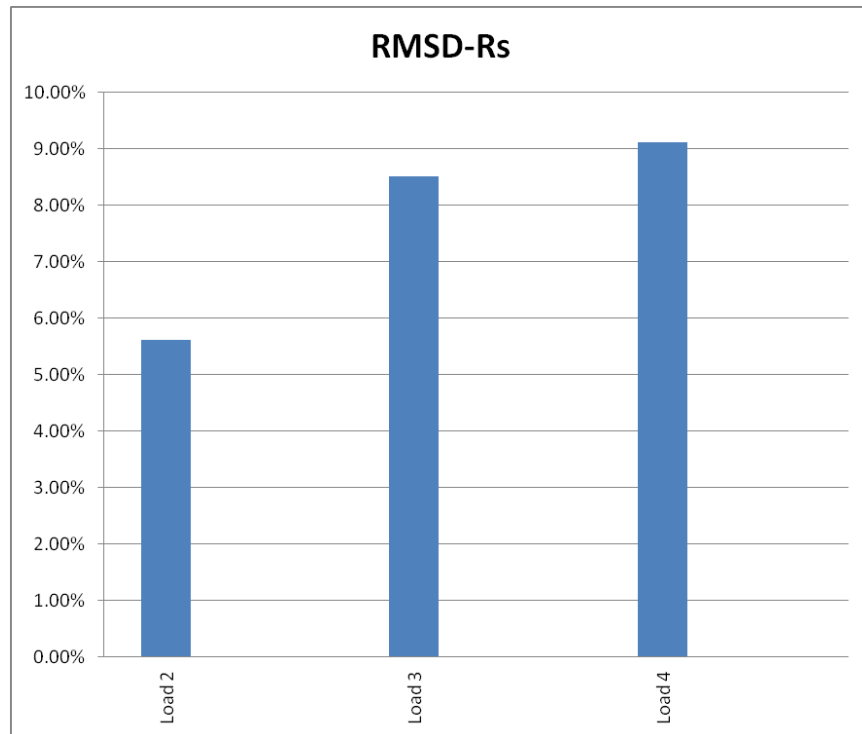
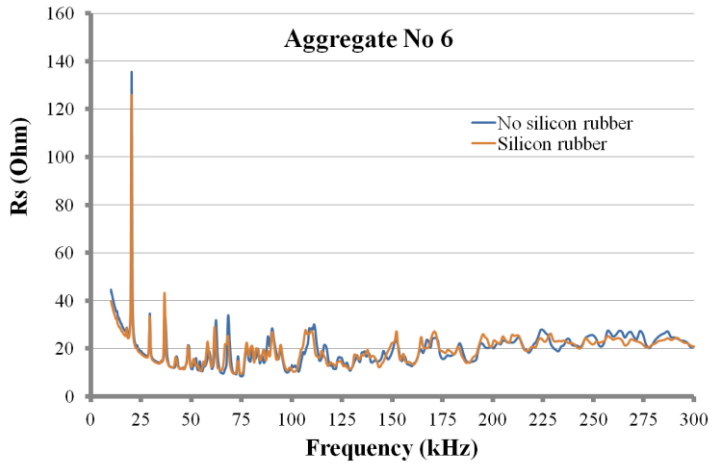


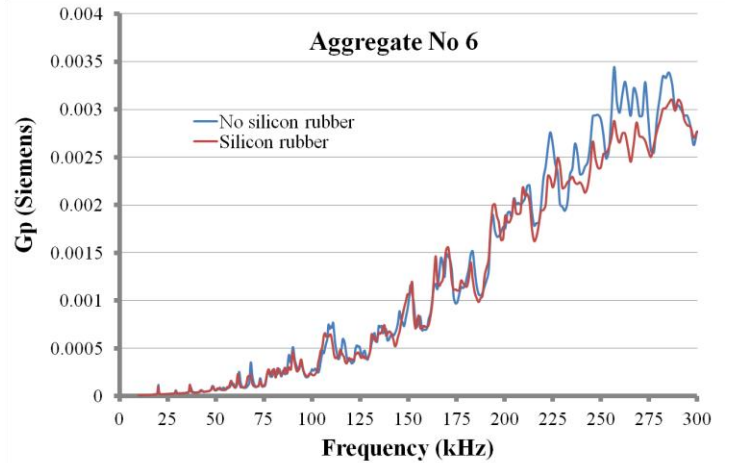
Chart 7.2 - RMSD chart for various compressive loads of S.A. 5

7.3 Aggregates No 6 and 7

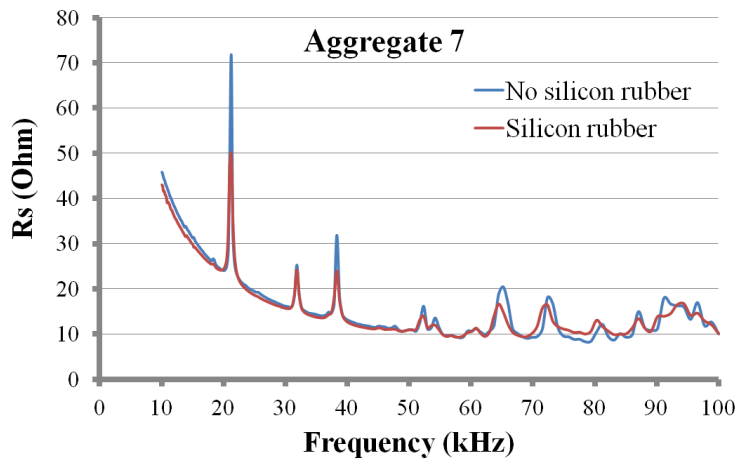
Aggregates 6 and 7 were not subjected to compression. Aggregate 6 was later embedded in the first concrete cube sized 150x150x150 mm. Aggregate 7 was embedded along with aggregate 4 in the first concrete beam specimen 150x150x750 mm. Although not compressed, they are included in this chapter to demonstrate the slight difference of signatures that is created by the silicone coating.



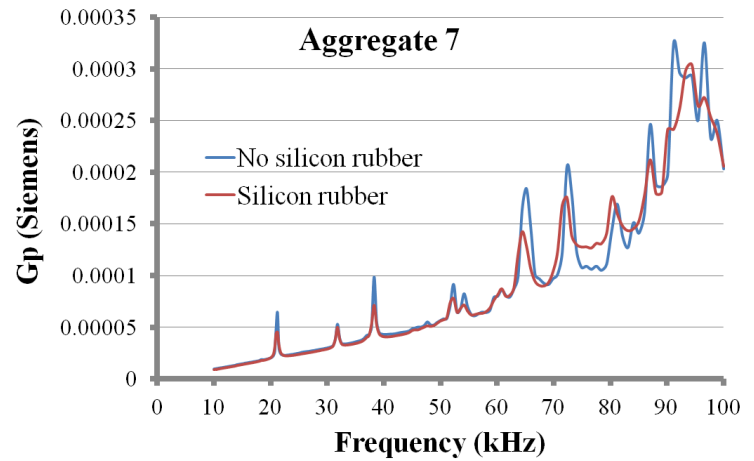
(k)



(l)



(m)

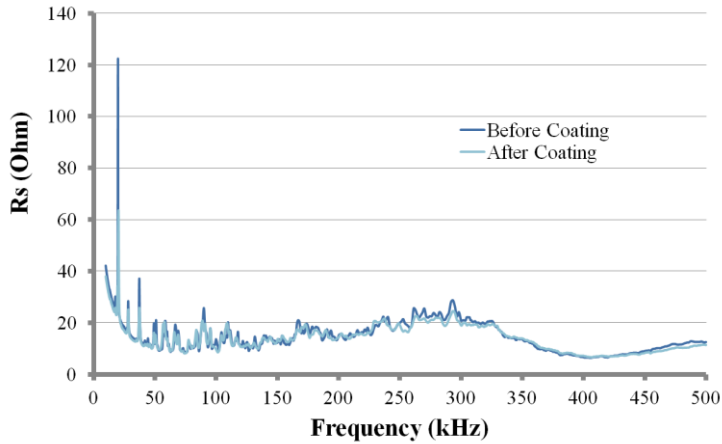


(n)

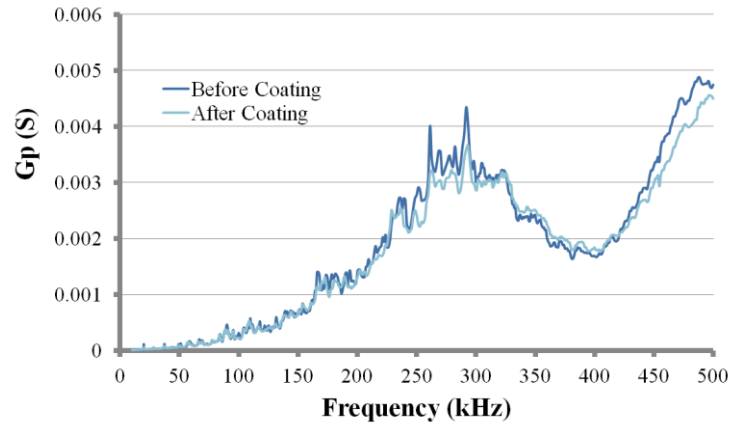
Plots 7.4 – (a) Resistance plot of S.A. 6 (b) Conductance plot of S.A. 6 (c) Resistance plot of S.A. 7 (d) Conductance plot of S.A. 7

7.4 Aggregate No 9

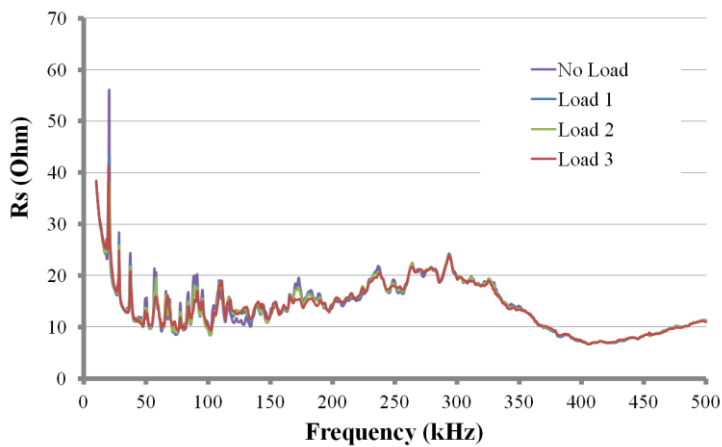
Aggregate 9 was embedded in the second cubic specimen. The results are similar to the ones that came up for the other previously measured aggregates and are demonstrated in the following plots:



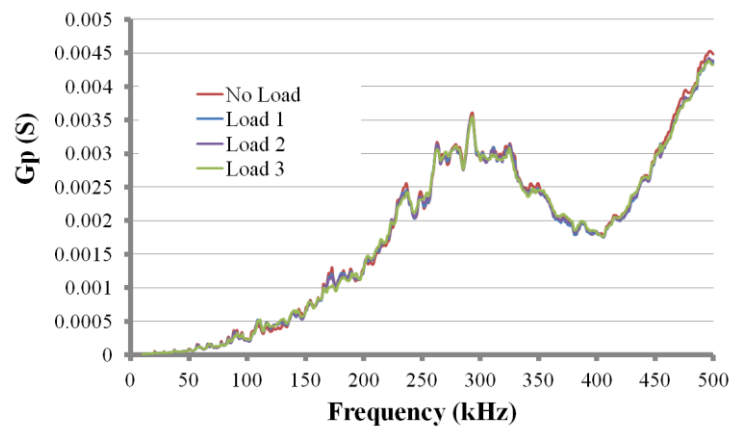
(a)



(b)



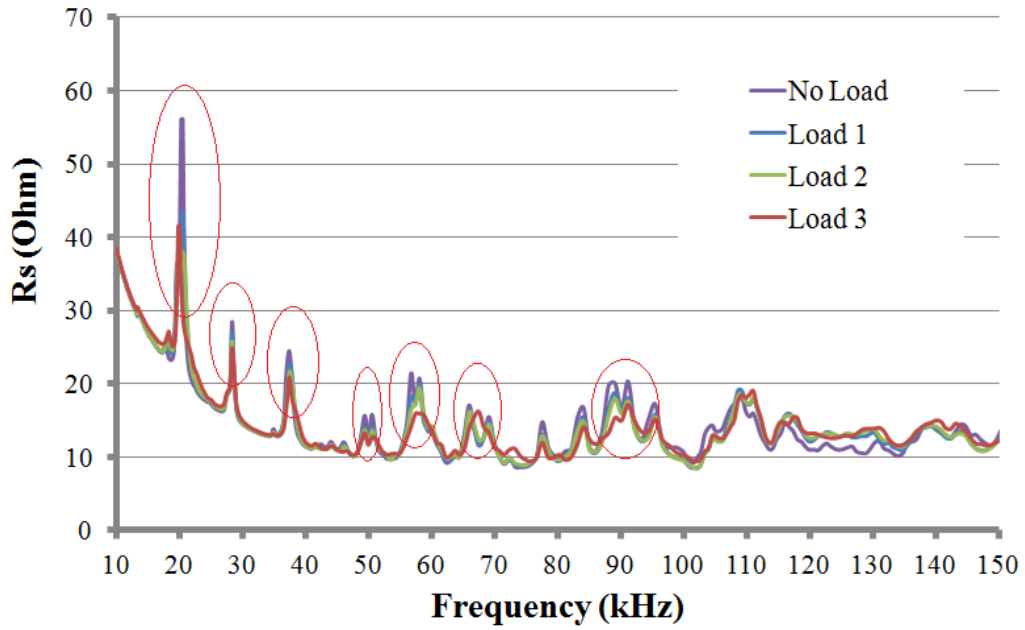
(c)



(d)

Plots 7.5 – (a) Resistance plot before and after silicon coating (b) Conductance plot before and after silicon coating (c) Resistance plot for various load values (d) Conductance plot for various load values

The difference in the signature plots for various loads is more obvious in the zoomed R_s plot that is presented below, concentrated in a bandwidth of 0-150 kHz. The RMSD chart is also presented.



Resistance plot of aggregate 9 – Zoomed at bandwidth 0-150 kHz

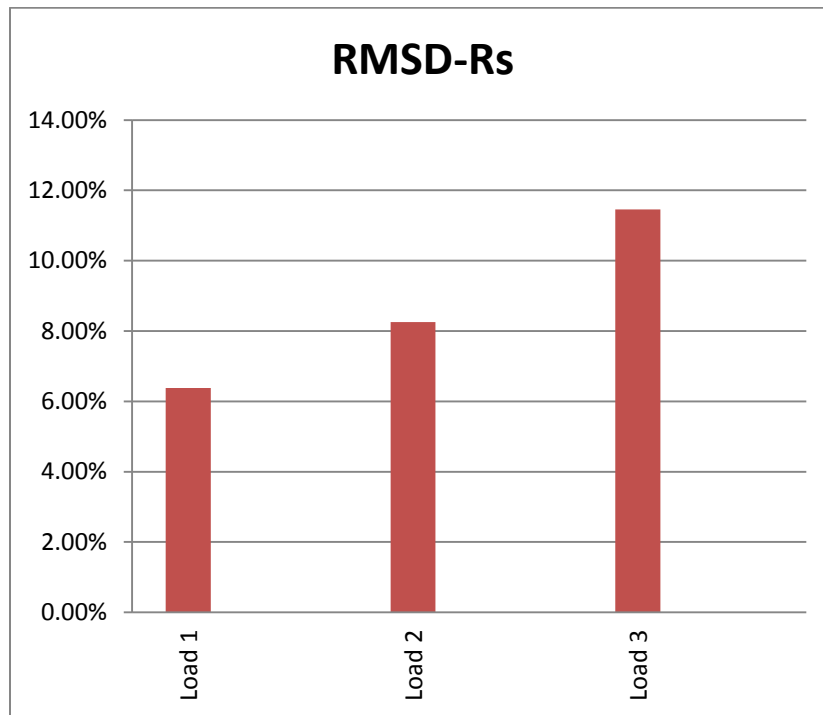


Chart 7.3 - RMSD chart for various compressive loads of S.A. 9

7.5 Aggregate No 10

Aggregate 10 was later embedded in the second beam specimen. The aggregate cracked during the compression but was kept in order for the great difference in RMSD to be shown, as well as the fact that when embedded it will continue to work having the same sensitivity. The results are the following:

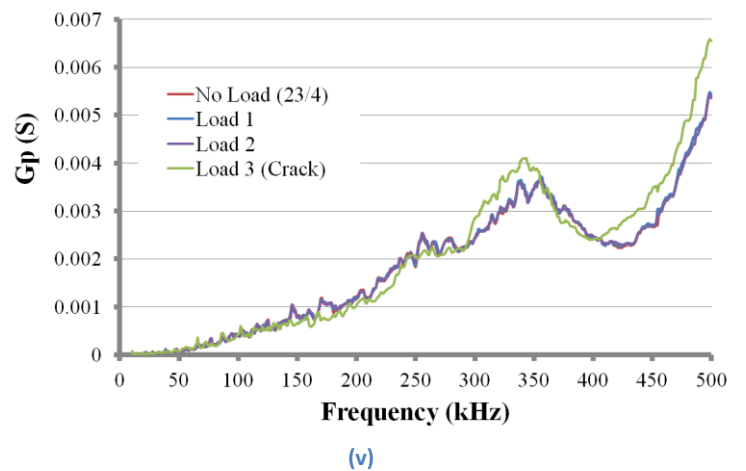
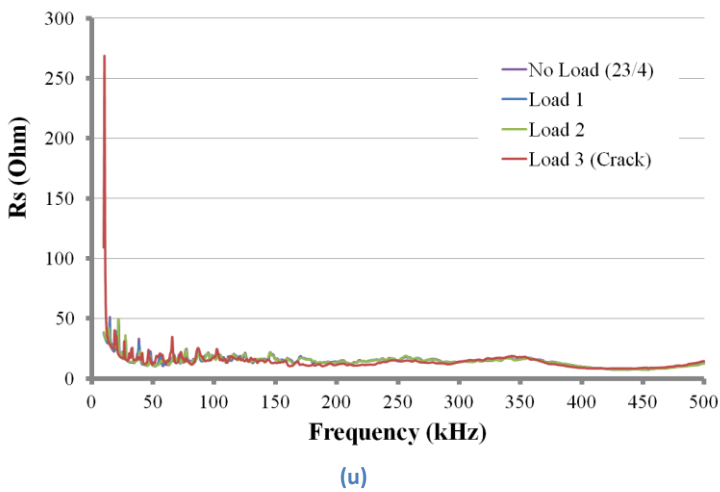
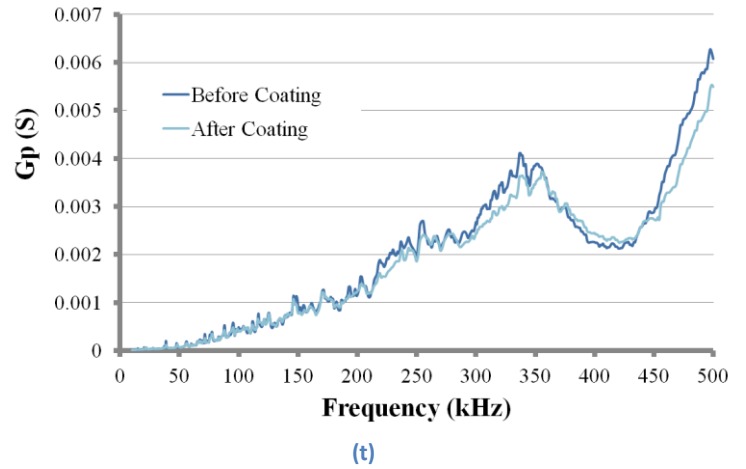
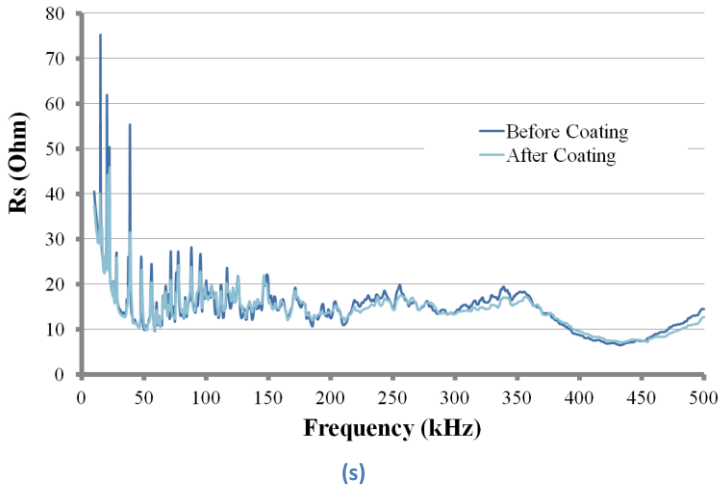


(a)



(b)

Picture 7.6 (a), (b) Aggregate 10 cracked during compression.



Plots 7.5 – (a) Resistance plot before and after silicon coating (b) Conductance plot before and after silicon coating (c) Resistance plot for various load values (d) Conductance plot for various load values

It can be easily observed that in this extent of damage, the resistance and conductance signatures changed completely and a dramatic increase in the damage metric (RMSD) was observed (see chart below).

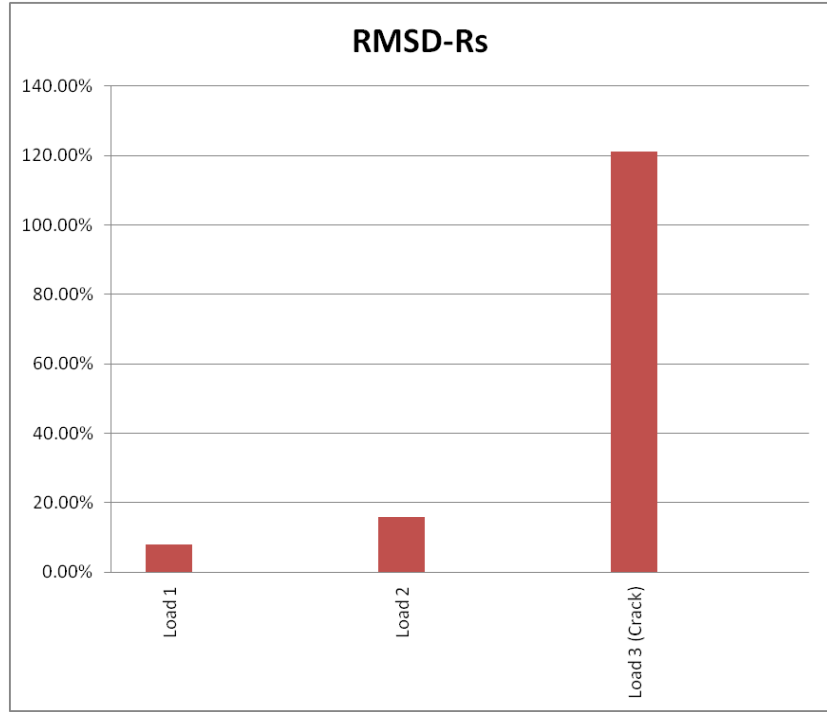
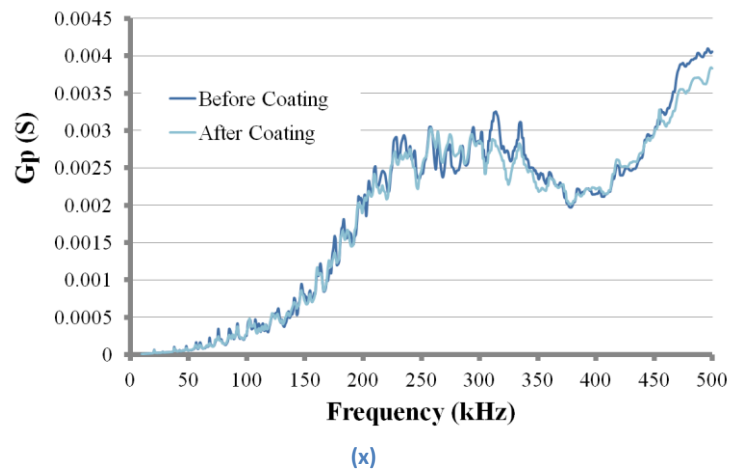
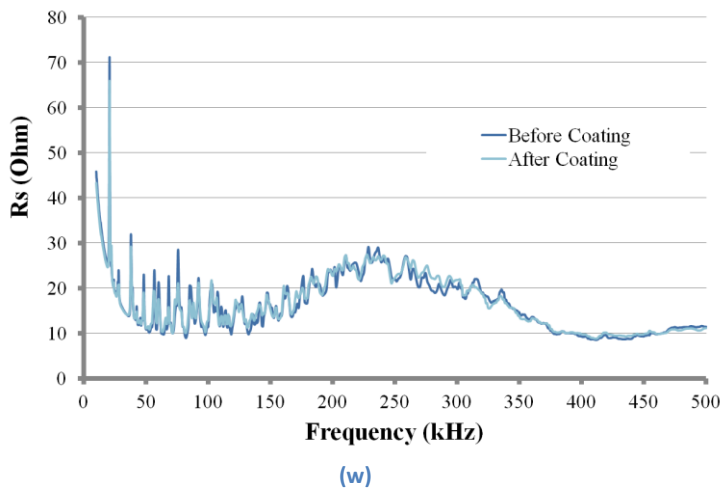
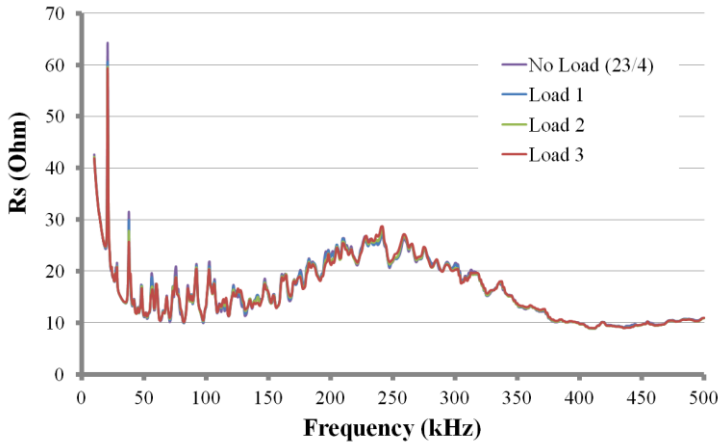


Chart 7.4 - RMSD chart for various compressive loads of S.A. 10

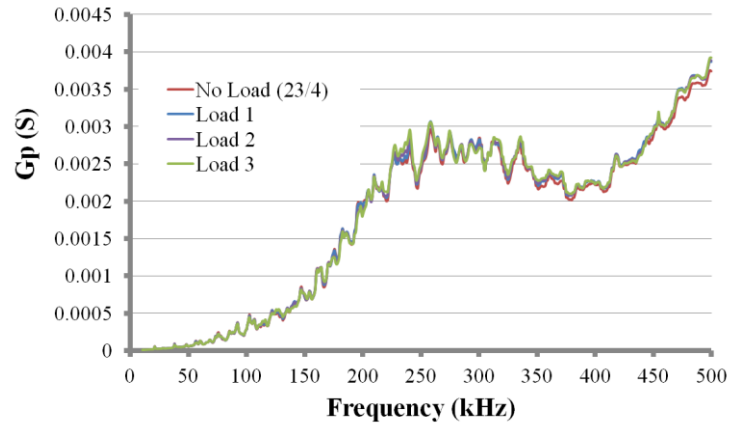
7.6 Aggregate No 11

Aggregate 11 was also embedded in the second beam specimen. The results are the following:





(c)



(d)

Plots 7.6 – (a) Resistance plot before and after silicon coating (b) Conductance plot before and after silicon coating (c) Resistance plot for various load values (d) Conductance plot for various load values

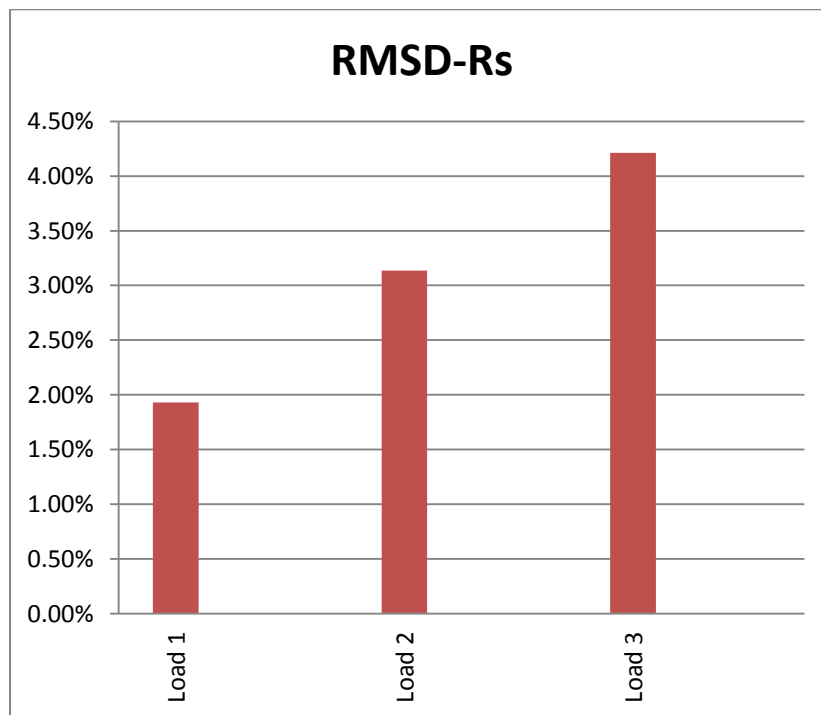


Chart 7.5 - RMSD chart for various compressive loads of S.A. 11

8 Monitoring of the curing process

Until today concrete has been the most commonly used material in buildings and civil infrastructures due to its comparatively low cost and its diversity in shape and meeting performance requirements. It is an heterogeneous material made of cement, aggregates water and admixtures. It is either produced in situ or pre-cast in factory and later installed in the construction site. Due to the great variety of shapes needed to be met the majority of concrete used in structures is casted in situ. This means that contrary to the pre-cast concrete, where concrete products exhibit great uniformity due to high standard of production, in situ concrete depends greatly on quality of materials, construction techniques, workmanship and exposures. Even concretes of the same mixture may vary in properties depending on the time of the casting and the conditions of curing. Therefore the monitoring of the concrete is very important to ensure its structural adequacy.

The hydration of cement is a complicated physical and chemical process which determines the microstructure of the concrete. Various methods have been developed to monitor and characterize the hydration of cementitious materials. During the construction of a concrete structure, strength monitoring is important to ensure the safety of both personnel and the structure itself. Furthermore, to increase the efficiency of in situ casting or precasting of concrete, determining the optimal time of demolding is very important for concrete suppliers. In the first few hours after mixing, the fresh concrete gradually achieves solid properties with reasonable compressive strength. The first and third day strengths are used to determine and identify any problems in the mix proportion, while the seventh day strength is used to determine the compressive strength of concrete as it is estimated that is about the 75% of the 28th day strength gain. Due to different type and amount of cementitious materials, concrete additives and curing temperature, different rates of hardening are expected. In addition, some other factors like the quality of the cementitious materials further increase the uncertainty in determining the appropriate time for demolding of concrete.

Various techniques have been used to determine the early age strength. The method with the higher precision is strength test on core samples taken from the structure, but is a destructive and intrusive method. Various non-destructive methods have also been used, like the ultrasonic technique, which needs to have access to both sides of the structure, has been widely employed to monitor the hydration process. A surface bonded PZT patch has also been used for hydration monitoring, however this technique could not monitor early hydration. In this master thesis, a variation of this technique is used, using embedded PZT patches via a smart aggregate, which is described analytically in the earlier chapters.

As proof of concept, four specimens were created, with the mix mentioned earlier in chapter 2, and were monitored during the curing process. Two cubic specimens sized 150x150x150 mm with one smart aggregate embedded in each, and two beam specimens sized 150x150x750 mm with two smart aggregates embedded in each. The aggregates were placed with a distance of 110-120 mm from the center of the beam and a distance of 230-240 mm between them. The following pictures demonstrate the procedure of creating the specimens.



Picture 8.1 150x150x150 mm matrices



Picture 8.2 150x150x750 mm matrix



Picture 8.3 Smart aggregate inside the cubic specimen



Picture 8.4 Smart aggregate inside the cubic specimen



Picture 8.5 Cubic specimen



Picture 8.6 Creation of the beam specimen



Picture 8.7 Creation of the beam specimen



Picture 8.8 Creation of the beam specimen



Picture 8.9 Final form of beam specimens

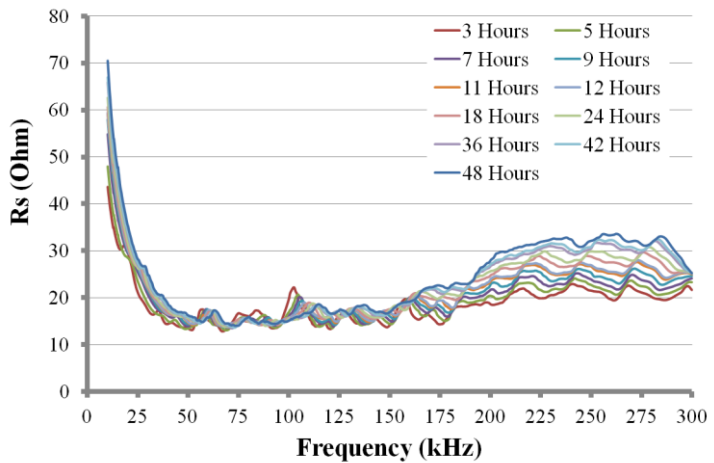


Picture 8.9 Final form of cubic specimens

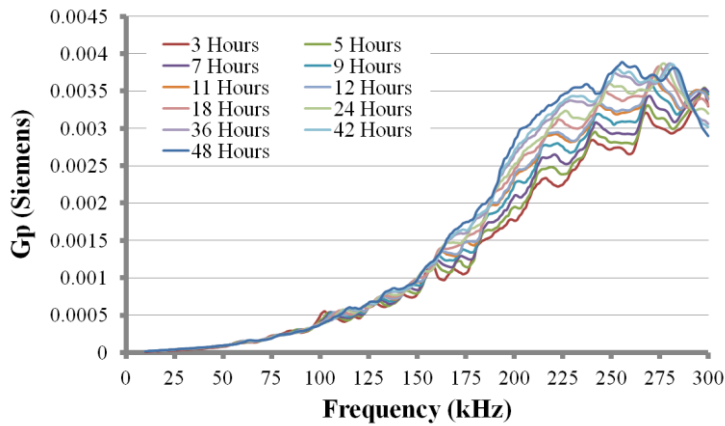
8.1 Monitoring of the curing process of Cube 1 (14/12/2012)

The following frequency plots are for Resistance R_s and conductance G_p . The imaginary parts of impedance and admittance are neglected and are only shown in the appendices for purposes of completeness. Three different plots are shown in each case, one for the whole scanned area, one for bandwidth of 50-150 kHz, which is the area affected by the host structure, and one in the bandwidth of 180-250 which is the area of the resonant peak of the PZT.

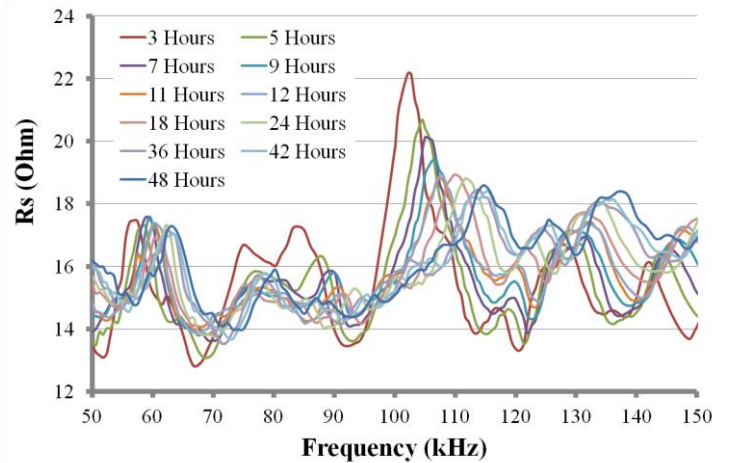
It is observed that with ageing, the peaks in R_s plots are shifting rightwards, indicating that stiffness is increasing with time. The opposite trend is observed in compression test. It is also observed that as the concrete becomes stiffer, measurements in high frequencies (greater than 180 kHz) become greatly affected by the resonance peak of the PZT, manifesting a big peak in the area of 200-250 kHz. The last observation is more obvious in the rest of the specimens.



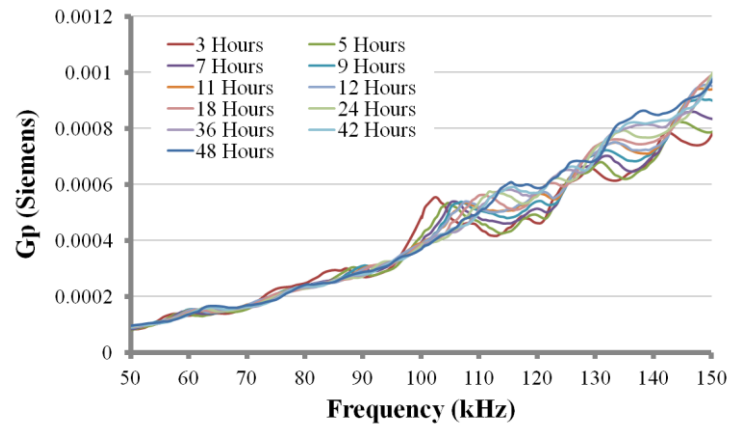
(y)



(aa)

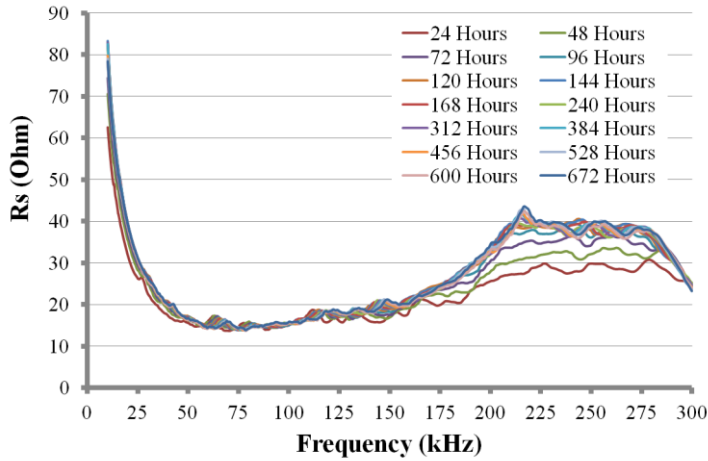


(z)

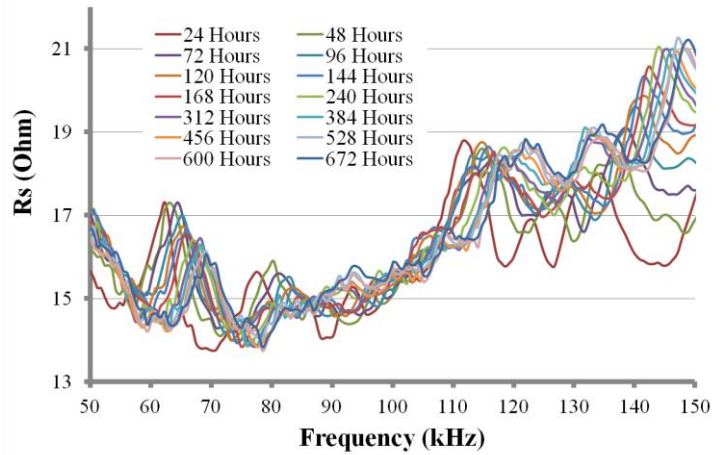


(bb)

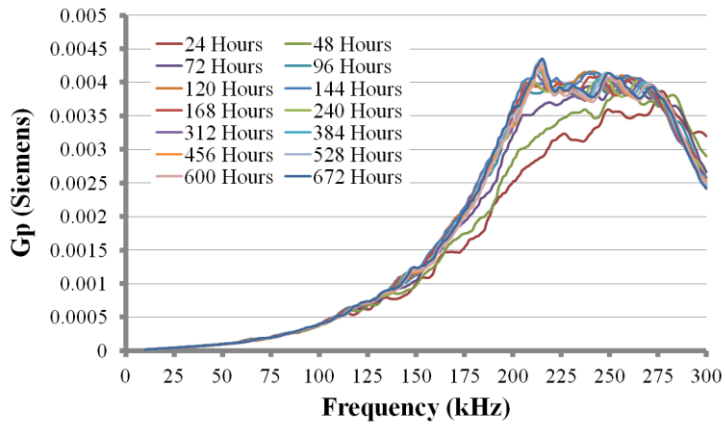
Plots 8.1 – (a) Resistance plot 0-300 kHz for the first 48 Hours (b) Resistance plot 50-150 kHz for the first 48 Hours (c) Conductance plot 0-300 kHz for the first 48 Hours (d) Conductance plot 50-150 kHz for the first 48 Hours



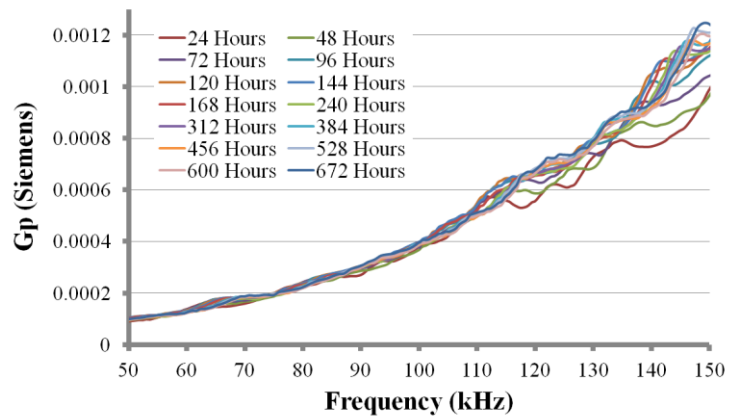
(cc)



(dd)

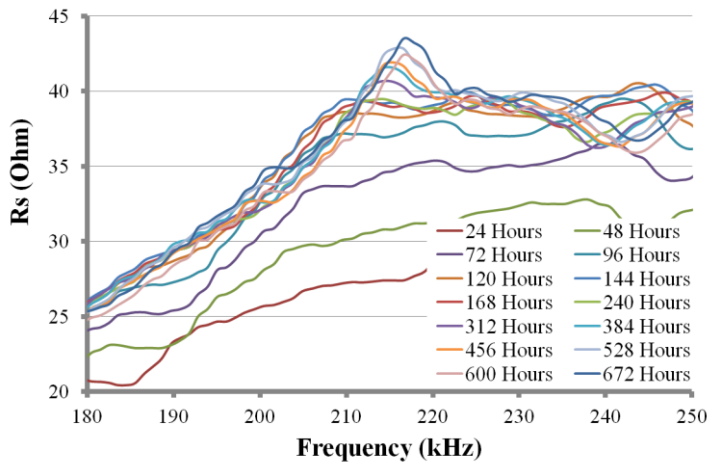


(ee)

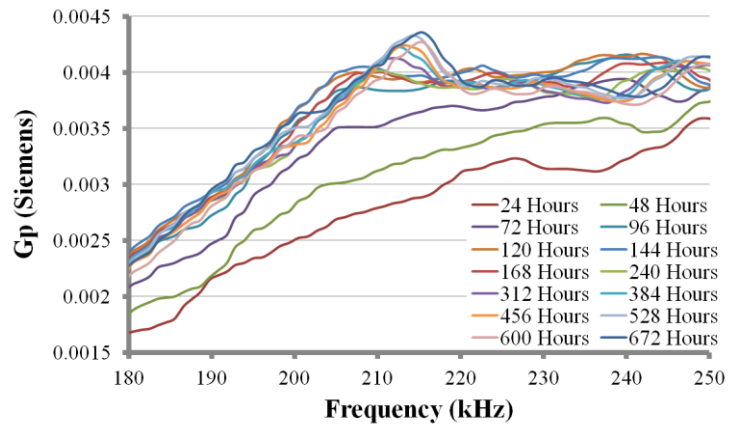


(ff)

Plots 8.2 – (a) Resistance plot 0-300 kHz for the first 28 Days (b) Resistance plot 50-150 kHz for the first 28 Days
(c) Conductance plot 0-300 kHz for the first 28 Days (d) Conductance plot 50-150 kHz for the first 28 Days



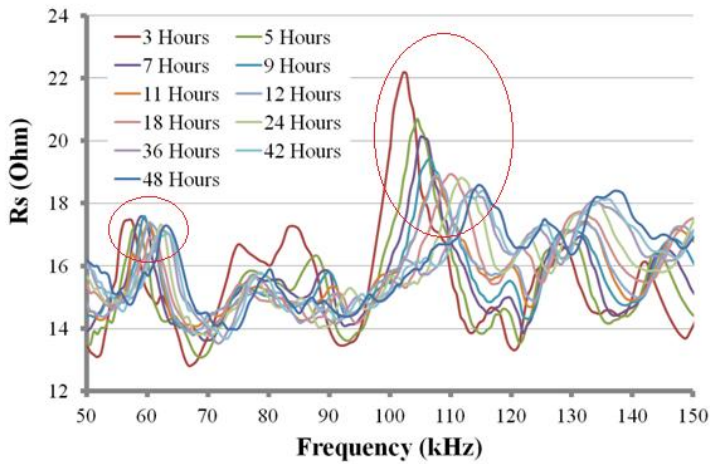
(gg)



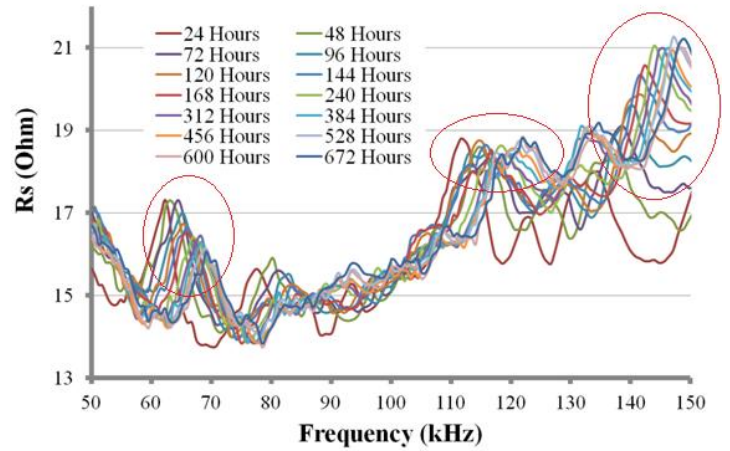
(hh)

Plots 8.3 – (a) Resistance plot 180-250 kHz for the first 28 Days (b) Conductance plot 180-250 kHz for the first 28 Days

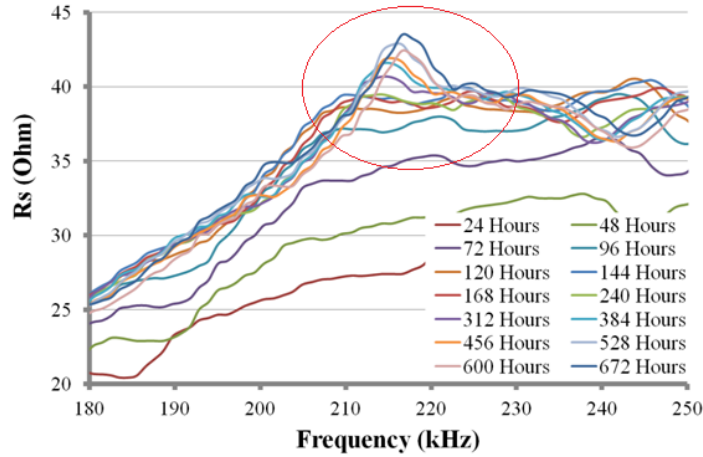
The changes mentioned earlier are obvious in the Rs signatures and are shown in the following plots zoomed:



(ii)



(ij)



(c)

Plots 8.4 – (a) Resistance plot 50-150 kHz for the first 48 Hours (b) Resistance plot 50-150 kHz for the first 28 Days (c) Conductance plot 180-250 kHz for the first 28 Days

As mentioned earlier, the frequency plots are a useful tool to observe changes in the host structure, but in order to quantify the change we use the RMSD metric. The following chart is with the measurement taken three hours after the casting as baseline. The RMSD value is observed to have a gradual increase for the first 120 hours (5 days) after the casting and then remain steady until the end of the monitoring (28 days). This is in accordance to what was expected, as concrete gains up to 75% of its final strength in the first 7 days after casting.

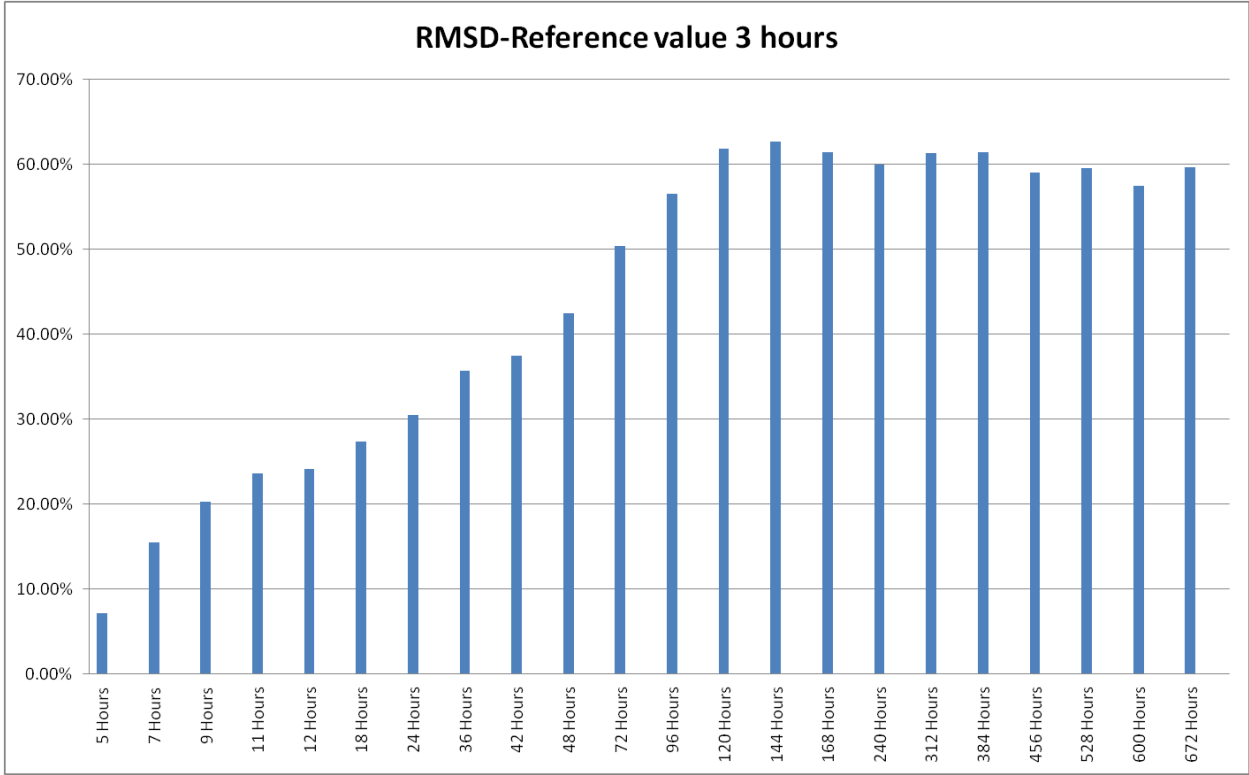
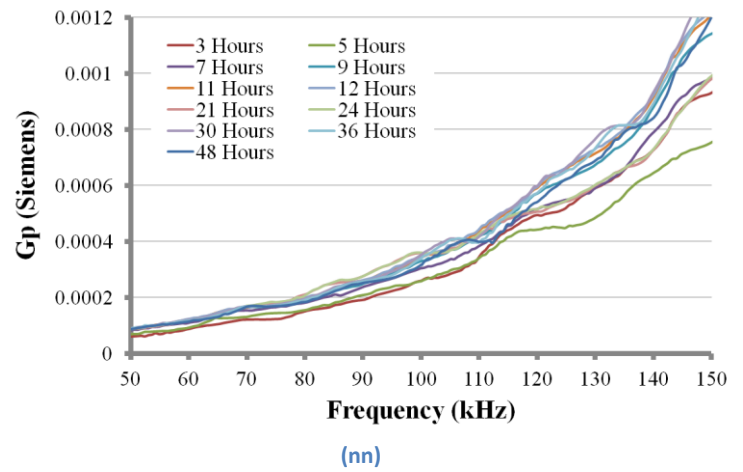
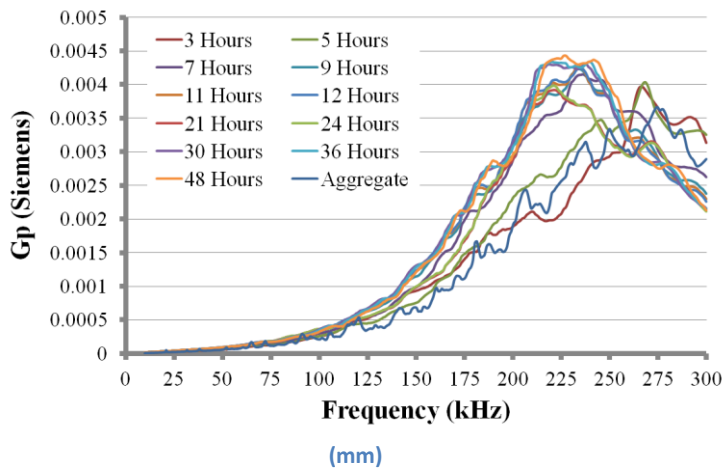
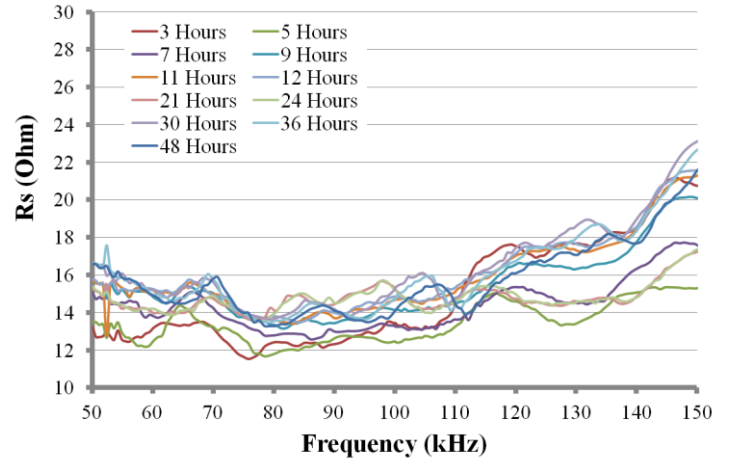
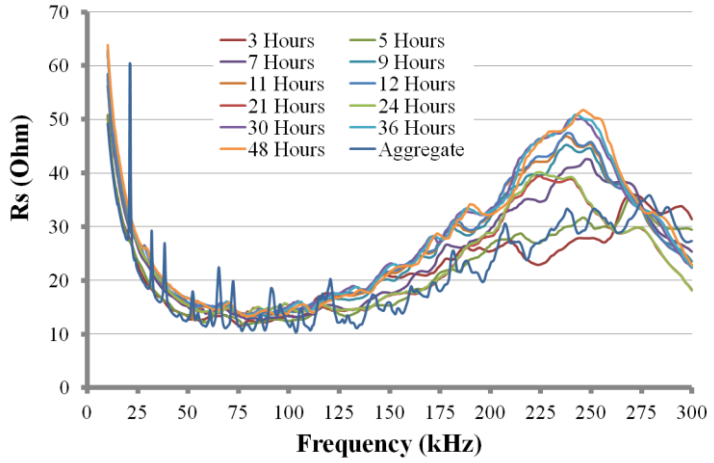


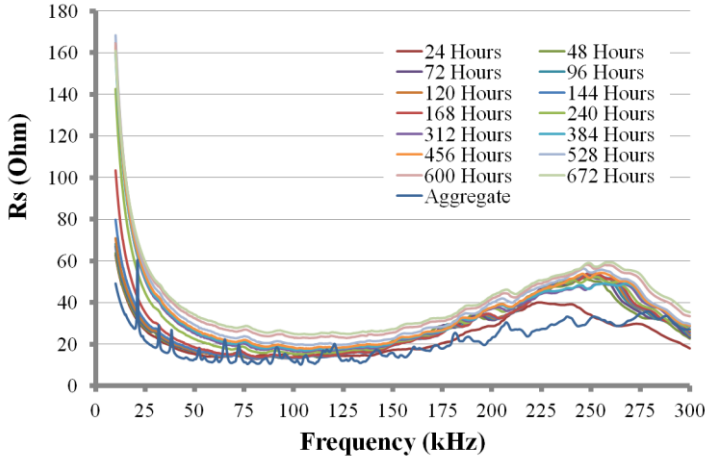
Chart 8.1 - RMSD chart for curing process of Cube 1 (Reference value-3 hours)

8.2 Monitoring of the curing process of Beam 1 (4/2/2013)

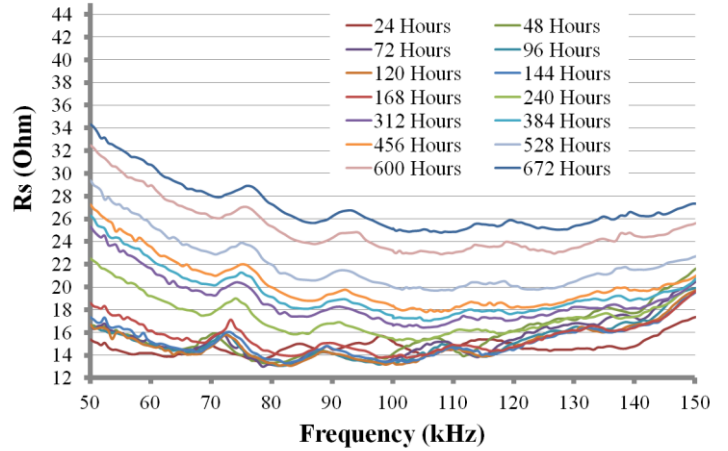
8.2.1 Aggregate 4



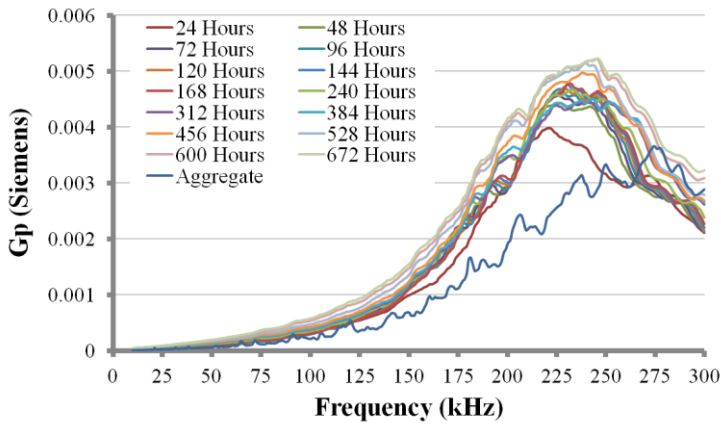
Plots 8.5 – (a) Resistance plot 0-300 kHz for the first 48 Hours (b) Resistance plot 50-150 kHz for the first 48 Hours (c) Conductance plot 0-300 kHz for the first 48 Hours (d) Conductance plot 50-150 kHz for the first 48 Hours



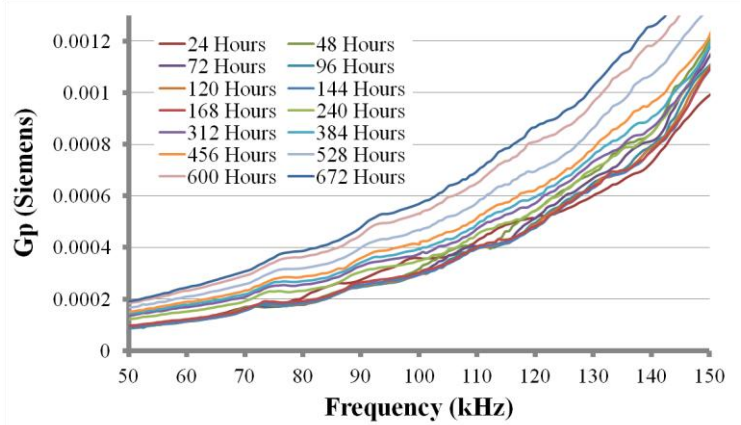
(oo)



(pp)

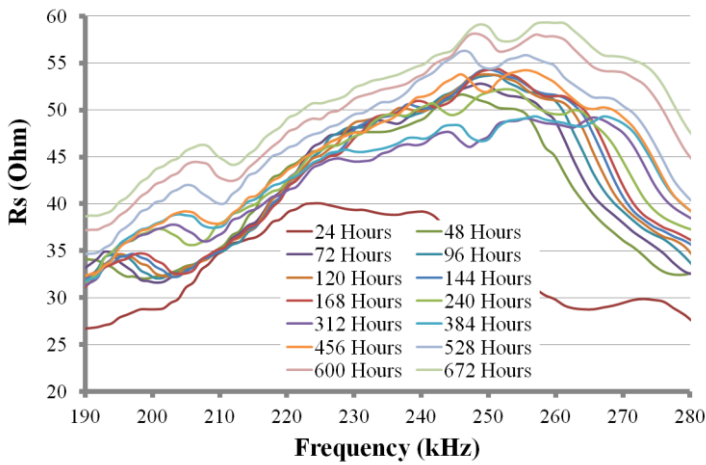


(qq)

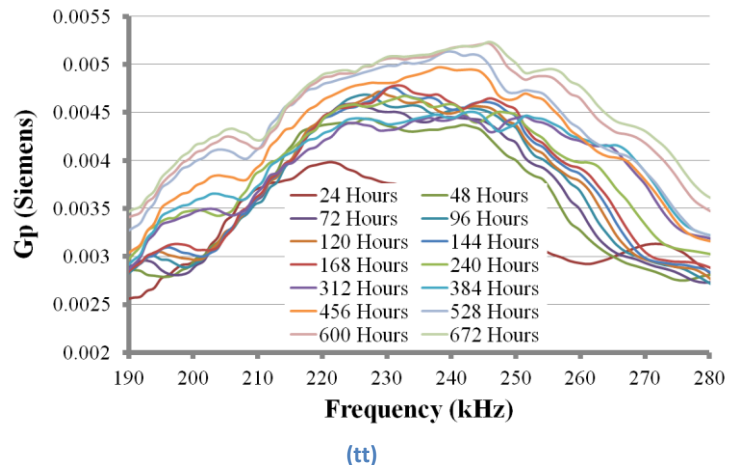


(rr)

Plots 8.6 – (a) Resistance plot 0-300 kHz for the first 28 Days (b) Resistance plot 50-150 kHz for the first 28 Days (c) Conductance plot 0-300 kHz for the first 28 Days (d) Conductance plot 50-150 kHz for the first 28 Days



(ss)



(tt)

Plots 8.7 – (a) Resistance plot 190-250 kHz for the first 28 Days (b) Conductance plot 190-250 kHz for the first 28 Days

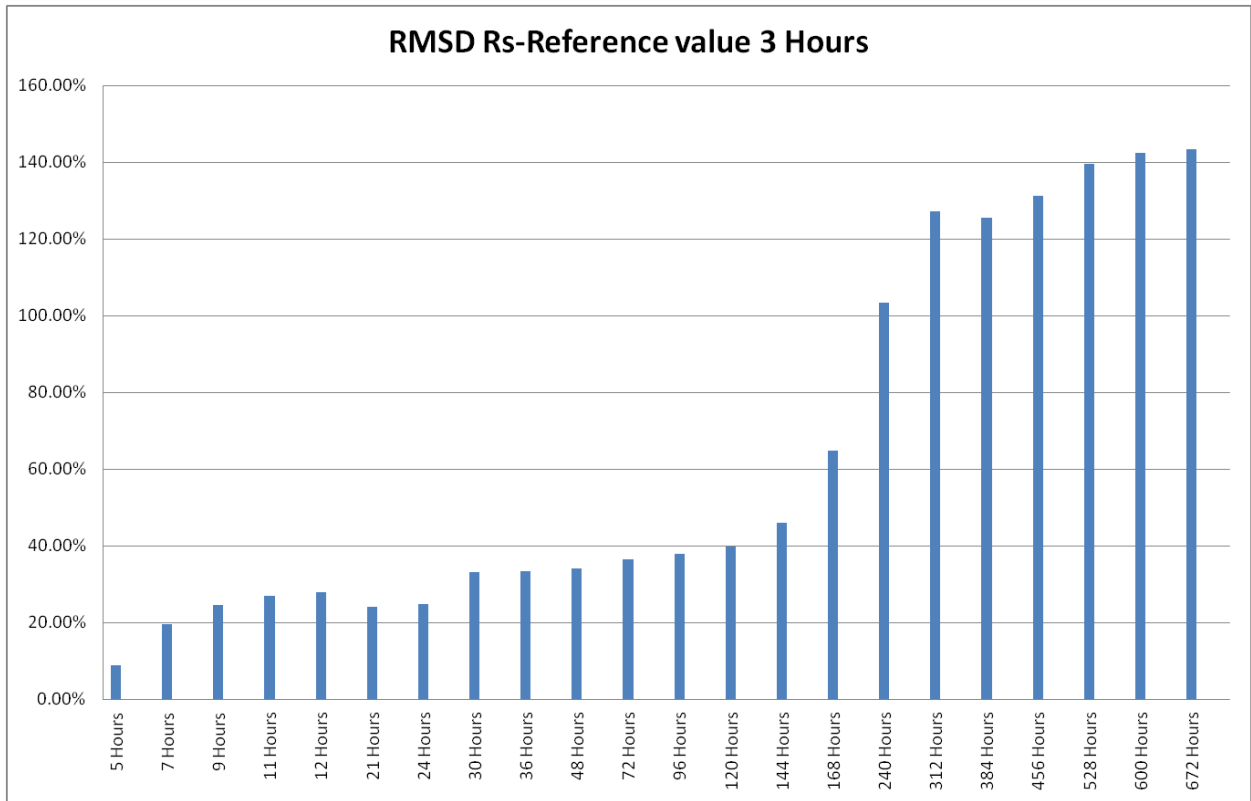
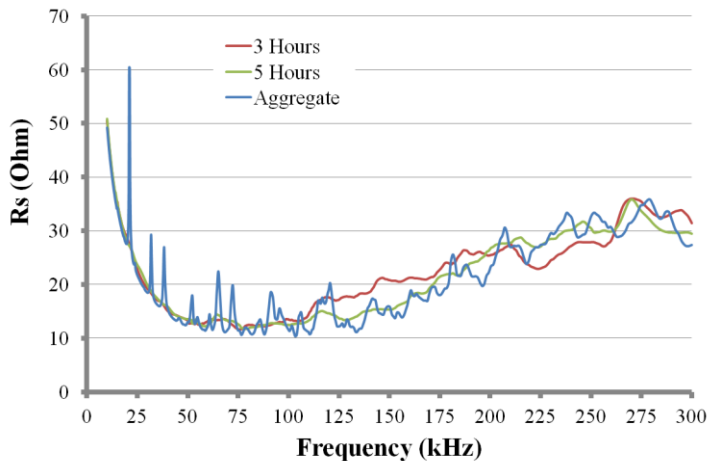
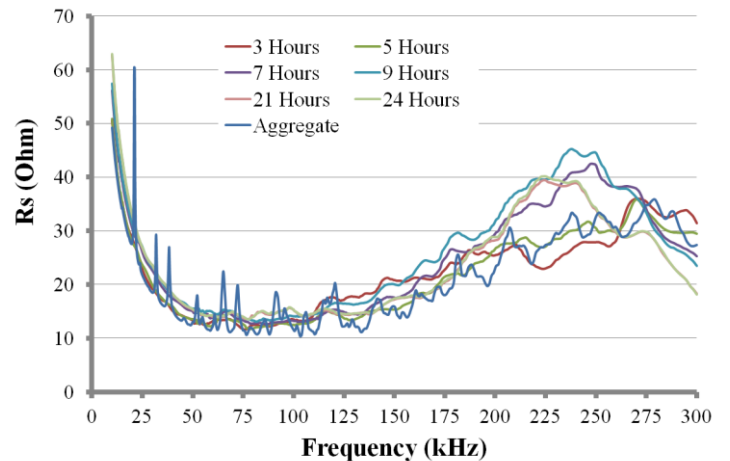


Chart 8.2 - RMSD chart for curing process of Beam 1 – Aggregate 4 (Reference value-3 hours)

Observing the above plots we can easily recognize what seems to be a slightly different behavior from the cubic specimen but this is not the case. The first hours after the casting, the plots are similar to the ones of the aggregate before embedding it in the beam (as shown in the plots below).



(uu)

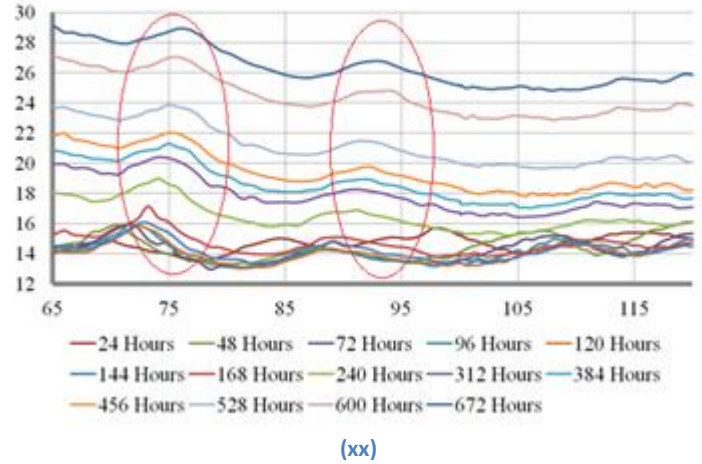
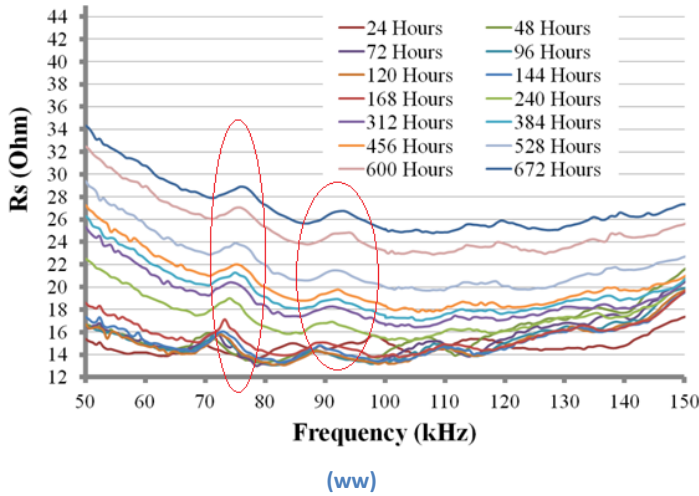


(vv)

Plots 8.8 – (a) Resistance plot 0-300 kHz for the first 5 Hours (b) Resistance plot 0-300 kHz for the first 24 Hours

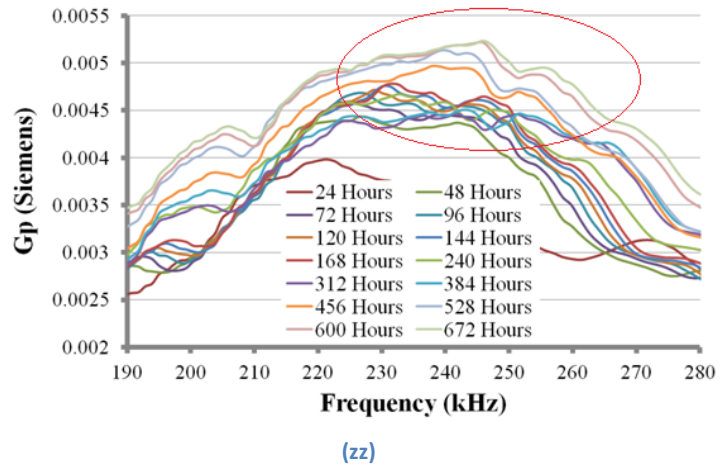
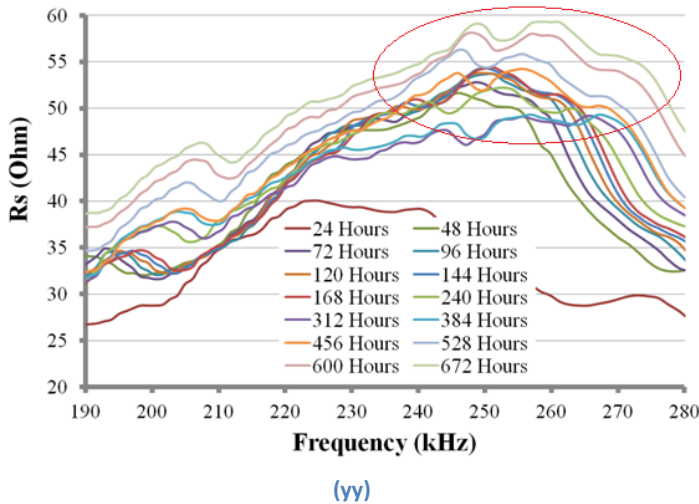
The difference between the plots is the absence of resonance peaks due to the high dumping of the fresh concrete. As time passes, concrete starts becoming stiffer and the difference in the form of the plot becomes more obvious, as shown in the plot 8.8 (b).

The absence of easily visible resonance peaks is owed to the size of the structure but even this way we can observe the same pattern when we focus in a smaller bandwidth (see plots below).



Plots 8.9 – (a) Resistance plot 50-150 kHz for the first 28 Days (b) Resistance plot 65-120 kHz for the first 28 Days

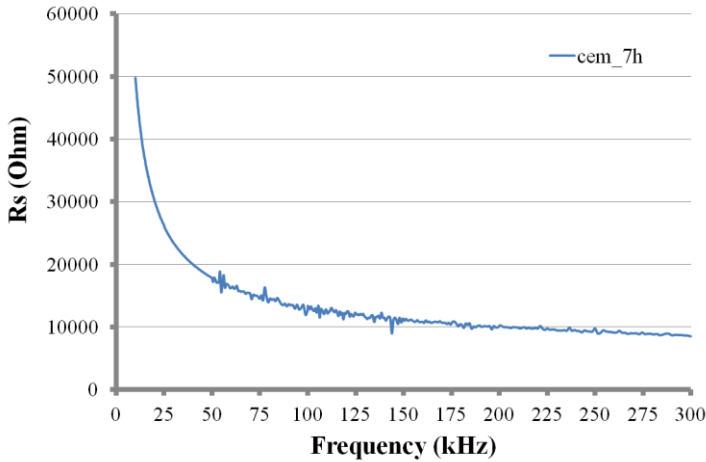
There is a slight rightwing shift of the small peaks that appear in the plots, combined with a general increase in the value of resistance. In the area of the resonance frequency of the patch the same trend is observed as shown in the plots below:



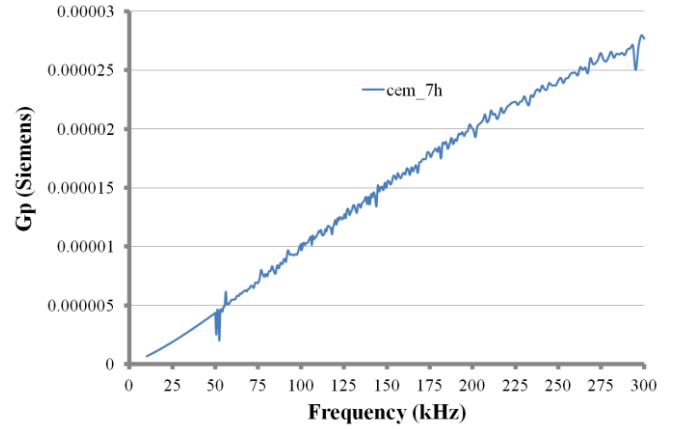
Plots 8.10 – (a) Resistance plot 190-280 kHz for the first 28 Days (b) Conductance plot 190-280 kHz for the first 28 Days

8.2.2 Aggregate 7

Aggregate 7 manifested a very unstable behavior that was also not consistent with the rest of the measurements and what was expected from theory. This was probably a result of insufficient water protection of the electrode cables during the casting of the concrete. The measurements of the first 12 hours after the casting of concrete were completely unrealistic (see plots below).



(aaa)



(bbb)

Plots 8.11 – (a) Resistance plot 7 Hours after the casting (b) Conductance plot 7 Hours after the casting

The following measurements (after the 12th hour after the casting) were logical, as far as their value was concerned, but manifested an unexpected behavior with a left-hand shift of the resonance peak of the PZT and a great leap in RMSD values in the 19th day that continued to rise until the 28th day.

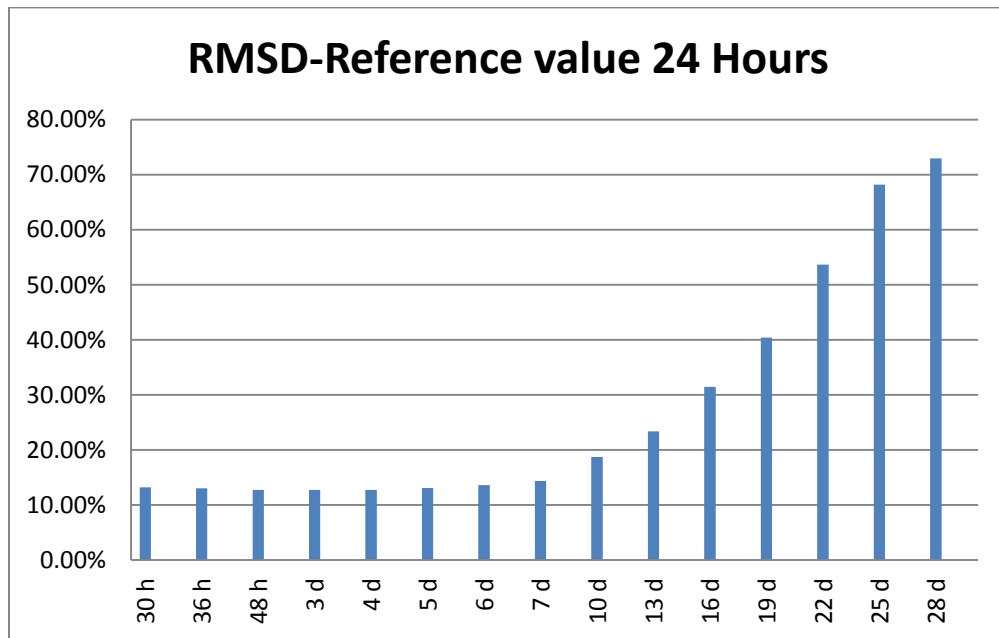
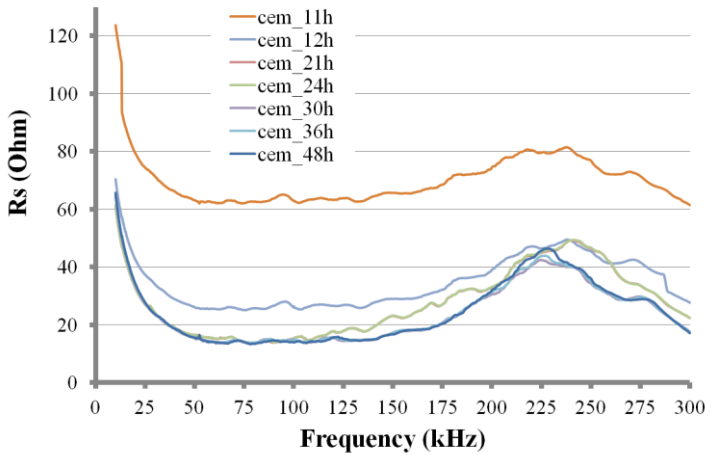
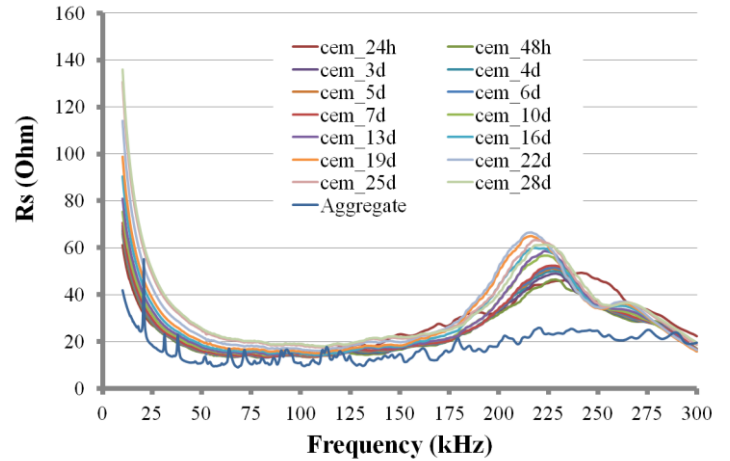


Chart 8.3 - RMSD chart for curing process of Beam 1 – Aggregate 7 (Reference value-24 hours)

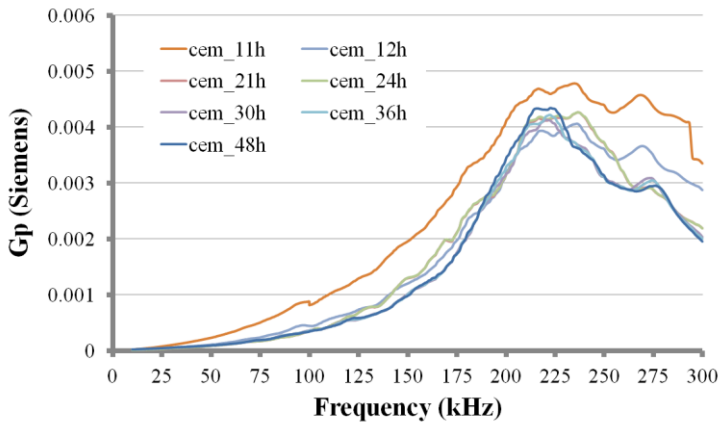
The interpretation of the above RMSD chart is that concrete gets stiffer after the 16th day and great changes regarding its stiffness continue to occur until the 28th day. Of course this is definitely not what happens in reality as great changes in the stiffness of concrete occur during the first week and especially the first 48 hours after the casting of concrete and has a very slow growth rate after the 15th day. Even so, the results are demonstrated in the following pages.



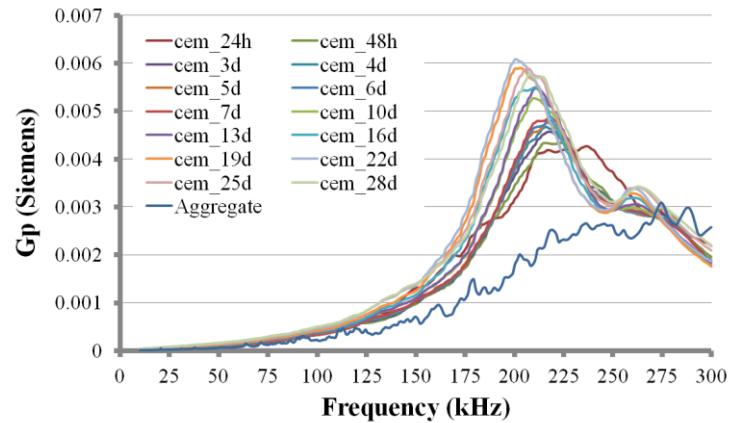
(ccc)



(ddd)

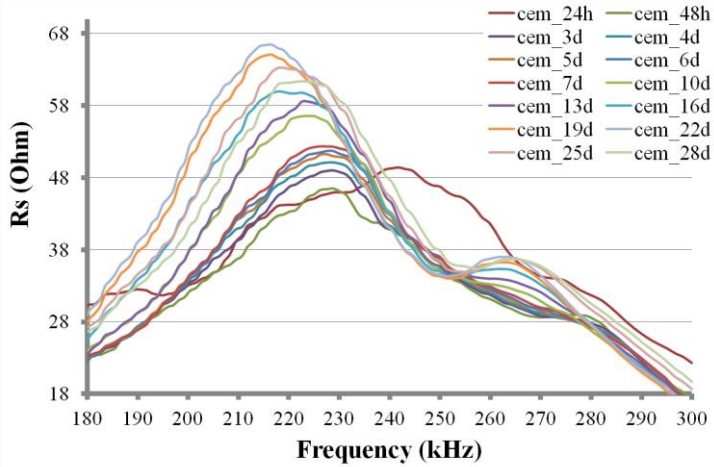


(eee)

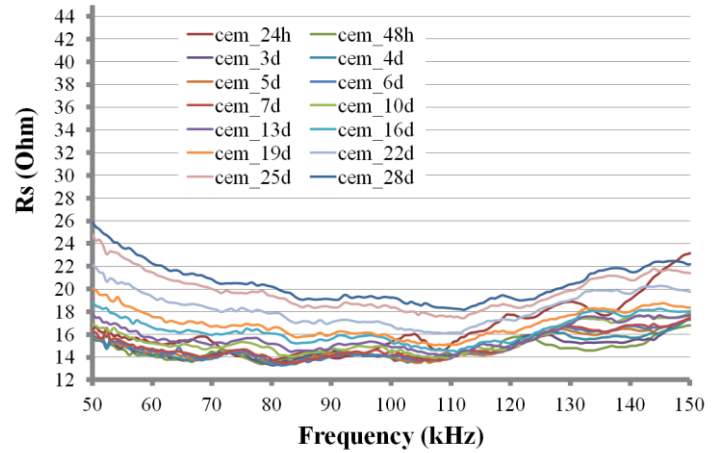


(fff)

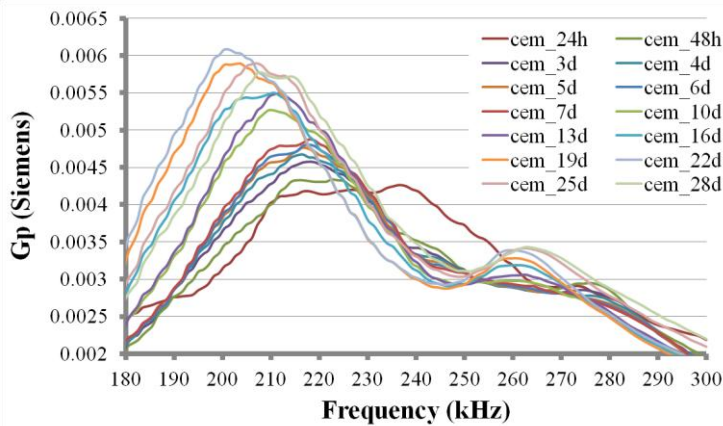
Plots 8.12 – (a) Resistance plot 0-300 kHz for the first 48 Hours (b) Resistance plot 0-300 kHz for the first 28 Days (c) Conductance plot 0-300 kHz for the first 48 Hours (d) Conductance plot 0-300 kHz for the first 28 Days



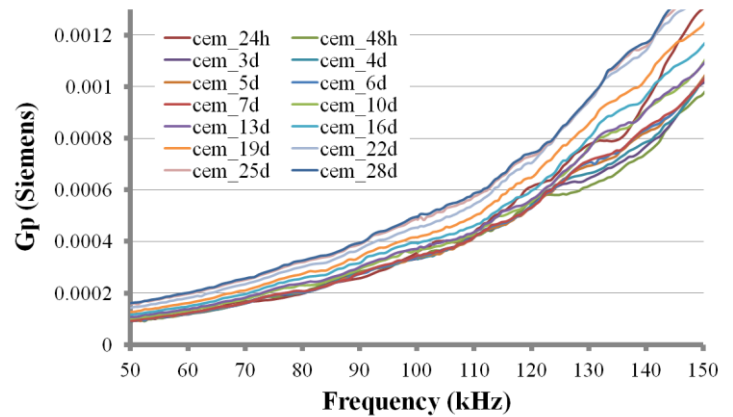
(ggg)



(hhh)



(iii)

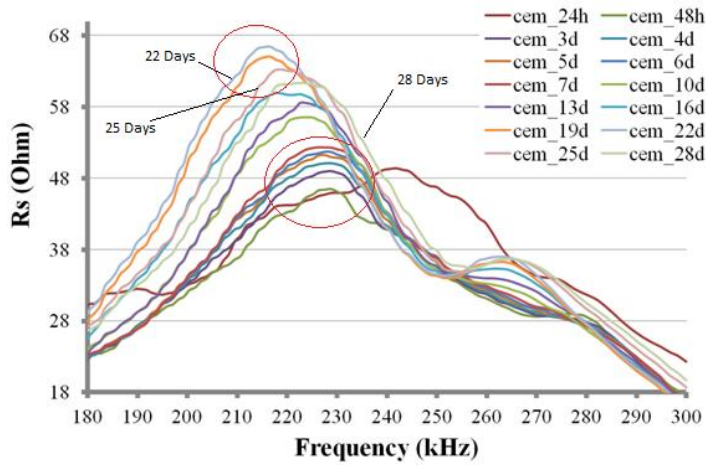


(jjj)

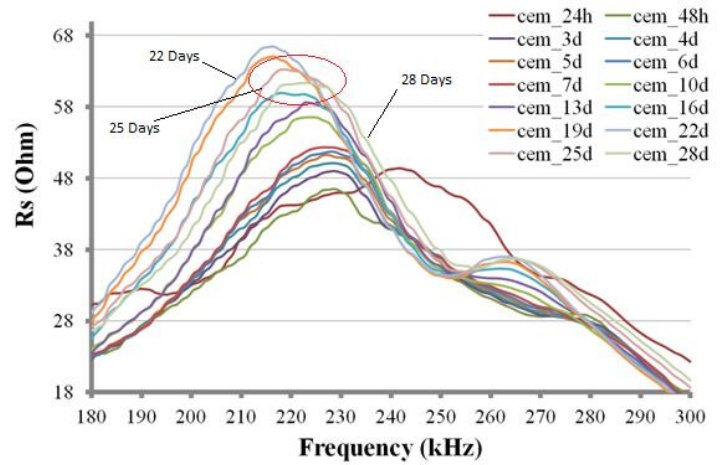
Plots 8.13 – (a) Resistance plot 180-300 kHz for the first 28 Days (b) Resistance plot 50-150 kHz for the first 28 Days (c) Conductance plot 180-300 kHz for the first 28 Days (d) Conductance plot 50-150 kHz for the first 28 Days

The results are very unstable and in some cases inconsistent with the theory. For example, as shown in the plots below (8.14 (a), (c)), there is a left hand shift in the resonance peak for the first 25 days of the measurements in both resistance and conductance plots. Only in the last two measurements, for days 25 and 28 we can observe a right hand shift of the resonance peak, as expected (plots 8.14 (b), (d)).

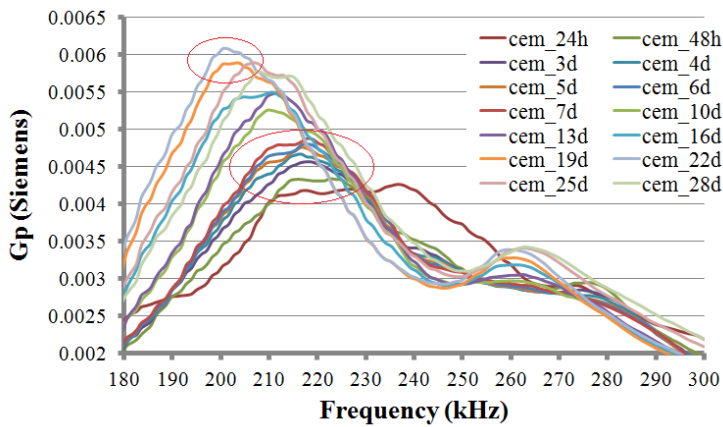
The following can be accounted for wetting the electrode cables during the casting of concrete. The results are indicative of the sensitivity of the method in humidity, even as far as the electrode cables are concerned. Although the sensor will continued to work as expected after the cable was dry again, both as a receiver as well as a transmitter, the monitoring of the curing process was not successful. It is also obvious that the whole process, from the preparation of the smart aggregate until its installation in the concrete structure must be done very meticulously.



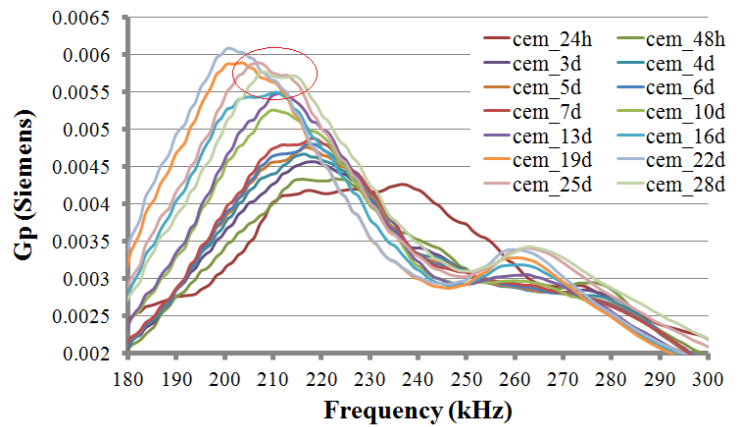
(kkk)



(lll)



(c)

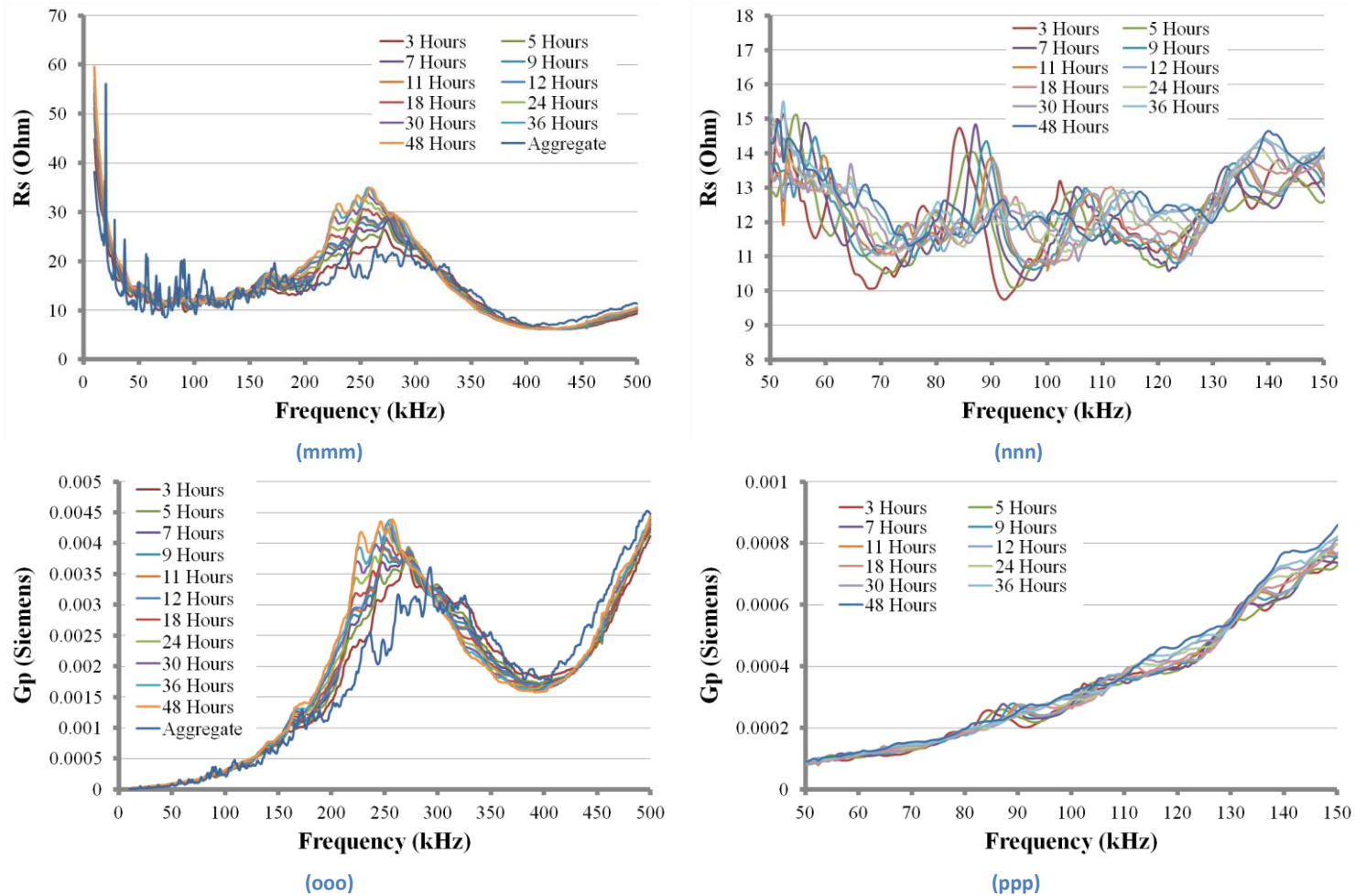


(d)

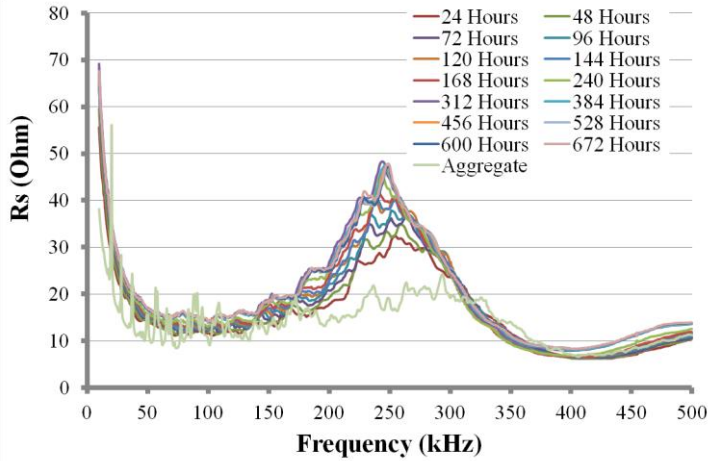
Plots 8.14 – (a) Unexpected left shift of the peak in resistance plot (b) Right shift of the peak in resistance plot for day 25 and 28 (c) Unexpected left shift of the peak in conductance plot (d) Right shift of the peak in conductance plot for day 25 and 28

8.3 Monitoring of the curing process of Cube 2 (24/4/2013)

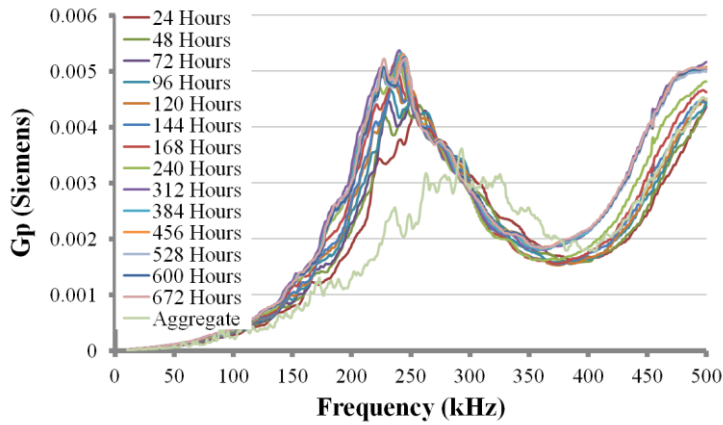
Observing the results of the monitoring for the second cube specimen, we jump to the same conclusions as in the previous specimens: right hand shift of the peaks in frequency plots and an increase in the RMSD values in the first two weeks of the monitoring and a stabilization of it in the last weeks. The results are presented in the following pages:



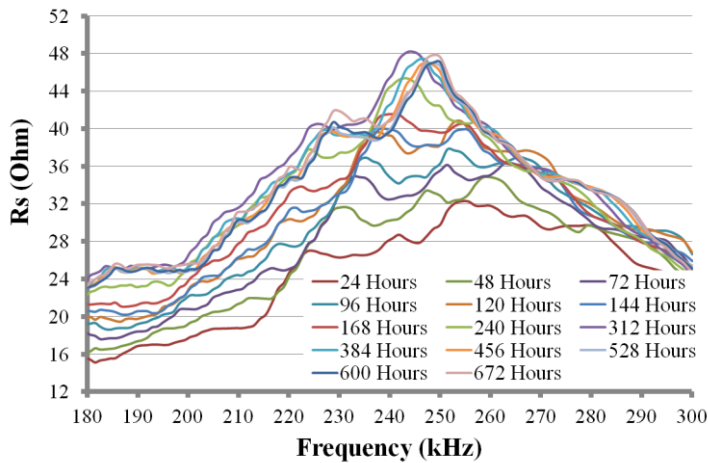
Plots 8.15 – (a) Resistance plot 0-500 kHz for the first 48 Hours (b) Resistance plot 50-150 kHz for the first 48 Hours (c) Conductance plot 0-500 kHz for the first 48 Hours (d) Conductance plot 50-150 kHz for the first 48 Hours



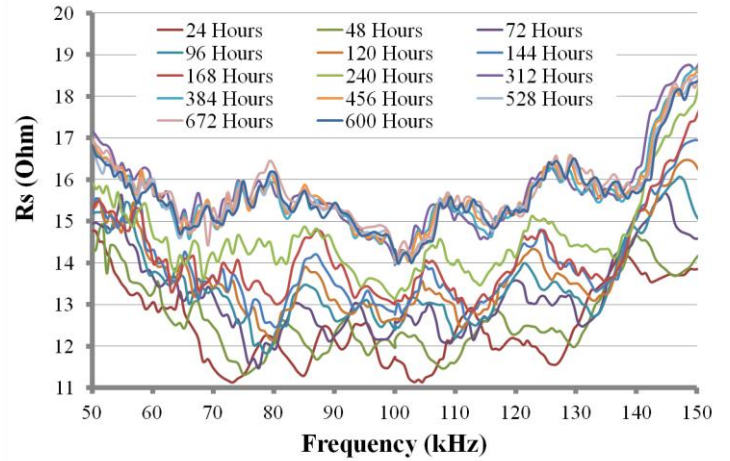
(qqq)



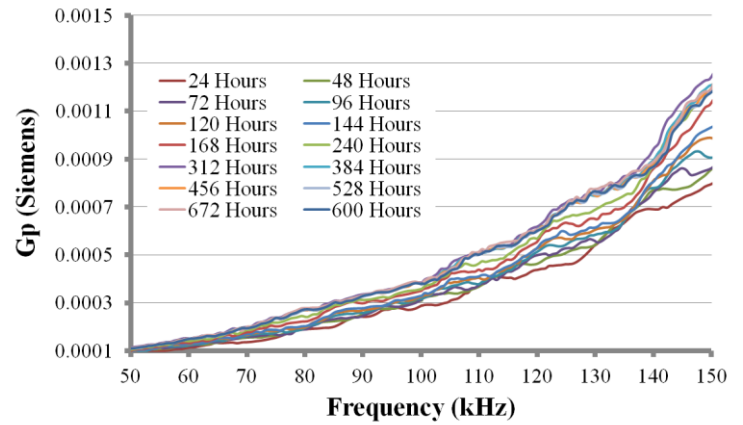
(sss)



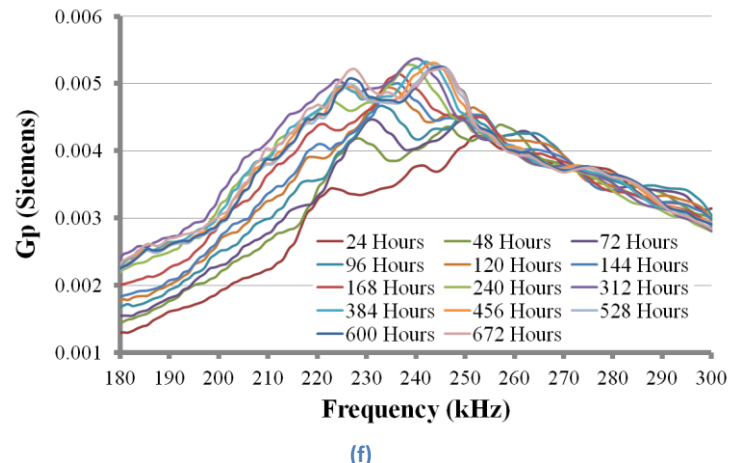
(e)



(rrr)



(ttt)



(f)

Plots 8.16 – (a) Resistance plot 0-500 kHz for the first 28 Days (b) Resistance plot 50-150 kHz for the first 28 Days (c) Conductance plot 0-500 kHz for the first 28 Days (d) Conductance plot 50-150 kHz for the first 28 Days (e) Resistance plot 180-300 kHz for the first 28 Days (f) Conductance plot 180-300 kHz for the first 28 Days

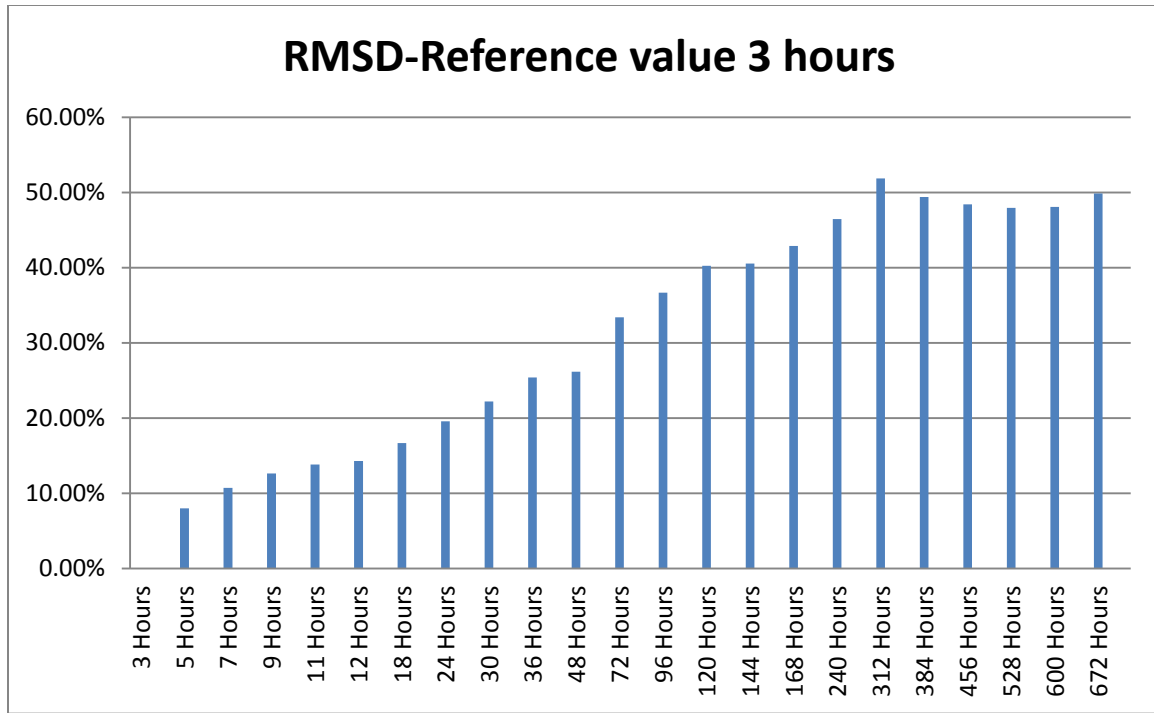
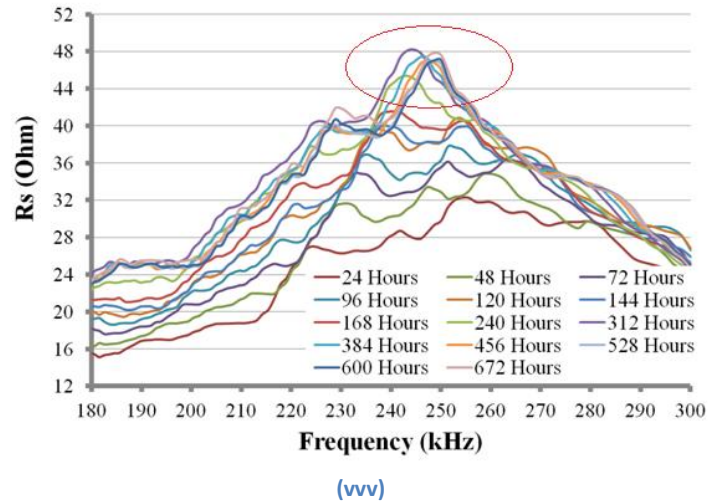
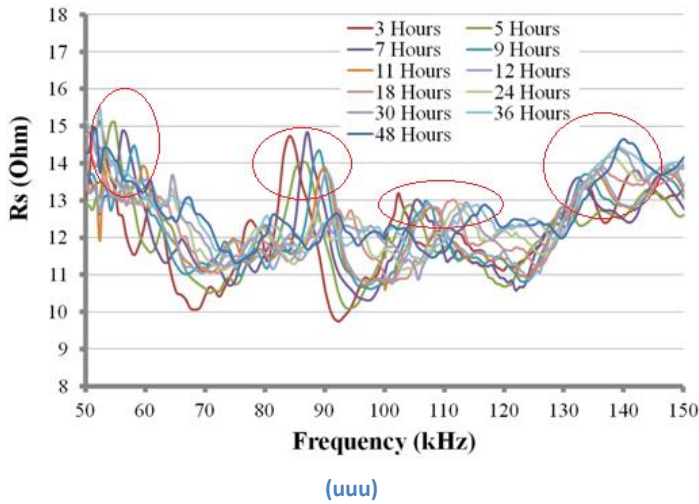
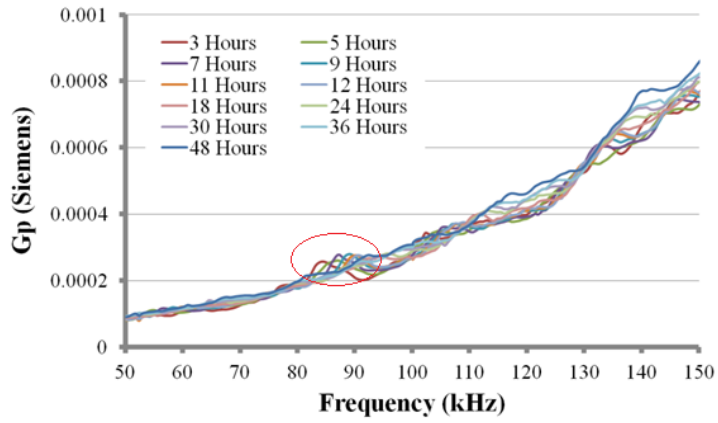
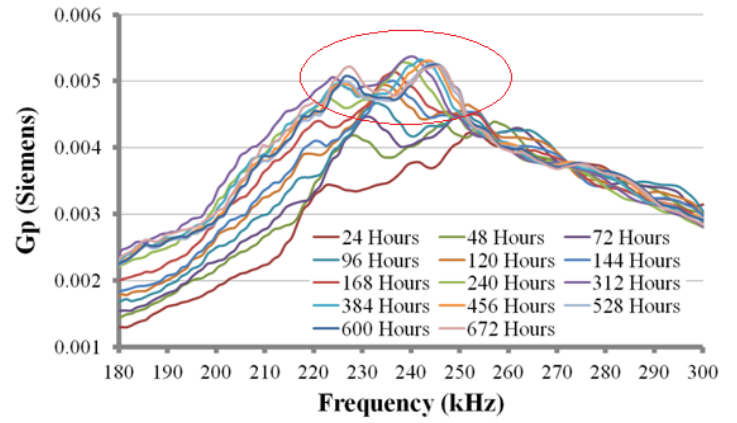


Chart 8.4 - RMSD chart for curing process of Cube 2 (Reference value-3 hours)





(c)

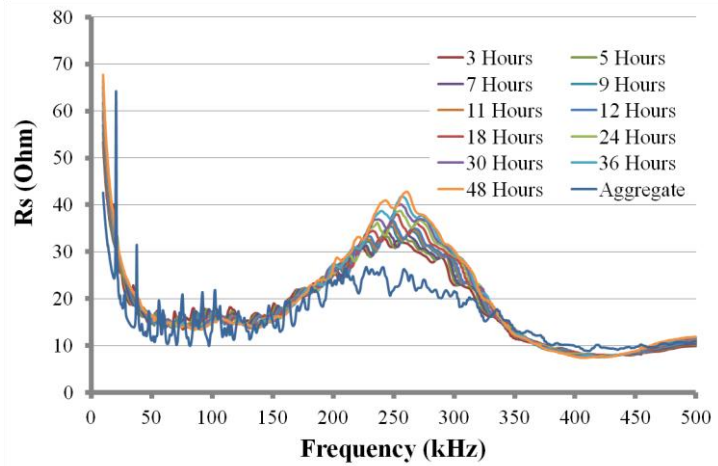


(d)

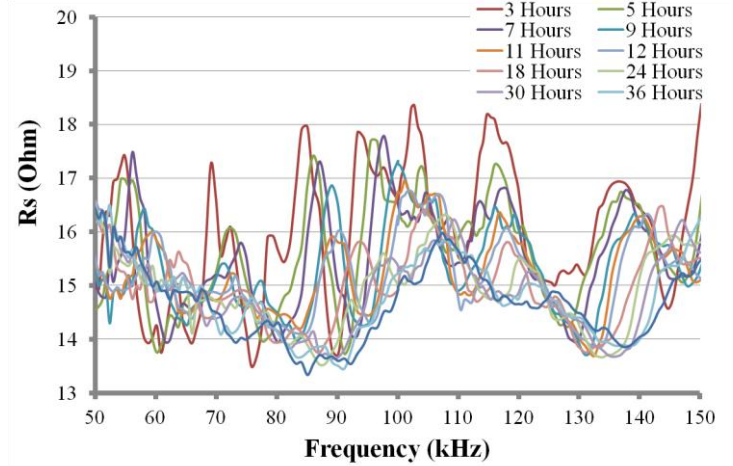
Plots 8.17 – (a) Resistance plot 50-150 kHz for the first 48 Hours (b) Resistance plot 180-300 kHz for the first 28 Days
 (c) Conductance plot 50-150 kHz for the first 48 Hours (d) Conductance plot 180-300 kHz for the first 28 Days

8.4 Monitoring of the curing process of Beam 2 (24/4/2013)

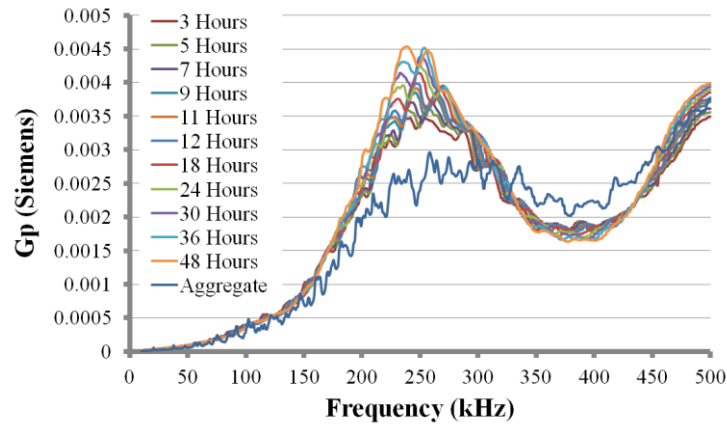
8.4.1 Aggregate 11



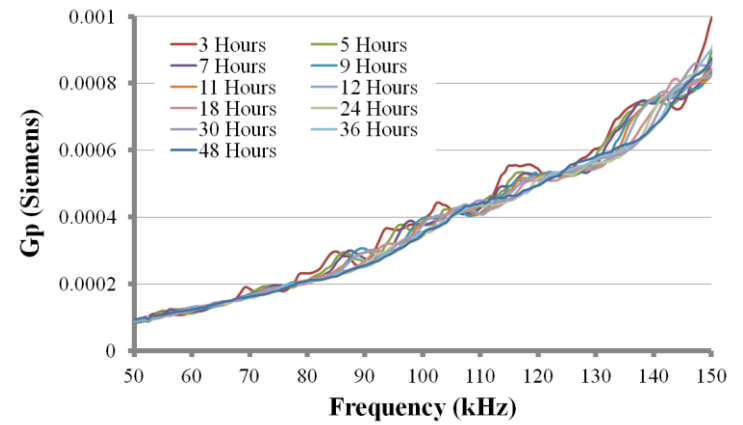
(www)



(xxx)

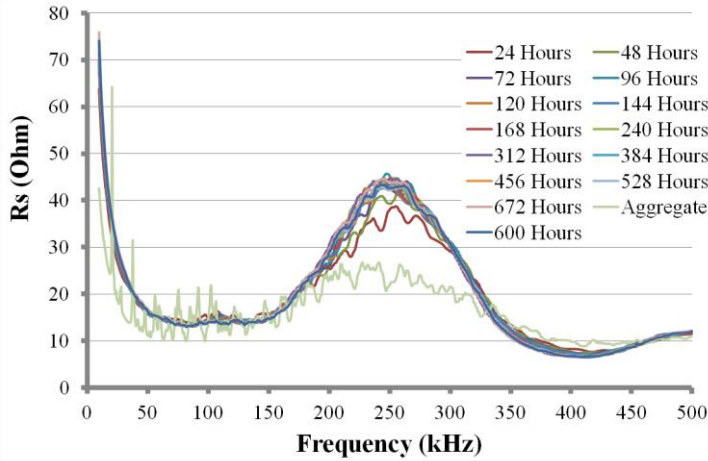


(yyy)

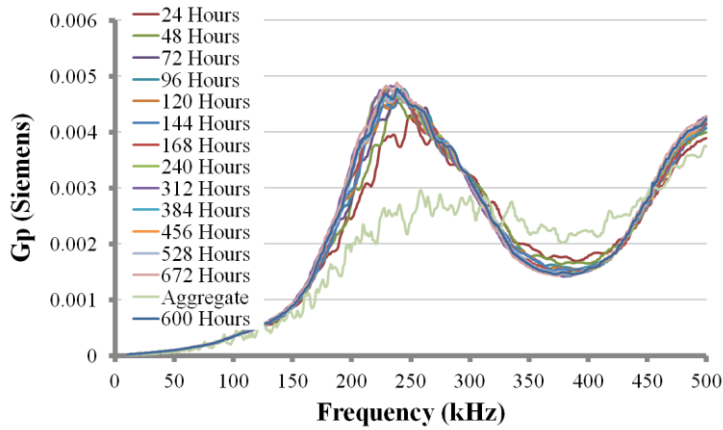


(zzz)

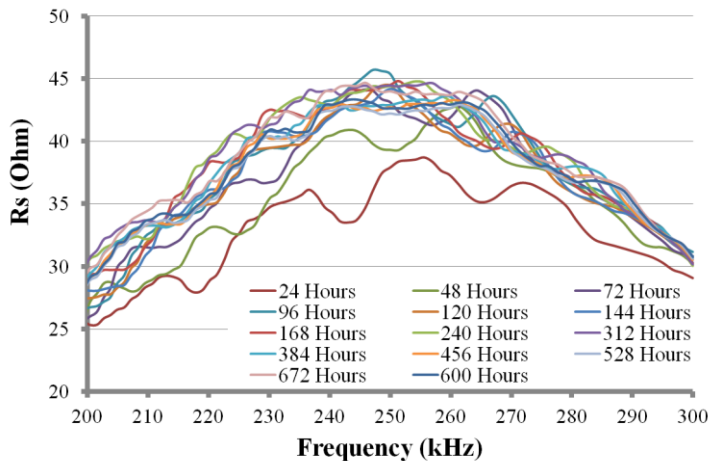
Plots 8.18 – (a) Resistance plot 0-500 kHz for the first 48 Hours (b) Resistance plot 50-150 kHz for the first 48 Hours (c) Conductance plot 0-500 kHz for the first 48 Hours (d) Conductance plot 50-150 kHz for the first 48 Hours



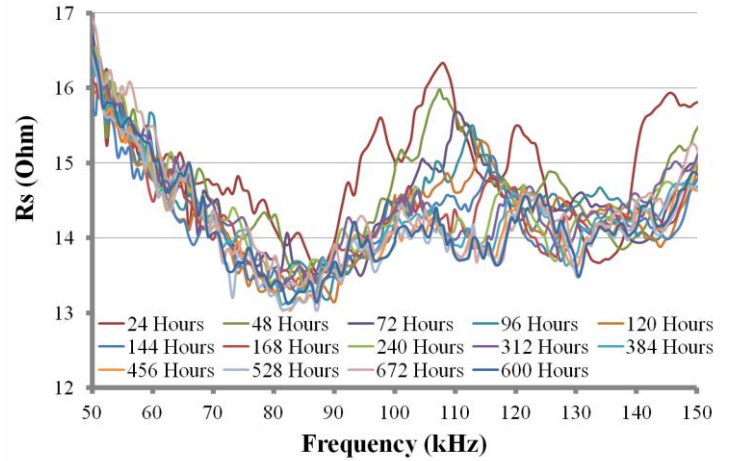
(aaaa)



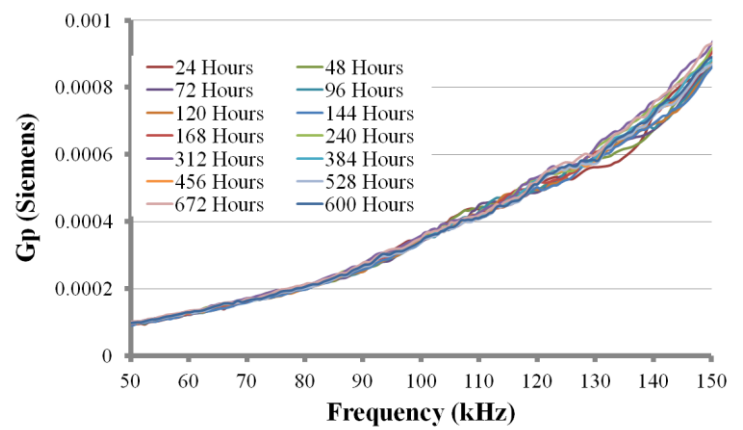
(cccc)



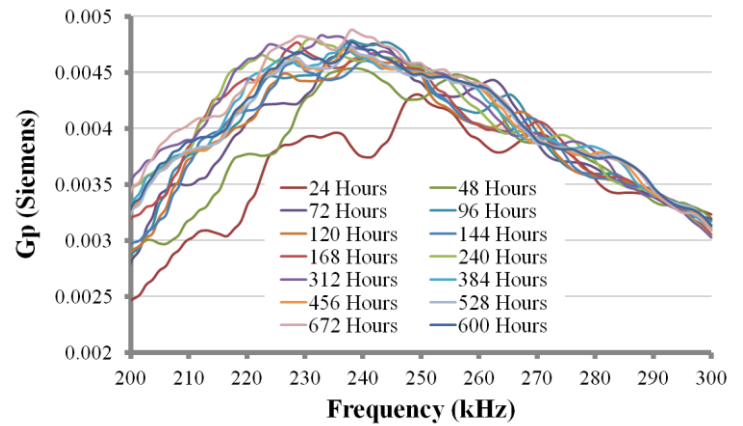
(e)



(bbbb)



(dddd)



(f)

Plots 8.19 – (a) Resistance plot 0-500 kHz for the first 28 Days (b) Resistance plot 50-150 kHz for the first 28 Days (c) Conductance plot 0-500 kHz for the first 28 Days (d) Conductance plot 50-150 kHz for the first 28 Days (e) Resistance plot 200-300 kHz for the first 28 Days (f) Conductance plot 200-300 kHz for the first 28 Days

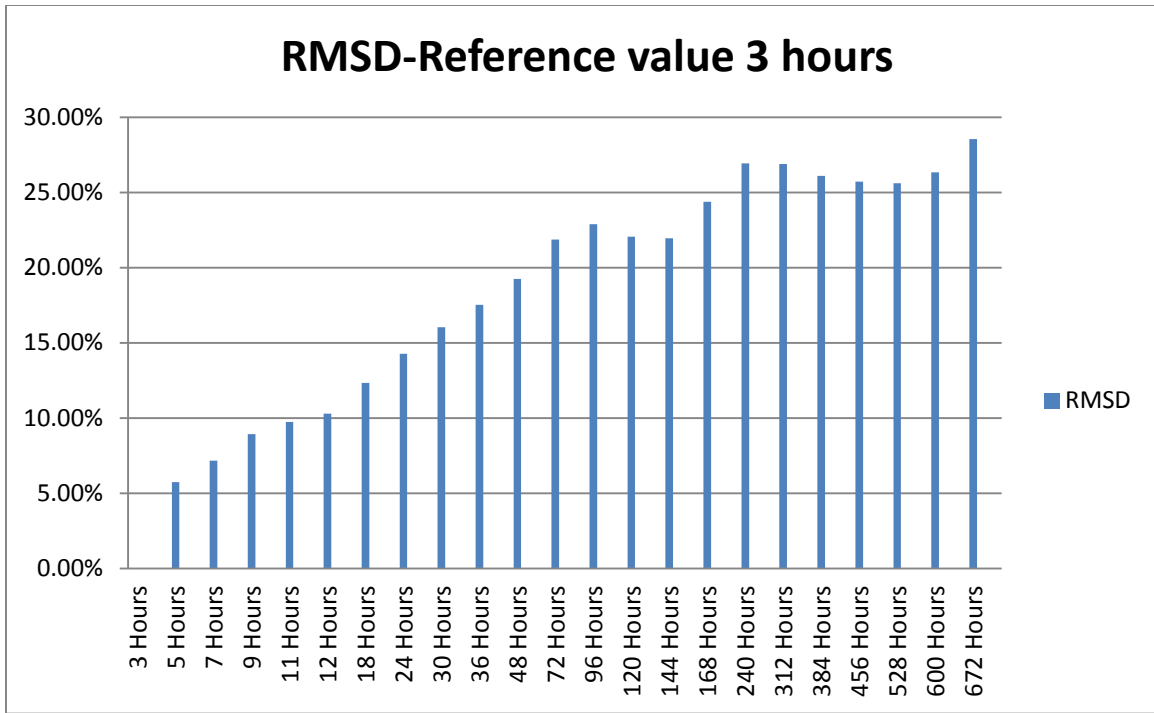
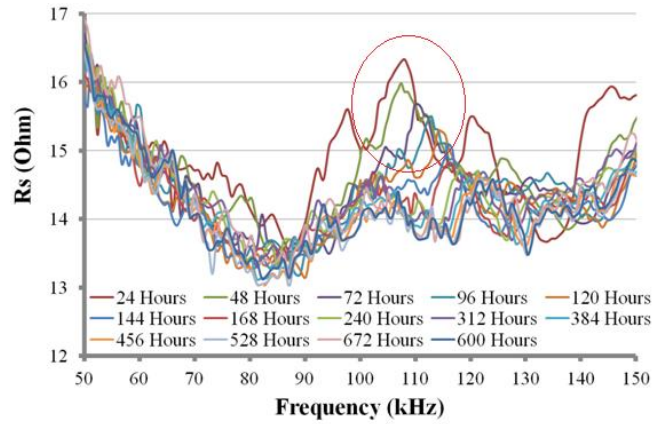
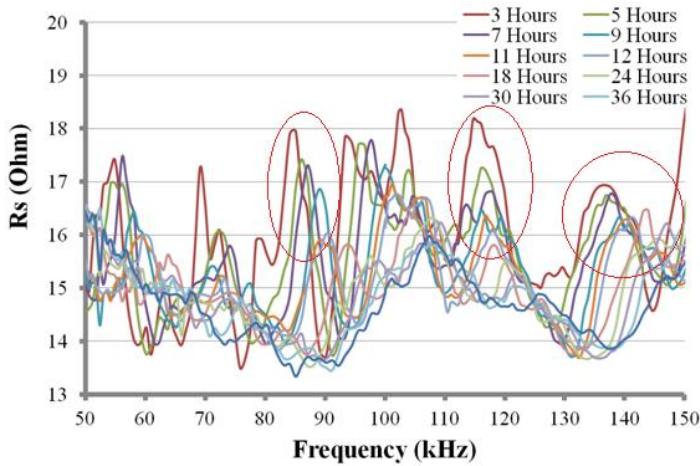


Chart 8.5 - RMSD chart for curing process of Beam 2 – Aggregate 11 (Reference value-3 hours)

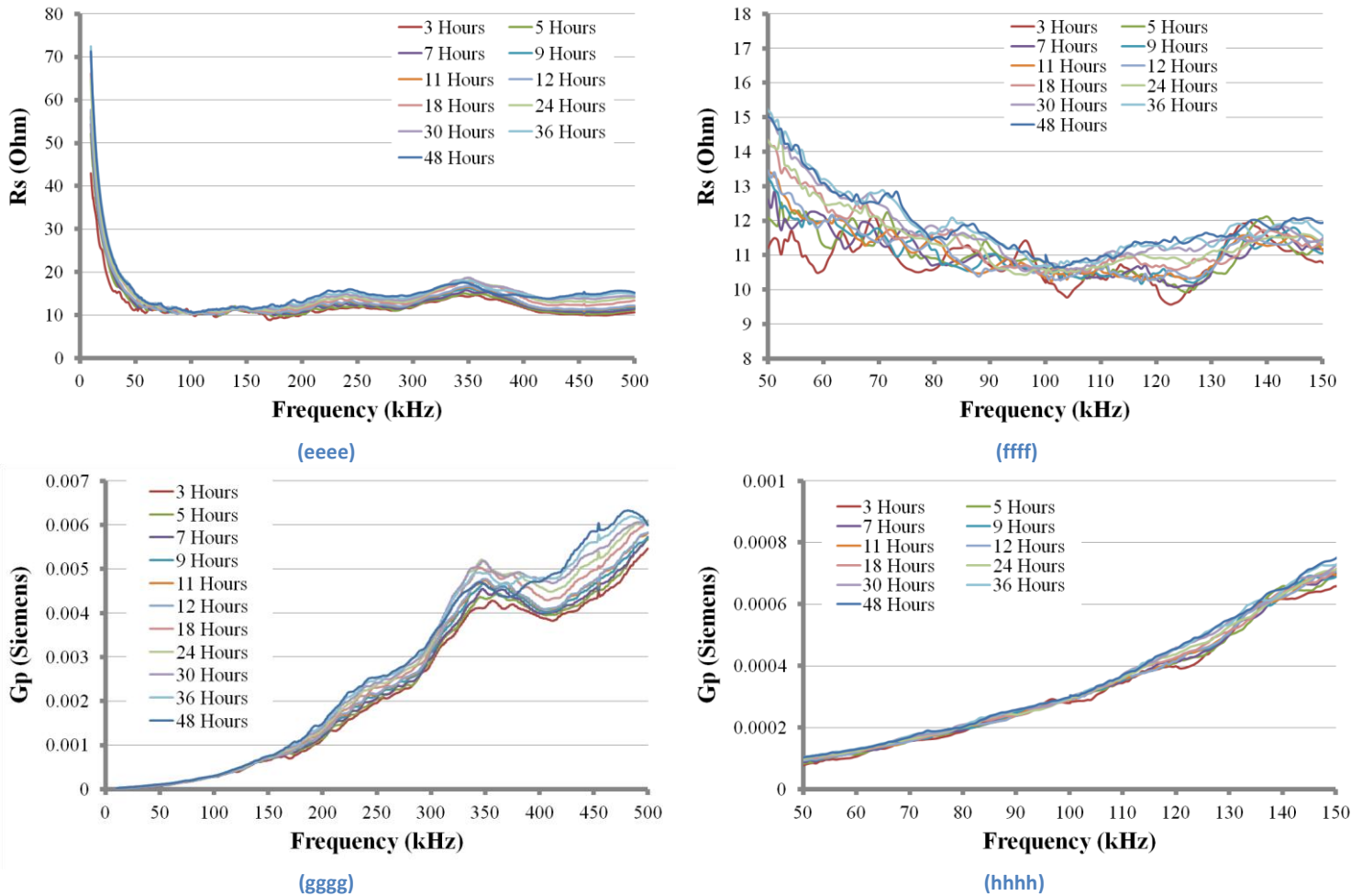


Plots 8.20 – (a) Resistance plot 50-150 kHz for the first 48 Hours (b) Resistance plot 50-150 kHz for the first 28 Days

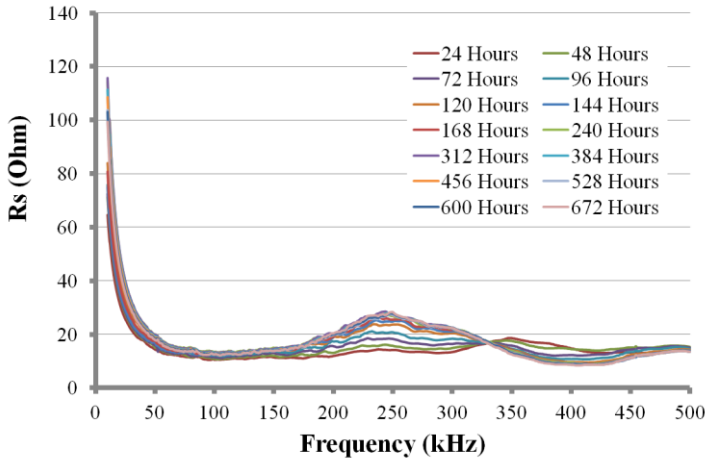
8.4.2 Aggregate 10

Aggregate 10 was embedded cracked in the beam, but was expected to continue to work properly in spite of the damage. However the results taken during the curing process manifested a lot of unexpected fluctuations. Although the PZT patch was intact, the existence of the crack makes the hardened cement mortar permeable and thus more vulnerable to humidity when placed inside the freshly poured concrete.

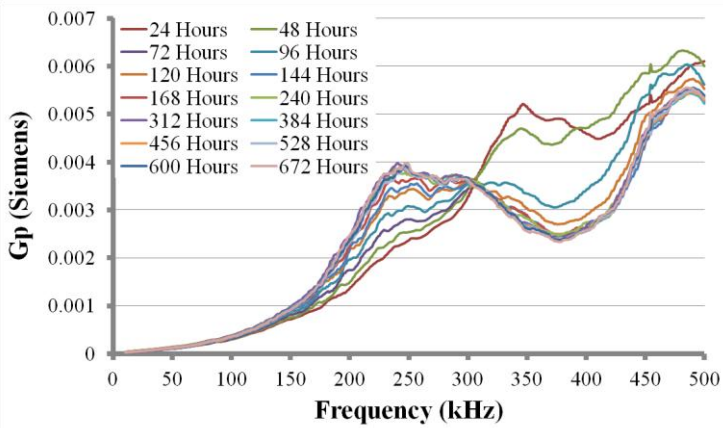
Although we can observe phenomena like the right hand shift of the peaks, gradual increase in the RMSD values for the first 96 hours after the casting, the results cannot be considered satisfactory. Except from the trends we expected to see, we can also observe an unjustified rise of all the R_s values in the 5th day (120 hours) and a sudden peak in the RMSD chart. The next two measurements for days 6 and 7 (144 and 168 hours) are back in the same level as in day 4. Then for the next two measurements for days 10 and 13, a great leap in RMSD values is observed once more (40% rise) comparing with the value for day 7, only to start dropping once more for the next measurements until the 28th day.



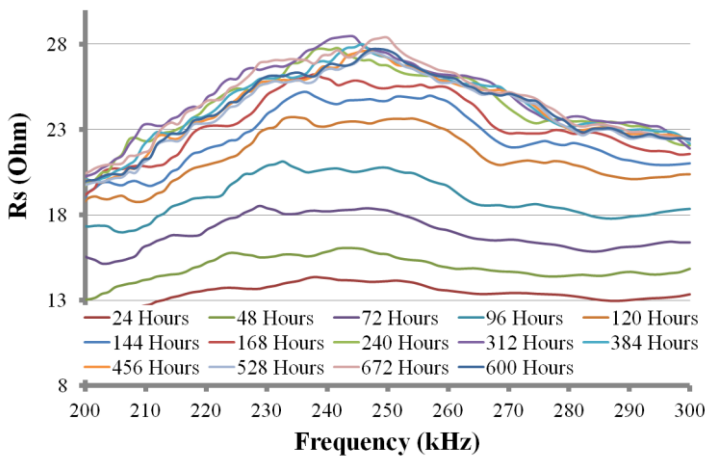
Plots 8.21 – (a) Resistance plot 0-500 kHz for the first 48 Hours (b) Resistance plot 50-150 kHz for the first 48 Hours (c) Conductance plot 0-500 kHz for the first 48 Hours (d) Conductance plot 50-150 kHz for the first 48 Hours



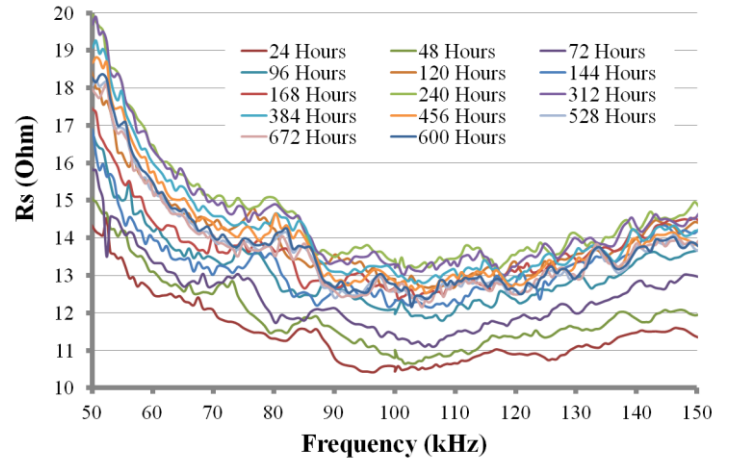
(iii)



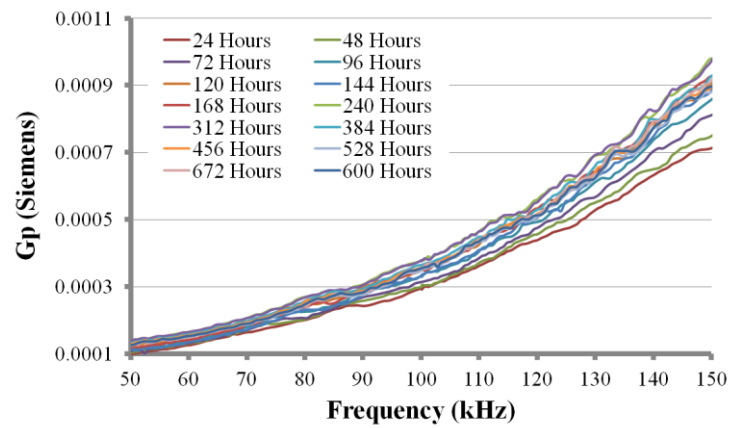
(kkkk)



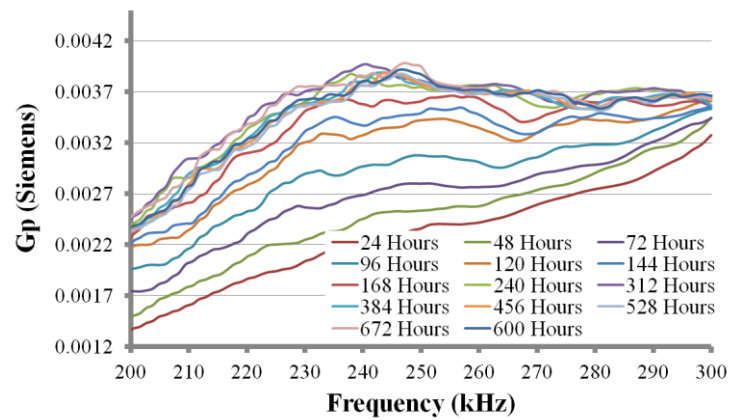
(e)



(jjj)



(lll)



(f)

Plots 8.22 – (a) Resistance plot 0-500 kHz for the first 28 Days (b) Resistance plot 50-150 kHz for the first 28 Days (c) Conductance plot 0-500 kHz for the first 28 Days (d) Conductance plot 50-150 kHz for the first 28 Days (e) Resistance plot 200-300 kHz for the first 28 Days (f) Conductance plot 200-300 kHz for the first 28 Days

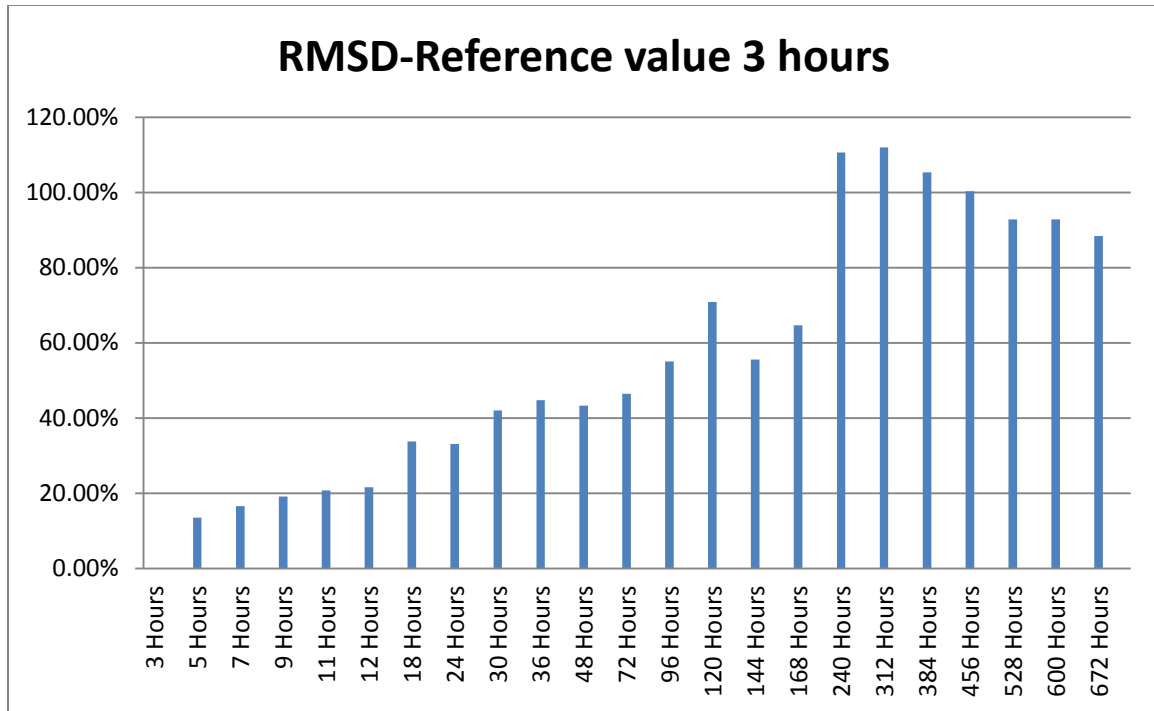


Chart 8.6 - RMSD chart for curing process of Beam 2 – Aggregate 10 (Reference value-3 hours)

8.5 Conclusions for monitoring of curing process

The trend observed in both techniques (surface bonded PZT patch and embedded PZT patch) is that the resonance peak of the PZT patch, which is in the area of 170-190 kHz, when bonded, it becomes stiffer and dampens in value depending on the quality of the bonding. The peak is now observed in the area of 210-280 kHz.

During the curing process, as the concrete becomes stiffer and the damping becomes smaller, the resonance peak of the PZT patch moves to the right (as the whole structure becomes stiffer) in both R_s and G_p plots, and the peak is getting sharper.

Changes are more easily visible near the resonance frequency of either the patch or the host structure. However changes also occur in the non-resonant frequencies with the area of 50-200 kHz being the area of interest as changes in the frequency plots in this bandwidth are due to changes in the host structure. The phenomenon of right hand shift of the - smaller for non resonant frequencies - peaks is also obvious in this bandwidth indicating the increase in stiffness (in this case, this behavior does not apply for all the smaller peaks that appear in the signature).

The monitoring of the curing process of the four specimens created for the needs of this master thesis, indicates the sensitivity of the method and the great attention needed throughout the whole procedure, as in some cases we encountered unexpected fluctuations in the results.

9 Damage Induction

This chapter describes the induction of damage in the specimens described in the earlier chapters. Specifically, in the first cube specimen damage was induced by drilling holes using a regular drill. The second cube specimen was subjected to cyclic compression load until failure using a compression machine. Finally the second beam specimen was subjected to cyclic bending until failure, using a bending machine.

9.1 Damage holes

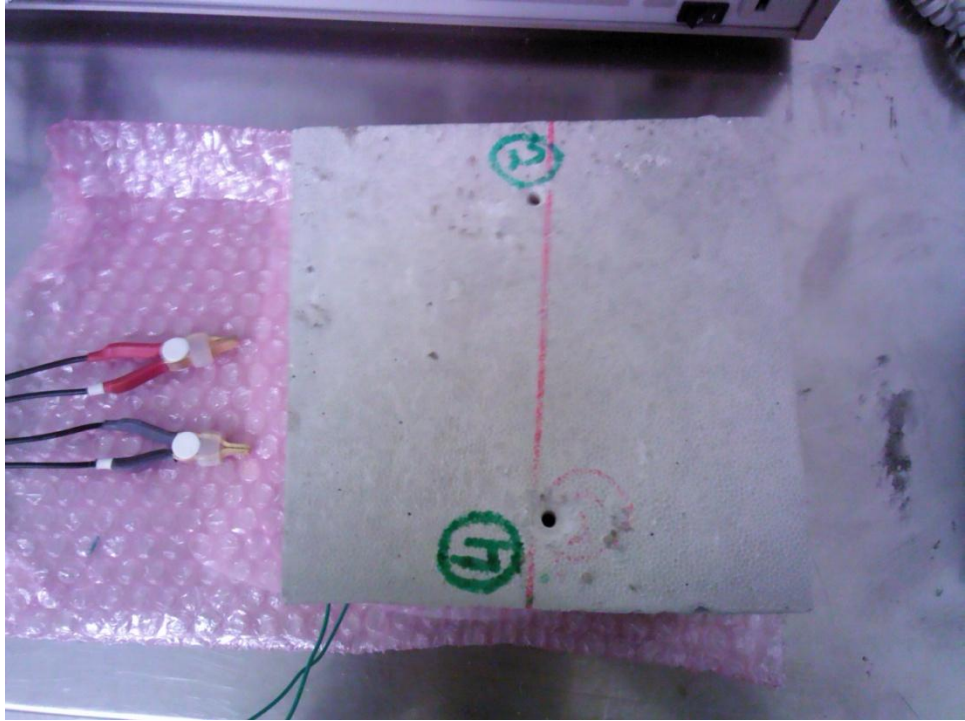
Damage was induced in cubic specimen 1 (created on 14/12/2012) by drilling holes on its surface. To create this damage, a rotary drill was used. Conventional methods of undisturbed cut of concrete could not be used as they involve soaking of the specimen that would affect the results of the measurements, as the PZT patches, even when protected by a layer of silicon, are very sensitive to moisture.

The use of the drill also meddled with the results. The energy that was transferred in the structure through the vibrations of the drill, made the short term measurements (directly after the drilling of the hole) unreliable. To overcome this obstacle, the measurements were taken 24 hours after the drilling of the hole.

The first step was the drilling of shallow, small diameter holes near the acmes of the cube. Specifically, seven holes were drilled with 25 mm distance from the acmes, two in each side of the cube except the side where the cables ran through (see pictures below). For the creation of these holes, a drill of 4.5 mm diameter and 47 mm working length was used. The first measurement was taken for a damaged state of these 7 holes.



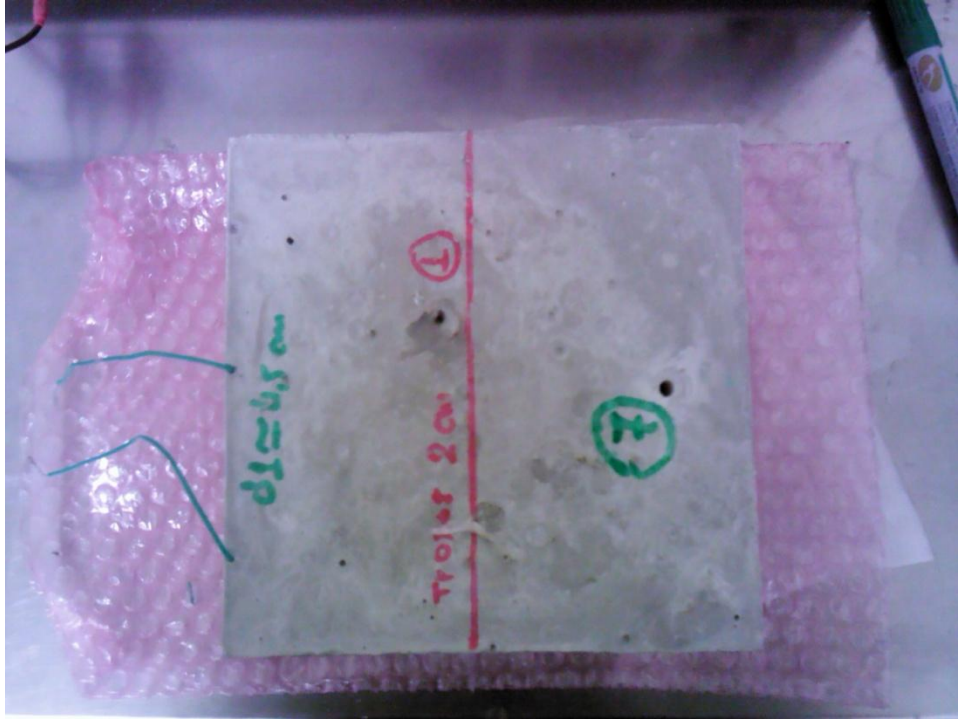
Picture 9.1 Damage holes 1,3



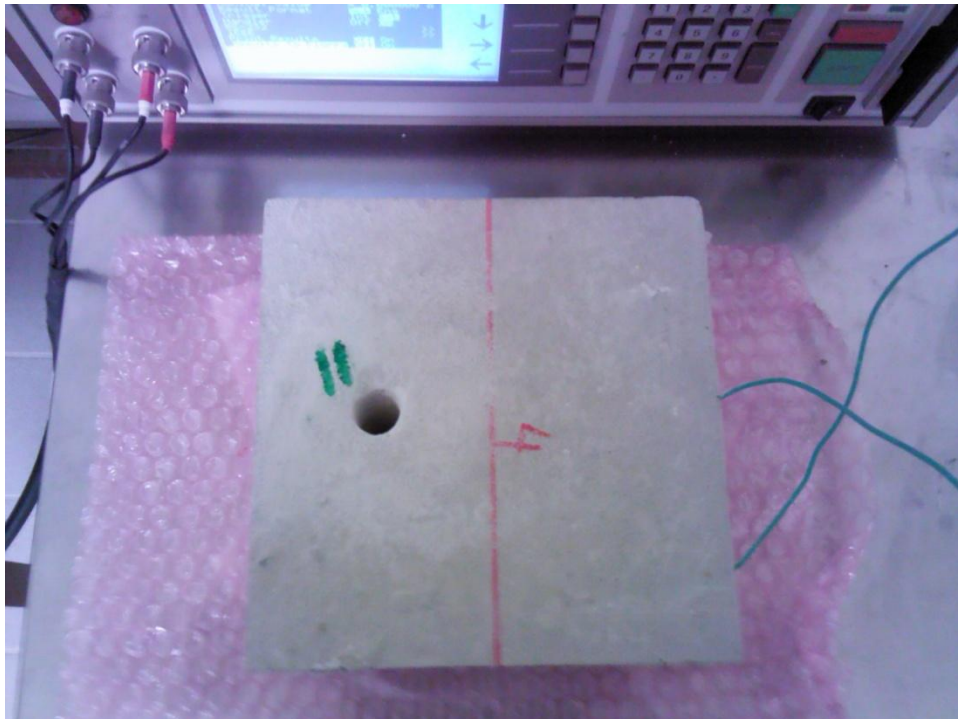
Picture 9.2 Damage holes 2,4



Picture 9.3 Damage holes 5,6

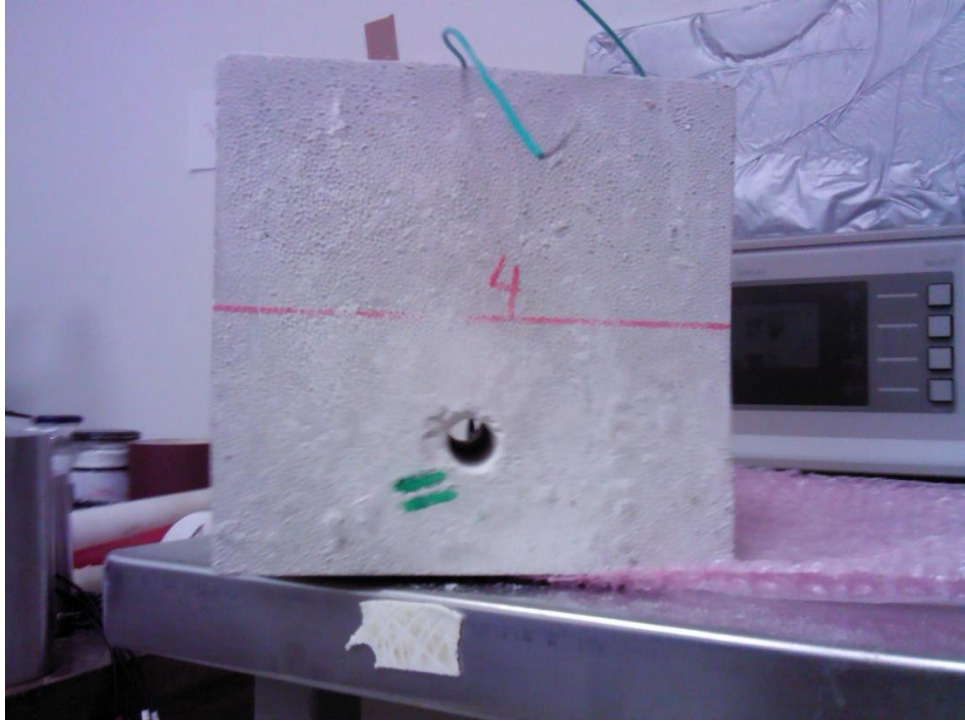


Picture 9.4 Damage hole 7

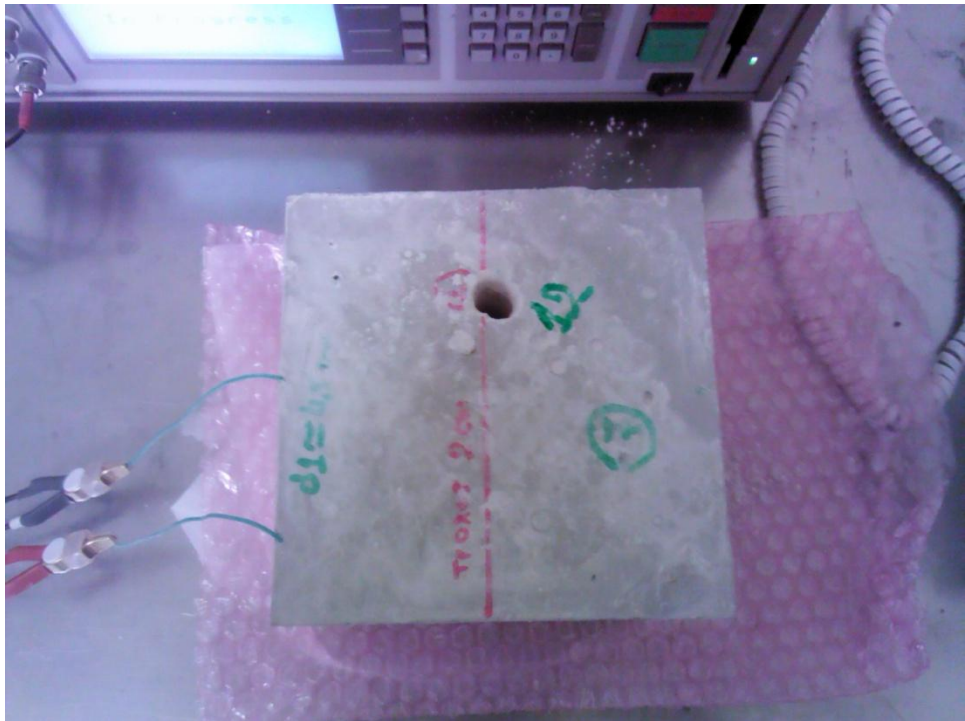


Picture 9.5 Damage hole 11

The next measurement was taken after inducing damage hole 11 (see figure 5.1.5). This hole, as well as damage hole 12, was end to end and was created using a 14 mm drill.

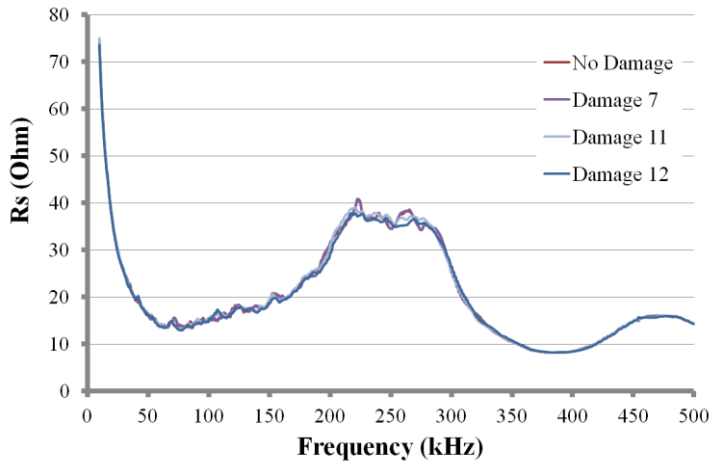


Picture 9.6 Damage holes 11

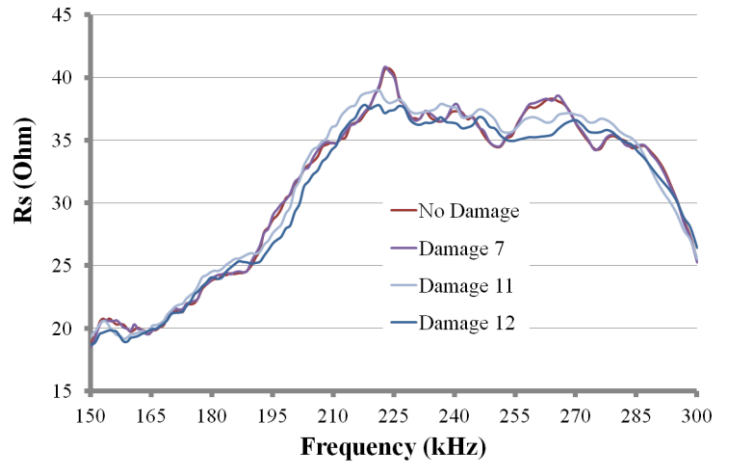


Picture 9.6 Damage holes 12

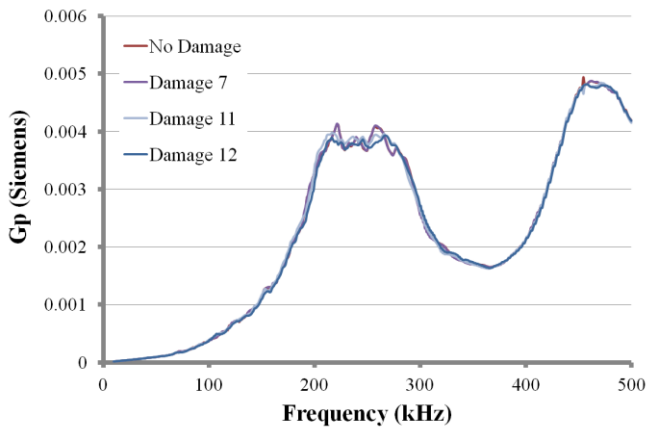
The results of the measurements are the following:



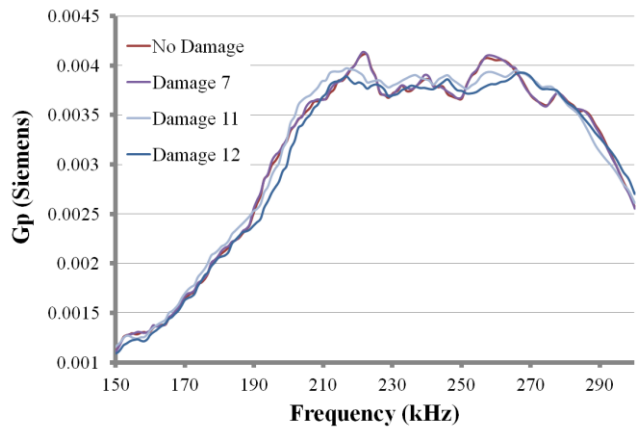
(mmmm)



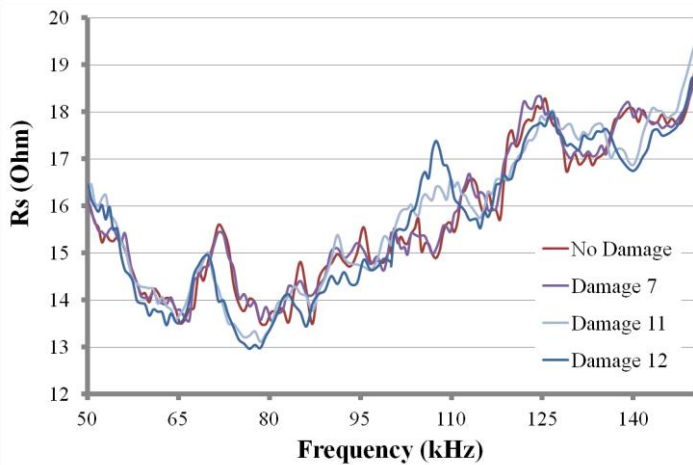
(nnnn)



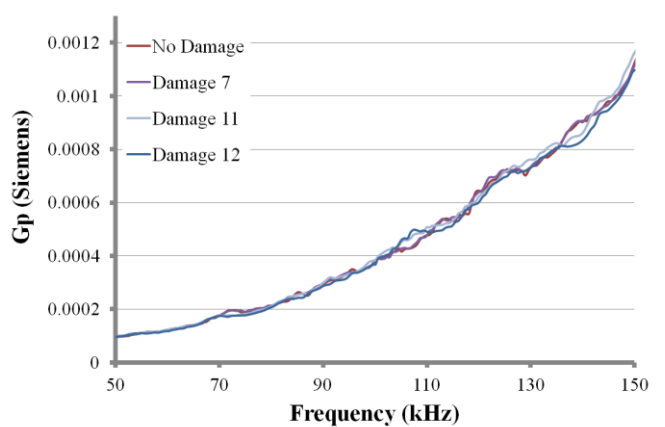
(oooo)



(pppp)



(e)



(f)

Plots 9.1 – (a) Resistance plot 0-500 kHz (b) Resistance plot 150-300 kHz
(c) Conductance plot 0-500 kHz (d) Conductance plot 150-300 kHz
(e) Resistance plot 50-150 kHz (f) Conductance plot 50-150 kHz

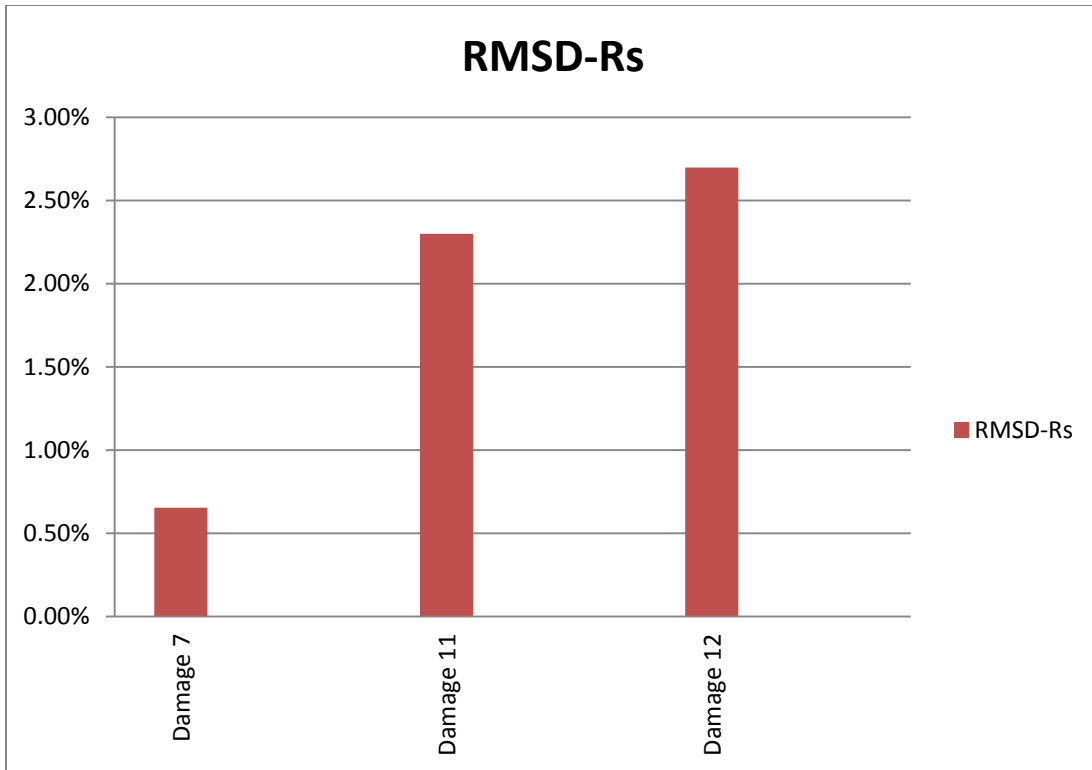


Chart 9.1 - RMSD (Rs) chart for damage different cases – Cube 1

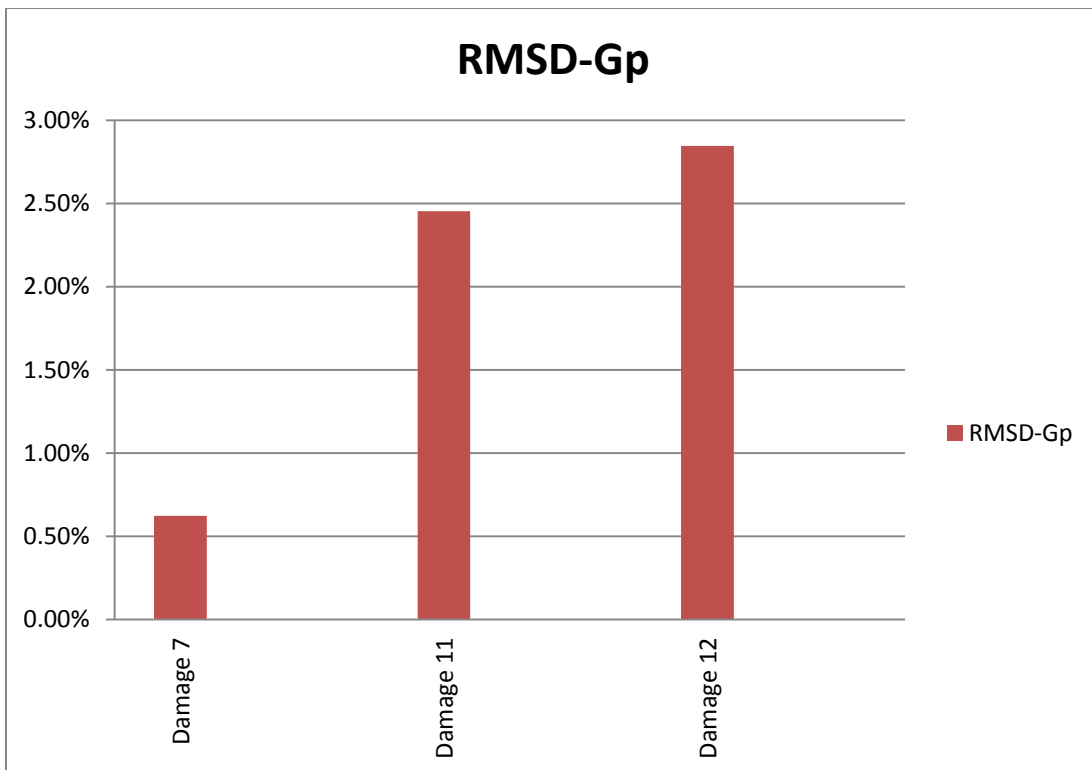
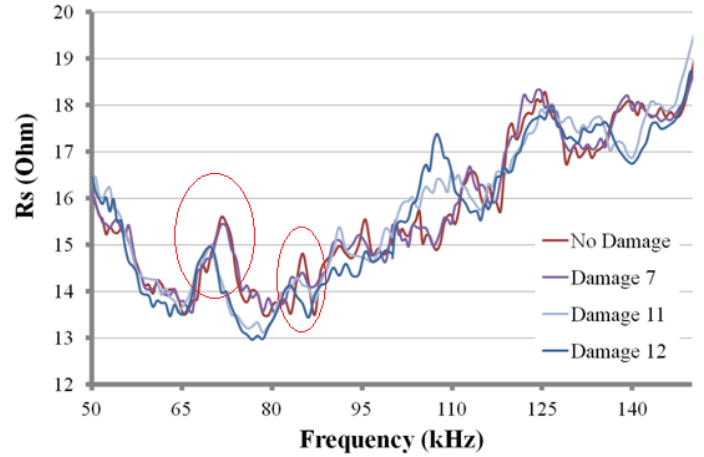
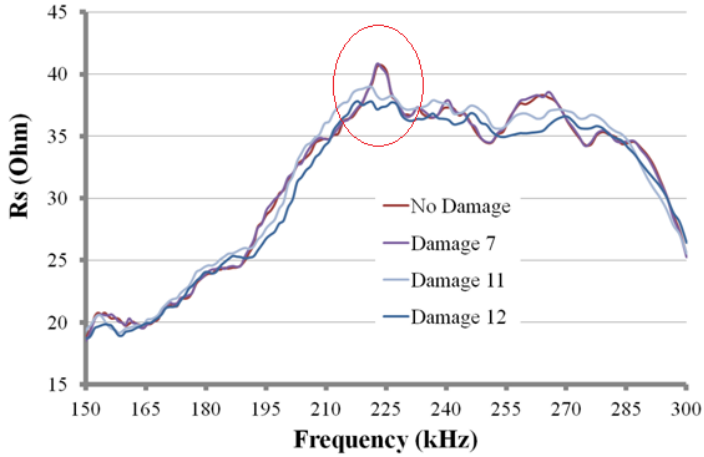


Chart 9.2 - RMSD (Gp) chart for damage different cases – Cube 1

Although the RMSD values were not the ones expected given the extent of the damage, however the difference in the signatures is quite obvious. Additionally, the changes in the signatures are the ones expected, i.e. left hand shift of the resonance peak, indicative of the loss in stiffness (see plots below).



(a)

(b)

Plots 9.2 – (a) Resistance plot 150-300 kHz (b) Resistance plot 50-150 kHz

9.2 Compression

For the purposes of this test, cubic specimen 2 (created on 24/4/2013) was subjected to cyclic compression until failure (experimental setup shown in figure 5.2.1). Measurements were taken after each cycle, as by the end of each cycle a different damage level exists in the structure. The compression rate of the cube was 0.5 kN/sec until the first predetermined load, which was for the 1/3 of the expected failure stress. It was then unloaded, and the first measurements to obtain the signatures were made. Then the cube was loaded to the next level of load and the signatures were once more acquired after unloading. The same procedure was repeated until failure.

To determine the failure stress, four more cubic specimens of the same mixture were made and were compressed until failure. One of those was left to cure in dry conditions, and the rest were cured in water. So the expected failure stress was roughly the average of the four, i.e. 23.4 MPa. The step between the cycles was approximately 0.5-2 MPa.

Specimen No	Failure Load (kN)	Failure Stress (MPa)
1 (Cured in dry conditions)	472.4	21.0
2 (Cured in water)	496.7	22.1
3 (Cured in water)	529.8	23.5
4 (Cured in water)	607.3	27.0
Average	526.55	23.4

Table 9.1 – Compression test results for cubic specimens of the same mix

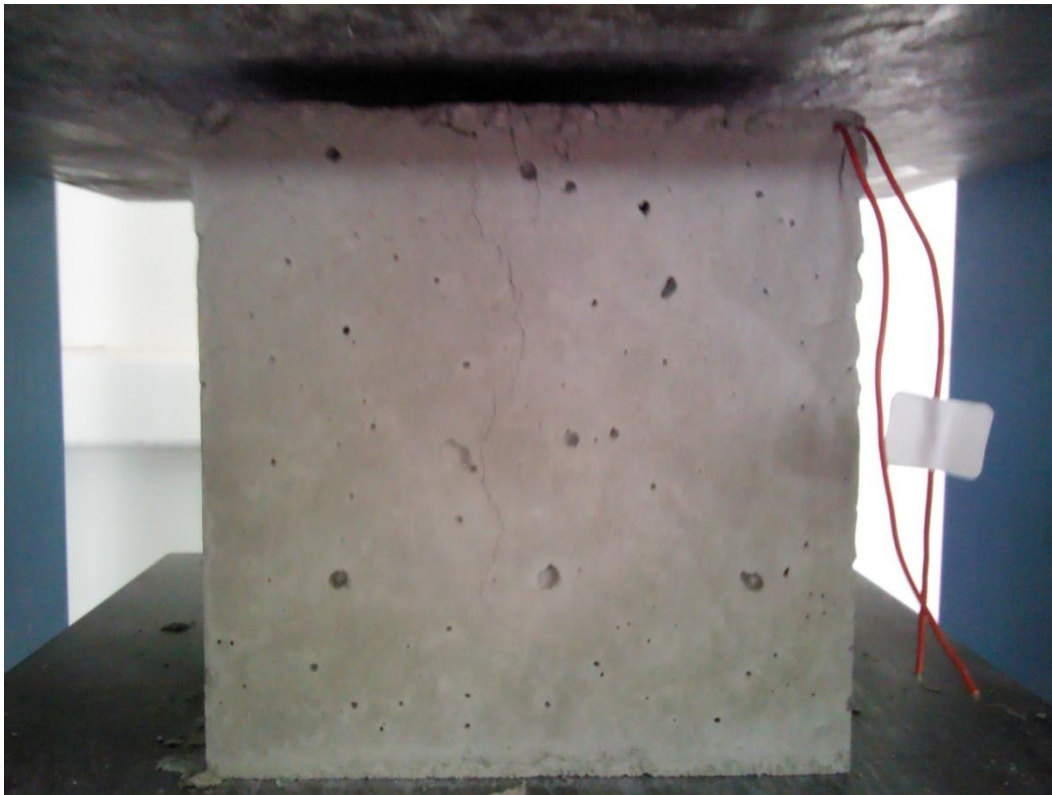


Picture 9.7 Experimental setup

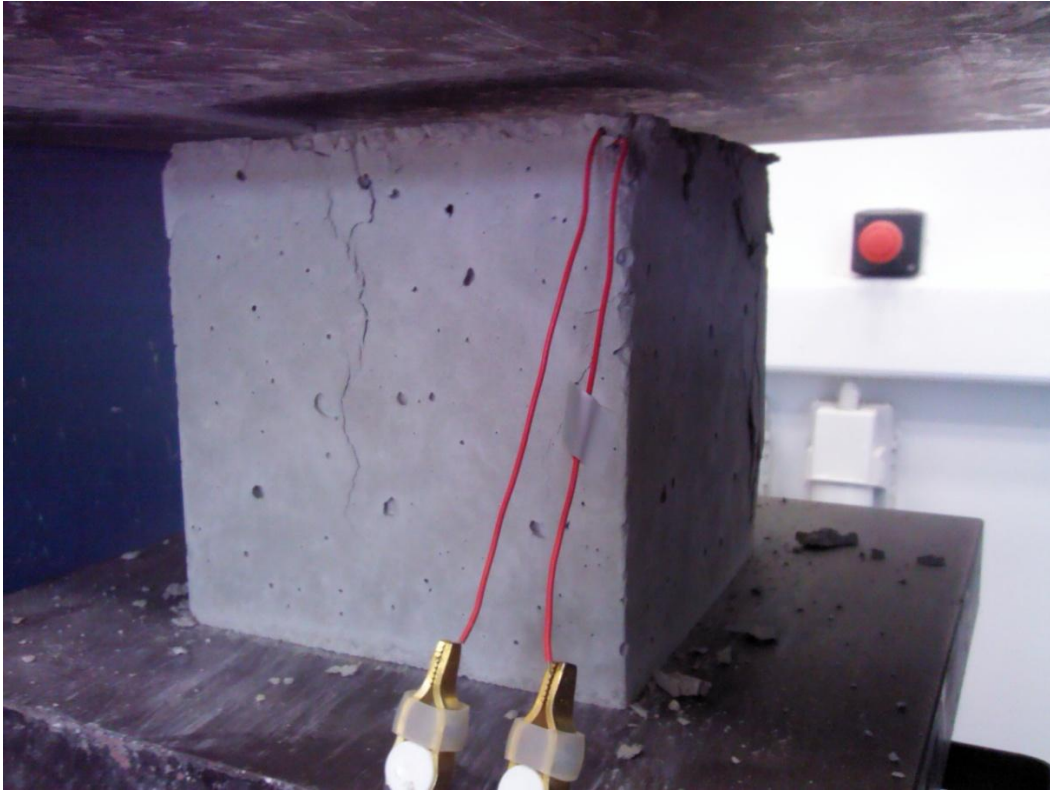
The following table presents the different load cases for each cycle. As expected due to the cyclic nature of the load, the failure stress was a little lower than the expected derived from the average.

Cycle No	Load (kN)	Stress (MPa)
Cycle 1	161.9	7.2
Cycle 2	181.4	8.1
Cycle 3	190.4	8.5
Cycle 4	202.1	9.0
Cycle 5	208.8	9.3
Cycle 6	220.0	9.8
Cycle 7	233.1	10.4
Cycle 8	256.4	11.4
Cycle 9	281.0	12.5
Cycle 10	301.9	13.4
Cycle 11	319.9	14.2
Cycle 12	337.7	15.0
Cycle 13	366.4	16.3
Cycle 14	406.3	18.1
Cycle 15	451.0	20.1
Cycle 16 (Failure)	430.4	19.1

Table 9.2 – Load cycles



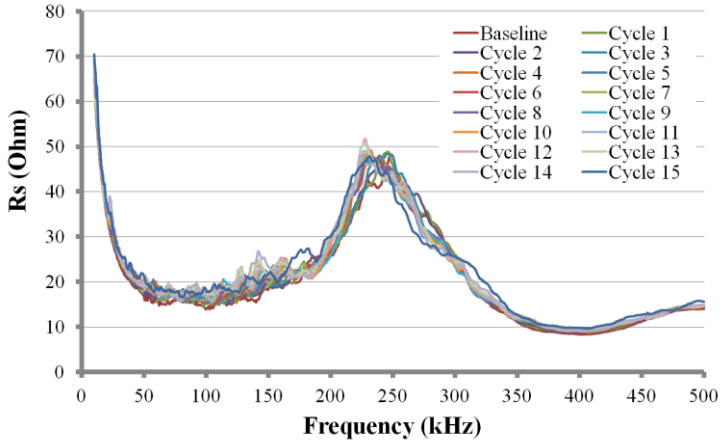
Picture 9.8 – Appearance of the first cracks (Cycle load 7)



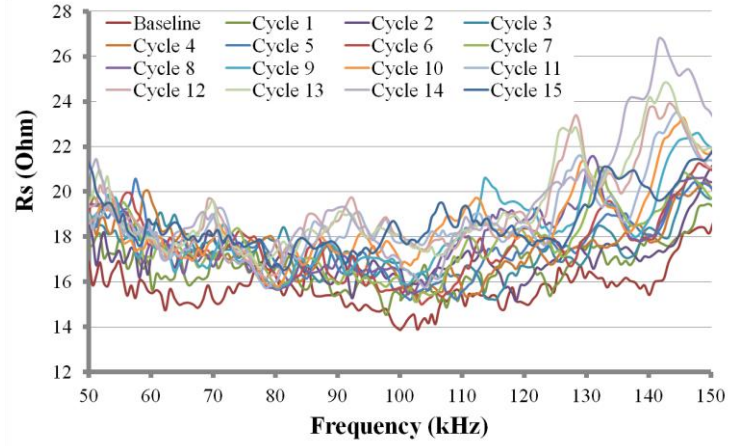
Picture 9.9 – Cycle load 15



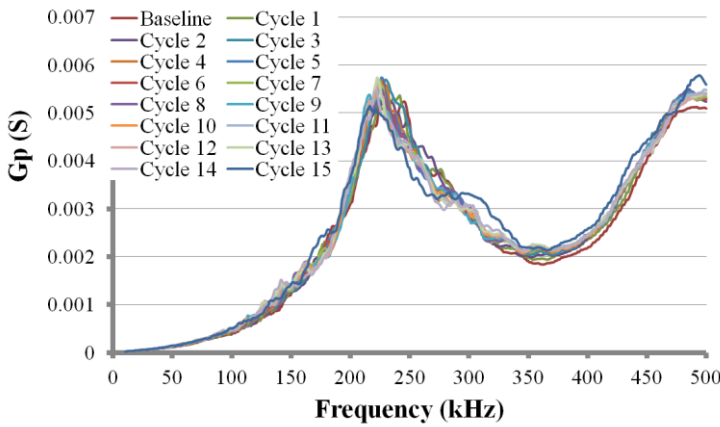
Picture 9.10 – Cycle load 16 (Failure)



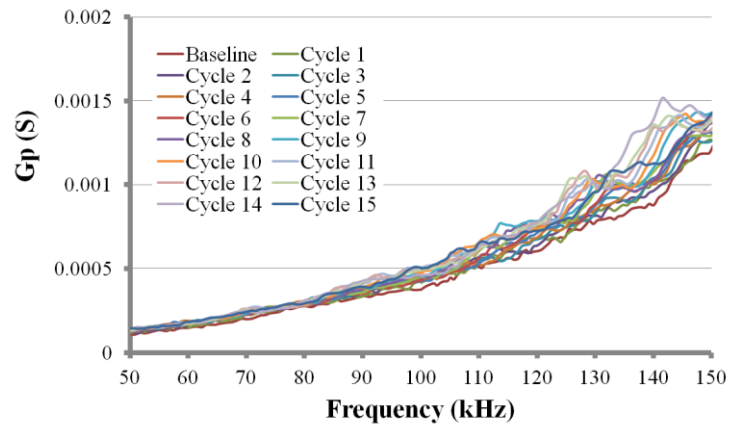
(qqqq)



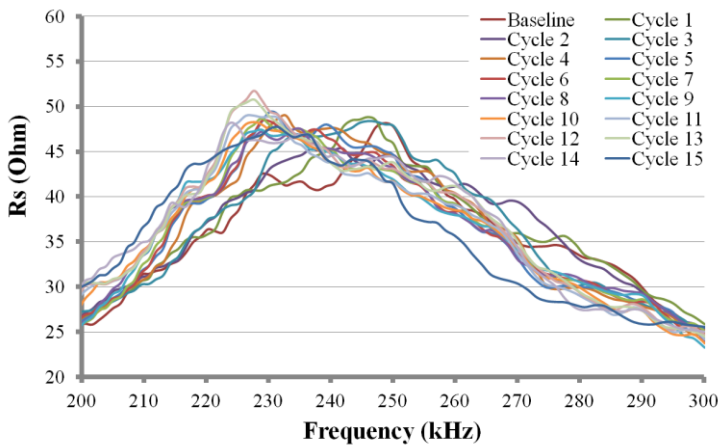
(rrrr)



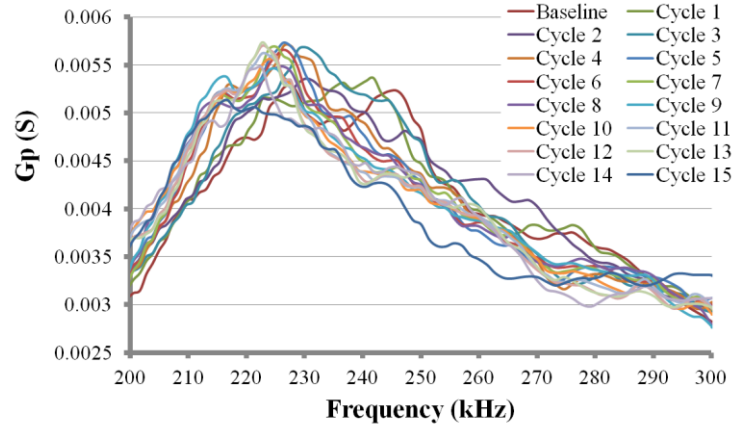
(ssss)



(tttt)



(e)



(f)

Plots 9.3 – (a) Resistance plot 0-500 kHz (b) Resistance plot 50-150 kHz
 (c) Conductance plot 0-500 kHz (d) Conductance plot 50-150 kHz
 (e) Resistance plot 200-300 kHz (f) Conductance plot 200-300 kHz

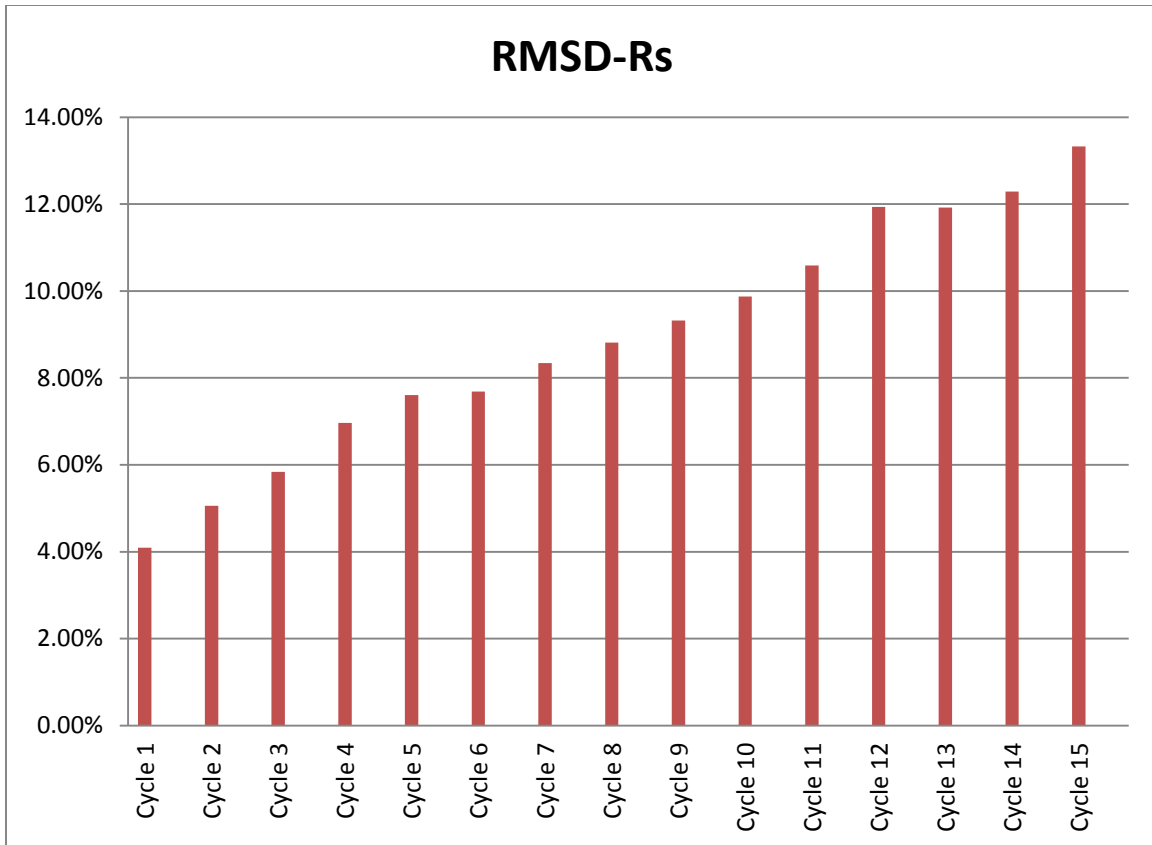
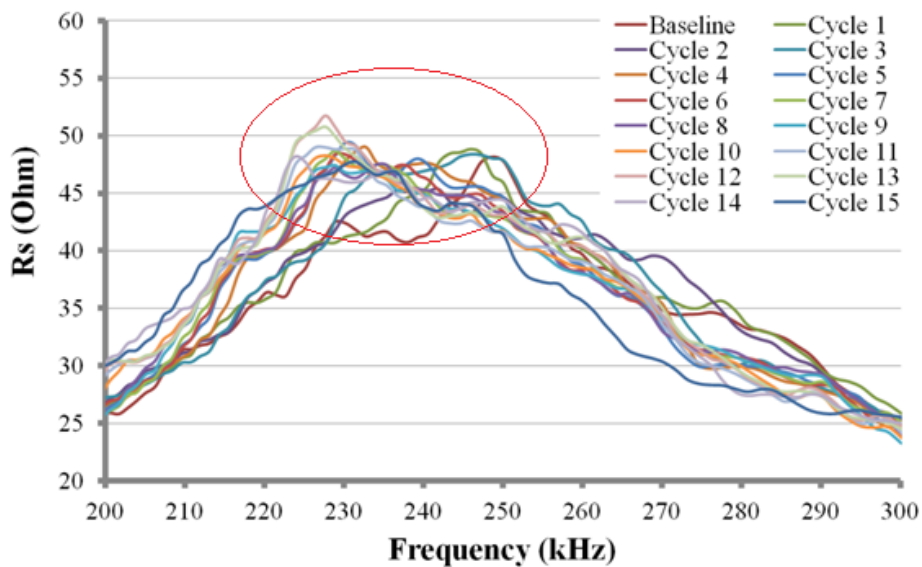


Chart 9.3 - RMSD chart – Compression of Cube 2

Observing the results, we can easily see that there is a steady, almost linear increase in the RMSD value as damage increases. There is also a clear left hand shift of the resonance peak indicating loss of stiffness (with some minor fluctuations as we can see in the chart)



Plot 9.4 – Resistance plot 200-300 kHz

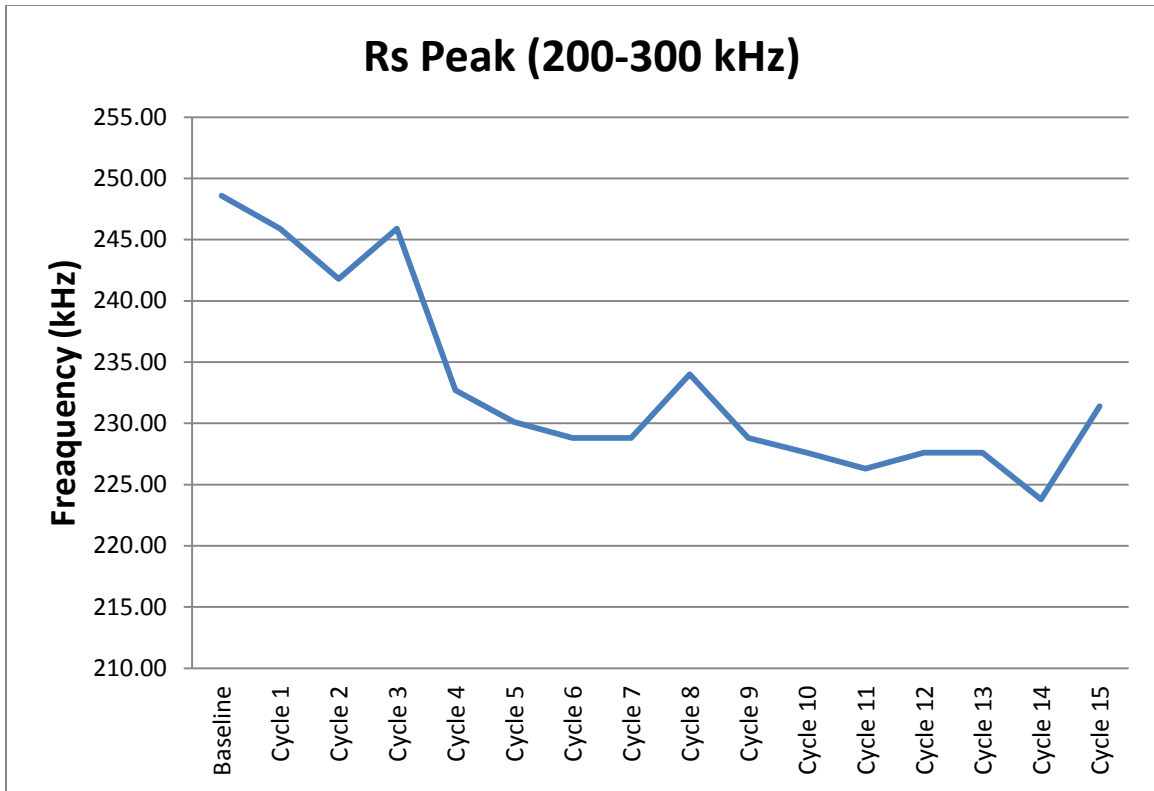


Chart 9.4 – Frequency of the resonance peak for different loads

9.3 Bending

For the purposes of this test, the second beam specimen (created on 24/4/2013) was subjected to cyclic, three point bending test until failure. Measurements were taken after each cycle, as by the end of each cycle a different damage level exists in the structure. It was then unloaded, and measurements to obtain the signatures were made. Then the beam was loaded to the next level of load and the signatures were once more acquired after unloading. The same procedure was repeated until failure. Given the dimensions of the beam and the set up, failure was expected for a load of approximately 20 kN. The first load was for 6.49 kN and the following were with step of 2-4 kN.

Cycle No	Load (kN)
Cycle 1	6.49
Cycle 2	10.07
Cycle 3	12.57
Cycle 4	14.87
Cycle 5	18.47

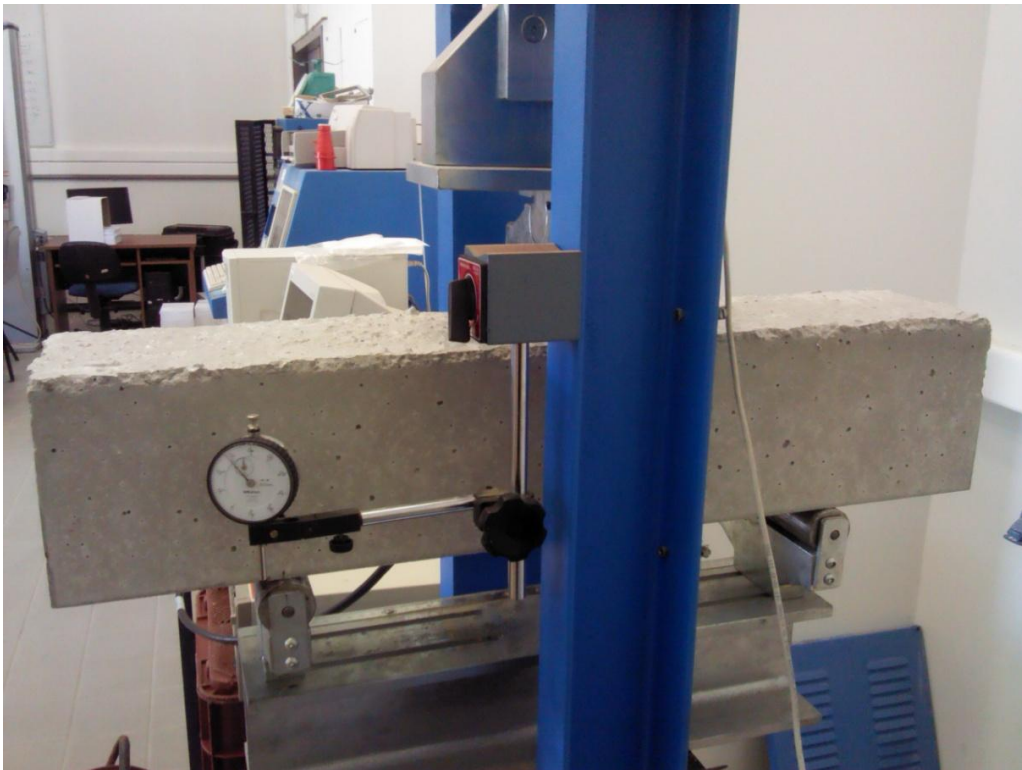
Table 9.3 – Loading cycles



Picture 9.11 – Experimental set up



Picture 9.12 – Experimental set up



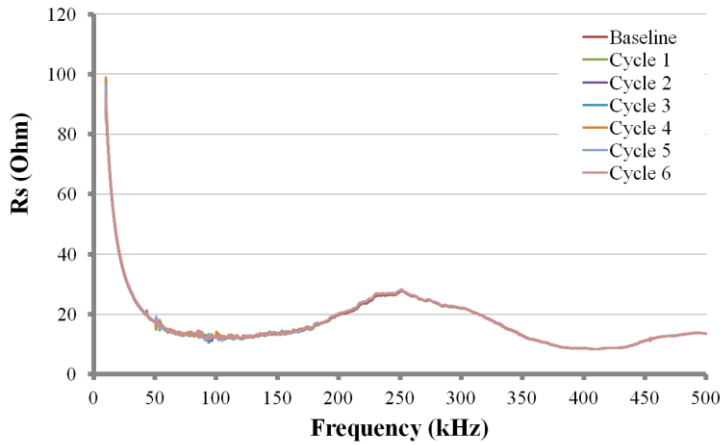
Picture 9.13 – Experimental set up



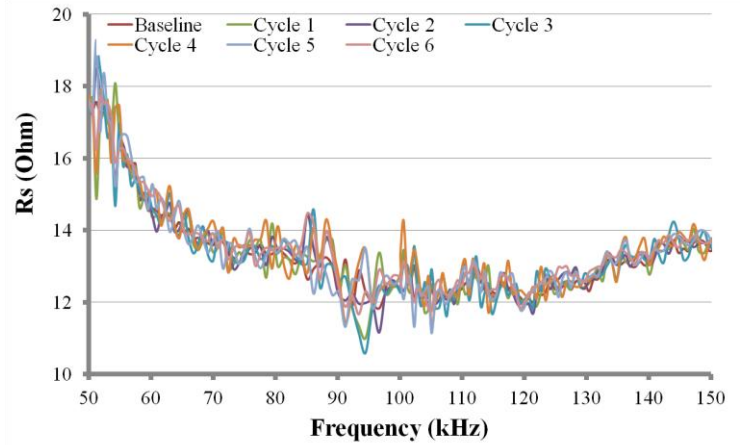
Picture 9.14 – Experimental set up

As mentioned in earlier chapters the smart aggregates were located 11 cm from the center of the beam. This made the test useless as the damage that occurred in the center of the beam was undetectable by both sensors. The results are presented in the following pages.

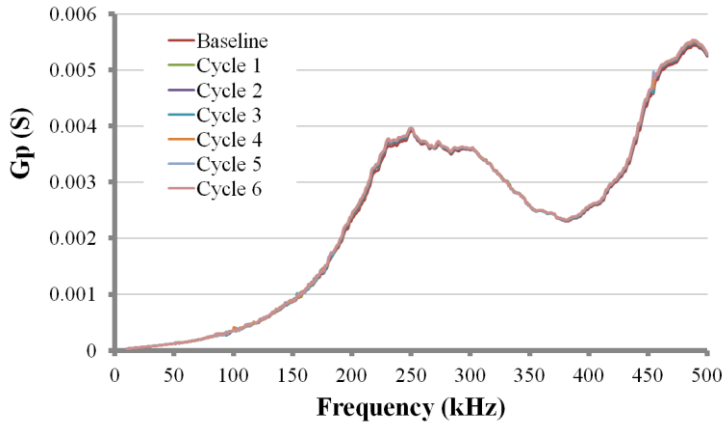
9.3.1 Aggregate 10



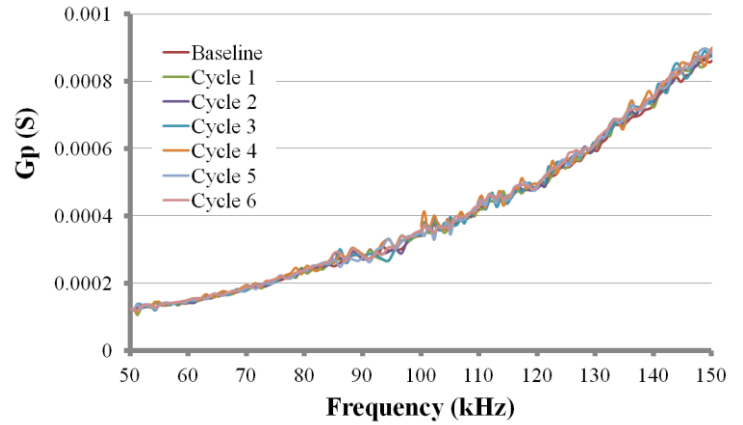
(a)



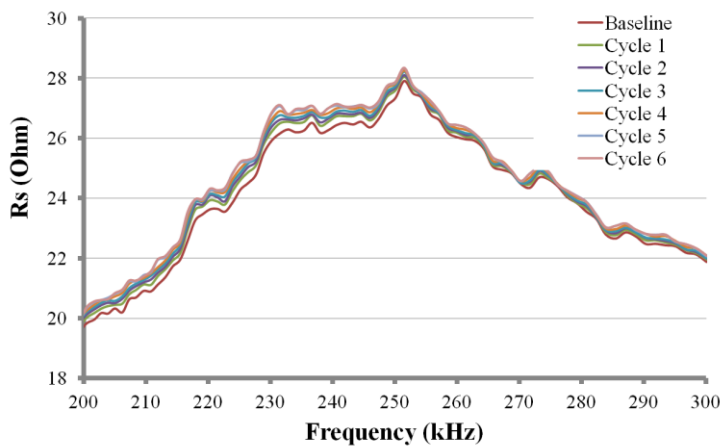
(b)



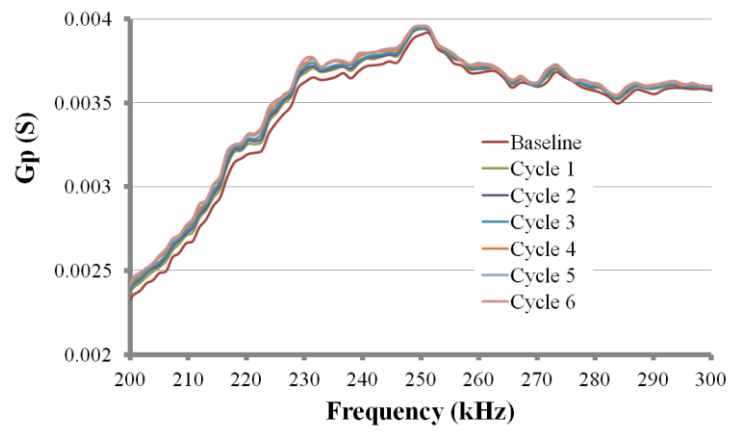
(c)



(d)



(e)



(f)

Plots 9.5 – (a) Resistance plot 0-500 kHz (b) Resistance plot 50-150 kHz (c) Conductance plot 0-500 kHz (d) Conductance plot 50-150 kHz (e) Resistance plot 200-300 kHz (f) Conductance plot 200-300 kHz

The results are indicative of the small range of the PZT patches in high attenuation materials like concrete. A crack occurred for load 5 in the center of the beam which was widened with load 6 (see pictures below). However no difference is observed in the plots as the damage is out of range. It is reminded that a PZT patch attached to concrete has an effective area that can be roughly and oversimplifying represented as a sphere of 5 cm radius. So in this case the damage is way off range. The differences in the RMSD chart are not accounted for the different damage scales, as they do not follow the degree of damage, like in the case of the compression test.

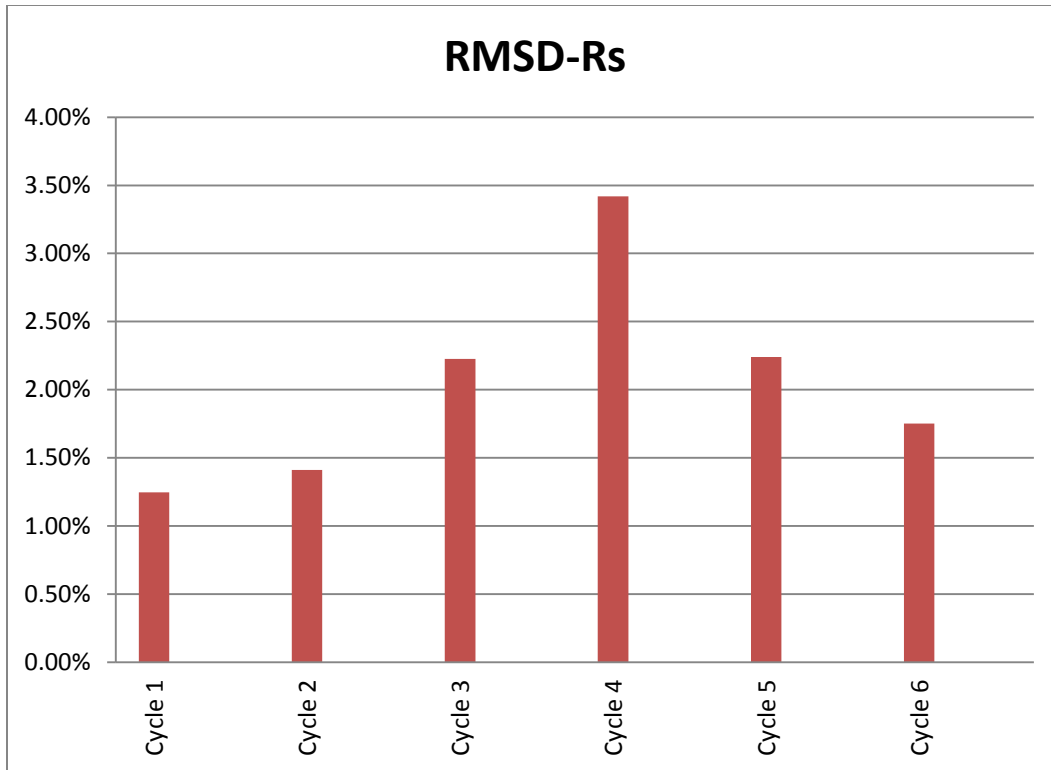
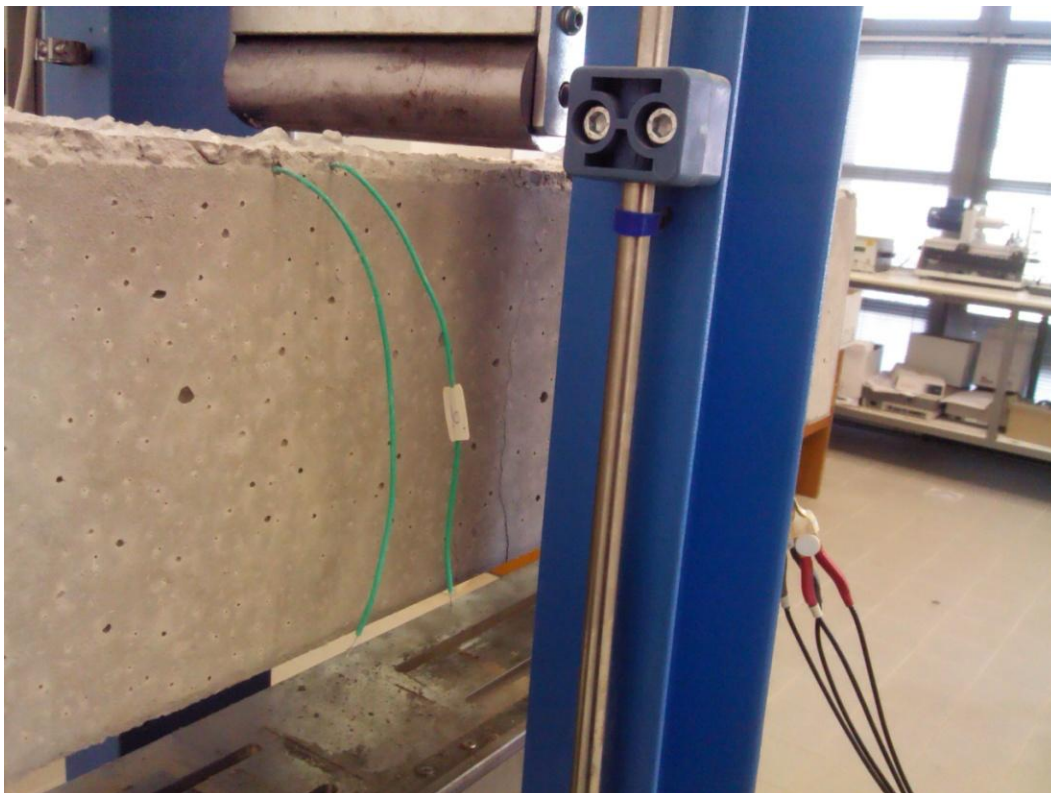


Chart 9.5 - RMSD chart – Bending of Beam 2 – Aggregate 10

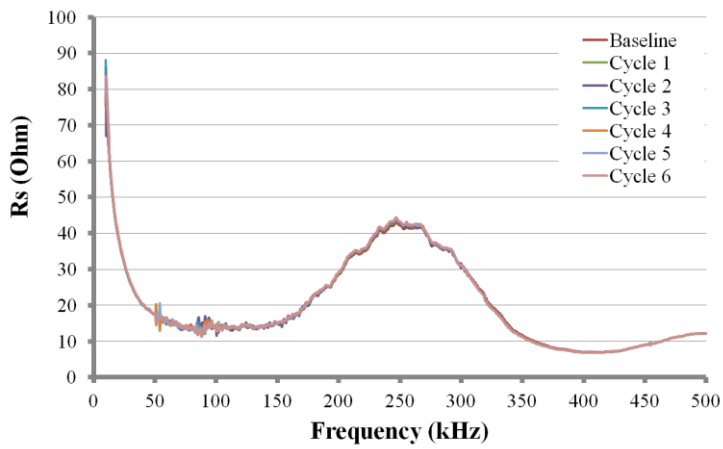


Picture 9.15 Crack occurred for load 5

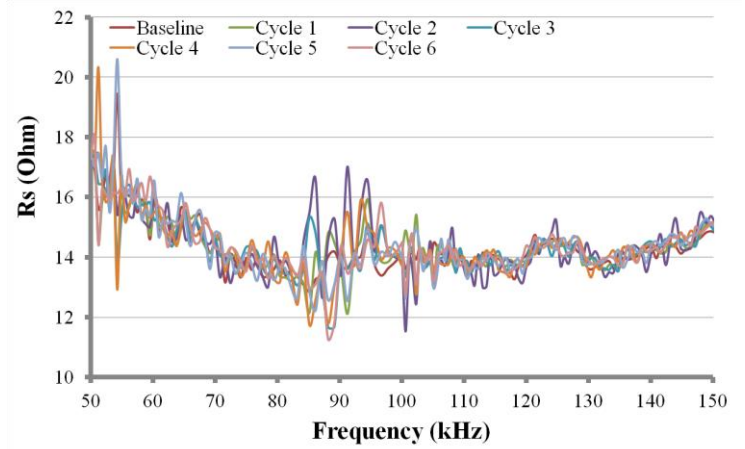


Picture 9.16 Crack occurred for load 6

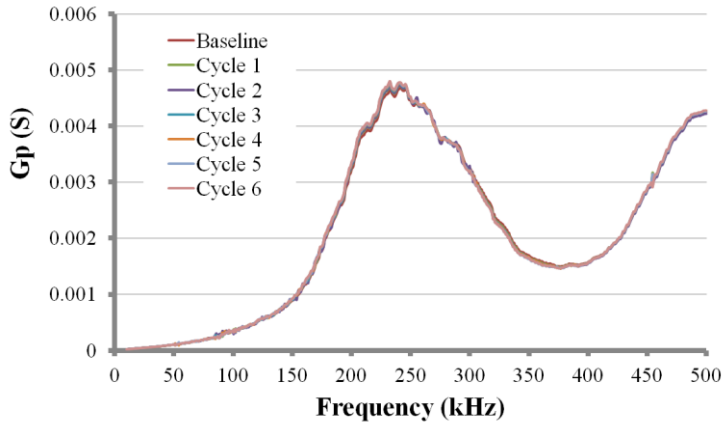
9.3.2 Aggregate 11



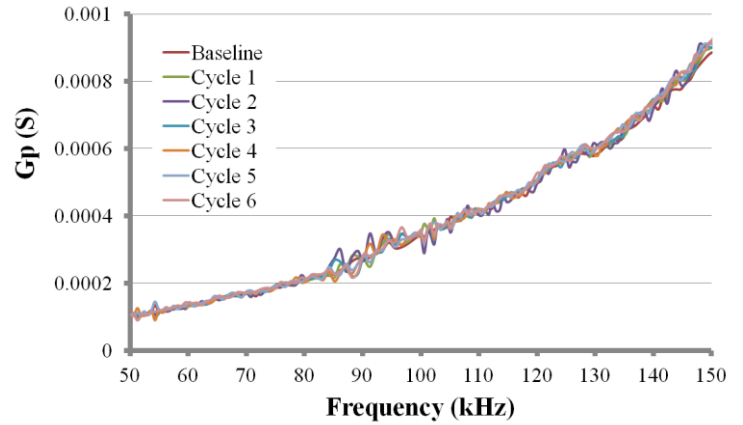
(a)



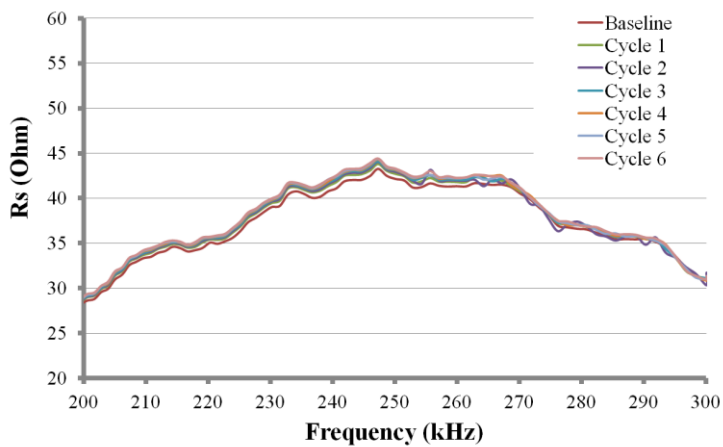
(b)



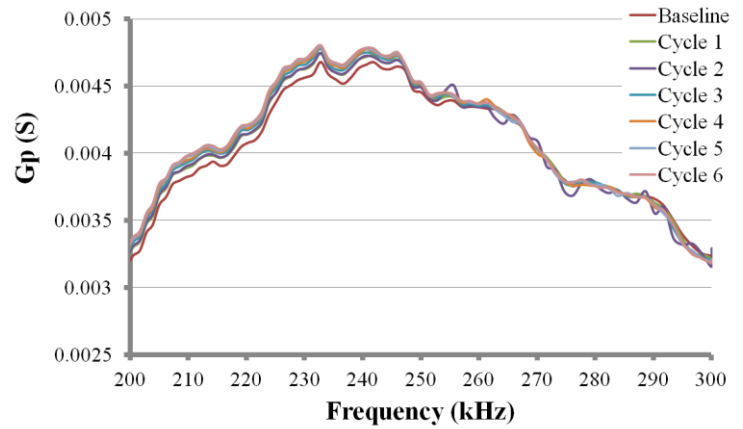
(c)



(d)



(e)



(f)

Plots 9.5 – (a) Resistance plot 0-500 kHz (b) Resistance plot 50-150 kHz (c) Conductance plot 0-500 kHz (d) Conductance plot 50-150 kHz (e) Resistance plot 200-300 kHz (f) Conductance plot 200-300 kHz

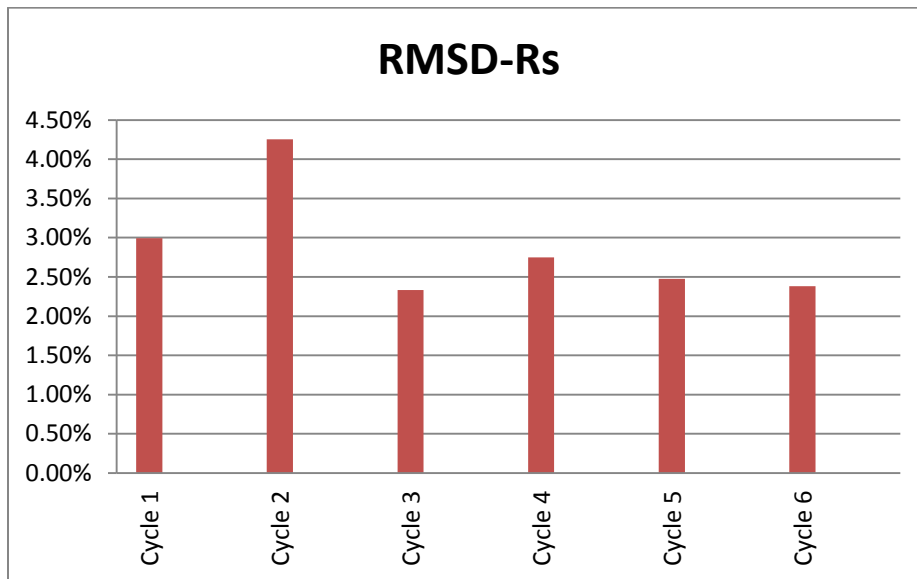


Chart 9.6 - RMSD chart – Bending of Beam 2 – Aggregate 11

9.3.3 Custom-made admittance measuring system to increase sensing area

For carrying out electrical admittance measurements various commercial admittance analyzer instruments could be used. Alternatively, the recently proposed miniaturized chip-based AD-5933 impedance converter network analyzer has been implemented to various applications. Unfortunately, such chip-based solution presents limited capabilities to concrete material-based structure monitoring applications since AD-5933 based measurements are suffering by a narrow frequency range (up to 100 kHz).

In order to measure admittance applying higher voltage than 2 volts that can be applied using commercial impedance analyzer (and thus expand the sensing area of the patch), the I-V methodology across the PZT poles is used. The unknown admittance is calculated via measured values of voltage and current. Current is calculated by using the voltage measurement across an accurately known low value calibrated resistor Ref (say 100 Ω). The set up used is shown in figure 5.5.1 below.

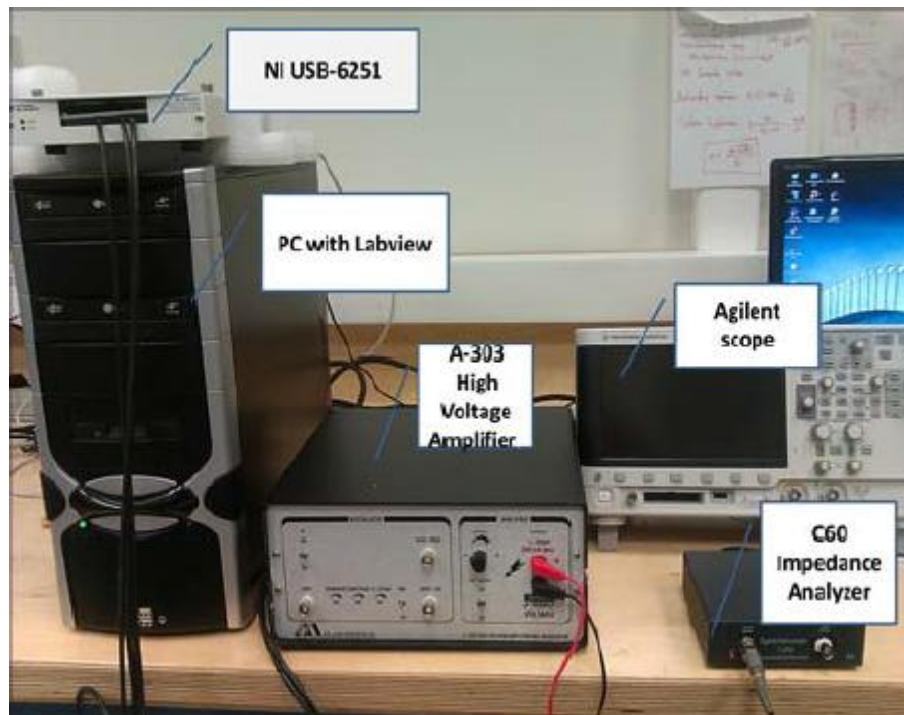


Figure 9.1 Experimental arrangement [5] (C. Providakis, K. Stefanaki, M. Voutetaki, J. Tsompanakis, M. Stavroulaki and J. Agadakos, *An Integrated Approach for Structural Health Monitoring of Concrete Structures Based on Electromechanical Admittance and Guided Waves*)

To excite the PZT, a National Instruments USB-6251 high-speed M series multifunction data acquisition (DAQ) module is utilized and optimized for accuracy at fast sampling. This DAQ card contains analog-to-digital (ADC) and digital-to-analog (DAC) converters with 1.25 MSamples/sec speed and 16-bit resolution. The excitation voltage V_{in} is of sinusoid-type having an amplitude of $|V_{in}|$ and a frequency sweeping from F_{start} to F_{end} (say 10kHz to 350kHz). A two-channel Agilent 2000X oscilloscope was used to record simultaneously the time history of voltage $V_{in}(t)$ at one of

the output channels of the USB-6251 card and the time history of voltage drop $V_{out}(t)$ on the calibrated resistor Ref. The time history of the current $I(t)$ flowing through the PZT also flows through the resistor Ref. The time history of current $I(t)$ can be calculated as $I(t)=V_{out}(t)/Ref$. Hence, the PZT admittance Y is calculated using an expression of the type [5]:

$$Y(t) = \frac{I(t)}{V(t)} = \frac{V_{out}(t) \cdot (1/Ref)}{V_{in}(t) - V_{out}(t)}$$

By Fourier transforming the above time domain equation to yield the frequency domain quantities $I(i\omega)$ and $V(i\omega)$, the admittance of PZT may be calculated as the transfer function of PZT [5]:

$$Y(i\omega) = \frac{I(i\omega)}{V(i\omega)}$$

Hence the complex admittance of the PZT is

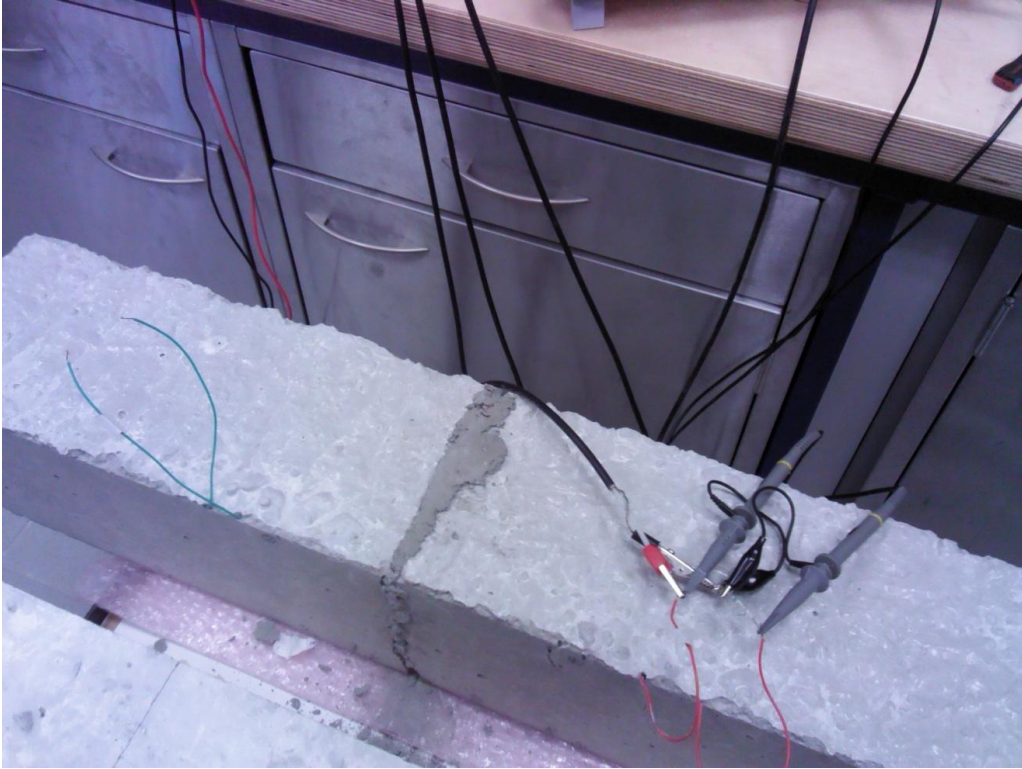
$$Y = \frac{FFT(V_{out}(t) \cdot (1/Ref))}{FFT(V_{in}(t) - V_{out}(t))} = G + j \cdot B$$

where, $FFT\{\}$ designates fast Fourier transform and G is the real part (conductance) and B the imaginary part (susceptance) of the complex admittance. With this approach, the admittance spectrum of an investigated specimen can be acquired even within one wideband excitation signal sweeping.

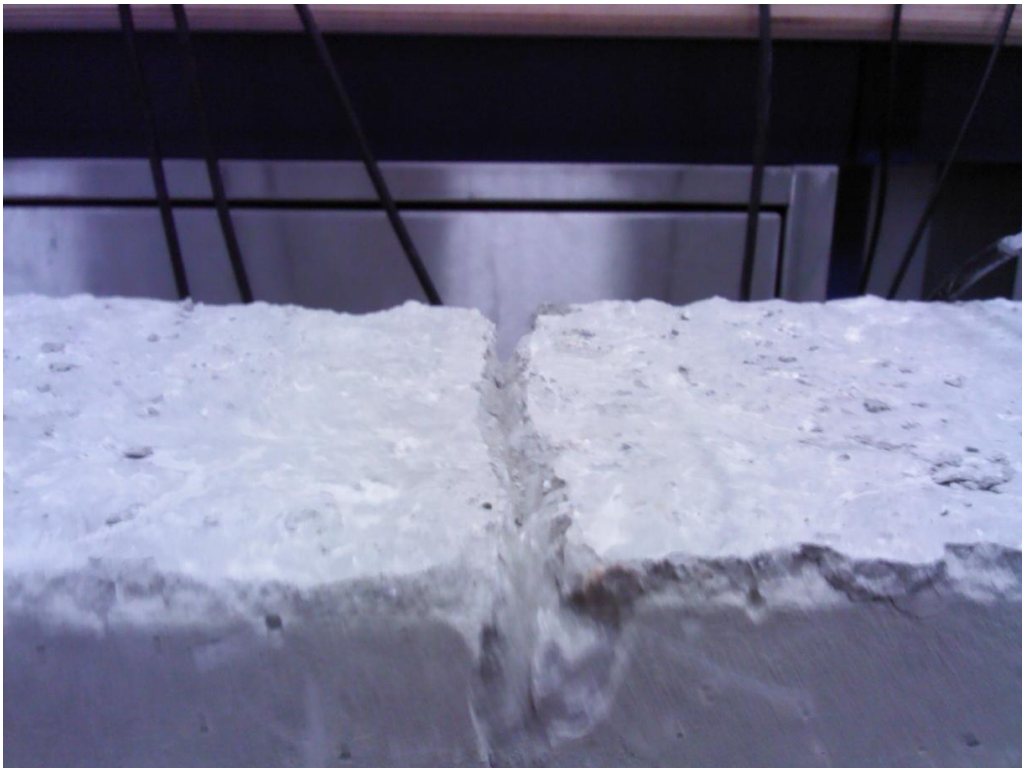
To achieve such a wide band excitation signal sweeping, a digitally synthesized linear chirp signal is generated ($F_{start}=10000$ kHz, $F_{end}=200000$ kHz, $F_s=1$ MHz sample rate, 500 samples) by using Labview Signal Express program and then transmitted to the admittance measuring circuit by the output channel of USB-6251 card. The actual excitation voltage V_{in} and the response of the PZT, V_{out} , were recorded synchronously by the two-channel BNC input port of Agilent 2000X oscilloscope. The admittance spectrum of the PZT equals FFT of the response signal over the FFT of the excitation signal according to the last equation.

9.3.3.1 Experimental results

In order to test the proposed set up described in 5.3.3, beam specimen 2 that was used in the bending test was repaired using low w/c ratio cement paste. A baseline measurement was taken for the repaired beam before introducing any damage. Then measurements were taken changing the degree of contact between the two repaired members (and thus changing the structure, introducing a joint in the middle) using a hammer and a chisel.



Picture 9.17 Repaired beam-Baseline measurement



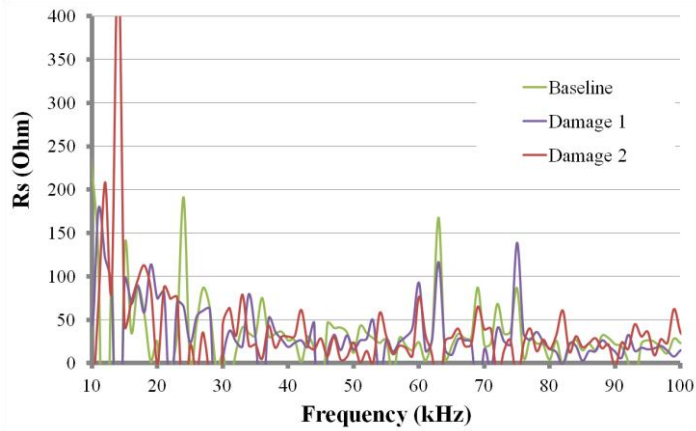
Picture 9.18 Damage 1



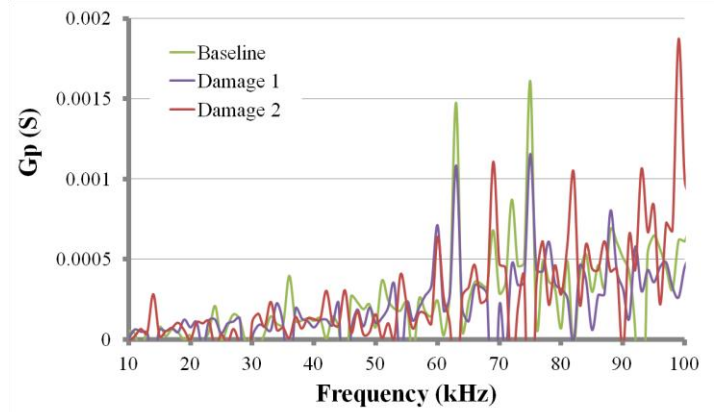
Picture 9.19 Damage 2-Detachment of the cement paste layer (failure)

Unfortunately, as expected, collapse came very quickly due to impact with the hammer measuring only 2 damage cases. The test was carried out with the repaired beam due to inability to create a new beam specimen due to lack of time. The results were promising, like in previous papers published by the Applied Mechanics Lab of Technical University of Crete [5] only this time the change in the dynamic characteristics of the structure was done through damage rather than applying masses on the structure.

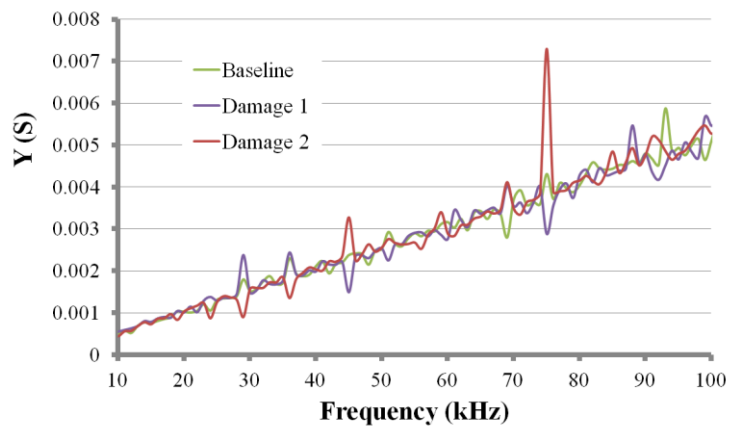
The results shown below are for a bandwidth of 10-100 kHz, as in order for the circuit to be stable and functional in higher frequencies a different reference resistance is needed.



(a)

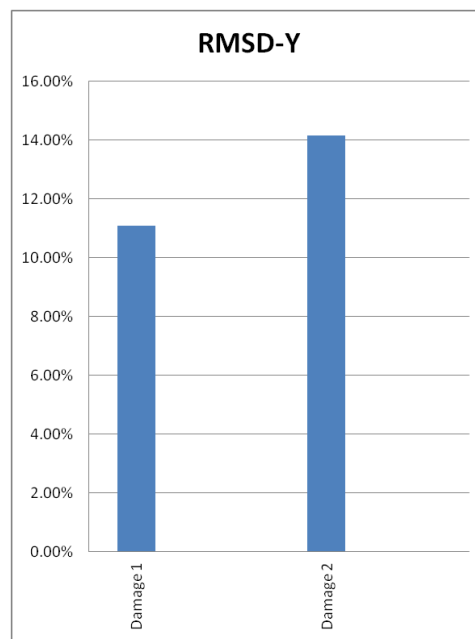
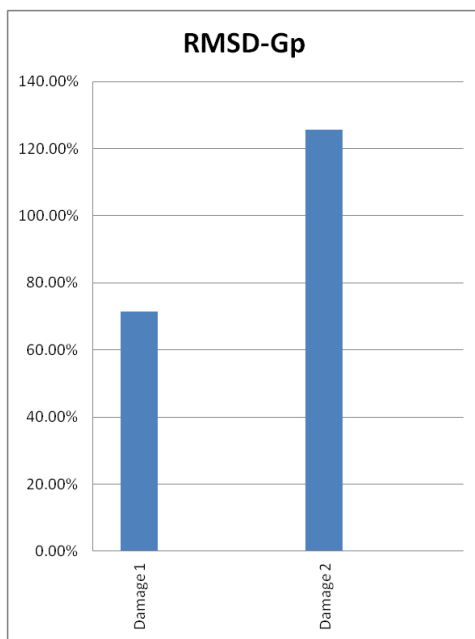


(b)



(c)

Plots 9.6 – (a) Resistance plot 0-100 kHz (b) Conductance plot 0-100 kHz (c) Admittance magnitude plot 0-100 kHz



Plot 4 – RMSD plots

9.4 Conclusions for damage detection

The applicability of EMI technique using embedded smart aggregates for damage detection purposes is well demonstrated by the series of experiments carried out for this master thesis. The trend observed is that the resonance peak of the PZT patch, which is in the area of 220-250 kHz for the baseline pristine state shifts to the left indicating loss of stiffness, in both damage induction by drilling holes as well as by cyclic compressive load. The RMSD values also follow the severity of the damage giving an indication of the structure's condition.

One of the shortcomings of the method observed during the bending of the beam specimen is the restricted sensing area of the PZT patch. This is mainly due to the low energy transferred via the impedance analyzer, introducing a voltage of 1 Volt amplitude (2 Volts peak to peak). The current impedance analyzers available can produce alternate current of up to 2 Volts amplitude. This makes the method sufficient only for near field damage detection. The above assumption is well supported by experimental results as the failure in the center of the beam (roughly 110 mm from the patches) was undetectable by both patches.

In order to overcome this weakness an attempt was made using a low cost set up using a function generator and a digital oscilloscope. This way we are no longer restricted in producing low energy waves, as we can reach even without an amplifier up to 10 Volts. This attempt described in the last chapter gives encouraging results, although further discussion is needed in order to overcome problems concerning the stability of the circuit and its proper electric insulation to ensure isolation from ambient noise from nearby electronic devices.

10 Conclusions and topics for further discussion

The advantages and disadvantages of the EMI technique over conventional NDE methods have already been discussed in previous chapters, as well as in other research works. To sum up the basic advantages are the following: i) no bulky equipment is involved, as the PZT patches are small and can be permanently bonded to the structure without changing its dynamic characteristics or rendering it out of service, ii) possesses great sensitivity in local damage compared with the global techniques, iii) results are taken in frequency domain without needing further processing, iv) the ability to provide an on line SHM system.

The basic drawbacks of the method are i) the great sensitivity of the PZT patches in environmental conditions (moisture and temperature), ii) the sensitivity of the patches in impacts and loading and iii) the restricted active sense area of the patch (although this leads to localization of the damage) making the use of large number of PZTs essential, raising the cost of the structure.

As far as the embedded technique that is proposed in the present, compared with conventional surface bonded EMI technique there are certain pros and cons as well as points that need further examination. The basic advantages are: i) the ability to perform early age monitoring of the concrete, as there is no need for hardened surface in order to bond the patch, like in surface bonded EMI, ii) the patch is very well protected from both environmental conditions as well as impacts and iii) better introduction of waves, as they propagate through the whole body of the structure rather than just the surface.

The basic drawbacks of the technique are: i) the inability of service in case of damage in the PZT (bad wiring, etc.), ii) high possibility of wiring tearing in the concrete resulting in bad measurements and iii) more materials are involved making the whole structure more complex, resulting into greater difficulty in modeling. In surface bonded technique we are only interested in the bonding quality between the PZT patch and the structure while in embedded technique we are also interested in the interaction between structure and the smart aggregate.

A lot of work needs to be done before the full commercialization of this very promising technique. A great amount of research is found in the literature in order to alleviate the shortcomings of the EMI technique, including the reusability or the application of an on-line SHM technique using AD5933 miniaturized chips, to name some. Specifically, as far as the EMI technique using embedded PZTs is concerned, the topics of discussion that come up from the experimental results carried out for this master thesis are the following: i) the expansion of the sensing area of the patch. Efforts are made in this direction with the application of the circuit described in chapter 9.3.3. The option of applying higher voltage, and thus greater energy, in the structure even without amplifier allows us to enlarge the sensing area. The combination of amplifying using a guided wave also gives us the ability to perform both near and far field damage detection. ii) The size of the smart aggregate. An attempt needs to be done to reduce the size of the smart aggregate to a size of coarse gravel aggregate, if it is to be used in real life structures. For example, inserting a 50x50x50 mm cube in a joint of a reinforced concrete frame, would create huge problems (if not making it impossible) in the procedure of casting the

concrete, due to the lack of free space. iii) The need to replace the silicon rubber which serves as water proofing of the patch, with a stiffer material as due to its high flexibility absorbs portion of the energy of the patch acting like a damper.

Appendix A – Ferroelectricity and Piezoelectricity

Piezoelectric materials having the following properties are generally classified as ferroelectric: a permanent dipole, the ability to switch the dipole orientation with the application of a sufficiently high electric field, and the existence of what is known as a Curie temperature above which the material enters a non-polar, non-ferroelectric, paraelectric crystal phase. Ferroelectric materials tend to behave as linear dielectrics under low electric fields and often have extremely high permittivities. The permittivity of all ferroelectric materials is dependent upon frequency, field, elastic stress, and temperature, although this dependence is generally more severe for polymeric ferroelectrics.

Linear reversible dipole rotation under electric field occurs in all dielectric materials, including ferroelectrics. However, when ferroelectric materials are subjected to high fields the energy in the material is sufficient to overcome internal energy barriers and cause permanent dipole rotation. This process is known as poling and the resulting permanent dielectric displacement is a phenomenon unique to ferroelectric materials. Poling tends to align the randomly oriented dipoles in an unpoled ferroelectric and thus produces a net non zero polarization in the bulk material. Poling is the mechanism through which ferroelectric materials become macroscopically piezoelectric.

As seen in Figure A.1.1, poling induced dipole reorientation results in a large charge displacement which remains after the applied field returns to zero. Application of a high field of the opposite polarity will result in dipole reversal and a large charge displacement of the opposite polarity. When subjected to high AC fields, ferroelectric materials exhibit a classical D/E hysteresis, as shown in Figure A.1.2. The hysteretic D/E relationship is the most fundamental description of ferroelectric behavior, with two key parameters: coercive field, E_c , and remnant polarization, P_r . E_c is defined as the field at which the total displacement is zero and is approximately equal to the field at which half of the dipole reversal has occurred. P_r is defined as the displaced charge remaining at zero field.

It is important to note that linear piezoelectricity occurs only in the linear regions shown in Figures A.1.1, 2. An unpoled ferroelectric material has a linear dielectric slope in the low field region of the D/E curve, but since $P_r = 0$ for this condition, all of the piezoelectric coefficients are ≈ 0 , as they are intrinsically a function of P_r . In this work it is assumed that all fields on piezoelectric materials remain below the point at which polarization reversal occurs and in the resulting constitutive equations piezoelectricity is a linear phenomena.

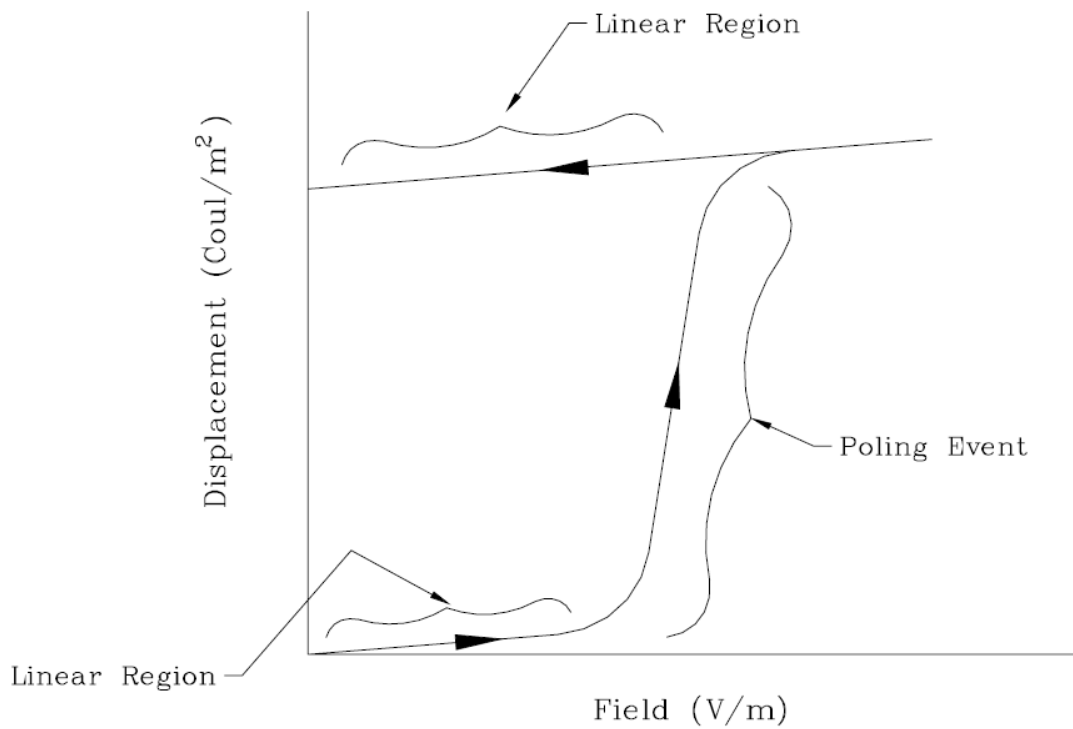


Figure A.1.1 Ferroelectric poling event, applied field cycled from 0 to maximum, then back to 0.

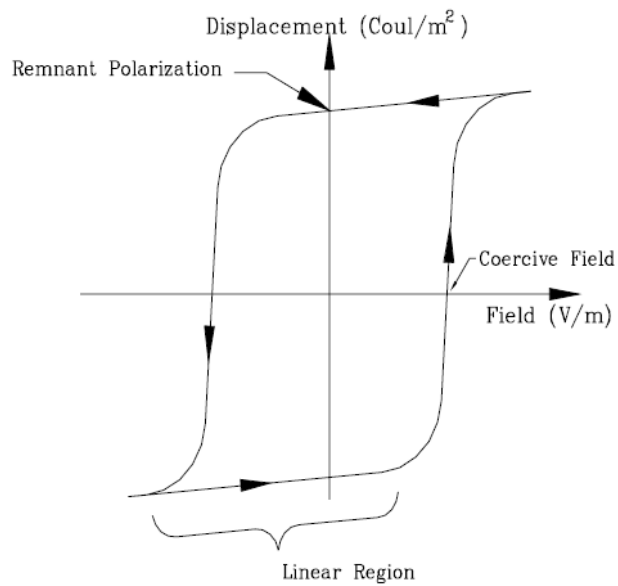


Figure A.1.2 Displacement/Electric field curve for a ferroelectric material showing typical switching hysteresis and linear dielectric regions.

All crystal structures can be classified into one of 32 possible forms of crystal symmetry. Eleven of these forms are centrosymmetric. Of the remaining 21 non-centrosymmetric groups, 20 are known to be piezoelectric, meaning these materials produce an electric surface charge in response to applied mechanical stress. In 10 of these crystal groups there is a permanent electric dipole, and the equilibrium of the electrostatic potential caused by this dipole is distorted by mechanical stress (piezoelectricity) or temperature change (pyroelectricity). Certain pyroelectric materials can be further classified as ferroelectric materials, as shown in the summary diagram in Figure A.1.3. Examples of the non-centrosymmetric (ferroelectric) and the centrosymmetric (paraelectric) crystal structures typical of common ceramic ferroelectric perovskites (ABO_3) are shown in Figure A.1.4.

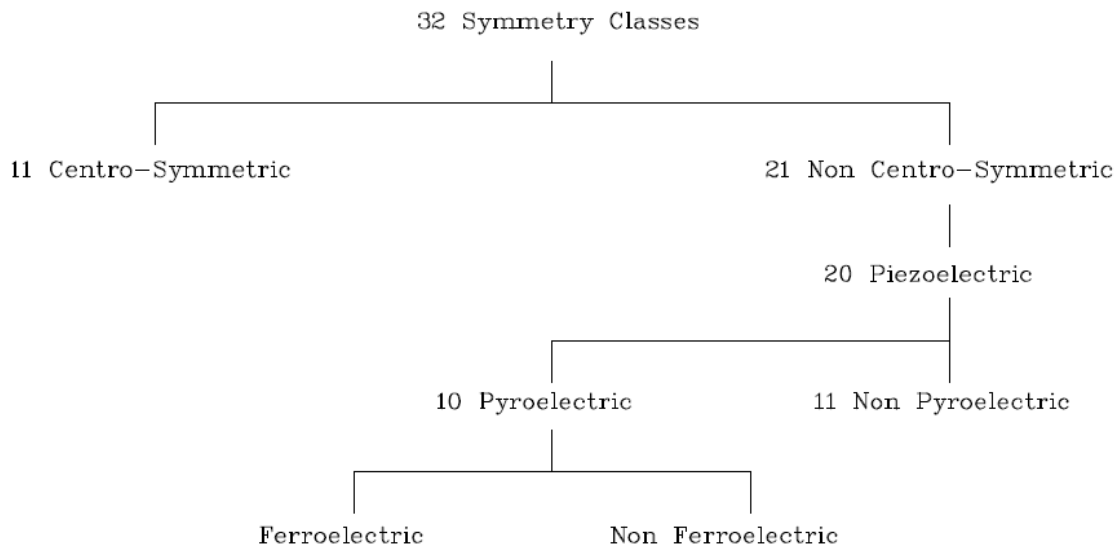


Figure A.1.3 Crystal symmetry diagram

Rochelle salt is the earliest reported piezoelectric material. It was first produced in France in 1665 for medicinal use by pharmacist Elie Seignette. Brewster discussed the pyroelectric properties of this material in 1824. Pioneering work on the direct piezoelectric effect (stress \rightarrow charge) in this material was presented by Jacques and Pierre Curie in 1880. In 1881, Lippmann proposed the converse piezoelectric effect based upon thermodynamic principals and this outcome was verified by the Curie brothers, whose early efforts included natural crystals such as tourmaline, topaz, quartz, in addition to Rochelle salt. Their work resulted in the development of the first scientific instruments using the piezoelectric effect to measure force in the direct mode and high voltages in the converse mode.

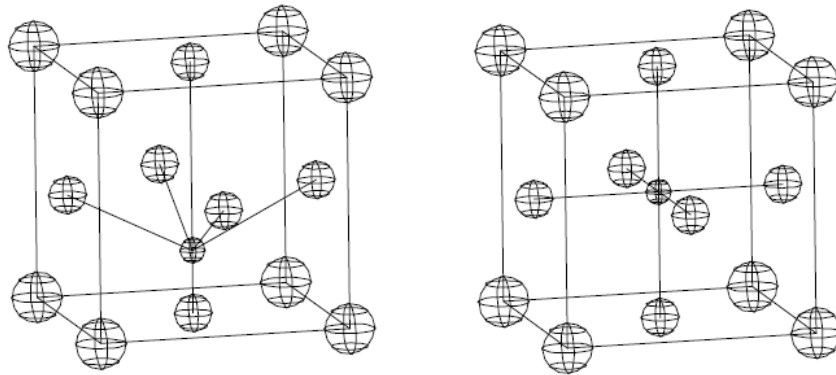


Figure A.1.4 Ferroelectric (left) and Paraelectric crystal phases of a perovskite. Note the asymmetry in the ferroelectric form

Research on these piezoelectric materials continued throughout the early twentieth century, in part stimulated by military interests arising from World War I. A major outcome of this research was the use of piezoelectric quartz in acoustic projectors and receivers. Ferroelectricity, described by hysteresis behavior, was suggested by Schrödinger in 1912, and was more firmly established by Valasek in the 1920's primarily working with triglycine sulphate (TGS) and Rochelle salt.

World War II brought increased attention to the study of piezoelectric materials, especially for use in radio communications and underwater acoustic applications. The discovery of BaTiO₃ and other highly piezoelectric materials with a perovskite structure in the latter half of the 1940's by researchers in the US, England, Russia, and Japan led to a renewed interest in the study of ferroelectric materials. In the early 1950's ferroelectric lead zirconium titanate ceramics (PZT) were introduced with even higher performance. This precipitated further work and led to a greater understanding of the structure and behavior of polycrystalline ferroelectrics. Extensive research and development throughout the last four decades has led to the use of piezoelectric ceramics in a wide variety of commercial, consumer, and military applications [2] ranging from inexpensive tonal buzzers used in toys to sophisticated ultrasound imaging transducers used in the latest medical procedures, from consumer fish finders to highly complex submarine sonar systems, and from simple grill ignitors to all manner of force and acceleration sensors.

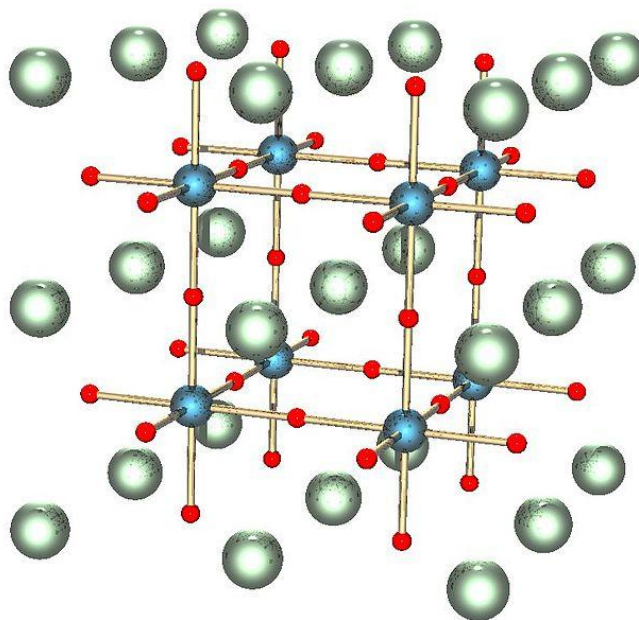
Appendix B – Perovskite structure

A perovskite structure is any material with the same type of crystal structure as calcium titanium oxide (CaTiO_3), known as the perovskite structure, or $^{\text{XII}}\text{A}^{2+\text{VI}}\text{B}^{4+\text{VI}}\text{X}^{2-}_3$ with the oxygen in the face centers. Perovskites take their name from this compound, which was first discovered in the Ural mountains of Russia by Gustav Rose in 1839 and is named after Russian mineralogist L.A. Perovski (1792–1856). The general chemical formula for perovskite compounds is ABX_3 , where 'A' and 'B' are two cations of very different sizes, and X is an anion that bonds to both. The 'A' atoms are larger than the 'B' atoms. The ideal cubic-symmetry structure has the B cation in 6-fold coordination, surrounded by an octahedron of anions, and the A cation in 12-fold cuboctahedral coordination. The relative ion size requirements for stability of the cubic structure are quite stringent, so slight buckling and distortion can produce several lower-symmetry distorted versions, in which the coordination numbers of A cations, B cations or both are reduced.

The perovskite structure is adopted by many oxides that have the chemical formula ABO_3 . In the idealized cubic unit cell of such a compound, type 'A' atom sits at cube corner positions (0, 0, 0), type 'B' atom sits at body centre position (1/2, 1/2, 1/2) and oxygen atoms sit at face centred positions (1/2, 1/2, 0). (The diagram shows edges for an equivalent unit cell with B at the corners, A in body centre, and O in mid-edge).

The relative ion size requirements for stability of the cubic structure are quite stringent, so slight buckling and distortion can produce several lower-symmetry distorted versions, in which the coordination numbers of A cations, B cations or both are reduced. Tilting of the BO_6 octahedra reduces the coordination of an undersized A cation from 12 to as low as 8. Conversely, off-centering of an undersized B cation within its octahedron allows it to attain a stable bonding pattern. The resulting electric dipole is responsible for the property of ferroelectricity and shown by perovskites such as BaTiO_3 that distort in this fashion. The orthorhombic and tetragonal phases are most common non-cubic variants. Complex perovskite structures contain two different B-site cations. This results in the possibility of ordered and disordered variants.

As pressure increases, the O^{2-} ions compress so olivine transforms to the spinel structure, which at still higher pressure converts to a perovskite structure and a coexisting periclase structure. At the high pressure conditions of the Earth's lower mantle, the pyroxene enstatite, MgSiO_3 , transforms into a denser perovskite-structured polymorph; this phase may be the most common mineral in the Earth. This phase has the orthorhombically distorted perovskite structure (GdFeO_3 -type structure) that is stable at pressures from ~24 GPa to ~110 GPa. However, it cannot be transported from depths of several hundred km to the Earth's surface without transforming back into less dense materials. At higher pressures, MgSiO_3 perovskite transforms to post-perovskite.



Structure of a perovskite with a chemical formula ABX_3 . The red spheres are X atoms (usually oxygen), the blue spheres are B-atoms (a smaller metal cation, such as Ti^{4+}), and the green spheres are the A-atoms (a larger metal cation, such as Ca^{2+}). Pictured is the undistorted cubic structure; the symmetry is lowered to orthorhombic, tetragonal or trigonal in many perovskites.

Although the most common perovskite compounds contain oxygen, there are a few perovskite compounds that form without oxygen. Fluoride perovskites such as $NaMgF_3$ are well known. A large family of metallic perovskite compounds can be represented by RT_3M (R: rare-earth or other relatively large ion, T: transition metal ion and M: light metalloids). The metalloids occupy the octahedrally coordinated "B" sites in these compounds. RPd_3B , RRh_3B and $CeRu_3C$ are examples. $MgCNi_3$ is a metallic perovskite compound and has received lot of attention because of its superconducting properties. An even more exotic type of perovskite is represented by the mixed oxide-aurides of Cs and Rb, such as Cs_3AuO , which contain large alkali cations in the traditional "anion" sites, bonded to O^{2-} and Au^- anions.

Perovskite materials exhibit many interesting and intriguing properties from both the theoretical and the application point of view. Colossal magnetoresistance, ferroelectricity, superconductivity, charge ordering, spin dependent transport, high thermopower and the interplay of structural, magnetic and transport properties are commonly observed features in this family. These compounds are used as sensors and catalyst electrodes in certain types of fuel cells and are candidates for memory devices and spintronics applications. Many superconducting ceramic materials (the high temperature superconductors) have perovskite-like structures, often with 3 or more metals including copper, and some oxygen positions left vacant. One prime example is yttrium barium copper oxide which can be insulating or superconducting depending on the oxygen content. Chemical engineers are considering a cobalt-based perovskite material as a replacement for platinum in catalytic converters in diesel vehicles.

References

- [1] Richard J. Wasley, *Stress Wave Propagation in Solids, An Introduction*, Marcel Dekker Inc, New York, 1973
- [2] Julian L. Davis, *Wave Propagation in Solids and Fluids*, Springer-Verlag, New York, 1988
- [3] Kyriakos K. Anastasiadis, *Dynamics of Structures vol I&II*, Ziti, Thessaloniki 1999
- [4] Ioanna Pappagianni-Pappadopoulou, *Behavior and properties of reinforced concrete*, University notes, Aristotle University of Thessaloniki, 2006
- [5] C. Providakis, K. Stefanaki, M. Voutetaki, J. Tsompanakis, M. Stavroulaki and J. Agadakos, *An Integrated Approach for Structural Health Monitoring of Concrete Structures Based on Electromechanical Admittance and Guided Waves*, 6th ECCOMAS Conference on Smart Structures and Materials, 24-26 June 2013
- [6] K. Efthymiadis, O. Kalogirou, I.M. Kyprianidis, K. Melidis, A. Siakavara, A. Sianou, G. Stoikos, I. Stoumpoulos, S. Hatzivasileiou, *Principles of Electric Circuits*, Sygxroni Paideia, Thessaloniki 2002
- [7] N. A. Oikonomou, *An Introduction to Solid Matter Physics*, Thessaloniki 1983
- [8] K. A. Karympakas, *General Electronics vol I*, Thessaloniki 1996
- [9] S. Bhalla and C. K. Soh, *Electro-Mechanical Impedance Technique for Structural Health Monitoring and Non-Destructive Evaluation*, Indian Institute of Technology Delhi, 2008
- [10] S. Bhalla and C. K. Soh, *Calibration of Piezo-Impedance Transducers for Strength Prediction and Damage Assessment of Concrete*, Institute of Physics Publishing, New Delhi, 2005
- [11] S. Bhalla, C.K. Soh, K.K-H. Tseng, A. Gupta, *Performance of Smart Piezoceramic Patches in Health Monitoring of a RC Bridge*, IOP Publishing Ltd, 2000
- [12] G. Song, H. Gu, Y. L. Mo, T. T. C. Hsu, H. Dhonde, *Concrete Structural Health Monitoring Using Embedded Piezoceramic Transducers*, IOP Publishing Ltd, 2007
- [13] K. K. Tseng, L. Wang, *Smart Piezoelectric Transducers for In Situ Health Monitoring of Concrete*, IOP Publishing Ltd, 2004
- [14] Y. Yang, Y. Hu, Y. Lu, *Sensitivity of PZT Impedance Sensors for Damage Detection of Concrete Structures*, Sensors MDPI, 2008
- [15] Y. Yang, B. S. Divsholi, C. K. Soh, *A Reusable PZT Transducer for Monitoring Initial Hydration and Structural Health of Concrete*, Sensors MDPI, 2010
- [16] W. Quinn, G. Kelly, J. Barrett, *Development of an Embedded Wireless Sensing System for the Monitoring of Concrete*, Structural Health Monitoring SAGE, 2012
- [17] Quadtech, *LCR Measurement Primer*, July 2003
- [18] S. Bhalla, A. Gupta, *Modelling Shear Lag Phenomenon for Adhesively Bonded Piezo-Transducers*, Piezoelectric Ceramics, book edited by Ernesto Suaste-Gomez, ISBN 978-953-307-122-0, Published: October 5, 2010
- [19] S. E. Prasad, D. F. Waechter, R. G. Blacow, H. W. King, *Application of Piezoelectrics to Smart Structures*, Sensor Technology Ltd, 2005

- [20] S. Bhalla, A. Gupta, S. Bansal, T. Gard, *Ultra Low-cost Adaptations of Electro-mechanical Impedance Technique for Structural Health Monitoring*, Structural Health Monitoring SAGE, 2009
- [21] S. W. Shin, A. R. Qureshi, J. Y. Lee and C. B. Yun, *Piezoelectric sensor based nondestructive active monitoring of strength gain in concrete*, IOP Publishing, Smart Materials And Structures, June 2008
- [22] Z. H. U. Jinsong, G. A. O. Change, H.E. Likun, *Piezoelectric-based Crack Detection Techniques of Concrete Structures: Experimental Study*, Journal of Wuhan University of Technology-Mater. Sci. Ed., April 2012
- [23] G. Song, H. Gu and Y. L. Mo, *Smart aggregates: multi-functional sensors for concrete structures a tutorial and a review*, IOP Publishing, Smart Materials And Structures, January 2008
- [24] S. Bhalla, C.K. Soh, *Structural impedance based damage diagnosis by piezo transducers*, John Wiley & Sons, Ltd., 2003
- [25] Z. H. U. Jinsong, H.E. Likun, *Study on Piezoelectric Actuator/sensor Wave Propagation based Nondestructive Active Monitoring Method of Concrete Structures*, November 2010
- [26] G. Park, D. J. Inman, *Structural Health Monitoring Using Piezoelectric Impedance Measurements*, Philosophical Transactions of the Royal Society, 2006
- [27] F. Hey, S. Bhalla and C. K. Soh, *Optimized Parallel Interrogation and Protection of Piezo-transducers in Electromechanical Impedance Technique*, Journal of Intelligent Material Systems and Structures, 2006
- [28] R. Tawie, H.K. Lee, *Monitoring the strength development in concrete by EMI sensing technique*, Construction and Building Materials, 2010
- [29] C. P. Providakis, E. V. Liarakos, and E. Kampianakis, *Nondestructive Wireless Monitoring Of Early-Age Concrete Strength Gain Using an Innovative Electromechanical Impedance Sensing System*, Hindawi Publishing Corporation, March 2013
- [30] S. Bhalla, C. G. Soh, *Structural Health Monitoring by Piezo-Impedance Transducer, I:Modelling*, Journal of Aerospace Engineering, volume 17, October 2004
- [31] K. Kabeya, *Structural Health Monitoring Using Multiple Piezoelectric Sensors and Actuators*, thesis submitted to the faculty of Virginia Polytechnic Institute and State University in partial fulfillment of the requirements of the degree of Master of Science in Mechanical Engineering, Virginia 1998
- [32] D. F. Jones, S. E. Prasad, J. B. Wallace, *Piezoelectric Materials and Their Applications*, Sensor Technology Ltd, 1996
- [33] Jim Emery, *Piezoelectricity*, 1997
- [34] A.L. Kholkin, N. A. Pertsev, A. V. Goltsev, *Piezoelectric and Acoustic Materials for Transducer Applications*, Springer-Verlag US, 2008
- [35] PI Ceramic, *Piezoelectric Ceramic Products*
- [36] W.G. Cady, *Piezoelectricity*, (McGraw-Hill, New York, 1946

- [37] R.J. Haüy, *Sur l'électricité produite dans les minéraux à l'aide de la pression*, *Mémoires du Muséum d'Histoire Naturelle* (Paris) 3, 223-228 (1817); reprinted in *Ann. Chim. Et Phys.* 5, 95-101 (1817)
- [38] A.C. Becquerel, "Sur le développement de l'électricité dans les corps par la pression et la dilatation," *Bulletin des Sciences*, par la Société Philomatique de Paris 7, 149-155 (1820); "Sur le développement de l'électricité par la pression; Lois de ce développement," *Ann. Chim. et Phys.* 22, 5-34 (1823)
- [39] Curie and P. Curie, *Développement par compression de l'électricité polaire dans les cristaux hémiédres à faces inclinées*, *Bulletin de la Société Minéralogique de France* 3, 90-93 (1880); also in *Compt. Rend.* 91, 294-295, 383-386 (1880)
- [40] G. Lippmann, *Sur le principe de la conservation de l'électricité*, *Compt. Rend.* 92, 1049-1051, 1149-1152 (1881); also in the *Journal de Physique* 10, 381-394 (1881); and in *Ann. Chim. et Phys.* 24, 145-172 (1881)
- [41] Curie and P. Curie, *Contractions et dilations produites par des tensions électriques dans les cristaux hémiédres à faces inclinées*, *Compt. Rend.* 93, 1137-1140 (1881); also in *Oeuvres de Pierre Curie*, (Gauthier-Villars, Paris, 1908)
- [42] Sir W. Bragg and R.E. Gibbs, *The structure of α and β quartz*, *Proc. Roy. Soc. A.* 109, 405-427 (1925)
- [43] S. Butterworth, *On electrically-maintained vibrations*, *Proc. Phys. Soc.* 27, 410-424 (1915)
- [44] W.G. Cady, *The piezo-electric resonator*, *Proc. I.R.E.* 10, 83-114 (1922)
- [45] K.S. Van Dyke, "The electric network equivalent of a piezo-electric resonator," *Phys. Rev.* 25, 895 (A) (1925); also "The piezo-electric resonator and its equivalent network," *Proc. I.R.E.* 16, 742-764 (1928)
- [46] I. Curie and P. Curie, French Patent Number 183,851, dated 27 May 1887
- [47] P. Langevin, French Patent Number 505,703, dated 14 May 1920; and P. Langevin and C.L. Florisson, French Patent Number 575,435, dated 22 April 1924.
- [48] A.M. Nicolson, *The piezo-electric effect in the composite Rochelle salt crystal*, *Trans. A.I.E.E.* 36, 1461-1485 (1919); and *Proc. A.I.E.E.* 36, 1315-1333 (1919)
- [49] G.W. Pierce, *Piezoelectric crystal resonators and crystal oscillators applied to the precision calibration of wavemeters*, in *Proceedings of the American Academy of Arts and Sciences* 59, 81-106 (1923)
- [50] F.V. Hunt, *Electroacoustics*, American Institute of Physics, New York, 1982
- [51] E. Buehler, *Growing quartz crystals*, *Bell Laboratories Record* 31, 241-246 (1953)
- [52] W.P. Mason, *Multiple reflection ultrasonic delay lines*, in *Physical Acoustics*, Volume 1 Part A, edited by W.P. Mason, (Academic, New York, 1964), pp. 485-500
- [53] G.W. Pierce, in *Proceedings of the American Academy of Arts and Sciences* 60, 269 (1925)
- [54] B. Jaffe, W.R. Cook, and H. Jaffe, *Piezoelectric Ceramics*, Academic Press, London, 1971
- [55] V.M. Goldschmidt, *Shrifter Norske Videnskaps-Akad. Oslo, I:Mat.-Naturv. Kl. No. 2*, 8 (1926)
- [56] H. Thumauer and J. Deaderick, U.S. Patent Number 2,429,588, dated 21 October 1947 (filed 2 October 1941).

- [57] B.M. Wul and I.M. Goldman, Dokl. Akad. Nauk SSSR 49, 179-182 (1945); and Compt. Rend. Acad. Sci. URSS 49, 177-120 (1945).
- [58] A. von Hippel, R.G. Breckenridge, F.G. Chesley, and L. Tisza, Ind. Eng. Chem. 38, 1097-1109 (1946).
- [59] R.B. Gray, U.S. Patent Number 2,486,560, dated 1 November 1949 (filed 20 September 1946).
- [60] S. Roberts, *Dielectric and piezoelectric properties of barium titanate*, Phys. Rev. 71, 890-895 (1947).
- [61] T.A. Perls and C.W. Kissinger, *A barium titanate accelerometer with wide frequency and acceleration ranges*, National Bureau of Standards Report 2390 (1953).
- [62] S. Edelman, E. Jones, E.R. Smith, B.D. Simmons, and R.C. Braunberg, *Self-noise of projectiles*, National Bureau of Standards Report 3465 (1954).
- [63] J.D. Wallace, J.R. Brown, D.H. Lewis, and D.H. Dietz, *Acoustic mapping within the heart*, J. Acoust. Soc. Am. 29, 9-15 (1957).
- [64] D.H. Lewis, D.H. Dietz, J.D. Wallace, and J.R. Brown, *Intracardiac phonocardiography in man*, Circulation 16, 764-775 (1957).
- [65] S. Wada and N. Yamamoto, *Honeycomb structured BaTiO₃ ceramics for heater applications*, NGK Technical Report R-75-2 (1975)
- [66] G. Shirane, S. Hoshino, and K. Suzuki, *X-ray study of the phase transition in lead titanate*, Phys. Rev. 80, 1105-1106 (1950); and I. Phys. Soc. Jpn. 5, 453-455 (1950)
- [67] G.A. Smolenskii, Zh. Tekhn. Fiz. 20, 137-148 (1950); and Dokl. Akad. Nauk SSSR 70, 405-402 (1950)
- [68] S. Roberts, *Dielectric properties of lead zirconate and barium-lead zirconate*, J. Am. Ceram. Soc. 33, 63-66 (1950)
- [69] E. Sawaguchi, H. Maniwa, and S. Hoshino, *Anti-ferroelectric structure of lead zirconate*, Phys. Rev. as, 1072 (1951)
- [70] G. Goodman, Am. Ceram. Soc. Bull. 31, 113 (1952); and *Ferroelectric properties of lead metaniobate*, J. Am. Ceram. Soc. 36, 368-372 (1953)
- [71] G. Shirane and K. Suzuki, *Crystal structure of Pb(Zr-Ti)O₃*, J. Phys. Soc. Jpn. 7, 333 (1952)
- [72] E. Sawaguchi, *Ferroelectricity versus anti-ferroelectricity in the solid solutions of PbZrO₃ and PbTiO₃*, J. Phys. Soc. Jpn. 8, 615-629 (1953)
- [73] B. Jafle, R.S. Roth, and S. Marzullo, *Piezoelectric properties of lead zirconate-lead titanate solid-solution ceramic ware*, J. Appl. Phys. 25, 809-810 (1954)
- [74] R.A. Ferren, *Synthesis of poly (vinylidene fluoride) and its copolymers*, in The Applications of Ferroelectric Polymers, edited by T.T. Wang, J.M. Herbert, and A.M. Glass, (Blackie, Glasgow, UK, 1988), pp. 6-20
- [75] G.M. Sessler, *Piezoelectricity in polyvinylidene fluoride*, J. Acoust. Soc. Am. 70, 1596-1608(1981)
- [76] A.J. Lovinger, *Ferroelectric polymers*, Science 220, 1115-1121 (1983)

- [77] P.E. Bloomfield and M.A. Marcus, *Production of ferroelectric polymer films*, in *The Applications of Ferroelectric Polymers*, edited by T.T. Wang, J.M. Herbert, and A.M. Glass, (Blackie, Glasgow, UK, 1988), pp. 21-36
- [78] G.T. Davis, *Structure, morphology, and models of polymer ferroelectrics*, in *The Applications of Ferroelectric Polymers*, edited by T.T. Wang, J.M. Herbert, and A.M. Glass, (Blackie, Glasgow, UK 1988), pp. 37-65
- [79] G.M. Garner, *Microphones, headphones, and tone generators*, in *The Applications of Ferroelectric Polymers*, edited by T.T. Wang, J.M. Herbert, and A.M. Glass, (Blackie, Glasgow, U.K, 1988), pp.190-208
- [80] ATOCHEM Sensors Technical Notes, (ATOCHEM Sensors Inc., Valley Forge, Pennsylvania, 1987), pp.43-44
- [81] Wikipedia